Quantum Circuit based on Electron Spins in Semiconductor Quantum Dots

Chang-Yu Hsieh

Thesis submitted to the
Faculty of Graduate and Postdoctoral Studies
in partial fulfillment of the requirements
for the degree of Doctor of Philosophy in Physics[1]

Department of Physics
Faculty of Science
University of Ottawa

[1]The Ph.D. program is a joint program with Carleton University, administered by the Ottawa-Carleton Institute Of Physics

Thesis advisor

Dr. Pawel Hawrylak

Author

Chang-Yu Hsieh

Quantum Circuit based on Electron Spins in Semiconductor Quantum Dots

Abstract

In this thesis, I present a microscopic theory of quantum circuits based on interacting electron spins in quantum dot molecules. We use the Linear Combination of Harmonic Orbitals-Configuration Interaction (LCHO-CI) formalism for microscopic calculations. We then derive effective Hubbard, t-J, and Heisenberg models. These models are used to predict the electronic, spin and transport properties of a triple quantum dot molecule (TQDM) as a function of topology, gate configuration, bias and magnetic field.

With these theoretical tools and fully characterized TQDMs, we propose the following applications:

1. Voltage tunable qubit encoded in the chiral states of a half-filled TQDM. We show how to perform single qubit operations by pulsing voltages. We propose the "chirality-to-charge" conversion as the measurement scheme and demonstrate the robustness of the chirality-encoded qubit due to charge fluctuations. We derive an effective qubit-qubit Hamiltonian and demonstrate the two-qubit gate. This provides all the necessary operations for a quantum computer built with chirality-encoded qubits.

2. Berry's phase. We explore the prospect of geometric quantum computing with chirality-encoded qubit. We construct a Herzberg circuit in the voltage space

and show the accumulation of Berry's phase.

3. Macroscopic quantum states on a semiconductor chip. We consider a linear chain of TQDMs, each with 4 electrons, obtained by nanostructuring a metallic gate in a field effect transistor. We theoretically show that the low energy spectrum of the chain maps onto that of a spin-1 chain. Hence, we show that macroscopic quantum states, protected by a Haldane gap from the continuum, emerge.

In order to minimize decoherence of electron spin qubits, we consider using electron spins in the p orbitals of the valence band (valence holes) as qubits. We develop a theory of valence hole qubit within the 4-band k.p model. We show that static magnetic fields can be used to perform single qubit operations. We also show that the qubit-qubit interactions are sensitive to the geometry of a quantum dot network. For vertical qubit arrays, we predict that there exists an optimal qubit separation suitable for the voltage control of qubit-qubit interactions.

Contents

List of Figures

Statement of Originality

The main body (Chapter [2] - Chapter [7]) of this thesis contains excerpts from a number of publications, submitted manuscripts, and soon-to-be submitted manuscripts that I have worked on as a Ph.D. student in Dr. Hawrylak's quantum theory group at IMS (Institute for Microstructural Sciences), NRC (National Research Council). The list below presents detailed information on the publications and manuscripts relevant for this thesis,

1. Chang-Yu Hsieh, Ross Cheriton, Marek Korkusinski, and Pawel Hawrylak, "Valence holes as Luttinger spinor based qubits in quantum dots", Phys. Rev. B **80**, 235320 (2009). (relevant for Chapter [7]).

2. Irene Gimenez, Chang-Yu Hsieh, Marek Korkusinski, and Pawel Hawrylak, "Charged-impurity-induced dephasing of a voltage-controlled coded qubit based on electron spin in a triple quantum dot", Phys. Rev. B **79**, 205311 (2009). (relevant for Chapter [3]).

3. Chang-Yu Hsieh and Pawel Hawrylak, "Quantum circuits based on coded qubits encoded in chirality of electron spin complexes in triple quantum dots", Phys. Rev. B **82**, 205311 (2010). (relevant for Chapter [3]).

4. Yun-Pil Shim, Anand Sharma, Chang-Yu Hsieh, and Pawel Hawrylak, "Artificial Haldane gap material on a semiconductor chip", Solid State Commun. **150**, 2065 (2010). (relevant for Chapter [4]).

5. Chang-Yu Hsieh, Yun-Pil Shim, and Pawel Hawrylak, "Theory of electronic properties and spin blockade in a gated linear triple quantum dot containing

(1,1,1) charge configuration", Phys. Rev. B **85**, 085309 (2012). (relevant for Chapter [6]).

6. Chang-Yu Hsieh, Alexandre René, and Pawel Hawrylak, "Herzberg circuit and Berry's phase in a triple quantum dot", submitted manuscript. (relevant for Chapter [5]).

7. Chang-Yu Hsieh, Yun-Pil Shim, Marek Korkusinski, and Pawel Hawrylak, "The physics of triple quantum dot molecules with controlled electron numbers", Report on Progress in Physics, in preparation. (relevant for Chapter [2]).

Except articles No. 4 and No. 7 on the list above, I have carried out all the calculations and derivations in full detail. As for article No. 4, Yu-Pil Shim, the first author, was mainly responsible for the derivation of effective models. Anand Sharma and I were mainly responsible for the numerical calculations. As for article No. 7, this is a review article and no new results are presented.

Acknowledgments

First of all, I would like to express my deepest gratitude towards my Ph.D. supervisor, Dr. Pawel Hawrylak, for putting up with me all these years. Although he has been an extremely busy person all year long, he always manages to set aside time for students and other group members for discussions. During our discussions, I am often inspired by his knowledge and physical insights. Beyond just physics and research, I have learnt other valuable skills, such as writing a good scholarship proposal and delivering a good presentation, from Dr. Hawrylak. Furthermore, I would like to thank him for creating a harmonious atmosphere, which allows group members to freely communicate ideas and learn from each other, in the group.

I would also like to acknowledge and thank the generous support of the Ontario government through the Ontario Graduate Scholarship that I received in the period of 2009-2011. With this generous financial support, I can worry less about living expenses and focus more on research. I also would like to thank IMS (Institute for Microstructural Sciences), NRC (National Research Council) for allowing me to work as a visitor in the institute during my Ph.D. program. Without this visitor worker agreement, I would not have been able to work under Dr. Hawrylak.

Next, I would like to thank all the colleagues, former and present, in Dr. Hawrylak's quantum theory group. Marek, thank you for your clear explanations of various subjects when I first joined the group. Your explanations always make things easier to understand. Yun-Pil, thank you very much for teaching me many things in physics. You have certainly set an example of how research should be done. Anand, I miss all the discussions, whether about physics or life in general. Without you in the office, it no longer feels the same! Eugene, thank you for your constant reminders on writing

the thesis early. You are right, I should have started way earlier! Ramin, thank you for sharing many things about research and life, and it has been a pleasure to work with you. Anna, thank you for being such an active person in the group and always trying to get everyone together to do something fun. Good luck with your thesis! Ross and Alexandre, it has been fun working with you two. Good luck with your graduate study! Alex, Devrim and Fernando, it is definitely my pleasure to get to know you. Thank you for all the good times we spent in the group. Alex, see you in Toronto!

I also would like to take this opportunity to thank Dr. Andy Sachrajda, Dr. Ghislain Granger, and Louis Gaudreau in the quantum physics group at IMS, NRC. Thank you all for taking the time to explain the experiments to me.

Last but not least, I want to thank all my family. I thank my parents for supporting my decision to pursue a career in doing research in physics. This support really means a lot to me. I also thank my wife, Irene, for her tremendous support in terms of running the household, keeping me from distractions, and encouraging me over the course of my Ph.D. program. Finally, I thank my brother and sister, Rick and Elena, are always willing to talk with me and encourage me over the phone or on Skype when I get stuck or frustrated with research. I wish to dedicate this thesis to all my family.

Chapter 1

Introduction

The goal of this thesis is to understand and exploit the electronic properties of quantum dots in order to construct a quantum circuit, an artificial device capable of storing and processing quantum information. In this chapter, we first present an overview of quantum computation and criteria for building a feasible qubit. We review a set of semiconductor systems proposed for qubit implementation. Next, we focus on semiconductor quantum dots. We discuss essential physical properties, the fabrication processes, and the experimental measurements to probe these nanostructures. We then move onto discussing the realization of quantum teleportation in a linear triple quantum dot. Teleportation is a truly quantum phenomenon which requires interactions of three qubits. Through the example of teleportation, we illustrate how the electron spin-based qubits in quantum dots can be manipulated in a realistic experiment.

1.1 Overview of Quantum Computation

In 1981, Richard Feynman [1] first discussed the fundamental difficulties of simulating a quantum system with a classical computer, whose hardware components obey the laws of classical physics, and proposed that only a quantum computer with elementary parts obeying the laws of quantum mechanics can simulate another quantum system. Around the same time, in parallel to Feynman's physics-oriented motivation of building a universal quantum simulator, the field of quantum information theory covering the topics of quantum cryptography and quantum communication had also advanced significantly with contributions from early pioneers, such as Wiesner [2], Bennett and Brassard [3, 4, 5]. However, the theoretical foundation of a quantum computer, which relies on quantum bits (qubits) to encode and process information by executing algorithms, was largely laid by David Deutsch [6].

Following Deutsch's generalization of a bit, the elementary computational resources, to a quantum mechanical two-level system, a qubit has a wavefunction of the form $|\psi\rangle = a\,|0\rangle + b\,|1\rangle$ where a and b are complex numbers under the constraint $|a|^2 + |b|^2 = 1$. The probability of finding the system in the state $|0\rangle$ is given by $|a|^2$. Similarly, the probability for state $|1\rangle$ is given by $|b|^2$. With two qubits, the overall wavefunction has the general form $|\Psi_2\rangle = a\,|00\rangle + b\,|01\rangle + c\,|10\rangle + d\,|11\rangle$, where $|a|^2 + |b|^2 + |c|^2 + |d|^2 = 1$. Similarly, for an array of N qubits, the wavefunction is expected to contain 2^N configurations in general. The facts that a set of qubits is isomorphic to a set of spin-1/2 particles (with $|0\rangle \rightarrow |\uparrow\rangle$ and $|1\rangle \rightarrow |\downarrow\rangle$) and that universal quantum computing can be constructed from single qubit gates and one double

qubit gate have established a common quantum computer model [7] of N qubits,

$$\hat{H} = \sum_{i=1}^{N} \mathbf{h}_i \cdot \mathbf{S}_i + \sum_{i>j} J_{ij} \mathbf{S}_i \cdot \mathbf{S}_j, \tag{1.1}$$

where $\mathbf{h}_i$ is an effective magnetic field acting on the i-th spin (qubit) and $\mathbf{S}_i$ is the vector of Pauli matrices for the i-th spin (qubit). This is certainly not the only feasible Hamiltonian to simulate qubits. For instance, a physical system with its constituents interacting via Ising interaction can also be used as qubits.

In 1994, Peter Shor invented an algorithm [8] for factoring a large number into its prime constituents on a quantum computer. The computational cost of Shor's algorithm is proportional to N^2 for an N-digit number, while the cost of the best classical factoring algorithm is of the order of $e^{N^{1/3}}$ for the same N-digit number. Factoring a large number is a classic example of an NP (nondeterministic polynomial time) problem in the theory of computational complexity, and Shor's algorithm proves that some NP problems can be solved "efficiently" on a quantum computer by reducing the exponential cost to a polynomial cost. The power of a quantum computer can essentially be attributed to two key properties of qubits: superposition and entanglement. With an exponential increase in the size of Hilbert space for N qubits, the superposition and entanglement allow us to simultaneously process a large number of inputs. The only dilemma for this "quantum parallelism" is due to the fundamental constraint associated with the measurement process, which can only provide access to one of the many computed outputs at a time. Therefore, the advantage of quantum parallelism is not readily available, and ingenious algorithms like Shor's and Grover's [9], which are very different from what a classical computer scientist is accustomed to, are much needed for taking advantage of the full potential of a quantum

computer. The invention of Shor's algorithm establishes the usefulness of a quantum computer for computational purposes other than simulating another quantum system and generated interest among researchers in different fields, and paves the way for the development of quantum computers.

1.1.1 DiVincenzo's Criteria: Search for a Physical Qubit

To guide construction of a quantum computer in a laboratory, the very first task is to identify a suitable quantum mechanical system to function as a qubit. Not only must the system be mapped onto a quantum computer model, such as Eq.(1.1), but it also has to possess several other desirable properties, such as long coherence time and scalability. To facilitate the process of selecting a promising physical system, DiVincenzo [10] proposed the following five criteria:

1. Well-defined two-level system with high scalability,
2. Initialization to a pure state,
3. Universal set of quantum gates,
4. Qubit measurement,
5. Long coherence time.

The one criterion that probably causes the most concern for many physical realizations of a qubit is the coherence property. There exists conflicting demands on the ability of a qubit to couple to its environment. Since quantum information is encoded in the phases, a continuous variable, of a qubit, it is necessary to have a way

to strongly couple the qubit to external circuitry in order to perform quantum information processing with high fidelity. On the other hand, a qubit has to be, at best, weakly coupled to its uncontrolled environment (for instance, phonons and nuclear spins in a solid state device) in order to preserve the encoded quantum information. The dilemma of weak / strong coupling to uncontrolled / controlled environment makes the "long coherence time" a less straightforward criterion. For a physical system with extremely long coherence time, it might take a long time to encode and manipulate the information; therefore, the system allows more time for error to be introduced due to decoherence. This issue is however settled, at least theoretically, with the invention of quantum error correction codes [11, 12] and the concept of fault tolerant computation [13, 14]. A theoretical threshold [15] of roughly 1 error per 10^4 quantum operations has been established for quantum error correction to reverse any errors during the computation process. Any physical system which satisfies the error correction threshold can be considered to possess a long coherence time. The last but not the least criterion, scalability, the capability of having more than just a few qubits working coherently together, turns out to be a crucial factor. Some advanced quantum computations have been demonstrated with qubits built with nuclear spins in liquid solution [16]. Nevertheless, due to the limited scalability (up to the order of 10 qubits), these systems are not likely to form the basis of future, large scale quantum computers.

1.1.2 Semiconductor Qubits

In this section, we discuss a subset of solid state qubits in further detail. In 1996, Brum and Hawrylak [17] proposed quantum information processing with electrons in quantum dots. In this study, a connection is made between the second quantization representations of electrons in a network of quantum dots and the representation of bits in computer science. For instance, for N electrons in N_{QD} dots (with one orbital in each dot), the second quantization representation of a possible configuration is $|0, 1, 1, 0, \dots\rangle$ where each 0 / 1 denotes the absence / presence of an electron on a particular dot and in a particular spin state. This led to the idea of charged qubits in a multi-dot device. For instance, a charged qubit in a double dot has two distinct states: electron in the left dot or in the right dot. Following Barenco's proposal, the controlled-NOT (CNOT) gate for two charged qubits in a 4-dot device was shown to be achievable with the use of an external electric field, which polarizes the dots and generates electric dipole interaction to couple the charges. Besides quantum circuits of charged qubits, the 4-dot device with two electrons was also shown to be capable of simulating quantum cellular automata.

In 1998, another proposal for implementing qubits with electrons in quantum dots was put forward by Loss and DiVincenzo [18]. The difference this time is that they proposed to implement each qubit with a single electron spin. In Ref. [18], Loss and DiVincenzo assumed that the electron-electron interaction can be conveniently modelled by the Heisenberg interaction defined in Eq.(1.1) with the exchange interaction J controlled by voltages on electrostatic gates. In this model, electron spins are rotated via electron spin resonance (ESR) techniques. A two qubit operation,

$\sqrt{SWAP}$, which is explained in detail in Sec.[1.3.2], can be generated by turning on-off exchange interactions.

Beyond electrons in quantum dots, Bayer et. al. [19] proposed to use a pair of vertically aligned self-assembled quantum dots to implement quantum gates. In this proposal, an exciton (electron-hole pair) is generated optically. With an electric field along the growth direction of the dots, the particles can be localized in either of the two dots, which form the two states of a qubit. The dependence of the emission spectrum on the inter-dot distance indicates that the electron and hole undergoes coherent tunneling through the double dot and the Coulomb interaction between the electron and hole leads to an entangled state.

In addition to electrons and holes, Kane [20] proposed a model of a quantum computer based on an array of phosphorous donors embedded in a silicon lattice. His proposal is often believed to combine the advantages of a NMR-based system and a quantum dots-based system. In this proposal, a single qubit is the spin state of the donor nucleus with an extremely long coherence time. Single qubit operation is achieved with a time-dependent magnetic field. Double qubit operation is facilitated by the presence of more itinerant electron spins. Electrostatic gates (as in quantum dots) are used to shape the electrostatic environment of the nuclear and electron spins. By modifying the electrostatic potential, electrons may either tunnel between two donor sites or not.

In addition to the proposals above, in which a qubit is directly related to a particle, there exists proposals to encode quantum information in collective quantum states of a many-body system in a semiconductor. In general, a coded qubit, based on the

many-body wavefunction, is a much more complex entity than a spin-1/2 particle. However, coded qubits also have desirable features. For instance, a technological challenge with the implementation of an electron spin-based qubit in a quantum dot is the difficulty of generating a highly localized oscillating magnetic field to perform ESR on individual spins. Several proposals [21, 22, 23] have been put forward to overcome this problem. In one approach [21], a micro-magnet is fabricated to generate a magnetic field gradient. An electron spin is then moved by an oscillating electric field. As the electron moves, it experiences different magnitudes of magnetic field. In the moving reference frame of the electron, it effectively sees an oscillating magnetic field. Since the electric field can be applied with high precision, individual spins can be electrically rotated. This solution involves no significant changes in the theoretical modelling of qubits in quantum dots. In other approaches [24, 25, 26] a coded qubit is constructed out of electrons in a double dot or a triple dot. For instance, Levy [24] proposed to define the qubit as the linear superposition of states $|\uparrow_1\downarrow_2\rangle$ and $|\downarrow_1\uparrow_2\rangle$, where the subscript indicates the dot number, in a double dot. A magnetic field gradient exist in the device. So the two states have different Zeeman energies, which allows the possibility of adding phases between the two states without changing the polarization of the spins. In other words, this is the σ_z operation. Since the two spins also interact with each other via an exchange interaction, this leads to the σ_x operation. Another proposed coded qubit by DiVincenzo et al. [25] involves three spins in three sites. DiVincenzo et. al. showed that such a coded qubit can be manipulated entirely by pulsing exchange interactions. There is no need for a magnetic field gradient. In 2005, the theoretical model of a three-spin coded qubit

was shown to map well onto the lowest two states of a half-filled triple quantum dot by Hawrylak and Korkusinski [27]. This finding by Hawrylak and Korkusinski has further motivated studies of the coded qubit in a triple quantum dot, and parts of this effort are summarized in Chapter [2] and Chapter [3] of this thesis.

1.2 Quantum Dots

In this section, we describe qualitatively the electronic properties of quantum dots, which are used to implement the electron spin-based qubits, valence hole spinor qubits (chapter [7]), the three-electron coded qubits (chapter [3]), and other quantum circuits (chapters [4, 5, 6]). In this thesis, we consider both the lateral gated quantum dots and self-assembled quantum dots fabricated at the Institute for Microstructural Sciences (IMS) of the National Research Council (NRC) in Ottawa, Canada. Almost all the theoretical works I have done over the course of my ph.D. study were motivated by the relevant experimental works by Sachrajda and co-workers in the quantum physics group at IMS. I think an introduction to these devices will help readers to appreciate the way we have chosen to model these quantum dots in the later chapters, as well as to provide a better perspective of how they may be used as quantum circuits.

Quantum dots [28, 29, 30, 31, 32, 33, 34] are artificial nanostructures capable of confining electrons in all three dimensions. This strong confinement in all directions leads to the formation of a discrete energy spectrum in the dots. Furthermore, quantum dots with circular symmetry, such as the vertical gated quantum dots with parabolic confining potentials, also exhibit well-defined shell structures [34, 35] in the energy spectrum analogous to atomic electronic shells. Indeed, by studying the

electronic properties of these highly symmetrical circular quantum dots as a function of the number of electrons, a periodic table of artificial atoms can be produced and a generalized Hund's rule[36] can be attained.

Besides many similarities between atoms and quantum dots, significant differences exist. One difference is that quantum dots are large objects when compared to atoms. For instance, a consequence of this size difference is that to reach a single magnetic flux quantum, $hc/e = BA$ where h is the Planck's constant, c is the speed of light, e is the unit for electron charge, and A is the cross section area, a typical atom would require a magnetic field $\mathbf{B}$ on the order of 10^6 T; whereas the flux quanta can be attained with a field on the order of 1T in a typical quantum dots of diameter $\sim$ 100nm. Again, due to the size difference, the relevant energy scale is meV in quantum dots as opposed to eV in atoms. The small energy spacing between levels requires experiments with quantum dots to be done at low temperature. For the lateral gated quantum dots [32], the electrostatically defined potential is shallow and cannot confine electrons when the temperature is above the 1 K range. Lastly, the electrons in a semiconductor like GaAs tend to have a smaller effective mass, m_e^* (around 0.067 m_e in GaAs with electron rest mass m_e) and also experience a smaller g-factor (for instance, $g = -0.44$ in GaAs). The change in orbital energy (diamagnetic shift) in response to an applied field B is measured by the cyclotron energy $\hbar eB/m_e^*$. The ratio of diamagnetic shift for orbital energies to the Zeeman splitting, $|g\mu_B B|$ for spin in GaAs is around 75 times larger than for atoms in vacuum because of both the lighter effective mass and smaller g-factor. These findings suggest that certain experiments (mostly those involving large magnetic fields) not realistic to carry out

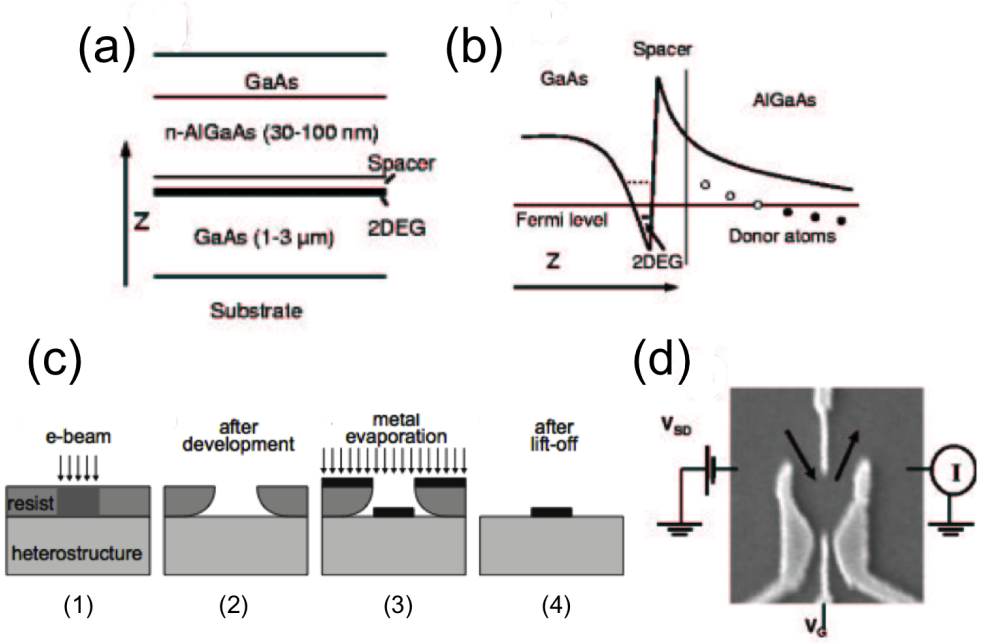

Figure 1.1: (a) Material composition of GaAs/AlGaAs heterojunction with 2DEG. (b) Conduction band profile along the growth direction. The mismatch of band across the heterojunction results in the formation of 2DEG. (c) Steps to depositing metallic gate pattern on top of the heterostructure. First, e-beam is used to etch gate pattern in a resist layer. Then the etched resist layer is locally removed. Evaporating metal. Finally, lift off the resist layer. (d) One of the first design of a gated quantum dot by IMS, NRC. (Panels (a), (b), and (d) are adapted from Ref. [37] and Fig.(c) is adapted from Ref. [38]

in atomic systems can actually be done in quantum dots.

1.2.1 Fabrication of Lateral Gated Quantum Dots

Fabrication procedures for lateral gated quantum dots can be divided into two main stages. In the first stage, molecular beam epitaxy (MBE) is used to grow a semiconductor heterostructure composed of GaAs and AlGaAs. This stage is the same for all kinds of lateral gated quantum dots (be it single, double, or triple dots). In the second stage, electron-beam (e-beam) lithography is used to define a metallic

gate pattern on top of the semiconductors. The gate pattern deposited onto the semiconductor is what determines whether the device can operate as a single quantum dot, a double quantum dot, or a triple quantum dot.

Fig.[1.1a] presents typical layers of GaAs and AlGaAs grown by MBE. First, a layer of GaAs (1-3 μm) is grown on the substrate. On top of this layer of GaAs, an undoped AlGaAs (spacer layer) is grown to form the heterostructure. Next, a layer of n-doped AlGaAs (usually doped with Si) is grown. Finally, another layer of GaAs is grown. The spacer layer is needed to shield the 2 dimensional electron gas (2DEG) from the effects of dopants. The last layer of GaAs separates the metallic gates from the dopant layer. Fig.[1.1b] shows the conduction band edge of the heterostructure along the growth direction. As we move from the GaAs towards the junction of AlGaAs along the growth direction, a triangular quantum well is developed. Conduction electrons from the n-doped layer will move to the junction and become trapped here to form a 2DEG, about 100 nm below the top surface. Fig.[1.1c] summarizes the process of depositing metallic gates with e-beam lithography. Fig.[1.1d] shows one of the earliest gate designs used to create a single quantum dot at IMS. The negative voltage applied on these gates is translated to an electrostatic potential that locally depletes the 2DEG and confines a few electrons around the local minimum of this potential.

1.2.2 Spectroscopic Tools for Lateral Gated Quantum Dots

Tunneling spectroscopy [39, 33, 40] and charge sensing [41, 42, 43, 44] are probably the most important experimental techniques available for characterizing lateral gated

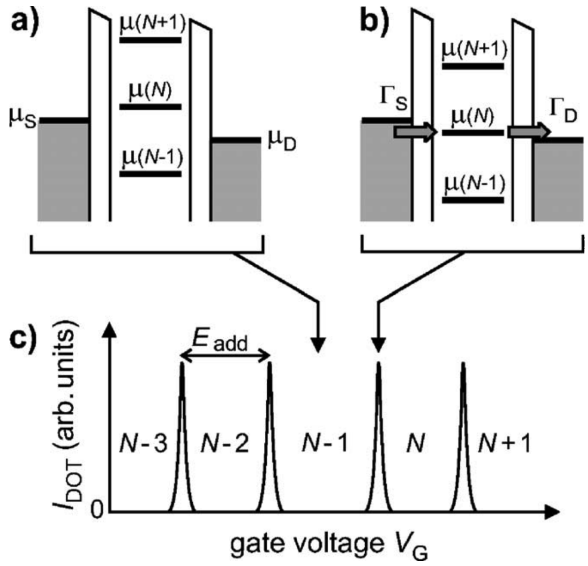

Figure 1.2: (a), (b) both show schematics of electrochemical potential of a quantum dot at low bias, thus the electrochemical potential involves only the ground states of different subspaces with fixed number of electrons. In (a), no levels fit in the transport window set by the chemical potential of the leads, μ_S and μ_D. Thus, the quantum dot is charged with $N-1$ electrons. In (b), there is a level in the transport window, so current flows and the number of electrons oscillates between $N-1$ and N in the quantum dot. The amplitude of the current depends on the tunnel coupling Γ_S and Γ_D. In (c), the current through the quantum dot is plotted as a function of the gate potential V_G, which control the potential depth of the dot. In the figure, the Coulomb blockade peak is a region where there exists a significant amount of current and it only happens when a chemical potential level is found within the transport window. The addition energy, E_{add}, is the energy spacing between Coulomb blockade peaks. Figures are adapted from Ref. [32]

quantum dots. These spectroscopic tools are used to extract information such as the charge and spin configurations of the dots, the single-particle energy spacing, the strength of Coulomb repulsion in a dot, and the strength of tunnel coupling between two adjacent dots.

When the quantum dot is weakly coupled to the source and drain leads at low temperature (but still higher than the Kondo temperature) and at low source-drain bias V_{sd}, only one electron can be transported at a time through the device because

of Coulomb blockade, which is explained in Fig.[1.2a] and Fig.[1.2b]. For a single dot, the energy spacing between Coulomb blockade peaks in the $I - V_{sd}$ diagram (as shown in Fig.[1.2c]) is the addition energy, $E_{add}(N) = \mu(N+1) - \mu(N)$ where $\mu(N)$ is the electrochemical potential for a dot with N electrons. From the addition energy, one can extract useful parameters such as the strength of Coulomb repulsion and the single-particle energy spacing in the quantum dots. When the quantum dot is connected to the spin polarized (for instance, spin down) leads in the presence of a magnetic field, an additional feature called the spin blockade [40] emerges in the transport spectroscopy. The spin blockade reduces the Coulomb blockade peak amplitude if the difference between the N and N+1 electron ground state is a spin up electron. Thus, the spin blockade allows for the probing of the spin properties with transport spectroscopy. Charge sensing [44, 45] provides an alternative spectroscopic tool, that is very useful when the tunnel coupling is so weak that no current can be measured in transport spectroscopy. The quantum point contact (QPC), defined by additional gates on the top surface, is a narrow channel nearby the quantum dot in the 2DEG. The conductance, G_{QPC}, of the QPC depends sensitively on the charge configurations of the nearby quantum dot. In other words, the conductance increases if an electron is removed from the dot or is moved from a nearer dot to a further dot, and the conductance dips when an electron is added onto the dot or is moved from a further dot to a nearer dot. However, it is often desirable to read the information obtained from the charge sensing technique by looking at the differential conductance, $\frac{dG_{QPC}}{dV_G}$, where V_G is the voltage on the gate controlling the potential depth of the dot. Fig.[1.3] shows a typical result of the charge sensing, which agrees well with results

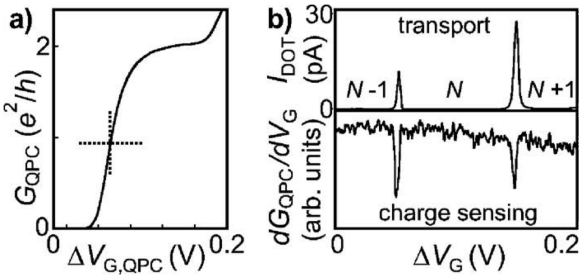

Figure 1.3: In (a), the figure shows how to pick an appropriate working condition of the QPC. This figure gives the conductance G_{QPC} versus gate potential used to define the QPC. In this case, the QPC gate is fined tuned such that G_{QPC} has the value marked by the cross. At this point, G_{QPC} has a steep slope and will be very sensitive to the surrounding charge environment. Upper and lower pannel of show measurement results obtained from direct transport measurement and charge sensing respectively. Figures are adapted from Ref. [32]

obtained from the direct transport measurement of a single quantum dot.

For multi-dot devices, information on physical properties of coupled quantum dots is usually obtained from the stability diagram, which plots the differential conductance, dV_{QPC}/dV_i, as a function of voltages on gates, which controls the potential depth of quantum dots. Similar to single dots, the spin blockade is useful for probing spin-related properties. In a multi-dot device, an electron might be trapped in the device due to the Pauli exclusion principle. Fig.[1.4] explains the spin blockade inside a triple quantum dot. This figure describes a semi-classical situation, which holds if the inter-dot tunnel coupling is weak. The spin blockade phenomenon in double quantum dots has already been demonstrated to be a valuable spectroscopic tool [41, 46] to distinguish two-electron singlet and triplet states as well as a valuable tool to achieve nuclear spin polarization [47, 48, 49] in the host material. Chapter [6] will further discuss the Spin Blockade phenomenon in a linear triple quantum dot device.

Fig.[1.5a] shows a very recent gate design which is used to obtain slices of the

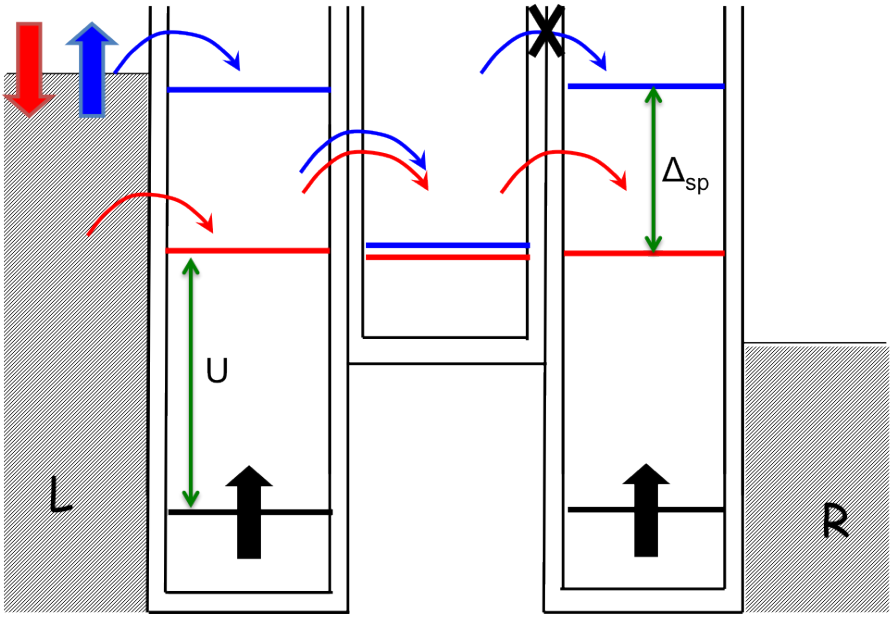

Figure 1.4: A semi-classical description of sequential tunneling of an electron through a linear triple quantum dot in the presence of two spin-up electrons trapped in the edge dots. The black bars in the quantum dots denote the electrochemical potentials of individual dots. An additional spin-up electron has to move along the blue-coloured path of the electrochemical potentials. In the edge dots, the blue bars are separated from the black bars by energy $U + \Delta_{sp}$ where U is the charging energy of a dot and Δ_{sp} corresponds to the energy spacing between single particle states in a dot. An additional spin-down electron moves across the triple dots along the red-coloured path of electrochemical potentials. In the edge dots, the red bars are only separated from the black bars by the charging energy U. This is because an incoming spin-down electron can occupy the same orbital as the trapped spin-up electron in the edge dot without violating the Pauli exclusion principle. As seen, this triple quantum dot is electrically tuned such that only the red electrochemical potentials in individual dots align perfectly for the sequential transport.

stability diagram of a triple quantum dot in a recent experiment by Granger and co-workers [50] at IMS. Fig.[1.5b] shows the stability diagram of the device as a function of R and L gates at $V_{sd} = 0$. In the figure, the numbers (N_1, N_2, N_3) denote the dominant charge configuration with N_i electron in dot i when the system is biased with voltage R and L. Fig.[1.5c] shows a similar stability diagram as a function of R and L at some finite V_{sd}. In the case of finite bias, 4 charge configurations $(1, 0, 1)$, $(2, 0, 1)$, $(1, 0, 2)$ and $(1, 1, 1)$ coexist close to each other in the circled region. Fig.[1.5d] shows a direct DC transport measurement, where the dark region represents a finite current, on the triple quantum dot. Corresponding to the "quadruple point" where the four charge configurations intersect, finite current is detected. In the white circled region in Fig.[1.5c], another set of 4 configurations, $(2, 0, 2)$,$(1, 0, 2)$, $(2, 0, 1)$, and $(1, 1, 1)$, come close together. This additional quadruple point in the stability diagram is also found in the direct DC transport measurement in Fig.[1.5d] and is the dark blob labelled number 2. For a triple quantum dot, resonant tunneling through the device only can take place at these specific quadruple points. The capability to identify these points with a triple dot device is the minimum requirement necessary to prove the tunability of the device. Different from double dots, where the stability diagram is a function of two gates (because of only two dots), the stability diagram of a triple quantum dot is a three-dimensional entity. Thus, it is in general more cumbersome to explore the parameter space of gate voltages to attain these quadruple points in triple dots.

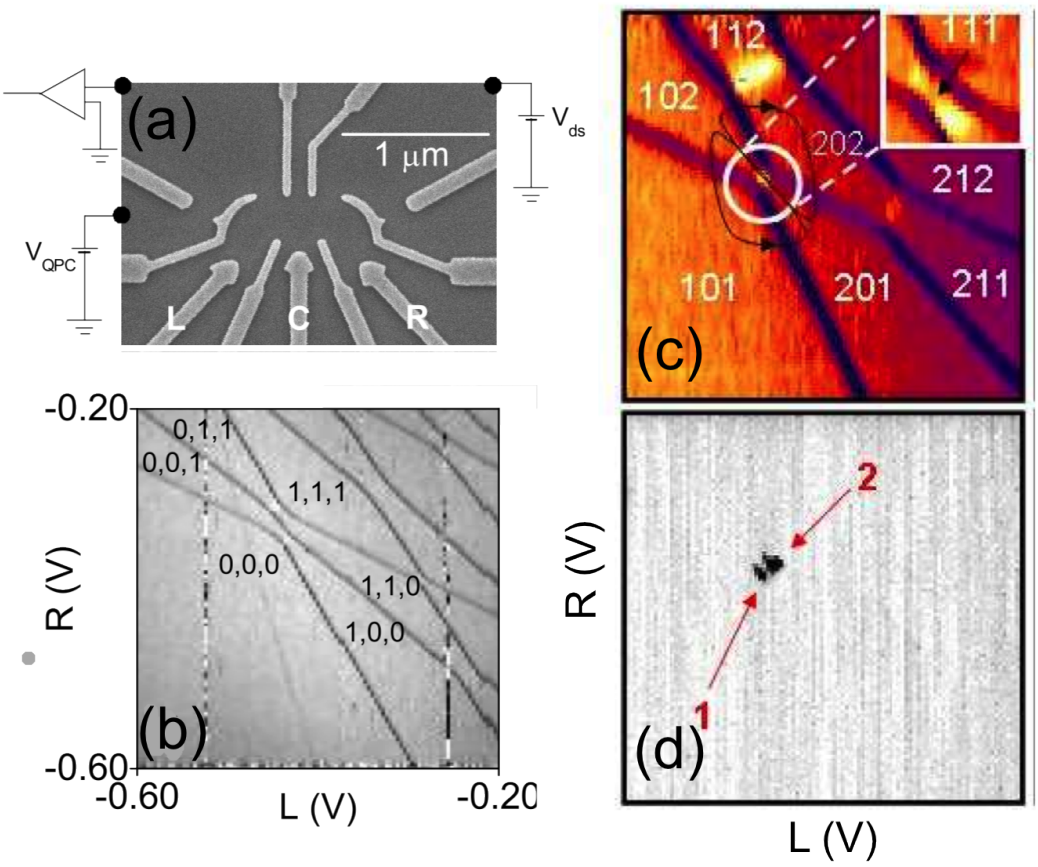

Figure 1.5: (a) The triple quantum dot studied in a recent experiment [50] at IMS, NRC. (b) The stability diagram of the triple quantum dot in absence of any source-drain bias. (c) The stability diagram of the triple dot in the presence of a finite source-drain bias. (d) DC current measurement of the triple quantum dots near the quadruple point: (1,0,1), (2,0,1), (1,1,1), and (1,0,2) present in the stability diagram in panel (b) and (c). These figures are adapted from Ref. [50].

1.2.3 Fabrication of Self-Assembled Quantum Dots

A major difference between the self-assembled dots (SADs) and the lateral gated dots is that the self-assembled dots can confine both electrons and valence holes. The SADs [51] are also fabricated with very different procedures, and they are used for generating on-demand entangled photons for applications in quantum cryptography. In chapter [7], we will discuss aspects of a valence hole spin based qubit in SADs.

The fabrication begins with epitaxially growing one material on another material with a slightly different lattice constant (the deviation is best kept between 1-10 percent). With a small lattice mismatch, the two materials can form a good junction although highly strained. As the growth of additional material continues, the strain intensity increases until a critical point where the planar growth of the additional material stops. If materials are still being deposited after the critical point, the additional material will start forming small islands on top of the wetting layer. This transition from growing a layer to growing islands on the wetting layer in epitaxy is called a "Stranski-Krastanow" phase transition.

The small islands function as quantum dots when the substrate material has a larger band gap than the deposited material. The problem with this standard approach of fabricating self-assembled dots is that the dots are formed with random locations, radii, and heights. This fact has led to an inhomogeneous broadening of measurements on an ensemble of SADs. Over the years, several techniques have been discovered to improve the fabrication of SADs at IMS. For instance, fabrication procedures involving an "indium flush" that led to the creation of SADs with uniform heights were developed.

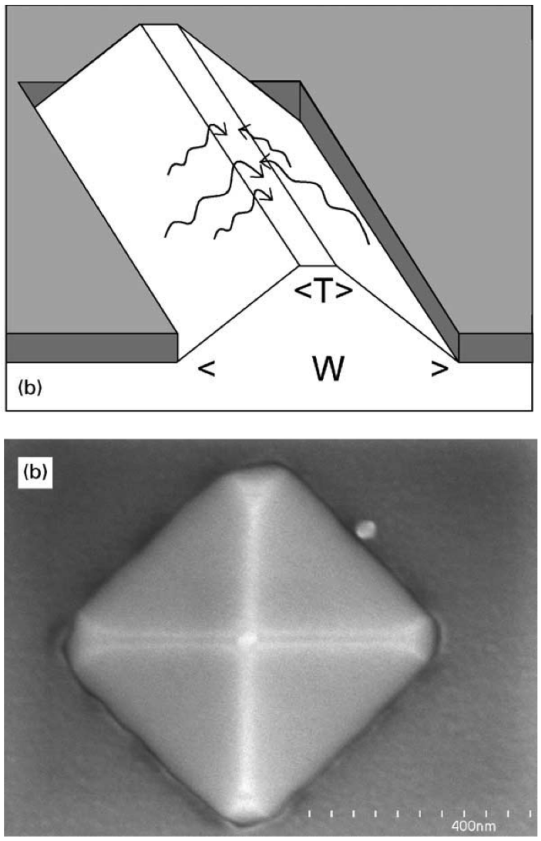

Figure 1.6: (a) Schematics of the diffusion process to form the pyramid on the ridge. (b) Scanning electron microscopy image of a single quantum dot on top of the pyramid. Figures adapted from Ref. [52]

To gain control over the positions of dot growth, Williams and co-workers at IMS developed a nano-template technique [52, 51] to address the issue. First, a mask with small rectangular openings of width W (several hundred nanometers) is deposited on top of the substrate. Further deposition of substrate material will adsorb materials only in the pre-defined locations, those openings in the mask, leading to the formation of a pyramid-like structure in these openings as shown in Fig.[1.6a]. The deposition of substrate material stops when the width, T, at the top of the pyramid reaches the critical size and allows only one or two SADs to be formed in this small area. Now, deposition of quantum dot material starts. The small island (SAD) will form once the Stranski-Krastanow phase transition is reached. Fig.[1.6b] shows a SAD at the tip of the pyramid. SADs grown on a nano-template tend to have a rectangular base. Thus, these quantum dots are usually modelled with rectangular boxes as opposed to disks in most other cases. Metallic gates can be placed on the sides of the pyramid to independently tune each quantum dot.

1.2.4 Photoluminescence Spectroscopy for Self-Assembled Quantum Dots

The primary experimental technique to probe the electronic properties of SADs is to excite the system with a laser field to create excitons, then wait for the electron-hole pairs to recombine by emitting photons to lower the overall energy of the system. The spectroscopy based on these emitted photons is called photoluminescence (PL) spectroscopy.

The emission of these photons by radiative relaxation can be predicted by the

Fermi's Golden rule,

$$E(\omega, i_N) = \frac{2\pi}{\hbar} \sum_f |\langle f_{N-1}| P^- |i_N\rangle|^2 \delta\left(E_{f_{N-1}} - E_{i_N} + \hbar\omega\right), \tag{1.2}$$

where P^- is the exciton annihilation operator, $|i_N\rangle$ is an N-exciton many-body state, and $|f_{N-1}\rangle$ is an (N-1)-exciton many-body state of the SAD. The energy of the emitted photon is $\hbar\omega$.

The energy position of the peaks in PL spectroscopy reveals the energy separation between N-exciton and N-1-exciton many-body states. The amplitude of the PL peak is given by the $|\langle f_{N-1}| P^- |i_N\rangle|^2$ term. Similar to an atomic system, selection rules exist to prohibit certain transitions. Thus, the height of PL peaks provide supplementary information on the symmetries of wave functions of the system.

1.3 Quantum Algorithm with Electron Spin-Based Qubits

Quantum teleportation is one of the simplest yet highly non-classical quantum algorithms proposed by Bennett et. al. [53]. Through the example of quantum teleportation with three particles, we illustrate how a quantum circuit is built with elementary constituents, qubits, and basic operations such as single qubit operations and double qubit operations. In this example, we will consider electron spin-based qubits in quantum dots as the physical realization of the quantum circuit. This also serves as a motivation for further investigations of a triple quantum dot molecule.

1.3.1 Single Qubit Operations

Preceding to the presentation of quantum teleportation algorithm, we would like to first discuss the relevant elementary operations. In this section, we first discuss how to rotate an electron spin in a quantum dot and perform single qubit operations.

For an electron spin-based qubit, any single qubit operation can be written down in the general form $e^{i\phi}R_{\mathbf{n}}(\theta)$ where ϕ represents an overall phase factor and $R_{\mathbf{n}}(\theta)$ is defined as,

$$\hat{R}_{\mathbf{n}}(\theta) = \exp\left(-\frac{i}{\hbar}\int_0^\tau dt\, g\mu_B B(t)\mathbf{n}\cdot\mathbf{S}\right), \tag{1.3}$$

where θ is the accumulated phase in the time integral,and $\mathbf{n}$ is the direction vector for the field $\mathbf{B}(t)$. Eq.(1.3) describes the unitary evolution of a spin in the presence of a magnetic field.

For instance, the Hadamard gate, a common single qubit operation used in various quantum algorithms, has the following matrix representation (with respect to the basis $\{|\uparrow\rangle, |\downarrow\rangle\}$),

$$\mathbf{H} = \frac{1}{\sqrt{2}}\begin{pmatrix} 1 & 1 \\ 1 & -1 \end{pmatrix}. \tag{1.4}$$

When expressed in the general form, it reads $e^{i\frac{\pi}{2}}\hat{R}_{\mathbf{n}}(\pi)$ with $\mathbf{n} = (1/\sqrt{2}, 0, 1/\sqrt{2})$.

We next show how to generate $\hat{R}_{\mathbf{n}}(\theta)$ through electron spin resonance (ESR) with a time-dependent magnetic field. For simplicity, we consider the following idealized model for an electron spin in a quantum dot,

$$i\hbar\frac{d|\psi\rangle}{dt} = g\mu_B\left(B_0 S_z + B_1 S_x\cos(\omega t+\phi)\right)|\psi\rangle, \tag{1.5}$$

where g is the g-factor and μ_B is the Bohr magneton.

Going into a rotating frame with coordinates $\{x', y', z'\}$ at frequency ω by applying the transformations $|\psi\rangle = e^{-i\omega t S_z} |\psi'\rangle$ and $\mathbf{S} = e^{i\omega t S_z} \mathbf{S}' e^{-i\omega t S_z}$, the time dependent Schrödinger equation for the spin reads

$$i\hbar \frac{d|\psi'\rangle}{dt} = \hbar \left[(\omega - \frac{g\mu_{B_0}}{\hbar}) S_{z'} + \frac{g\mu_B B_1}{\hbar} \left(S_{x'} \cos(\phi) + S_{y'} \sin(\phi) \right) \right] |\psi'\rangle \,. \tag{1.6}$$

If the applied frequency ω is identical to the Larmor frequency $g\mu_{B_0}/\hbar$, then the electron spin sees a time-independent effective field $\mathbf{B}_{ESR} = (B_1 \cos(\phi), B_1 \sin(\phi), 0)$. Thus, with a proper phase ϕ of the time-dependent field, we can generate rotation of the electron spin in the rotating frame with respect to either the x' or y' axis. Since rotation around an axis along direction $\mathbf{n}$ can be decomposed into three consecutive rotations around x' and y' via the Euler angle construction, this analysis shows that one can generate any arbitrary single qubit rotation by addressing the electron spin with a time-dependent magnetic field.

1.3.2 Double Qubit Operations

Next, we consider double qubit operations in a double quantum dot with one electron spin in each dot. In this case, it is well-known that the two spins interact via the Heisenberg exchange interaction $J\mathbf{S}_1 \cdot \mathbf{S}_2$, where the exchange constant $J = \frac{4t^2}{U-V}$ depends on microscopic details such as t the tunnel coupling across the dots, U the strength of Coulomb repulsion between two electrons in the same dot, and V the strength of Coulomb repulsion between two electrons in different dots. Since the tunnel barrier between two dots can be electrically tuned by the voltages applied to the gates, J is a controllable parameter.

The Heisenberg model commutes with the total spin operator for the two spins;

thus, the eigenstates are the triply-degenerate triplets and the singlet with energy $\hbar\omega^T$ and $\hbar\omega^S$ respectively. The energy gap is $\hbar\omega^T - \hbar\omega^S = J$. For simplicity, we will focus on the $S_z = 0$ subspace with states $|T^0\rangle = \frac{1}{\sqrt{2}}(|\uparrow_1\downarrow_2\rangle + |\downarrow_1\uparrow_2\rangle)$ and $|S\rangle = \frac{1}{\sqrt{2}}(|\uparrow_1\downarrow_2\rangle - |\downarrow_1\uparrow_2\rangle)$.

If we begin with a state $|\psi_2(0)\rangle = |\uparrow_1\downarrow_2\rangle = \frac{1}{\sqrt{2}}(|T^0\rangle + |S\rangle)$, then the state at a later time t is proportional to $|\psi_2(t)\rangle = \frac{1}{\sqrt{2}}\left(e^{-i\frac{Jt}{\hbar}}|T^0\rangle + |S\rangle\right)$. At $t^* = \hbar\pi/J$, the state $|\psi_2(t^*)\rangle$ is proportional to $|\downarrow_1\uparrow_2\rangle$ where the spin up and spin down electrons have swapped place.

To summarize, the time evolution of a pair of spins under the Heisenberg Hamiltonian is given by

$$\hat{U}(\theta) = \exp\left(-\frac{i}{\hbar}Jt\mathbf{S}_1 \cdot \mathbf{S}_2\right), \tag{1.7}$$

where θ is the accumulated dynamical phase under the unitary evolution. When $t = t^*$ and $\theta = \pi$, we denote the unitary operator $\hat{U}(\pi) = U_{SW}$, which swaps a pair of spins localized on different dots. We denote $\hat{U}(\pi/2) = \hat{U}_{SW}^{1/2}$, the square root of swap. The unitary operator $\hat{U}_{SW}^{1/2}$ entangles the pair of spin qubits. Furthermore, by using the square root of swap together with a sequence of single qubit operations can lead to other useful double qubit operations such as the controlled-NOT (CNOT) gate and the controlled-phase gate.

The matrix representation of the controlled-phase gate (expressed in the basis of

$\{|\uparrow_1\uparrow_2\rangle, |\uparrow_1\downarrow_2\rangle, |\downarrow_1\uparrow_2\rangle, |\downarrow_1\downarrow_2\rangle\}$ is given by

$$\mathbf{U}_{cphase} = \begin{pmatrix} 1 & 0 & 0 & 0 \\ 0 & 1 & 0 & 0 \\ 0 & 0 & 1 & 0 \\ 0 & 0 & 0 & -1 \end{pmatrix}. \tag{1.8}$$

This operation can be performed by a sequence of gate operations

$$\hat{U}_{cphase} = e^{i\pi/2}\hat{R}^1_{\mathbf{z}}(\pi/2)\hat{R}^2_{-\mathbf{z}}(\pi/2)U^{1/2}_{SW}\hat{R}^1_{\mathbf{z}}(\pi)U^{1/2}_{SW}, \tag{1.9}$$

where $\hat{R}^i_{\mathbf{z}}$ denotes that the spin is rotated with respect to the $\hat{z}$ axis, and the superscript $i = 1, 2$ denotes either the qubit on the first dot (i=1), or the second dot (i=2).

Next, we discuss the operations needed to generate the controlled-NOT gate, which has the following matrix representation (in the same basis as above),

$$\mathbf{U}_{CNOT} = \begin{pmatrix} 1 & 0 & 0 & 0 \\ 0 & 1 & 0 & 0 \\ 0 & 0 & 0 & 1 \\ 0 & 0 & 1 & 0 \end{pmatrix}, \tag{1.10}$$

and the controlled-NOT operator can be generated by

$$\hat{U}_{CNOT} = e^{i\pi}\hat{H}^2\hat{R}^1_{\mathbf{z}}(\pi)U_{cphase}\hat{H}^2, \tag{1.11}$$

where $\hat{H}^2$ is the Hadamard operation on the spin in dot 2.

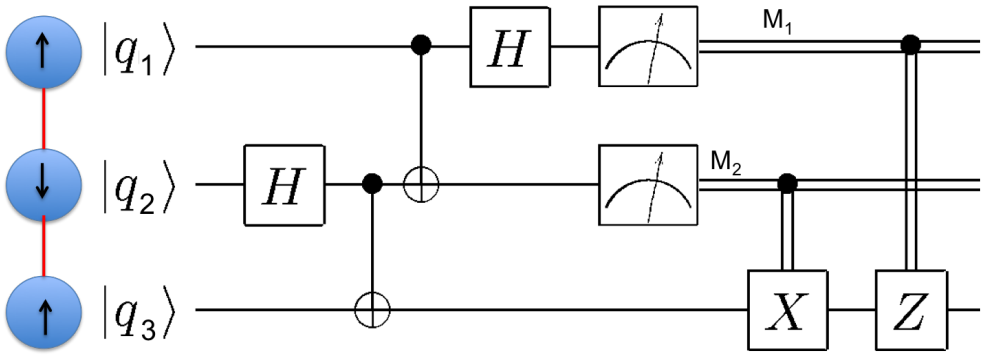

Figure 1.7: Quantum circuit diagram for teleportation. At the left side of the circuit diagram, a linear triple quantum dot schematics shows where each electron spin (qubit) locates in the circuit diagram. As shown, the teleportation protocol only involves single qubit operations (Hadamard gate, X gate and Z gate), and one specific double qubit operation (CNOT).

1.3.3 Quantum Teleportation in a Linear Triple Quantum Dot

Fig.[1.7] shows a diagram of one of the possible quantum circuits for teleportation. A linear triple quantum dot with one electron each, shown at the left end of the figure, can be used as a physical realization of this quantum circuit.

A quantum circuit diagram, such as Fig.[1.7], should be read from left to right. In the quantum circuit for teleportation, we have three parallel lines, each corresponding to a qubit. In this diagram, several commonly used quantum gates are presented. The box with the capital letter "H" denotes the Hadamard gate. The box with the letters, "X" and "Z", represent single qubit rotation, $e^{i\pi/2}\hat{R}_{\mathbf{x}}(\pi)$ and $e^{i\pi/2}\hat{R}_{\mathbf{z}}(\pi)$ respectively. The circuit element, which spans across two qubits, represents the CNOT gate. The meter-like objects represent measurements of qubit (or spin orientation) on qubit 1 and 2 with output M_1 and M_2 respectively. The double lines coming out of the measurement represent classical transmissions of measurement results.

At the beginning of the quantum circuit, the three qubits are initialized with the following state,

$$|\psi_0\rangle \;=\; (a\,|\uparrow_1\rangle + b\,|\downarrow_1\rangle)\,|\uparrow_2\rangle\,|\uparrow_3\rangle \tag{1.12}$$

where the leftmost (qubit 1) state represents the topmost qubit in the circuit diagram, the middle state (qubit 2) represents the middle qubit in the circuit diagram, and the rightmost state (qubit 3) represents the bottom qubit. Coefficient a and b are arbitrary complex numbers satisfying the relation $|a|^2 + |b|^2 = 1$. Thus, at the initial stage, the qubit 1 is in a superposition of states and qubits 2 and 3 are in the state $|\uparrow\rangle$.

First, a Hadamard operation is applied to qubit 2, and the system evolves to a new quantum state

$$\begin{aligned} |\psi_1\rangle &= \frac{1}{\sqrt{2}}\,(a\,|\uparrow_1\rangle + b\,|\downarrow_1\rangle)\,(|\uparrow_2\rangle + |\downarrow_2\rangle)\,|\uparrow_3\rangle \\ &= \frac{1}{\sqrt{2}}\,((a\,|\uparrow_1\rangle + b\,|\downarrow_1\rangle)\,|\uparrow_2\uparrow_3\rangle + (a\,|\uparrow_1\rangle + b\,|\downarrow_1\rangle)\,|\downarrow_2\uparrow_3\rangle)\,. \end{aligned} \tag{1.13}$$

After that, a CNOT operation is applied on qubits 2 (control qubit) and 3 (target qubit). Thus, qubit 3 undergoes spin flip when qubit 2 is in the state $|\downarrow\rangle$. The quantum state, at this stage, reads:

$$\begin{aligned} |\psi_2\rangle &= \frac{1}{\sqrt{2}}\,((a\,|\uparrow_1\rangle + b\,|\downarrow_1\rangle)\,|\uparrow_2\uparrow_3\rangle + (a\,|\uparrow_1\rangle + b\,|\downarrow_1\rangle)\,|\downarrow_2\downarrow_3\rangle)\,, \\ &= \frac{1}{\sqrt{2}}\,(a\,|\uparrow_1\rangle\,(|\uparrow_2\uparrow_3\rangle + |\downarrow_2\downarrow_3\rangle) + b\,|\downarrow_1\rangle\,(|\uparrow_2\uparrow_3\rangle + |\downarrow_2\downarrow_3\rangle))\,, \end{aligned} \tag{1.14}$$

where we see that the qubits 2 and 3 form an EPR pair.

Another CNOT operation is applied to qubit 1 (control qubit) and 2 (target qubit),

so the quantum state of the system now reads

$$|\psi_3\rangle = \frac{1}{\sqrt{2}}\left(a\,|\uparrow_1\rangle\left(|\uparrow_2\uparrow_3\rangle + |\downarrow_2\downarrow_3\rangle\right) + b\,|\downarrow_1\rangle\left(|\downarrow_2\uparrow_3\rangle + |\uparrow_2\downarrow_3\rangle\right)\right). \tag{1.15}$$

Similarly, a Hadamard gate is applied to qubit 1 and the system now has the following state

$$\begin{aligned} |\psi_4\rangle &= \frac{1}{2}\left(a\left(|\uparrow_1\rangle + |\downarrow_1\rangle\right)\left(|\uparrow_2\uparrow_3\rangle + |\downarrow_2\downarrow_3\rangle\right) + b\left(|\uparrow_1\rangle - |\downarrow_1\rangle\right)\left(|\downarrow_2\uparrow_3\rangle + |\uparrow_2\downarrow_3\rangle\right)\right), \\ &= \frac{1}{2}\left[|\uparrow_1\uparrow_2\rangle\left(a\,|\uparrow_3\rangle + b\,|\downarrow_3\rangle\right) + |\uparrow_1\downarrow_2\rangle\left(b\,|\uparrow_3\rangle + a\,|\downarrow_3\rangle\right)\right. \\ &\quad \left. + |\downarrow_1\uparrow_2\rangle\left(a\,|\uparrow_3\rangle - b\,|\downarrow_3\rangle\right) + |\downarrow_1\downarrow_2\rangle\left(b\,|\uparrow_3\rangle - a\,|\downarrow_3\rangle\right)\right], \end{aligned} \tag{1.16}$$

For any projective measurement performed on qubit 1 and 2, we will get one of the four possible combinations for $M_{1(2)} = 0$ (for spin up) or 1 (for spin down). As shown in the figure, after learning the result of projective measurements on qubits 1 and 2 via classical communication channel, we apply the operator Z^{M_1} and X^{M_2} on qubit 3 accordingly. For instance, if $M_1 = 0$, we do not apply the operator Z, and if $M_2 = 1$, we apply the operator X. At the end of the quantum teleportation protocol, the quantum state, $a\,|\uparrow\rangle + b\,|\downarrow\rangle$, originally initialized with the qubit 1 has been successfully transferred to qubit 3.

This is a remarkable result of quantum information. We transfer the quantum state without necessarily knowing the exact values of a and b. The Quantum teleportation protocol can be incorporated into a larger quantum circuit to transmit information between various parts of the circuit. To realize quantum teleportation, we need to construct a triple quantum dot with one electron each.

Chapter 2

Electronic and Spin Properties of a Triple Quantum Dot

In this chapter, we analyze the electronic and spin properties of a triple quantum dot. We first present a detailed description of the set of theoretical tools that we use to study quantum dots. Next, we present these properties of a triple quantum dot as a function of the number of electrons, topology (triangular versus linear), and bias voltage applied to one of the dots. At the end, we discuss the Aharonov-Bohm effect in a triangular triple quantum dot. The results presented in this chapter lay the foundation for discussions in the remaining chapters.

2.1 Models

In this section, we discuss a systematic approach to studying the electronic properties of a nano-structure. We begin with the effective mass model of electrons confined

in a gated lateral triple quantum dot. We solve the highly correlated electronic system with the LCHO-CI (Linear Combination of Harmonic Orbitals - Configuration Interaction) formalism. Next we present the Hubbard model for a simpler description of a triple quantum dot in the few-electron regime, and discuss briefly how the Hubbard parameters may be derived from the LCHO-CI calculations. Finally, we discuss the effective Heisenberg and t-J models for the low-energy states when the system is either half-filled or close to being half-filled.

2.1.1 Linear Combination of Harmonic Orbitals - Configuration Interactions

We now consider electrons confined in the electrostatic potential of a triple quantum dot and subject to a magnetic field $\mathbf{B}$. However, for the present section, we focus on the electronic orbital degrees of freedom and ignore the Zeeman term in the Hamiltonian, because we do not consider the spin-orbit couplings. Fig.[2.1a] illustrates a theoretical model of a triple quantum dot. In the figure, the green gates are used to adjust the depth of the nearby quantum dot (white circle in the figure) potential minimum, while the blue gates are used to shape the potential barrier between a pair of neighbouring dots without significant modifications to the depths of the quantum dots. In this chapter, we express all the energies in units of the effective Rydberg, $Ry^* = m_e^* e^4/2\epsilon^2\hbar^2$, and lengths in the effective Bohr radius, $a_B = \epsilon\hbar^2/m_e^* e^2$, where m_e^* is the conduction electron effective mass and ϵ is the dielectric constant of the

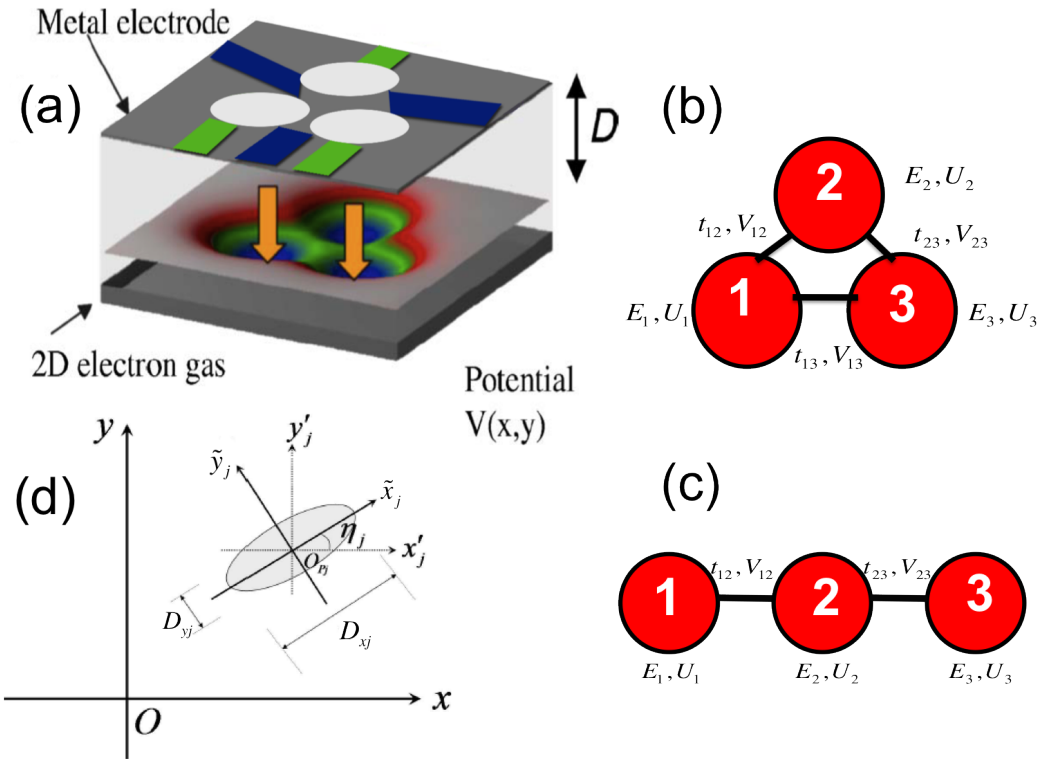

Figure 2.1: (Color online) (a) Schematic of a lateral gated TQD. The grey rectangular gate contains three circular openings, which translate into minima of the electrostatic potential at the level of the two-dimensional electron gas. The green gates can be used to shift the potential minima of the dots underneath them with respect to the rest of the system. The blue gate (plunger gate) is used to tune the tunneling barrier between dots 1 and 3. (b) A simple representation of a triangular TQD device. Hubbard parameters are defined in the text. (c) A simple representation of a linear TQD device, where there is no direct tunnel coupling between the two edge dots. (d) The local coordinates $(\tilde{x}_j, \tilde{y}_j)$ for the plunger gate potential. The grey-shaded region is where the plunger gate potential is expected to be.

material. Thus, the effective mass model for a single electron in a TQD then reads,

$$\hat{H}_{sp} = \left(-i\nabla + \frac{\Omega_c}{2}\mathbf{A}(\mathbf{r})\right)^2 + \sum_{i=1}^{3} V_i\left(\mathbf{r}\right) + \sum_{i=1}^{3} V_{B,i}\left(\mathbf{r}\right), \tag{2.1}$$

where $\mathbf{A}(\mathbf{r})$ is the vector potential due to $\mathbf{B}$, $\Omega_c = \hbar\omega_c/Ry^*$, $\omega_c = eB/m_e^*c$, $V_i(\mathbf{r})$ is the confinement potential of dot i, and $V_{B,i}(\mathbf{r})$ is one of the potential barriers between a pair of dots.

In this thesis, we always define the quantization axis of the spin along the direction of the field. If $\mathbf{B}$ is applied perpendicular to the 2DEG, then we choose the symmetric gauge $A = (1/2)\hat{B} \times \hat{r}$. However, if $\mathbf{B}$ is applied in-plane, then the Landau gauge is chosen for simplification. In this chapter, we apply $\mathbf{B} = B\hat{z}$ perpendicular to the 2DEG. The in-plane spatial coordinate $\mathbf{r} = (x, y)$ is defined.

We take a quantum dot's confining potential, $V_i(\mathbf{r})$, to be an inverted Gaussian function centered on the position $\mathbf{r}_i = (x_i, y_i)$ of dot i,

$$\begin{aligned} V_i(\mathbf{r}) &= -V_i^0 \exp\left[-\left(\frac{\mathbf{r}-\mathbf{r}_i}{d_i}\right)^2\right], \\ &= -V_i^0 + \frac{\Omega_{i,0}^2}{4}\left(\frac{\mathbf{r}-\mathbf{r}_i}{d_i}\right)^2 + \delta V_i, \\ &= V_i^{HO} + \delta V_i, \end{aligned} \tag{2.2}$$

where $V_i^0 > 0$, and the Gaussian potential can be separated into a harmonic contribution, V_i^{HO} and anharmonic correction, δV_i. The harmonic part is characterized by the confinement frequency $\Omega_{i,0} = \sqrt{2}V_{i,0}/d_i$. The anharmonic correction is important because the electron is not tightly confined to a single dot but may tunnel between dots. Under such conditions, the harmonic approximation might not yield satisfactory results in the electronic calculations.

As for the potential barrier between dots, we model them by anisotropic Gaussians,

$$V_{B,i}(\mathbf{r}) = V^0_{B,i} \exp\left(-\frac{\tilde{x}_j^2}{D_{xj}^2} - \frac{\tilde{y}_j^2}{D_{yj}^2}\right), \tag{2.3}$$

where $V^0_{B,i} > 0$, and the local coordinates $\{\tilde{x}_{,j}, \tilde{y}_{,j}\}$ and the global coordinates $\{x, y\}$ are related by

$$\begin{aligned} \tilde{x}_j &= (x - x_{Bj})\cos\eta_j + (y - y_{Bj})\sin\eta_j, \\ \tilde{y}_j &= -(x - x_{Bj})\sin\eta_j + (y - y_{Bj})\cos\eta_j, \end{aligned} \tag{2.4}$$

where (x_{Bj},y_{Bj}) gives the position coordinates of the center of the potential by the plunger gate, and η_j denotes the orientation of the local coordinate axes with respect to the global axes as depicted in Fig.[2.1d].

In the LCHO formalism, we solve the single particle Hamiltonian, Eq.(2.1), by building the Hamiltonian matrix in the basis of localized Fock-Darwin (FD) orbitals, which reduces to the harmonic oscillator orbitals in the limit of zero field, then performing the exact diagonalization of the matrix. The details of the Hamiltonian matrix element evaluations are provided in Appendix [A]. The eigenstates (also called molecular states) are expressed as $\psi_\gamma(\mathbf{r}) = \sum_{i,n,m} a^\gamma_{inm}\phi_{inm}(\mathbf{r})$, where i indexes quantum dots in the network, n and m are quantum numbers to specify the FD orbitals. This approach is analogous to the Linear Combination of Atomic Orbitals (LCAO) method in solid state physics. The FD orbitals, $\phi_{inm}(\mathbf{r})$, on dot i with quantum number n and m are given by

$$\phi_{inm}(\mathbf{r}) = \exp\left(-i\frac{\Omega_c}{4}(-y_i x + x_i y)\right)\tilde{\phi}_{nm}(\mathbf{r} - \mathbf{r}_i), \tag{2.5}$$

where $\tilde{\phi}_{nm}(\mathbf{r} - \mathbf{r}_i)$ are eigenstates of an auxiliary problem defined with respect to dot

i,

$$\left(\left[-i\nabla + \frac{\Omega_c}{2}\mathbf{A}_i(\mathbf{r})\right]^2 + V_i^{HO}\right)\tilde{\phi}_{nm}(\mathbf{r}-\mathbf{r}_i) = \epsilon_{inm}\tilde{\phi}_{nm}(\mathbf{r}-\mathbf{r}_i), \tag{2.6}$$

where the parabolic potential V_i^{HO} on dot i is defined in Eq.(2.2). The gauge transformation $\exp(-i(\Omega_c/4)(-y_i x + x_i y))$ in Eq.(2.5) is used to relate the wave function $\tilde{\phi}_{nm}(\mathbf{r})$ defined with localized gauge $\mathbf{A}_i(\mathbf{r}) = (1/2)\hat{B}\times(\mathbf{r}-\mathbf{r}_i)$ in Eq.(2.6) and the wave function $\phi_{inm}(\mathbf{r})$ defined with the global gauge $\mathbf{A}(\mathbf{r}) = (1/2)\hat{B}\times\mathbf{r}$ in Eq.(2.1). The eigenenergy in Eq.(2.6) is given by

$$\epsilon_{inm} = -V_0^i + \Omega_{i,+}(n+\frac{1}{2}) + \Omega_{i,-}(m+\frac{1}{2}), \tag{2.7}$$

where $\Omega_{i,\pm} = \sqrt{\Omega_{i,o}^2 + \Omega_c^2/4} \pm \Omega_c/2$.

With respect to the set of FD orbitals $\{\phi_{inm}(\mathbf{r})\}$, we construct a matrix representation of Eq.(2.1),

$$\mathbf{H}_{sp}\mathbf{a}^\gamma = \epsilon_\gamma \mathbf{S}\mathbf{a}^\gamma, \tag{2.8}$$

where $\mathbf{S}_{inm,i'n'm'} = \langle\phi_{inm}|\phi_{i'n'm'}\rangle$ is the overlap matrix for non-orthogonal FD orbitals on different dots. The generalized eigenvalue problem, Eq.(2.8), can be converted to a regular eigenvalue problem, $\mathbf{H}'_{sp}\mathbf{b}^\gamma = \epsilon_\gamma\mathbf{b}^\gamma$ by the following transformation, $\mathbf{H}'_{sp} = \mathbf{S}^{-1/2}\mathbf{H}_{sp}\mathbf{S}^{-1/2}$, and $\mathbf{b}^\gamma = \mathbf{S}^{1/2}a^\gamma$. This matrix transformation essentially performs an orthogonalization on the FD orbitals.

The dimension of the matrix $\mathbf{H}_{sp}$ is $N_{orb} = 3n_0$, where n_0 is the number of FD orbitals taken from each dot. In order to properly retain the symmetries of the system, it is essential to take complete shells of FD orbitals on each dot for the calculation. As described in Chapter [1], a quantum dot is an artificial atom with discrete energy levels, which are often grouped into shells due to the symmetry of the confining

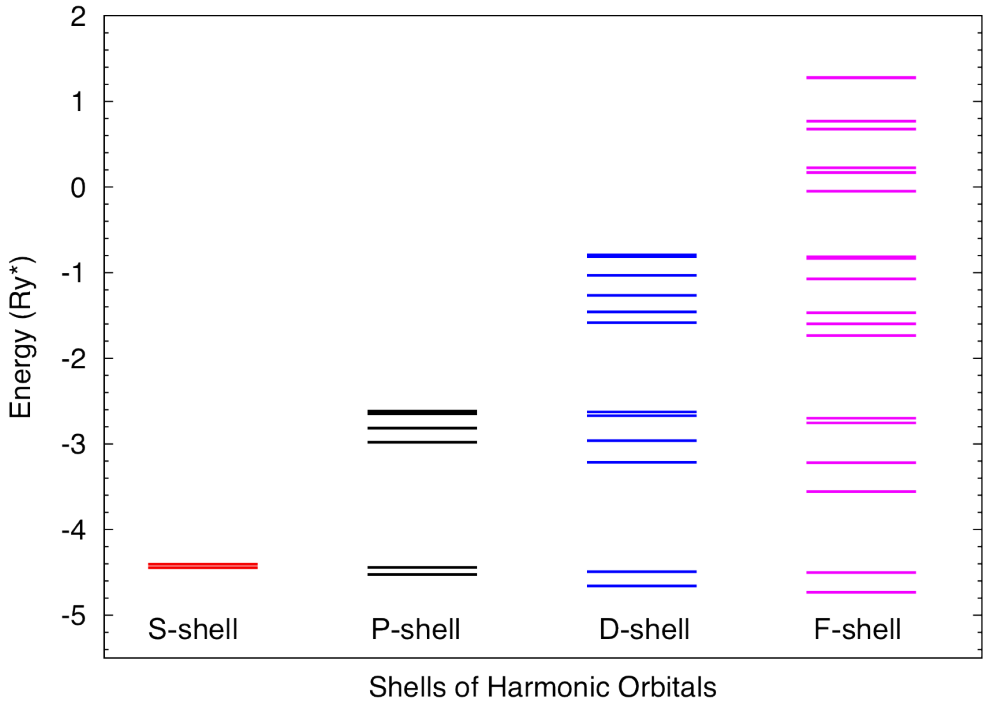

Figure 2.2: Single particle energy spectra of a triangular triple quantum dot as a function of complete shells of FD orbitals included in the basis for exact diagonalization.

potential. In particular, for our case of FD orbitals, a shell consists of states with the same value of $n+m$, where n and m are the quantum numbers in $\phi_{inm}(\mathbf{r})$. The lowest shell is called the S-shell, which contains the three lowest orbitals: $\phi_{100}(\mathbf{r})$, $\phi_{200}(\mathbf{r})$, and $\phi_{300}(\mathbf{r})$ with $n+m=0$. The next shell is the P-shell, which contains 6 orbitals from three dots with $n+m=1$. The names of shells are borrowed from the familiar notations of s, p, d, f shells in atomic physics.

Fig.[2.2] presents the single particle energy spectra of a triangular triple quantum dot as a function of the number of shells included in the calculation. Since exact diagonalization of a Hamiltonian with a finite basis is equivalent to a variational approach of solving the Schrödinger equation, the calculated energy levels tend to

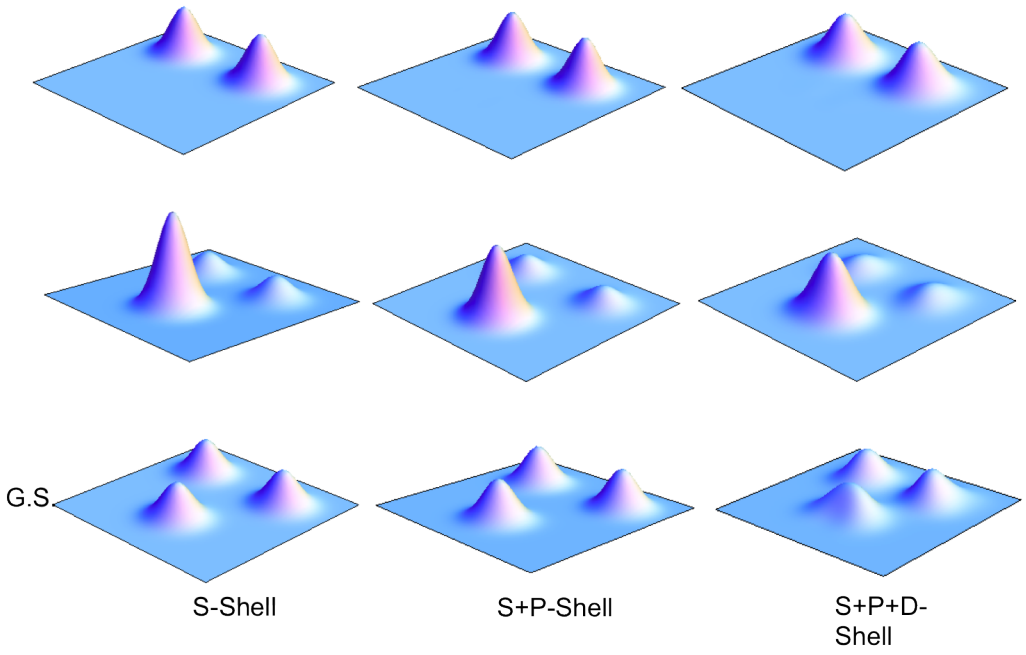

Figure 2.3: Each column gives the probability density of the lowest three single particle molecular states $\psi_\gamma(\mathbf{r})$ obtained from LCHO calculations with different shells of FD orbitals. The bottom row is the ground state, and the upper rows are the doubly degenerate excited states.

move towards lower values as the basis size increases. As the basis size enlarges, a clear pattern of shells for molecular states emerges for a triple quantum dot. With only the S-shell included in the LCHO formalism, we may only calculate the three lowest states as shown at the leftmost column in Fig.[2.2]. However, the lowest-shell approximation still yields the correct degeneracy of the levels. Next, Fig.[2.3] shows the probability density of the three lowest molecular states obtained from LCHO calculations with different number of shells. Again, the wavefunctions obtained from the S-shell approximation are similar to the ones obtained with larger basis size. The qualitative trend is that these wavefunctions tend to delocalize more as the number of shells in the LCHO basis increases.

We next consider the multi-electron, $N_e > 1$, problem. In the second quantized form, the many-body Hamiltonian reads,

$$\hat{H}_{N_e} = \sum_{i\sigma} \epsilon_{\gamma_i,\sigma} d^\dagger_{\gamma_i,\sigma} d_{\gamma_i,\sigma} + \frac{1}{2} \sum_{i,,j,k,l} \sum_{\sigma,\sigma'} \langle \gamma_i \gamma_j | \hat{V}_C | \gamma_k \gamma_l \rangle d^\dagger_{\gamma_i,\sigma} d^\dagger_{\gamma_j,\sigma'} d_{\gamma_l,\sigma'} d_{\gamma_k,\sigma}, \tag{2.9}$$

where $d_{\gamma_i,\sigma}$ ($d^\dagger_{\gamma_i,\sigma}$) annihilates (creates) a particle on the spin-orbital (γ_i, σ_i). ϵ_γ is the energy of molecular orbitals in Eq.(2.8) and $\gamma' s$ denote the molecular orbitals $\psi_\gamma(\mathbf{r})$, σ is the spin index, and the Coulomb matrix elements are defined as follows

$$\begin{aligned}
\langle \gamma_i \gamma_j | \hat{V}_C | \gamma_k \gamma_l \rangle &= \int d\mathbf{r} \int d\mathbf{r}' \psi^*_{\gamma_i}(\mathbf{r}) \psi^*_{\gamma_j}(\mathbf{r}') \frac{2}{|\mathbf{r} - \mathbf{r}'|} \psi_{\gamma_k}(\mathbf{r}) \psi_{\gamma_l}(\mathbf{r}'), \\
&= \sum_{c_1,c_2,c_3,c_4} \left(a^{\gamma_i}_{c_1}\right)^* \left(a^{\gamma_j}_{c_2}\right)^* a^{\gamma_k}_{c_3} a^{\gamma_l}_{c_4} \int d\mathbf{r} \int d\mathbf{r}' \phi^*_{c_1}(\mathbf{r}) \phi^*_{c_2}(\mathbf{r}') \frac{2}{|\mathbf{r} - \mathbf{r}'|} \phi_{c_3}(\mathbf{r}) \phi_{c_4}(\mathbf{r}'), \\
&= \sum_{c_1,c_2,c_3,c_4} \left(a^{\gamma_i}_{c_1}\right)^* \left(a^{\gamma_j}_{c_2}\right)^* a^{\gamma_k}_{c_3} a^{\gamma_l}_{c_4} \ \langle \phi_{c_1} \phi_{c_2} | \hat{V}_C | \phi_{c_3} \phi_{c_4} \rangle,
\end{aligned} \tag{2.10}$$

where $\psi_\gamma(\mathbf{r})$ is the spatial representation of the molecular orbital $|\gamma\rangle$, and $c_k = (i, n, m)$ with $k = 1, 2, 3, 4$ is a composite index for the localized FD orbitals. The Coulomb matrix elements in the FD basis can be computed analytically, and details are provided in Appendix [A].

We choose to solve the many-body Hamiltonian, Eq.(2.9), by configuration interaction (CI) method, a commonly used method to study electronic properties of molecules in quantum chemistry. Several other theoretical formalisms, such as Hartree-Fock, density-functional theory (DFT), and quantum Monte Carlo, have been applied to study the many-body physics contained in Eq.(2.9). Each method has its own merits and drawbacks. Please see Ref. [54] for further discussions on theoretical methods for calculating the electronic properties of quantum dots. However, for a system containing just a small number of highly correlated electrons, CI seems to be the ideal

method to approach the problem. In this formalism, we have to first construct configurations, which are used to represent the Hamiltonian $\hat{H}_{N_e}$ in a matrix form. A configuration $|p_{N_e}\rangle$ with N_e electrons is specified as follows

$$|p_{N_e}\rangle = \left|i_1^p\sigma_1^p, i_2^p\sigma_2^p, \ldots, i_{N_e}^p\sigma_{N_e}^p\right\rangle = d^\dagger_{i_1^p\sigma_i^p} d^\dagger_{i_2^p\sigma_2^p} \ldots d^\dagger_{i_{N_e}^p\sigma_{N_e}^p} |0\rangle\,, \tag{2.11}$$

where a set of N_e spin-orbitals $\{(i_1^p\sigma_1^p), (i_2^p\sigma_2^p), \ldots, \left(i_{N_e}^p\sigma_{N_e}^p\right)\}$ are occupied. Each configuration represents a Slater determinant, because of the anticommutation relations of the fermionic operators: $\{d^\dagger_{i\sigma}, d_{j\sigma'}\} = \delta_{i,j}\delta_{\sigma,\sigma'}$. With $N_\uparrow + N_\downarrow = N_e$ electrons and N_{orb} molecular orbitals, a total of

$$N_{cfg} = \left(\begin{array}{c} N_{orb}! \\ \\ N_\uparrow!(N_{orb}-N_\uparrow)! \end{array}\right)\left(\begin{array}{c} N_{orb}! \\ \\ N_\downarrow!(N_{orb}-N_\downarrow)! \end{array}\right) \tag{2.12}$$

configurations can be built under the premise of the Pauli exclusion principle.

With the basis $\{|p_{N_e}\rangle\}$, the Schrödinger equation, Eq.(2.9), is represented in the matrix-vector form ,

$$\mathbf{H}_{N_e} C_M = E^M_{N_e} C_M. \tag{2.13}$$

The exact eigenstate corresponding to M-th eigenenergy $E^M_{N_e}$ is given by

$$\left|\Psi^M_{N_e}\right\rangle = \sum_{p=1}^{N_{cfg}} C^p_M \left|i_1^p\sigma_1^p \ldots i_{N_e}^p\sigma_{N_e}^p\right\rangle, \tag{2.14}$$

where C^p_M is the p-th component of the vector C_M in Eq.(2.13).

2.1.2 Hubbard Model

In the strongly correlated regime, where the Coulomb matrix elements $\langle\gamma_i\gamma_j|\hat{V}_C|\gamma_k\gamma_l\rangle$ in Eq.(2.10) contain the dominant energy terms in Eq.(2.9), the electrons are highly

localized and the Hubbard model provides an intuitive framework to analyze the electronic and spin properties of such a system.

In the Hubbard model, molecular states are expressed in terms of Hubbard orbitals, which have highly localized spatial representation and form an orthogonal basis. In this section, we discuss the derivation of Hubbard orbitals from the LCHO formalism, and express them as linear combinations of FD orbitals. For simplification, we consider the case of having one FD orbital, i.e. the S orbital, in each dot.

In our earlier discussion of the effective mass model, we solved the generalized eigenvalue problem in Eq.(2.8) by making the transformations $\mathbf{H}'_{sp} = \mathbf{S}^{-1/2}\mathbf{H}_{sp}\mathbf{S}^{-1/2}$ and $\mathbf{b}^\gamma = \mathbf{S}^{1/2}\mathbf{a}^\gamma$ to obtain a regular eigenvalue problem $\mathbf{H}'_{sp}\mathbf{b}^\gamma = \epsilon_\gamma \mathbf{b}^\gamma$. The original Hamiltonian $\mathbf{H}_{sp}$ was represented in the basis of FD orbitals, and we now show that the transformed Hamiltonian $\mathbf{H}'_{sp}$ is represented in the basis of Hubbard orbitals.

The molecular orbital $|\gamma\rangle$ derived in the LCHO formalism can be expressed as

$$\begin{aligned}
|\gamma\rangle &= \sum_j a_j^\gamma \, |\phi_j\rangle \,, \\
&= \sum_{j,k} \left(\mathbf{S}^{-1/2}\right)_{jk} b_k^\gamma \, |\phi_j\rangle \,, \\
&= \sum_k b_k^\gamma \left[\sum_j \left(\mathbf{S}^{-1/2}\right)_{jk} |\phi_j\rangle\right] , \\
&= \sum_k b_k^\gamma \, |\chi_k\rangle \,, \qquad (2.15)
\end{aligned}$$

where in the second line we use the relation $\mathbf{a}^\gamma = \mathbf{S}^{-1/2}\mathbf{b}^\gamma$, and in the last line we introduce the Hubbard orbital $|\chi_k\rangle$, defined in the bracket in the third line.

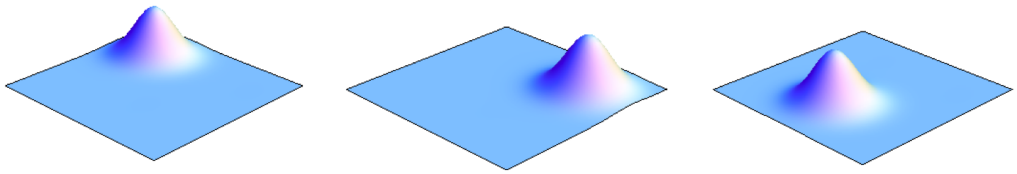

Figure 2.4: Spatial representation of localized Hubbard orbitals.

We first prove the orthogonality of the Hubbard orbitals,

$$\begin{aligned}\langle\chi_{k'}|\chi_k\rangle &= \sum_{j',j}\left(\mathbf{S}^{-1/2}\right)_{k'j'}\left(\mathbf{S}^{-1/2}\right)_{jk}\langle\phi_{j'}|\phi_j\rangle,\\ &= \sum_{j',j}\left(\mathbf{S}^{-1/2}\right)_{k'j'}\mathbf{S}_{j',j}\left(\mathbf{S}^{-1/2}\right)_{jk},\\ &= \mathbf{I}_{kk'},\end{aligned} \tag{2.16}$$

where $\mathbf{I}$ is the identity matrix. Next, we show that the Hubbard orbitals $|\chi_k\rangle$ are highly localized. The inverse of the square root of the overlap matrix reads

$$\mathbf{S}^{-1/2} = \frac{1}{3}\begin{bmatrix} \frac{2}{\sqrt{1-s}}+\frac{1}{\sqrt{1+2s}} & -\frac{1}{\sqrt{1-s}}+\frac{1}{\sqrt{1+2s}} & -\frac{1}{\sqrt{1-s}}+\frac{1}{\sqrt{1+2s}} \\ -\frac{1}{\sqrt{1-s}}+\frac{1}{\sqrt{1+2s}} & \frac{2}{\sqrt{1-s}}+\frac{1}{\sqrt{1+2s}} & -\frac{1}{\sqrt{1-s}}+\frac{1}{\sqrt{1+2s}} \\ -\frac{1}{\sqrt{1-s}}+\frac{1}{\sqrt{1+2s}} & -\frac{1}{\sqrt{1-s}}+\frac{1}{\sqrt{1+2s}} & \frac{2}{\sqrt{1-s}}+\frac{1}{\sqrt{1+2s}} \end{bmatrix}, \tag{2.17}$$

where $s = \langle\phi_i|\phi_j\rangle$ is the overlapping matrix element and it is usually a small number. Thus the off-diagonal matrix elements in Eq.(2.17) are close to zero. This ensures that each Hubbard orbital, $|\chi_k\rangle = \sum_j \left(\mathbf{S}^{-1/2}\right)_{jk}|\phi_j\rangle$, contains mostly just one localized FD orbital. Fig.[2.4] shows the spatial representation $\chi_k(\mathbf{r})$ localized on each dot.

Once we have obtained the Hubbard orbitals and the single-particle Hubbard Hamiltonian matrix $\mathbf{H}'_{sp}$, we then proceed to derive the parameters in the full Hubbard

Hamiltonian,

$$\begin{aligned}\hat{H}_{hubb} =& \sum_{i=1}^{3} E_i \hat{n}_{i\sigma} + \sum_{\substack{i,j=1 \\ i\neq j}}^{3} \sum_{\sigma} t_{ij} \hat{c}^{\dagger}_{i\sigma} \hat{c}_{j\sigma} + \frac{1}{2} \sum_{\substack{i,j=1 \\ i\neq j}}^{3} V_{ij} \hat{\rho}_i \hat{\rho}_j \\ &+ \sum_{i=1}^{3} U_i \hat{n}_{i\uparrow} \hat{n}_{j\downarrow} + \sum_{\alpha} g\mu_B \mathbf{S}_{\alpha} \cdot \mathbf{B}, \\ =& \hat{H}_0 + \hat{H}_T + \hat{H}_V + \hat{H}_U + \hat{H}_Z, \end{aligned} \tag{2.18}$$

where $\hat{c}_{i\sigma}$ ($\hat{c}^{\dagger}_{i\sigma}$) annihilates (creates) an electron with spin σ on Hubbard orbital i, $\hat{\rho}_i = \hat{n}_{i\uparrow} + \hat{n}_{i\downarrow}$, E_i is the on-site energy of orbital i, t_{ij} is the tunnel coupling between orbitals i and j and acquires a Peierl's phase when field $\mathbf{B}$ is applied perpendicular to the TQD , V_{ij} is the long range Coulomb interaction between electrons in orbitals i and j, U_i is the on-site Coulomb interaction of orbital i, g is the g-factor of the host semiconductor, μ_B is the Bohr magneton, and $\mathbf{S}_{\alpha}$ is the spin for the α-th particle. Each term on the right hand side (r.h.s.) of the second equality sign in (2.18) represents the corresponding term on the r.h.s. of the first equality sign. The Hubbard Hamiltonian can also be solved by an exact diagonalization approach within the configuration-interaction method.

The parameters E_i and t_{ij} are taken from the matrix elements $\left(\mathbf{H}'_{sp}\right)_{ii} = \langle \chi_i | \hat{H}_{sp} | \chi_i \rangle$ and $\left(\mathbf{H}'_{sp}\right)_{ij} = \langle \chi_i | \hat{H}_{sp} | \chi_j \rangle$, respectively. The Coulomb matrix elements are calculated as follows,

$$\langle \chi_k \chi_l | \hat{V}_c | \chi_{k'} \chi_{l'} \rangle = \sum_{a,a',b,b'} \left(\mathbf{S}^{-1/2}\right)^{-1}_{ka} \left(\mathbf{S}^{-1/2}\right)^{-1}_{lb} \left(\mathbf{S}^{-1/2}\right)^{-1}_{a'k'} \left(\mathbf{S}^{-1/2}\right)^{-1}_{b'l'} \langle \phi_a \phi_b | \hat{V}_c | \phi_{a'} \phi_{b'} \rangle. \tag{2.19}$$

To get U_i, we simply set $k = k' = l = l' = i$ in the equation above. To get V_{ij}, we set $k = k' = i$ and $l = l' = j$. This concludes the derivation of the Hubbard Hamiltonian

from the effective mass model with one orbital per dot.

Now, we turn to a brief discussion of the derivation of a single-band Hubbard model from an effective mass model with more than one orbital per dot. We apply an iterative perturbation theory to separate the high energy states from the low energy states, which are characterized predominantly by the S orbitals. This procedure allows us to renormalize the interactions between S orbitals and integrate out other orbitals, so we may simply use S orbitals in our description of low energy states. We separate the single particle Hilbert space into two disjoint subspaces: $\mathcal{D}_A$, the set of S orbitals in each dot, and $\mathcal{D}_B$, the set of all other orbitals. The perturbation theory is applicable when the energy difference between any two configurations in different subspaces is much larger than the mixing (off-diagonal matrix elements in the Hamiltonian) between the two subspaces. The goal of the perturbation theory is to transform the single-particle Hamiltonian matrix into an approximate block-diagonal form (corresponding to subspaces $\mathcal{D}_A$ and $\mathcal{D}_B$) with off-diagonal block matrix elements bounded by a desired order of the perturbation. The transformed block matrix corresponding to the $\mathcal{D}_A$ subspace contains the single-particle Hubbard parameters and the transformed basis in this subspace is the set of Hubbard orbitals. Further details of this transformation are summarized in Appendix [B.3].

2.1.3 Effective Models

Although a single-band Hubbard model already provides an intuitive framework to study a triple quantum dot, an even simpler descriptions can be attained when only the lowest few states are of interest. We note that a single-band Hubbard Hamiltonian

is suitable for studying a triple quantum dot filled with up to six electrons. For $N_e = 1$, 5, and 6, the Hilbert space is small and the Hubbard Hamiltonian can be diagonalized easily. The benefit of further perturbative analysis comes in the case of $N_e = 2$, 3, and 4. When there are either two electrons or two holes (4 electrons) in a triple quantum dot, a t-J model can be derived from Löwdin perturbation theory and used to describe the few lowest states. When the triple dot is half filled, i.e. $N_e = 3$, a Heisenberg model can be derived.

First, let us discuss the two-electron case. The two-hole case is almost identical; we just have to first apply the particle-hole transformation to the Hubbard Hamiltonian preceding the analysis. So, for the two-electron case, the Hilbert space can be separated into a singlet subspace ($S = 0, S_z = 0$) and triplet subspaces ($S = 1, S_z = \pm 1, 0$). We note that each of the triplet subspaces consists of just three configurations. For instance, the $S_z = 1$ subspace contains $|T_{12}\rangle = \hat{c}^\dagger_{1\uparrow}\hat{c}^\dagger_{2\uparrow}|0\rangle$, $|T_{13}\rangle = \hat{c}^\dagger_{1\uparrow}\hat{c}^\dagger_{3\uparrow}|0\rangle$, $|T_{23}\rangle = \hat{c}^\dagger_{2\uparrow}\hat{c}^\dagger_{3\uparrow}|0\rangle$. All the states in the triplet subspaces are composed of "singly-occupied" configurations, in which every dot contains at most one electron spin. The singlet subspace has six configurations: $|S_{12}\rangle$, $|S_{13}\rangle$, $|S_{23}\rangle$, $|S_{11}\rangle$, $|S_{22}\rangle$, and $|S_{33}\rangle$, where $|S_{ij}\rangle = \frac{1}{\sqrt{2}}\left(\hat{c}^\dagger_{i\uparrow}\hat{c}^\dagger_{j\downarrow} + \hat{c}^\dagger_{j\uparrow}\hat{c}^\dagger_{i\downarrow}\right)|0\rangle$ for $i \neq j$, and $|S_{ii}\rangle = \hat{c}^\dagger_{i\uparrow}\hat{c}^\dagger_{i\downarrow}|0\rangle$. The first three states listed for the singlet subspace are also singly occupied configurations, while the last three states are doubly occupied configurations, in which at least one dot contains two electrons.

In order to derive the effective $t - J$ model by Löwdin perturbation theory, we treat the hopping term $\hat{H}_T$ in Eq.(2.18) as perturbation and separate the Hilbert space into two subspaces: $\mathcal{D}_A$ of singly occupied configurations and $\mathcal{D}_B$ of doubly occupied

configurations. We again perform a transformation on the Hamiltonian matrix to obtain an approximate block-diagonal matrix. The effective t-J model describes the subspace $\mathcal{D}_A$, which is energetically separated from subspace $\mathcal{D}_B$ by the order of U, the Coulomb repulsion in a dot. We remark that the three triplet subspaces contain only singly-occupied states and the hopping term $\hat{H}_T$ does not allow mixing between the triplets states and the doubly occupied configurations; thus, our perturbative analysis do not affect the triplet subspaces. As for the singlet subspace, the t-J Hamiltonian reads,

$$\hat{H}_{t-J} = \hat{H}_0 + \hat{H}_U + \hat{H}_V + \hat{H}_T + \hat{H}_Z + \hat{H}_J + \hat{H}_3, \tag{2.20}$$

where $\hat{H}_0$, $\hat{H}_U$, $\hat{H}_V$ represent the unperturbed (zeroth-order) term, and each term is defined in Eq.(2.18), $\hat{H}_T$ represents the first order perturbation and is also defined in Eq.(2.18), $\hat{H}_J$ and $\hat{H}_3$ are derived in the second order perturbation calculations and defined as follows:

$$\hat{H}_J = \sum_{\substack{i,j \\ i \neq j}} J_{ij} \left(\mathbf{S}_i \cdot \mathbf{S}_j - \frac{1}{4} \hat{n}_i \hat{n}_j \right), \tag{2.21}$$

$$\hat{H}_3 = \sum_{i \neq j \neq l (\neq i)} J_{ijl} \sum_{\sigma} \left(\hat{c}^{\dagger}_{i\sigma} \hat{n}_{j\bar{\sigma}} \hat{c}_{l\sigma} + \hat{c}^{\dagger}_{i\sigma} \hat{c}^{\dagger}_{j\bar{\sigma}} \hat{c}_{j\sigma} \hat{c}_{l\bar{\sigma}} . \right), \tag{2.22}$$

where

$$J_{ij} = 2|t_{ij}|^2 \left[\frac{1}{U_i - V_{ij} + (\epsilon_i - \epsilon_j)} + \frac{1}{U_j - V_{ij} - (\epsilon_i - \epsilon_j)} \right], \tag{2.23}$$

$$J_{ijl} = -\frac{1}{2} t_{ij} t_{jl} \left[\frac{1}{U_j - V_{jl} + (\epsilon_j - \epsilon_l)} + \frac{1}{U_j - V_{jl} + (\epsilon_j - \epsilon_l)} \right]. \tag{2.24}$$

Eq.(2.21) and Eq.(2.22) describe hopping of electron spins via an intermediate doubly occupied configuration. In the case of $\hat{H}_J$, the Heisenberg Hamiltonian, hopping can

be effectively described as the superexchange of spins localized on neighbouring dots. The spin operator is related to the fermionic operators by $\mathbf{S}_i = \frac{1}{2}\hat{c}^\dagger_{i\alpha}\sigma_{\alpha,\beta}\hat{c}_{i\beta}$, where i denotes the site and α, β denote the spins. As for $\hat{H}_3$, it describes a two-step hopping process involving all three dots. First, remove an electron spin from dot l and add it onto dot j to form a doubly occupied configuration. Next, remove an electron spin (not necessarily the same one just added) from dot j then add it to dot i.

Fig.[2.5] presents the six lowest two-electron energies calculated with different approaches. As shown in the figure, the Hubbard model with parameters derived from the LCHO-CI results provides a good approximation of the energies of the two-electron system. Similarly, the results from t-J model also provide an equally good approximation.

Next, we turn to discussion of a half-filled ($N_e = 3$) triple quantum dot. Similar to the previous case, we can again separate the Hilbert space into spin-resolved subspaces. The fully polarized subspaces are trivial, as the subspaces each contain just one state each. For instance, $S_z = 3/2$ only have this state $|3/2, 3/2\rangle = \hat{c}^\dagger_{1\uparrow}\hat{c}^\dagger_{2\uparrow}\hat{c}^\dagger_{3\uparrow}|0\rangle$. Thus, only $S_z = \pm 1/2$ subspaces are of interest. However, due to the symmetry (just flipping all the electron spins) between these two subspaces, we just pick the $S_z = 1/2$ subspace, which contains three singly occupied configurations and six doubly occupied configurations, for discussions. We again separate the space into $\mathcal{D}_A$ of singly occupied configurations and $\mathcal{D}_B$ of doubly occupied configurations.

In the subspace $\mathcal{D}_A$, we repeat the perturbative analysis, but up to the third order

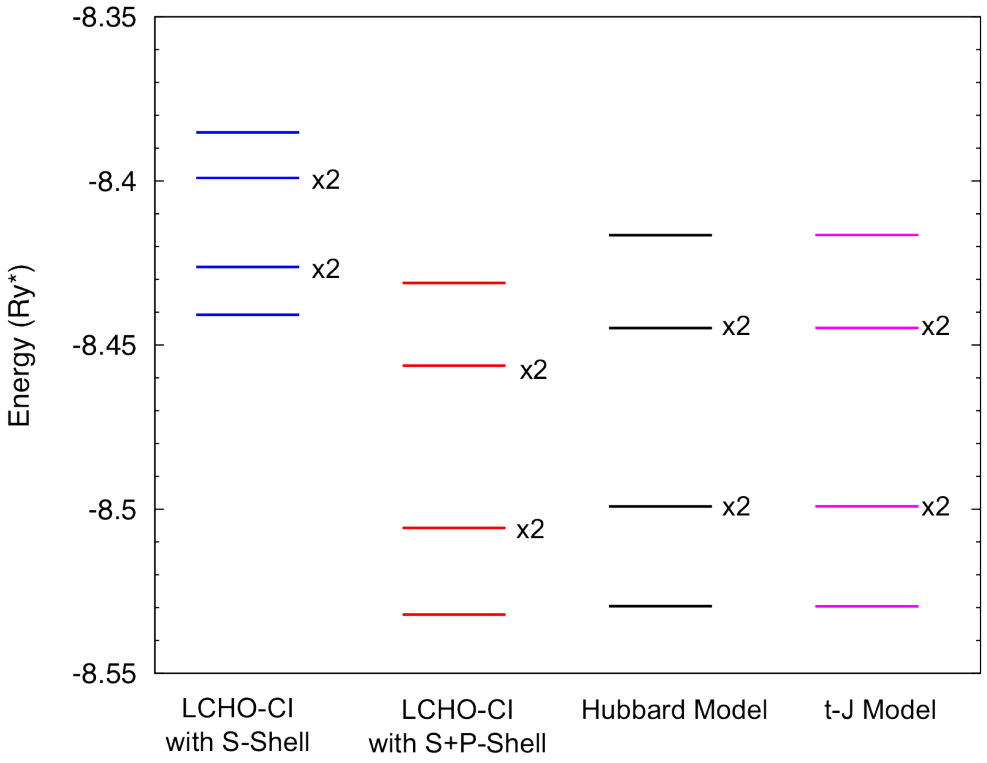

Figure 2.5: Energy spectra of the six lowest two-electron states in the $S_z = 0$ subspace of a triangular triple quantum dots. The first column presents calculations with LCHO-CI method with only S-shell in the single particle basis. The second column presents calculations with LCHO-CI with both S- and P-shells included in the single particle basis. The third column gives results by a Hubbard model whose parameters are obtained from the LCHO-CI model with S- and P-shells included. The fourth column shows the results by a t-J model derived from the Hubbard model. "X2" denotes doubly degenerate levels.

in this case, to derive the effective Heisenberg Hamiltonian with a chirality term,

$$\begin{aligned}\hat{H}_{Heis} &= \hat{H}_J + \hat{H}_\chi + \hat{H}_z, \\ &= \sum_{i<j} J_{ij}\left(\mathbf{S}_i \cdot \mathbf{S}_j - \frac{1}{4}\right) + \sum_{i<j<k} \chi_{ijk}\, \mathbf{S}_i \cdot (\mathbf{S}_j \times \mathbf{S}_k) + \hat{H}_z, \end{aligned} \tag{2.25}$$

where $\hat{H}_\chi$ is derived in the third order of the transformation and the coefficient $\chi_{ijk} = \frac{24|t_{ij}||t_{jk}||t_{ki}|}{(U-V)^2}\sin(2\pi\phi)$ exists only when the magnetic flux $\phi \neq 0$ and the field $\mathbf{B}$ is applied perpendicular to the triple quantum dot. It is important to derive the effective Hamiltonian up to the third order when $N_e = 3$, because the Heisenberg Hamiltonian $\hat{H}_J$ has a doubly degenerate ground state when $J_{ij} = J$ in the $S_z = -1/2$ subspace. This doubly degenerate ground state can be split due to the magnetic flux-induced term $\hat{H}_\chi$. In Eq.(2.25), we ignore the term $H_0 + H_V + H_U$ because they provide a constant shift of energy for all states.

2.2 Electronic and Spin Properties as a Function of Number of Electrons, Topology and Biasing of Central Dot

In this section, we study the electronic and spin properties of a triple quantum dot by exact diagonalization of the Hubbard Hamiltonian, Eq.(2.18). In particular, we consider two different topologies: linear (Fig.[2.1b]) versus triangular (Fig.[2.1b]) triple dots. However,we do not consider magnetic field in this section. For a triangular triple dot, we consider an almost fully resonant case where all the similar Hubbard parameters are identical, i.e. $t_{ij} = t$, $U_i = U$, and $V_i = V$, except the on-site energy

of dot 2 may be shifted by the bias Δ with respect to on-site energies of other two dots, i.e. $E_1 = E_3 = 0$ and $E_2 = \Delta$. For a linear triple dot, we consider the Hubbard model with the following parameters: $t_{12} = t_{23} = t$, $t_{13} = 0$, $U_1 = U_2 = U_3 = U$, $V_{12} = V_{23} = V_2$, $V_{13} = V$, $E_1 = E_3 = 0$, and $E_2 = \Delta$. The topology of the triple quantum dot depends on whether t_{13} equals to zero or not. The bias of the central dot, Δ, is used to electrically tune the singlet-triplet transition in a triangular triple quantum dot charged with 2 holes (4 electrons) in Chapter [4], and is also used to tune a linear triple dot into a particular quadruple point involving the following four charge configurations: $(1,0,1)$, $(1,1,1)$, useful for quantum information processing, $(2,0,1)$, and $(1,0,2)$ in Chapter [6]. In this section, we discuss the triple dots with up to $N_e = 5$ electrons. The sixth electron case does not require analysis, as there is only one possible configuration $|N_e = 6\rangle = c^\dagger_{1\uparrow} c^\dagger_{2\uparrow} c^\dagger_{3\uparrow} c^\dagger_{1\downarrow} c^\dagger_{2\downarrow} c^\dagger_{3\downarrow} |0\rangle$, where each molecular orbital is doubly occupied. The energy associated with this configuration is given by $E_F = 2\sum_i E_i + \sum_i U_i + \sum_{i\neq j} 2V_{ij}$.

2.2.1 One-Electron and One-Hole Case

First, we look at the single electron case. We consider the $S_z = -1/2$ subspace and use a localized basis $\{|1\rangle, |2\rangle, |3\rangle\}$, where $|i\rangle = c^\dagger_{i\downarrow}|0\rangle$. In this basis, the Hubbard Hamiltonian, Eq.(2.18), reads,

$$H_{1e} = \begin{bmatrix} 0 & t & t' \\ t & \Delta & t \\ t' & t & 0 \end{bmatrix}. \tag{2.26}$$

As mentioned, t' (tunnel coupling between dots 1 and 3) in the single-particle matrix above assumes value t for triangular triple dots and value 0 for linear triple dots.

By inspection we see that the state $|D\rangle = (|1\rangle - |3\rangle)/\sqrt{2}$ is an eigenstate of Hamiltonian, Eq.(2.26), for both values of t' considered. This state $|D\rangle$ is a quantum dot analogue of the "dark state" [55, 56, 36] in atomic physics and quantum optics. The dark state $|D\rangle$ is always the eigenstate of the system when Δ on dot 2 is the only changing parameter, since the dark state has no $|2\rangle$ contribution. This state will not conduct current when the triple quantum dot is coupled to the leads. The occupation of this dark state in a TQD should lead to negative differential conductance [56] in the transport spectroscopy. The coherent population trapping property of the dark state has been proposed as a useful resource for performing the Coherent Tunneling via Adiabatic Passage (CTAP) protocol [55] for transfer of quantum information encoded in a double-dot charge qubit.

There are two states orthogonal to the dark state $|D\rangle$: the bright state $|B\rangle = \frac{1}{\sqrt{2}}(|1\rangle + |3\rangle)$ and the central state $|C\rangle = |2\rangle$. The 2 by 2 Hamiltonian matrix spanned by the bright and central state can be analytically diagonalized, and the two eigenstates expressed as a linear combination of the bright and central state: $|M_1\rangle = \cos(\phi)|B\rangle + \sin(\phi)|C\rangle$ and $|M_2\rangle = -\sin(\phi)|B\rangle + \cos(\phi)|C\rangle$, where $\tan(2\phi) = 2\sqrt{2}t/(\Delta - t')$. The eigenenergies associated with $|D\rangle$, $|M_1\rangle$ and $|M_2\rangle$ are given by

$$\begin{aligned} E_D &= -t', \\ E_{M_1} &= \frac{t'+\Delta}{2} - \frac{1}{2}\sqrt{(\Delta - t')^2 + 8t^2}, \\ E_{M_2} &= \frac{t'+\Delta}{2} + \frac{1}{2}\sqrt{(\Delta - t')^2 + 8t^2}. \end{aligned} \tag{2.27a}$$

We note that $E_D = E_{M_1}$ is a doubly degenerate excited state when we have a fully

resonant triangular triple dots under the following conditions $t' = t < 0$ and $\Delta = 0$. Under the full resonance, the states $|M_1\rangle = \frac{1}{\sqrt{6}}(|1\rangle - 2|2\rangle + |3\rangle)$, $|M_2\rangle = |k_0\rangle = \frac{1}{\sqrt{3}}(|1\rangle + |2\rangle + |3\rangle)$, and $|D\rangle$ are commonly referred to as the Jacobi states. Since $|D\rangle$ and $|M_1\rangle$ are degenerate, we can have a linear combination of these two eigenstates, $|k_\pm\rangle = \frac{1}{\sqrt{3}}\left(|1\rangle + e^{\pm i2\pi/3}|2\rangle + e^{\pm i4\pi/3}|3\rangle\right)$. Representing the doubly degenerate excited states with $|k_\pm\rangle$ is useful when we discuss the Aharonov-Bohm oscillations in presence of a magnetic flux, and when we discuss the coded qubit in Chapter [3].

We remark that the single particle energy spectrum of a linear triple dot satisfies a specific order of energies, $E_{M_1} < E_D < E_{M_2}$, for all values of $\Delta > 0$.

Next, we discuss the electronic properties of one hole (five electrons). In the $S_z = -1/2$ subspace, there exists three possible hole configurations, which are obtained from the fully-occupied six-electron configuration $|N_6\rangle$ by removing a spin-down electron from one of the three localized orbitals. For instance, a hole on orbital i denotes $\left|i^h\right\rangle = h^\dagger_{i\downarrow}|N_e = 6\rangle$, where $h^\dagger_{i\downarrow} = (-1)^i c_{i\downarrow}$. If we build the Hamiltonian matrix in the basis of $\{\left|1^H\right\rangle, \left|2^H\right\rangle, \left|3^H\right\rangle\}$, the matrix has identical structure as the single electron matrix, Eq.(2.26). The only differences are (1) the diagonal matrix elements E_i should be replaced with $E_F - E_i - U_i - \sum_{j\neq i} 2V_{ij}$, where E_F is the energy for the six-electron configuration, and (2) the tunnel coupling acquires a negative sign, i.e. $t_{ij} \to -t_{ij}$. With these modifications made to the Hamiltonian matrix, Eq.(2.26), it now describes a single hole in the TQD. The eigenstates of the modified Hamiltonian remain intact from the particle-hole transformation, and still assumes the form (with the understanding that $|i\rangle$ should be replaced with $\left|i^H\right\rangle$ in the hole picture) described earlier. However, due to the negative sign introduced in the off-diagonal matrix ele-

ments, the energetic relatons among these eigenstates are reversed. For instance, for a fully resonant triangular TQD, a single hole has a doubly degenerate ground state given by $\left|D^H\right\rangle$ and $\left|M_1^H\right\rangle$ and a unique excited state $\left|M_2^H\right\rangle$.

2.2.2 2-Electrons and 2-Holes Case

We first discuss the two electron triplet $S_z = 1$ subspace with three basis vectors, $\{|T_{12}\rangle, |T_{13}\rangle, |T_{23}\rangle\}$, and their definitions are already provided in the section [2.1.3]. The Hubbard Hamiltonian in this basis reads

$$H_{2T} = \begin{bmatrix} \Delta + V^{'} & t & -t' \\ t & V & t \\ -t' & t & \Delta + V^{'} \end{bmatrix}, \tag{2.28}$$

where $t' = t$ and $V' = V$ for triangular triple dots and $t' = 0$ and $V' = V_2$ for linear triple dots. We observe that the Hamiltonian matrix, Eq(2.28), looks very similar to the Hamiltonian matrix, Eq.(2.26), when we subtract $\Delta + V'$ from the diagonal elements in Eq.(2.28). The negative phase associated with t' in Eq.(2.28) arises whenever an electron with spin σ is moved from dot 1 to dot 3 or vice versa when there is another electron with the same σ in dot 2. This is because of the anticommutation relation between fermion operators and the choice of the basis vector which order the fermion operators in a particular way.

Similarly, by inspection, we note that a triplet dark state $|T_D\rangle = (|T_{12}\rangle - |T_{23}\rangle)/\sqrt{2}$ is an eigenstate. Therefore, we define the triplet bright state $|T_B\rangle = (|T_{12}\rangle + |T_{23}\rangle)/\sqrt{2}$ and the triplet central state, $|T_C\rangle = |T_{13}\rangle$. Rotating the Hamiltonian, Eq. (2.28), into the basis of bright, central, and dark states, a 2 by 2 Hamiltonian matrix coupling the

bright and central states is derived. The other two eigenstates of the triplet subspace can then be obtained in the form of, $|M_1^T\rangle = \sin(\phi)|T_B\rangle + \cos(\phi)|T_C\rangle$ and $|M_2^T\rangle = -\cos(\phi)|T_B\rangle + \sin(\phi)|T_C\rangle$, where $\tan(2\phi) = -2\sqrt{2}t/(\Delta_v + t')$, and $\Delta_v = V - \Delta - V'$. The corresponding eigenenergies of the three states are

$$E_{T_D} = \Delta + V^{'} + t', \tag{2.29a}$$

$$E_{M_1^T} = \Delta + V^{'} + \frac{1}{2}\left((\Delta_v - t') - \sqrt{(\Delta_v + t')^2 + 8t^2}\right), \tag{2.29b}$$

$$E_{M_2^T} = \Delta + V^{'} + \frac{1}{2}\left((\Delta_v - t') + \sqrt{(\Delta_v + t')^2 + 8t^2}\right). \tag{2.29c}$$

For the fully resonant triangular triple dots, $t' = t$, $V' = V$ and $\Delta = 0$, the ground state is doubly degenerate with $E_{T_D} = E_{M_2^T}$, and the wave functions $\left|M_1^T\right\rangle = \frac{1}{\sqrt{6}}\left(|T_{12}\rangle + 2\,|T_{13}\rangle + |T_{23}\rangle\right)$, $\left|M_2^T\right\rangle = \frac{1}{\sqrt{3}}\left(|T_{12}\rangle - |T_{13}\rangle + |T_{23}\rangle\right)$, and $|T_D\rangle$ resemble the Jacobi states defined in the single particle case. A notable difference is the negative phase associated with $|T_{13}\rangle$ in $\left|M_1^T\right\rangle$ and $\left|M_2^T\right\rangle$ is mismatched with the phase of $|2\rangle$ in $|M_1\rangle$ and $|M_2\rangle$. This is because of the corresponding negative phase associated with t' in the Hamiltonian matrix Eq.(2.28). For the linear triple dots, similar to the single particle case, the 2-electron triplet spectrum always satisfy the relation: $E_{M_2^T} > E_{T_D} > E_{M_1^T}$ for all values of $\Delta > 0$. We next remark that the energy differences between the triplet states are proportional to a single particle property, the tunnel coupling t, because the two electrons in a triplet state do not occupy the same orbital due to the Pauli exclusion principle. This can be most easily shown when we consider a fully resonant triangular triple dot, the energy gap between the excited state and the doubly degenerate ground state is $3|t|$.

Next, we proceed to the analysis of the two-electron singlet subspace, which contains three singly occupied configurations and three doubly occupied configurations.

By specifying the basis vectors, $\{|S_{12}\rangle, |S_{13}\rangle, |S_{23}\rangle, |S_{11}\rangle, |S_{22}\rangle, |S_{33}\rangle\}$, the Hubbard Hamiltonian matrix reads,

$$H_{2S} = \begin{bmatrix} \Delta + V^{'} & t & t' & \sqrt{2}t & \sqrt{2}t & 0 \\ t & V & t & \sqrt{2}t' & 0 & \sqrt{2}t' \\ t' & t & \Delta + V^{'} & 0 & \sqrt{2}t & \sqrt{2}t \\ \sqrt{2}t & \sqrt{2}t' & 0 & U & 0 & 0 \\ \sqrt{2}t & 0 & \sqrt{2}t & 0 & 2\Delta + U & 0 \\ 0 & \sqrt{2}t' & \sqrt{2}t & 0 & 0 & U \end{bmatrix}. \tag{2.30}$$

The upper 3 by 3 matrix corresponds to the singly occupied configurations in the singlet subspace. This sub-matrix should be compared with Eq.(2.28) of triplet states, and the only difference is the sign factor associated with t', which matters only for a triangular topology. Thus, in a triangular topology, the singlet and triplet states can be discerned by the phase of t'.

Analytical expressions for all eigenvectors and eigenvalues of Eq.(2.30) are not easy to obtain under the most general case; however, we may obtain analytical results within the $t - J$ model if we are only interested in the three lowest states, which are approximated by the singly occupied configurations in the singlet subspace, when $U \gg V, \Delta$. Keeping the order of the basis vectors as in Eq.(2.30), the $t - J$ model for 2-electron singlets reads,

$$\mathbf{H}_{tj} = \begin{bmatrix} \tilde{E}_1 & \tilde{t} & \tilde{t'} \\ \tilde{t} & \tilde{E}_2 & \tilde{t} \\ \tilde{t'} & \tilde{t} & \tilde{E}_1 \end{bmatrix}, \tag{2.31}$$

where

$$\tilde{E}_1 = V + \Delta - J', \tag{2.32a}$$

$$\tilde{E}_2 = V' - J, \tag{2.32b}$$

$$\tilde{t} = t + 2J_3, \tag{2.32c}$$

$$\tilde{t'} = t' + 2J_3', \tag{2.32d}$$

where quantities in Eq.(2.32a's) are given as follows

$$J = 2|t|^2 \left[\frac{1}{U - V' + \Delta} + \frac{1}{U - V' - \Delta}\right], \tag{2.33a}$$

$$J_3 = -\frac{1}{2}|t|^2 \left[\frac{1}{U - V' + \Delta} + \frac{1}{U - V' - \Delta}\right], \tag{2.33b}$$

$$J' = 4|t'|^2 \left[\frac{1}{U - V}\right], \tag{2.33c}$$

$$J_3' = -|t||t'|\frac{1}{U - V}. \tag{2.33d}$$

For our following discussion, we will simply look at the ground state energy of the singlet subspace $E_S = \frac{1}{2}\left(\tilde{E}_1 + \tilde{E}_2 + \tilde{t'} - \sqrt{(\tilde{E}_1 - \tilde{E}_2 + \tilde{t'})^2 + 8\tilde{t}^2}\right)$, and the singlet-triplet gap given by

$$E_s - E_{M_1^T} = \begin{cases} t - \frac{2|t|^2}{U-V}, & triangular \\ -\frac{J}{2} - \frac{1}{2}\left[\sqrt{(V - V_2 + J)^2 + 8\tilde{t^2}} - \sqrt{(V - V_2)^2 + 8t^2}\right], & linear \end{cases} \tag{2.34}$$

when $\Delta = 0$. Since $t', t \leq 0$, we see that the singlet-triplet gap is negative for the 2-electron case for both topologies. If we consider now $U \gg \Delta \gg t$, then the singlet-triplet gap is approximately given by

$$E_s - E_{M_1^T} = \begin{cases} -\frac{4|t|^2}{U-V}, & triangular \\ -\frac{|t|^2}{U-V'+\Delta} - \frac{|t|^2}{U-V'-\Delta}. & linear \end{cases} \tag{2.35}$$

Eq.(2.34) and Eq.(2.35) together indicate that the 2-electron ground state is a singlet state for both topologies when $\Delta \ll U$.

When Δ approaches the values of U, the $t-J$ model is no longer applicable because the two subspaces $\mathcal{D}_A$ and $\mathcal{D}_B$ are no longer separated by a well-defined energy gap, a necessary condition to carry out the above perturbative analysis. We now consider $\Delta = U - V$, the two singly occupied states $|S_{12}\rangle$ and $|S_{23}\rangle$ become degenerate and hybridize with doubly occupied states $|S_{11}\rangle$ and $|S_{33}\rangle$ respectively, as checked by looking at the diagonal matrix elements in Eq.(2.30). Thus, we rotate the Hamiltonian matrix into a new basis set: $\{|S_{13}\rangle, \left|U_{12}^{\pm}\right\rangle, \left|U_{23}^{\pm}\right\rangle, |S_{22}\rangle\}$ where $\left|U_{12}^{\pm}\right\rangle = \frac{1}{\sqrt{2}}(|S_{12}\rangle \pm |S_{11}\rangle)$ and $\left|U_{23}^{\pm}\right\rangle = \frac{1}{\sqrt{2}}(|S_{23}\rangle \pm |S_{33}\rangle)$, which takes into account of hybridization. The state $|S_{22}\rangle \sim 3U$ (because the central dot is significantly biased with $\Delta \approx U$) becomes too high in energy and can be neglected. The state $|S_{13}\rangle$, not affected by the bias Δ on the central dot, becomes clearly the dominant ground state configuration. The ground state energy, up to 2nd order perturbation theory, is given by

$$E_S = V - 4t^2 \left(\frac{1}{2(U-V) + V' + 2\sqrt{t}} + \frac{1}{2(U-V) + V' - 2\sqrt{t}} \right), \tag{2.36}$$

for the linear topology. Compared with $E_{M_1^T}$, the 2-electron ground state is still a singlet state which is predominantly characterized by $(1, 0, 1)$ charge configuration when $\Delta = U - V$.

Next, we discuss two holes, removing two electrons from a complete shell of $N_e = 6$ electrons, in a triple dot. The Hubbard model can be converted for analysis in the hole picture; we need to apply the following transformations to single particle properties: $t_{ij} \rightarrow -t_{ij}^*$ and $E_i \rightarrow E_F - E_i - U_i - 2\sum_{j \neq i} V_{ij}$. Different from the electron picture, the hole tunnel coupling satisfies $t_{ij} > 0$, and increasing the on-site

energy E_i actually lowers the confining potential of a hole. Updating the parameters in Eq.(2.28), Eq.(2.30), and Eq.(2.20) accordingly, one can immediately deduce 2-hole properties from the equations derived when studying the 2-electron system. An interesting result arises in Eq.(2.34) for the triangular topology. Now, the fact that $t > 0$ implies the 2-hole ground state is a triplet when $\Delta = 0$. When $\Delta \gg t$, Eq.(2.35) implies a singlet-triplet transition such that the singlet becomes the 2-hole ground state. Fig.[2.6] shows the energy gap between the lowest singlet and triplet states as a function of bias Δ. Predicted by both the Hubbard and t-J models, the numerics confirms an electrically tuned singlet-triplet transition in a triangular triple quantum dot. This remarkable result demonstrates that the magnetic properties of a 2-hole triangular dot can be electrically manipulated. This idea inspired a scheme to electrically control the spin-spin interactions (ferromagnetic versus antiferromagnetic) between two electrons in a pair of neighbouring dots by coupling a third dot with two electrons to form a triple dot. This subject will be discussed in greater detail in Chapter [4].

2.2.3 Three-Electron Case

Finally, we consider three electrons in a triple dot. We focus on the unpolarized subspace $S_z = -1/2$ for discussions. In the regime of $U \gg |\Delta|, |t|$, the Heisenberg Hamiltonian provides an accurate approximation to the three lowest states. Fig.[2.7] shows the nine three-electron energy levels in $S_z = -1/2$ subspace calculated with the LCHO-CI (with S-shell only) and the Hubbard model, as well as the three lowest levels calculated with the Heisenberg model. As shown in the figure, the lower band

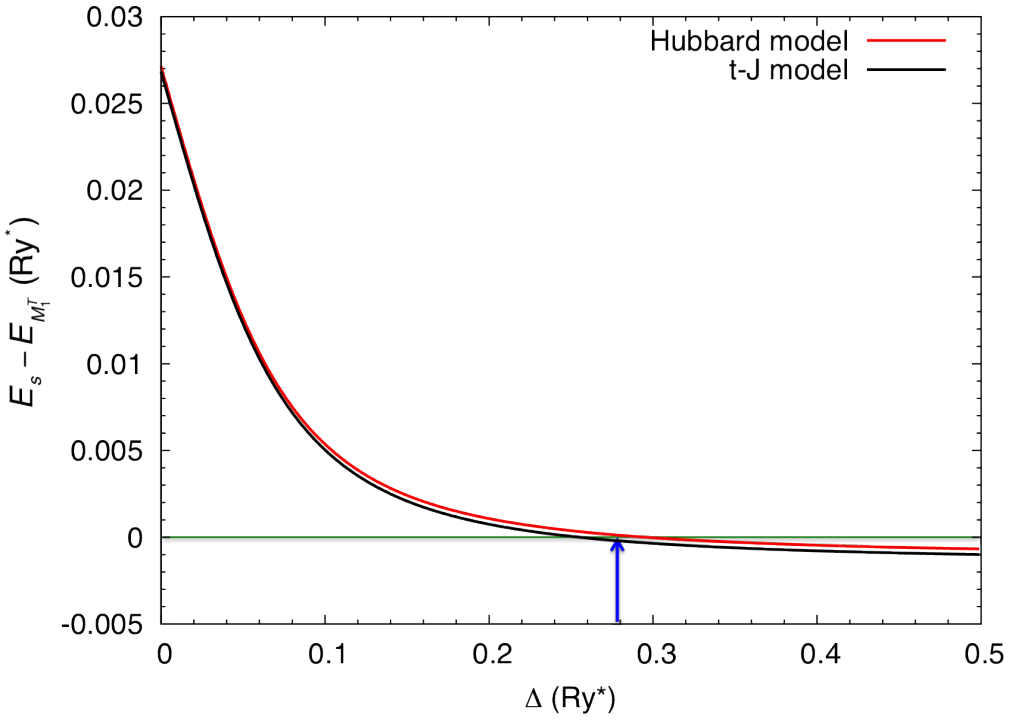

Figure 2.6: The triplet-singlet gap of two holes in a triangular triple quantum dot as a function of biasing on dot 2. The electrically tuned singlet-triplet transition is only expected to occur in the triangular topology.

of three lowest levels are well separated from the upper band of six levels by the order of $U - V$.

The Heisenberg Hamiltonian matrix in the basis of $\{|a\rangle, |b\rangle, |c\rangle\}$ reads,

$$\hat{H}_3 = \begin{bmatrix} -\frac{J}{2} - \frac{J'}{2} & \frac{J}{2} & \frac{J'}{2} \\ \frac{J}{2} & -J & \frac{J}{2} \\ \frac{J'}{2} & \frac{J}{2} & -\frac{J}{2} - \frac{J'}{2} \end{bmatrix}, \tag{2.37}$$

where J and J' are defined in Eq.(2.33a) and the basis vectors are defined as follows: $|a\rangle = \hat{c}^\dagger_{1\uparrow}\hat{c}^\dagger_{2\uparrow}\hat{c}^\dagger_{3\downarrow}|0\rangle$, $|b\rangle = \hat{c}^\dagger_{1\uparrow}\hat{c}^\dagger_{2\downarrow}\hat{c}^\dagger_{3\uparrow}|0\rangle$, $|c\rangle = \hat{c}^\dagger_{1\downarrow}\hat{c}^\dagger_{2\uparrow}\hat{c}^\dagger_{3\uparrow}|0\rangle$. The eigenenergies of Heisenberg model read,

$$E_0^3 = -\frac{J}{2} - J', \tag{2.38}$$

$$E_1^3 = -\frac{3J}{2}, \tag{2.39}$$

$$E_2^3 = 0. \tag{2.40}$$

with the corresponding eigenvector $|L_0\rangle = \frac{1}{\sqrt{2}}(|a\rangle - |c\rangle)$, $|L_1\rangle = \frac{1}{\sqrt{6}}(|a\rangle - 2|b\rangle + |c\rangle)$, $|L_2\rangle = \left|S_{3/2}\right\rangle = \frac{1}{\sqrt{3}}(|a\rangle + |b\rangle + |c\rangle)$. We see that $|L_{0,1}\rangle$ are spin-1/2 states, while state $|L_2\rangle$ is a spin-3/2 state. For a fully resonant triangular triple dot, $E_0^3 = E_1^3$ is the degenerate ground state. The two states $|L_0\rangle$ and $|L_1\rangle$ represent a good artificial two level system, which is energetically separated by $3J/2$ from the nearest state, $\left|S_{3/2}\right\rangle$. In Chapter [3], we discuss a three-electron logical qubit,which is a linear combination of $|L_{0,1}\rangle$ states. Sometimes it is more convenient to represent the three-electron logical qubit levels by $|q_\pm\rangle = \frac{1}{\sqrt{3}}\left(|c\rangle + e^{i\pm 2\pi/3}|b\rangle + e^{i\pm 4\pi/3}|a\rangle\right)$, which are eigenstates of the Heisenberg Hamiltonian matrix when $J = J'$ and also eigenstates of the chirality operator $\chi = \sum_{i<j<k} \mathbf{S}_i \cdot (\mathbf{S}_j \times \mathbf{S}_k)$. Therefore, the applications of the B_z field actually acts as a σ_z operator in the logical qubit's computational subspace.

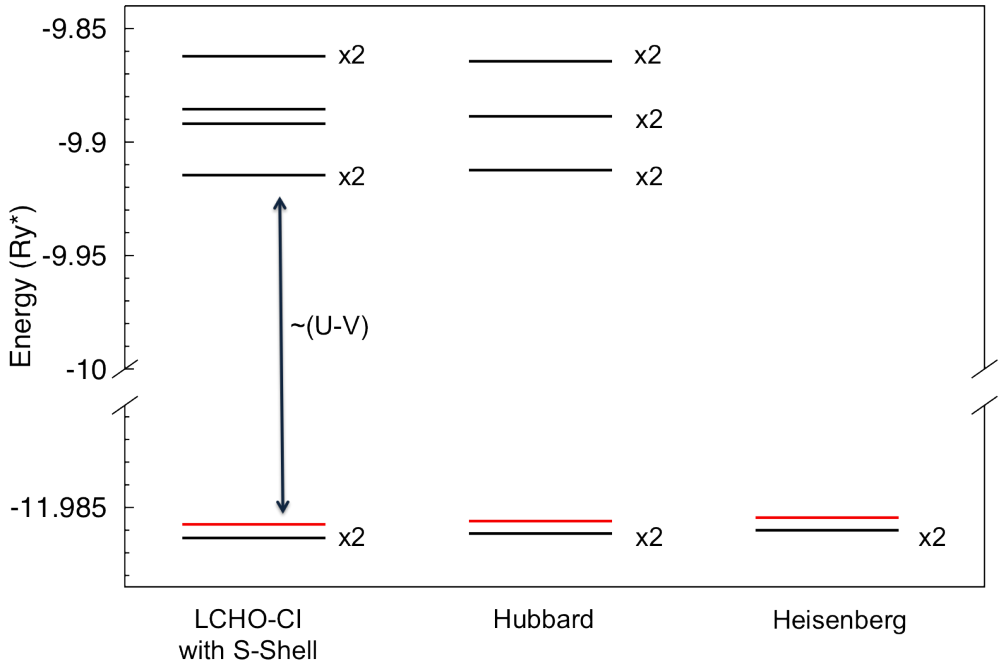

Figure 2.7: Energy spectra of three electrons in the $S_z = -1/2$ subspace of a triangular triple quantum dot. The left column gives results by LCHO-CI calculations with only S orbitals. The right column gives results by the corresponding Hubbard model. "X2" in the figure denotes doubly degeneracy. The last column on the right is obtained from Heisenberg model, which contains only localized spin configurations and only gives the three lowest states in the subspace. The red bars represent the $S = 3/2$ spin state in the subspace. The other black bars represent $S = 1/2$ states. The doubly degenerate ground state of this three-electron complex constitutes a well-isolated two-level system, which can be used as a coded qubit as discussed in the Chapter [3].

Next, we consider the case $\Delta \sim U$. In this limit, the Heisenberg model no longer remains valid. Analysis of the electronic structure has to be carried out within the Hubbard model. When Δ is large, two doubly occupied configurations $|d\rangle = \hat{c}^{\dagger}_{1\uparrow}\hat{c}^{\dagger}_{1\downarrow}\hat{c}^{\dagger}_{3\uparrow}|0\rangle$, and $|e\rangle = \hat{c}^{\dagger}_{1\uparrow}\hat{c}^{\dagger}_{3\uparrow}\hat{c}^{\dagger}_{3\downarrow}|0\rangle$ become close in energy with the three singly occupied configurations. This is because it costs roughly the same energy to place an electron on an empty dot 2 or an already occupied dot 1 or 3. Now, we include $|d\rangle$ and $|e\rangle$ in our previous perturbative analysis of the singly occupied configurations. To facilitate analysis, we define $|X\rangle = \frac{1}{\sqrt{2}}(|d\rangle + |e\rangle)$, and $|Y\rangle = \frac{1}{\sqrt{2}}(|d\rangle - |e\rangle)$. In the reduced basis,$\{|L_0\rangle, |X\rangle, |L_1\rangle, |Y\rangle\}$, the 3-electron Hubbard Hamiltonian reads,

$$H_{3el} = \begin{bmatrix} \Delta + 2V^{'} + V & -t & 0 & 0 \\ -t & U + 2V & 0 & 0 \\ 0 & 0 & \Delta + 2V^{'} + V & \sqrt{3}t \\ 0 & 0 & \sqrt{3}t & U + 2V \end{bmatrix}. \tag{2.41}$$

With a proper selection of basis functions, the 3-electron Hamiltonian matrix separates into a pair of sub-matrices describing logical qubit states $|L_0\rangle$ and $|L_1\rangle$, each entangled a specific linear combination of the doubly occupied configurations. Each sub-matrix can be independently diagonalized and the eigenstates read $|L_0^{+}\rangle = \cos(\phi)|L_0\rangle + \sin(\phi)|X\rangle$, $|L_0^{-}\rangle = \sin(\phi)|L_0\rangle - \cos(\phi)|X\rangle$, $|L_1^{+}\rangle = \cos(\theta)|L_1\rangle + \sin(\theta)|Y\rangle$, $|L_1^{-}\rangle = \sin(\theta)|L_1\rangle - \cos(\theta)|Y\rangle$, where $\tan(2\phi) = t/\xi$, $\tan(2\theta) = \sqrt{3}t/\xi$, and $\xi = (\Delta + 2V' - U - V)/2$. We remark that by tuning the bias Δ on the central dot, the few lowest eigenstates undergo smooth transition from predominantly characterized by $(1,1,1)$ configurations useful for quantum information processing to the regime where the hybridization between localized orbitals becomes important and the three-electron

wavefunctions become almost equal admixtures of $(1,1,1)$, $(2,0,1)$, and $(1,0,2)$ configurations needed for transport of electrons through a particular quadruple point discussed in greater detail in Chapter [6].

2.2.4 Stability Diagrams

Stability diagrams provide means to present important electronic and spin properties of a triple quantum dot. Fig.[2.8] presents the stability diagrams for linear and triangular triple quantum dots. The diagrams are calculated as follows. For given values of on-site energies (E_1, E_2, E_3) (however, $E_1 = E_3$ in Fig.[2.8]), we first compute the ground-state energy $E_{GS}(N_e)$ for each possible number of electrons (from $N_e = 1$ to $N_e = 6$). We then use these energies to calculate the chemical potential $\mu(N_e) = E_{GS}(N_e + 1) - E_{GS}(N_e)$. When $\mu(N_e)$ is below the chemical potential of the leads (which is taken to be 0 in this calculation), then the $(Ne + 1)$-th electron is added to the N_e-electron triple quantum dot. When N_e is the smallest number such that $\mu(N_e)$ is greater than the chemical potential of the leads, the number of electrons in the ground state is N_e. In Fig.[2.8], the spin of the ground state in the N_e subspace is shown.

In Fig.[2.8], we see that two-electron subspace always has spin-0 ground state in both topologies of the triple quantum dot. However, four-electron (two-hole) subspace allows singlet-triplet transitions in the triangular topology. Near the resonance condition, $E_1 = E_2 = E_3$, the 2-hole subspace admits triplet ground states in the triangular topology. Our result also shows that the three-electron ground state is always spin-1/2 in the absence of a magnetic field.

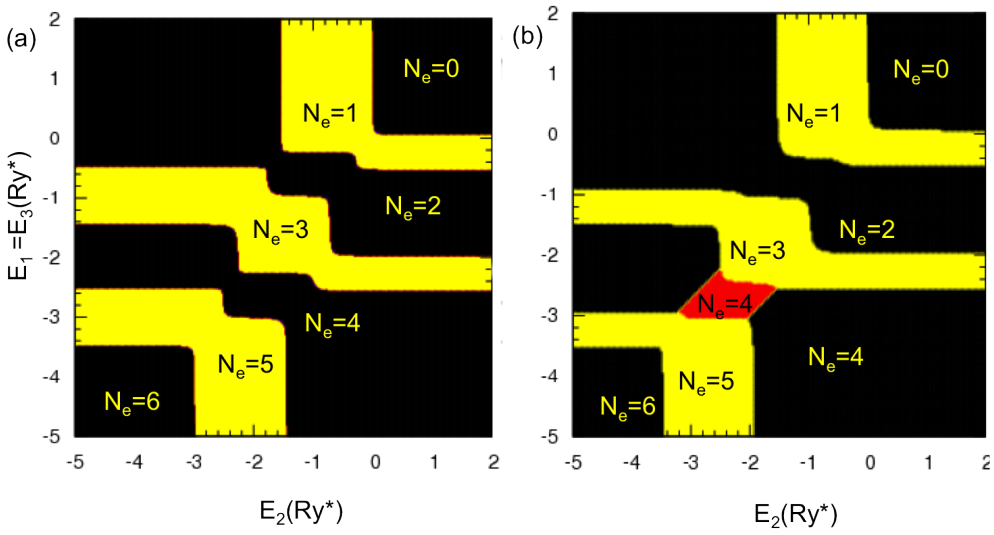

Figure 2.8: (a) Stability diagram of a linear triple quantum dot under the condition $E_1 = E_3$. (b) Stability diagram of a triangular triple quantum dot under the same condition. In both diagrams, the yellow-coloured regions have spin-1/2 ground states, the red-coloured regions have spin-1 ground states, and the black-coloured regions represent either spin-0 ground states or no electrons.

2.3 Aharonov-Bohm Oscillations in a Triple Quantum Dot

Now we discuss the effects of magnetic flux on electronic and spin properties of TQDs. We focus on a fully resonant triangular TQD ($\Delta = 0$, $t' = t$, and $V' = V$) subject to a perpendicular field $\mathbf{B}$, which generates a flux ϕ penetrating the closed-loop structure. As discussed in Ref. [57], a non-zero flux causes the Hubbard model's tunnel couplings to acquire Peierl's phases, $-|t_{ij}|e^{-i2\pi\phi_{ij}}$ with $\phi_{ij} = -\phi_{ij}$ and $\phi_{12} = \phi_{23} = \phi_{31} = \phi$ where ϕ is the flux and is expressed in the unit of the flux quanta $\phi_0 = hc/e$. The Peierl's phase is responsible for the Aharonov-Bohm (AB) oscillations in the energy spectra of TQDs. Furthermore, the Zeeman energy $g\mu_B BS_z$ also plays

an important role in favouring polarized spin states as the ground state. The spin property of the ground state is the interplay of the two factors.

First, we consider the single particle case. Under a B_z field, the total S_z is a good quantum number and we separate the Hilbert space into S_z-resolved subspaces. Therefore, we analyze just the $S_z = -1/2$ subspace for the one-electron case. The energies computed in the $S_z = -1/2$ subspace can be related to the energies in the $S_z = 1/2$ subspace by adding the proper Zeeman energy gap.

The single-particle Hamiltonian matrix, Eq.(2.1), is updated with $t_{ij}(\phi)$. The eigenstates are the Fourier transformation of the localized basis, $|k_s\rangle = \frac{1}{\sqrt{3}} \sum_{j=1}^{3} e^{si\frac{2\pi}{3}(j-1)} |j\rangle$ with $s = -1, 0, 1$. The corresponding eigenenergies (without the Zeeman energies) read $E_s(\phi) = -2|t| \cos(2\pi(\phi + s)/3)$. As shown in Fig.[2.9], these single particle energy levels undergo AB oscillations with periodicity of 3 flux quanta. At $\phi = (2n+1)/2$ with $n = 0, 1, 2, ...$ the system has a degenerate ground state and a unique ground state. At $\phi = n$, the spectrum is inverted with a degenerate ground state. The one-hole system has also eigenstates that are obtained by applying the discrete Fourier transformation on the localized configurations and its energy spectrum also manifest the AB oscillation at the same frequency. However, the degeneracy of the spectrum is inverted, i.e. whenever the one-electron spectrum has a degenerate ground state, the one-hole spectrum has a degenerate excited state, and vice versa.

Next, we proceed to the analysis of 2-electron and 2-hole cases. Again, we consider the 2-electron triplet subspace $S_z = 1$. The triplet Hamiltonian, Eq.(2.28), is also modified with the Peierl's phase factor added to the tunnel couplings; nevertheless, the triplet Hamiltonian still looks similar to the single particle Hamil-

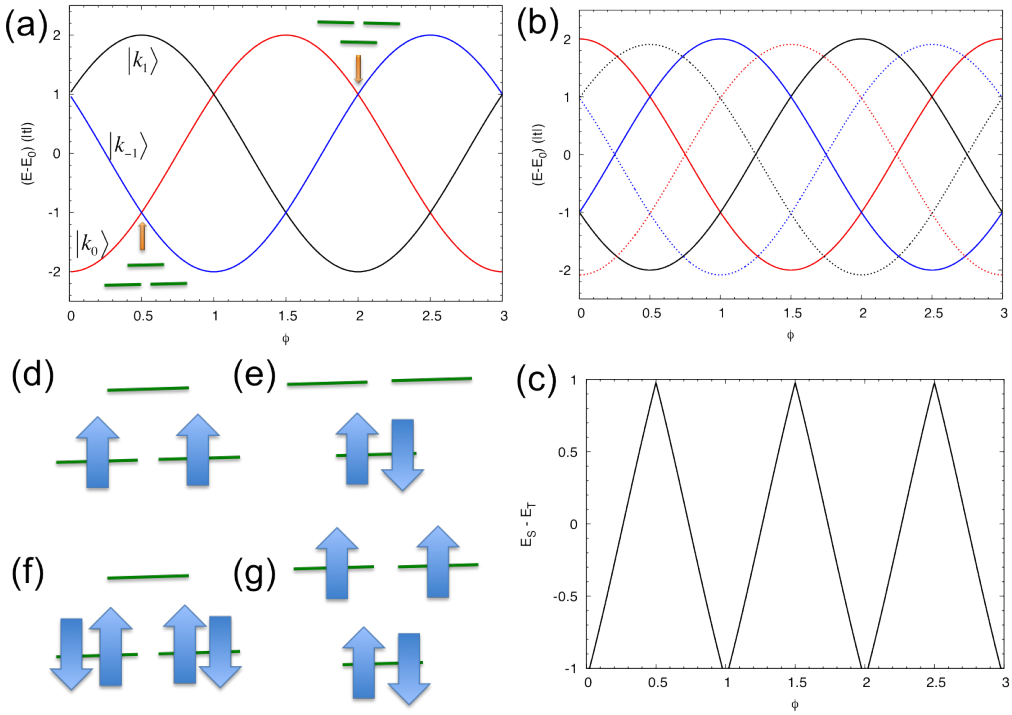

Figure 2.9: (a) Single-particle molecular levels (without the Zeeman energies) with $S_z = -1/2$ as function of ϕ. The three levels can be identified with states $|k_i\rangle$. As shown in the inset, the degeneracy point in the single particle spectrum is periodically inverted between the ground state and the excited state. (b) Two-electron energy spectra (without the Zeeman energies) as function of ϕ. The dashed curves represent the three lowest levels in the singlet subspace, and the solid curves are the three lowest levels from the triplet $S_z = 1$ subspace. (c) The two-electron singlet-triplet transition (without the Zeeman energies) as function of ϕ. (d) Two-electron ground state is a triplet when there is a molecular ground state that is doubly degenerate. The energy of the triplet configuration is lowered by the exchange interaction. (e) Two-electron ground state is a singlet when there is a unique molecular ground state. (f)-(g): similar to (d)-(e), but for 4-electron (two-hole) case. The situation is reversed. When the molecular ground state is unique, a two-hole triplet is the ground state and vice versa. The flux ϕ in all figures is given in units of flux quanta ϕ_0.

tonian. Thus, we identify the eigenstates for the 2-electron triplet subspace to be $\left|\bar{T}_k\right\rangle = \frac{1}{\sqrt{3}}\left(\left|T_{12}\right\rangle + e^{i\frac{2\pi}{3}k}\left|T_{13}\right\rangle + e^{i\frac{4\pi}{3}k}\left|T_{23}\right\rangle\right)$, with $k = -1, 0, 1$. The eigenenergies in this subspace are given by $E_T^s = V + 2|t|\cos\left(2\pi(\phi+s)/3\right)$. The 2-electron triplet energies (not including the Zeeman term) oscillate at the same frequency and the same order of magnitude as the single particle energies, as shown in Fig.[2.9b]. Next, we consider the 2-electron singlet subspace. We note the 3 by 3 sub-matrix in the upper corner again resembles the single particle Hamiltonian. So we rotate the Hamiltonian to the new basis $\{\left|\bar{S}_0\right\rangle, \left|\bar{S}_1\right\rangle, \left|\bar{S}_{-1}\right\rangle, \left|S_{11}\right\rangle, \left|S_{22}\right\rangle, \left|S_{33}\right\rangle\}$, where $\left|\bar{S}_k\right\rangle$ is defined similarly to the triplet states $\left|\bar{T}_k\right\rangle$. In this new basis, the three lowest energies (correspondingly approximately to $\left|\bar{S}_k\right\rangle$ with $k = -1, 0, 1$) are given by $E_S^k = V - 2|t|\cos(2\pi(\phi+s)/3) - \frac{8|t|^2}{3}\frac{\cos^2(2\pi(\phi+k)/3)}{(U-V+2|t|\cos(2\pi(\phi+k)/3)}$. As shown in Fig.[2.9b], the singlet energies oscillate at the same frequency as the triplet states as well as single particle states. The coherent oscillations of the triplet and singlet energies imply an oscillating triplet-singlet transition in the ground state of the 2-electron subspace as shown in Fig.[2.9c]. However, at high field limit, the Zeeman energy term forces the ground state to be polarized. The oscillation of the singlet-triplet transition may be understood from the periodic inversions of the degeneracy points in the single particle spectrum. When the system has a doubly degenerate single particle excited state, the 2-electron ground state is a singlet state as in Fig.[2.9e]; on the other hand, the 2-electron ground state is a triplet state as in Fig.[2.9d] when there is a doubly degenerate single particle ground state.

Now, we consider the two-hole case. We apply the particle-hole transformation to the 2-electron Hamiltonian matrices. After applying these changes, we find that both

two-hole triplet and singlet energies oscillate at the same frequency of 3 flux quanta as in the 2-electron case and the single particle case. Similar to the one-electron and one-hole case, the two-hole singlet-triplet ground state transition is out of phase with the two-electron case. Whenever the two-electron system has a triplet ground state, the two-hole system has a singlet ground state and vice versa. Fig.[2.9f] and Fig.[2.9g] illustrate the singlet-triplet configuration in the two-hole subspace. Finally, upon the introduction of the Zeeman energy, the system favours the polarized configuration at high field and suppresses further triplet-singlet transitions as in the case with 2-electron system.

At last, we discuss the magnetic flux-induced behaviour in the three-electron system, described by the Heisenberg model. The exchange interaction parameter J_{ij} depends only on the norm of the tunnel coupling $|t_{ij}|^2$; thus any flux dependent Peierl's phases get cancelled out. However, additional flux-dependent behaviours emerge in the third order perturbation analysis with the derivation of the chirality term, Eq.(2.25), when $\phi \neq 0$. The chirality operator has a coefficient $\chi_{ijk} = \frac{24|t_{ij}||t_{jk}||t_{ki}|}{(U-V)^2}\sin(2\pi\phi)$. Thus the two lowest states, the three-electron logical qubit levels $|q_{\pm}\rangle$ in each of the $S_z = \pm 1/2$ subspace undergo coherent oscillations with an amplitude $|t|^3/(U-V)^2$, and the oscillations frequency is only one third the frequency of the single particle AB oscillation. Since the three-electron energies oscillate with small amplitude, the effect is dominated by the Zeeman term. The Zeeman energy is on the order of 20 μeV / Tesla while the chirality-dependent splitting is on the order of 0.5 μeV for realistic GaAs parameters. Thus, in Fig.[2.10], the three-electron energy spectrum exhibits almost a linear dependence (a signature of Zeeman energy)

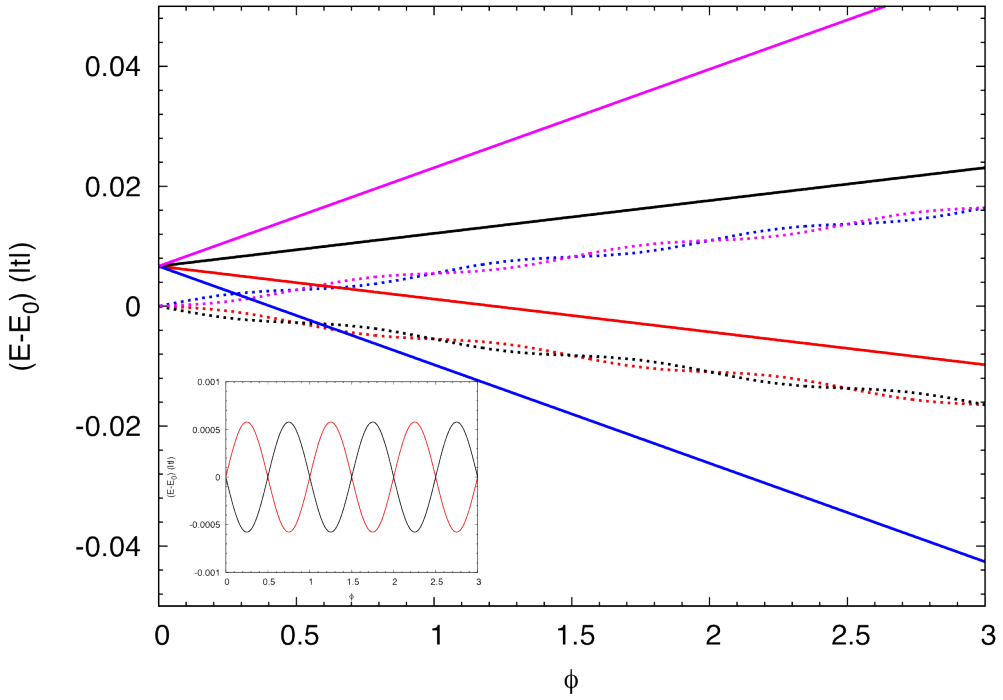

Figure 2.10: The 8 lowest three-electron levels as a function of ϕ in the entire Hilbert space with possible S_z projections. The Zeeman energy is included. The four lowest states (dashed curves) represent the degenerate levels in the $S_z = \pm 1/2$ subspaces, respectively, at zero field. Due to the chirality term in Eq.(2.25), the two levels in each branch undergoes oscillations. The inset shows the oscillations between black and red curves in the lower branch in detail. The flux ϕ in both figures is given in units of flux quanta ϕ_0.

on ϕ with some small oscillations within the two lowest branches in the figure. In the inset, the AB oscillations due to this chirality term is shown. The levels oscillate at 1/3 the frequency of the single particle states. At certain point, a transition of the ground state goes from spin-1/2 to spin-3/2 when the Zeeman term dominates and the polarized state is the preferred ground state.

Fig.[2.11] provides a summary of the electronic properties of a triple quantum dot as a function of on-site energies ($E_1 = E_2 = E_3$) and magnetic flux ϕ. As seen in the figure, the two-electron and two-hole subspaces undergoes AB oscillations as a function of ϕ, and make transitions between singlet and triplet ground states. However, at higher flux limit, the Zeeman term becomes important and the region of triplet as ground state is widened in the parameter space. As discussed already, the AB oscillation is exactly out of phase between the two-electron and two-hole subspace. For one-electron, three-electron, and one-hole subspace, the AB effects do not involve states from different total spin subspaces. In the three-electron subspace, the transition between spin-1/2 and spin-3/2 states is simply due to the Zeeman energy.

2.4 Conclusion

In this chapter, we introduced the set of theoretical tools we use to study the electronic and spin properties of a nanostructure, such as a gated lateral triple quantum dot, capable of confining a few electrons.

We next analyzed the electronic and spin properties of a triple quantum dot as a function of topology, bias, and number of electrons. We commented on the

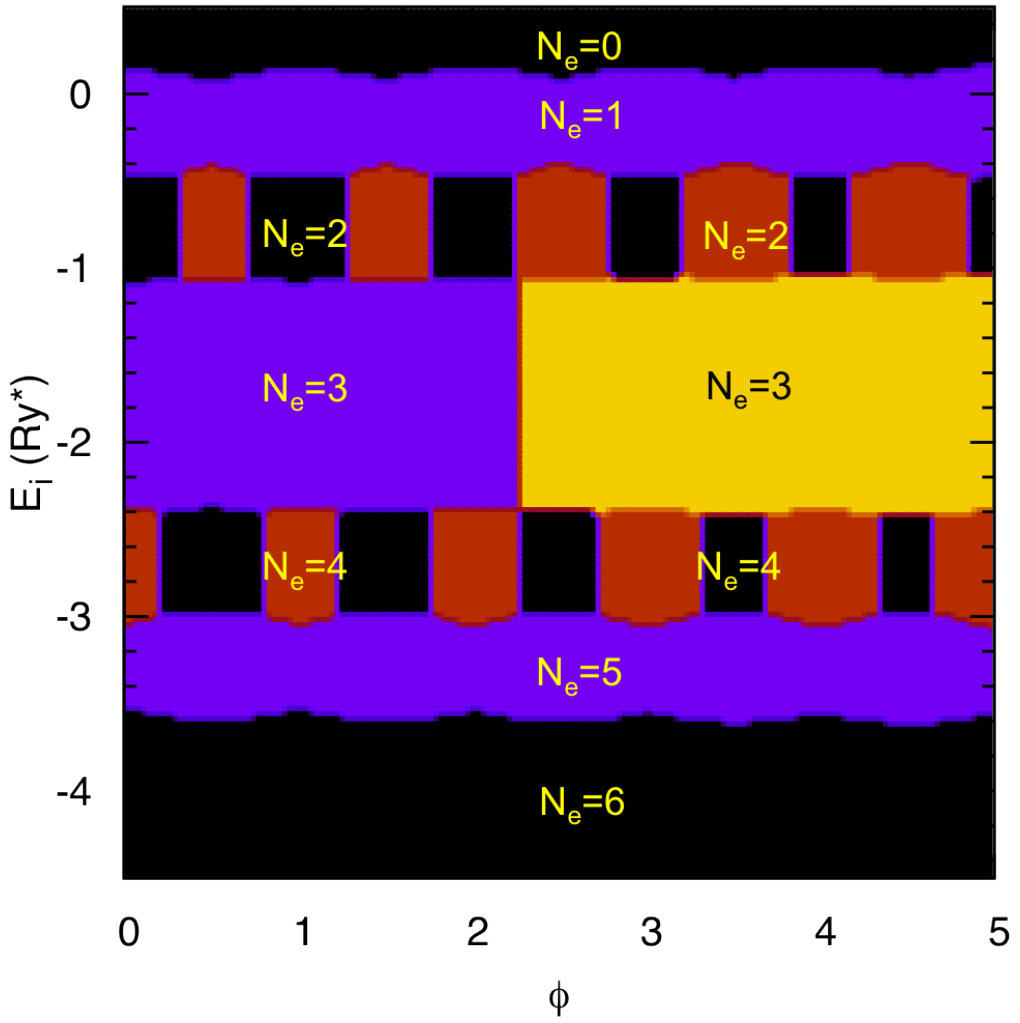

Figure 2.11: Stability diagram of a triangular triple quantum dot as a function of on-site energy $E_1 = E_2 = E_3$ and the magnetic flux ϕ threaded through the structure. The black-coloured regions denote spin-0 ground state or no electrons. The purple-coloured regions denote the spin-1/2 ground state. The orange-coloured regions denote the spin-1 ground states. The yellow-coloured regions denote the spin-3/2 ground states. As shown the stability diagram is separated into rows with well-defined number of confined electrons. The flux ϕ is given in units of flux quanta ϕ_0.

possibility of realizing a coded qubit with the lowest states in a half-filled TQD. We also pointed out the electrically-tuned magnetism, possible with 2 holes (or 4 electrons) in a triangular TQD.

We then analyzed the electronic and spin properties of a triangular triple quantum dot in the presence of a perpendicular field. In the two-electron and two-hole regime, the triple quantum dot manifests alternating singlet-triplet transitions, which gradually die out at higher field where the Zeeman energy dominates. In the three-electron regime, the chirality states also undergo AB oscillation. However, the magnitude of this oscillation is small.

Chapter 3

Chirality-based Coded Qubits in Triple Quantum Dot Molecules

3.1 Introduction

There is currently interest in exploiting electron spins for nano-spintronic [58] and quantum information processing [17, 59, 18, 32]. This is partly motivated by electron spin long coherence times [60] and availability of scalable semiconductor technology. In the simplest approach, a physical qubit is identified with the two states of an electron spin, which can be manipulated by utilizing electron spin resonance (ESR) with highly localized magnetic fields. Experiment demonstrating the basic single spin rotation with ESR was reported in Ref. [61]. As discussed in Chapter [1], the simple ESR proved to be very difficult to realize in a nanostructure. Much progress has been achieved in using the Electric Dipole Spin Resonance (EDSR) based approaches such as micro-magnet [62, 21] technology, and combination of oscillating electric field with

spin-orbital coupling [22], to drive coherent oscillations of electron spin qubits. An alternative approach is to encode a qubit in two levels of many-electron spin complexes [59]. This includes a singlet-triplet two electron coded qubit [24] and a qubit encoded in a degenerate ground state of a linear three-spin complex [25]. DiVincenzo et. al. [25] proposed the encoding of a qubit in the many-body states of a three-spin complex. They showed how to perform universal quantum computation by only tuning the exchange interaction between pairs of spins. The ability to manipulate the state of a coded qubit with voltages is due to the interplay of Coulomb interactions and the Pauli exclusion principle. Our proposed coded qubit in a triple quantum dot (TQD) is identified with the chirality of the three electron spin complex. Similar proposals implementing coded qubits with spins in TQDs [63] as well as atomic traps [64, 65] exist.

The advantages of working with a coded qubit are two-fold. First, every quantum gate can be implemented electrically. In such a scheme, the magnetic field is only used for initialization and measurement of a coded qubit. Second, the coded qubit operates in a Decoherence Free Subspace [26, 66, 63, 67] (DFS) and is immune to channels of collective decoherence. In later sections, we will look at decoherence due to fluctuating charged impurities [68] in semiconductor host material. Any qubit architecture that exploits the charge degree of freedom of an electron suffers decoherence due to electrostatic fluctuations such as 1/f or random telegraph noise.

Other interesting phenomena involving TQD molecules include non-Fermi liquid behaviour when coupled to leads [69, 70, 71], potential for generating maximally entangled three-partite GHZ and W states [72, 73, 74], and manipulation of the total

spin [39] of the four-electron complex in TQD.

In this work we develop a microscopic theory of logical qubits encoded in the chirality of electron spin complexes in TQD molecules. We use the Linear Combination of Harmonic Orbitals - Configuration Interaction (LCHO-CI) [75] formalism, Hubbard and Heisenberg models to determine a set of optimal conditions for coded qubit operations and derive an effective model of two qubit operations. We show that there exists an optimal in-plane magnetic field for the operation of coded qubits. However, the application of a magnetic field induces an undesired rotation of the coded qubit states; we show that the undesired rotation can be reversed by tuning the gate voltage on one of the dots. In our analysis of fluctuating charged impurity-induced decoherence, we find the coded qubit to be robust against this particular channel of decoherence. This suggests that the dominant source of decoherence for coded qubit is probably hyperfine-induced decoherence [76, 77, 78, 79]. In short, a coded qubit combines the advantages of a charge qubit, such as the possibility of performing coherent quantum operations with only electrostatic means, and that of the spin qubit, such as the long coherence time.

3.2 Models of Chirality-based Coded Qubits

Fig.[3.1a] presents the schematics of a large-scale quantum circuit consisting of N_M triangular triple quantum dot molecules (TQDMs). The circles in the schematics denote individual gated lateral quantum dots. The gates are tuned to confine a single electron, denoted by arrows, in each dot. With one spin per dot, each TQDM constitutes a coded qubit in this architecture. Additional gates (not shown here)

are used to control tunneling, shown schematically as solid lines, between dots in the same TQDM. Dashed lines indicate tunneling of electrons across neighbouring TQDMs. The tunneling effect mediates the exchange interaction between electron spins localized on neighbouring QDs. The brackets in the schematics indicate that the two TQDMs are isolated from the rest of the circuit. It is assumed that any number of TQDMs can be isolated from the rest of the circuit by simply turning off the boundary exchange interactions with gate voltages.

For comparison, Fig.[3.1b] shows another possible quantum circuit composed of linear, instead of triangular, TQDMs. This layout is similar to the linear chain of spins originally proposed by DiVincenzo et. al. [25], in which there is effectively no exchange interaction between spins on the edge dots. Fig.[3.1c] is another possible architecture studied by Weinstein [63] et. al. for spin system. However, this architecture allows the possibility of having a strong next-nearest neighbour coupling between TQDMs when the inter-TQDM distance falls below some critical distance. We prefer the architecture illustrated in Fig.[3.1a] because the system is much easier to operate when only nearest neighbours on the chain are coupled. Under the assumption that we can electrically control the exchange interactions between QDs, the study of this large-scale quantum circuit is essentially reduced to study of the fundamental circuit components: single TQDM and two coupled TQDMs.

In order to thoroughly analyze a single TQDM, the most elementary component of a quantum circuit described in this study, we apply the LCHO-CI formalism to describe its electronic properties with microscopic details. It is important to start the analysis with a microscopic model for two reasons. First, we want to present a

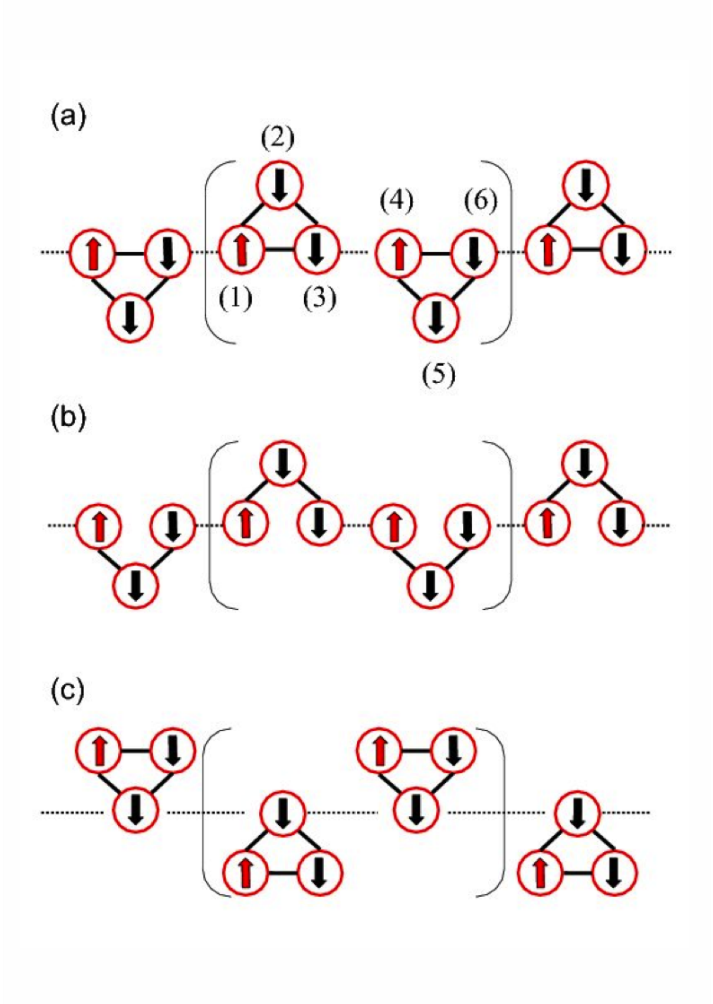

Figure 3.1: Three possible layouts for a chain of coded qubits. Each solid and dash line represents an exchange interaction between a pair of QDs. The layouts (a) and (b) differ in that the constituent coded qubits are implemented with triangular TQD in (a) and with linear TQD in (b). The layouts (a) and (c) differ in the way coded qubits are connected in a chain. If the inter-qubit distance is reduced beyond a threshold, an additional set of exchange interactions will arise and dominate the behaviour of the system in layout (c).

more comprehensive analysis of the chiral states starting from the microscopic model. Secondly, to properly account for the decoherence induced by the fluctuating charged impurity, we should incorporate the Coulomb interaction between electron spins and the charged impurity in the microscopic model. Based on the LCHO-CI calculations, we then derive the Hubbard and Heisenberg model of a single TQDM, and we will use these effective Hamiltonians as the basis to describe the large-scale quantum circuits composed of N_M TQDMs.

3.2.1 LCHO-CI Microscopic Model

For completeness, we briefly remind readers of the LCHO-CI formalism, Hubbard model and Heisenberg model introduced in Chapter [2]. With energy measured in terms of effective Rydberg, Ry^*, and length in effective Bohr radius, a_B, the dimensionless Hamiltonian of N_e electrons confined in a single TQD read

$$\hat{H}_{N_e} = \sum_i \left(-\vec{\nabla}_i^2 + V_{TQD}(\vec{r}_i) \right) + \sum_{i<j} \frac{2}{|\vec{r}_i - \vec{r}_j|}, \tag{3.1}$$

where $\vec{r}_i$ is the (x, y) position of i^{th} electron. The first term in Eq.(3.1) is the sum of one electron hamiltonians $\hat{H}_{sp}$ with the TQD potential $V_{TQD}(\vec{r}_i)$ given in Eq.(2.2), and the second term accounts for the mutual Coulomb interaction among electrons.

Solving the single-particle Hamiltonian, $\hat{H}_{sp}$, by the S-shell LCHO formalism described in Chapter [2], the single-particle molecular states of a resonant triangular

TQD reads

$$|k_0^{HO}\rangle = 1/\sqrt{3(1+2s)}\,(|\phi_1\rangle + |\phi_2\rangle + |\phi_3\rangle) \tag{3.2a}$$

$$|k_1^{HO}\rangle = 1/\sqrt{3(1-s)}\left(|\phi_1\rangle + e^{i2\pi/3}|\phi_2\rangle + e^{i4\pi/3}|\phi_3\rangle\right)$$

$$|k_{-1}^{HO}\rangle = 1/\sqrt{3(1-s)}\left(|\phi_1\rangle + e^{-i2\pi/3}|\phi_2\rangle + e^{-i4\pi/3}|\phi_3\rangle\right),$$

where $\phi_i(\mathbf{r})$ is the S orbital on dot i, and s is the overlap matrix element $\langle\phi_i|\phi_j\rangle$, $i \neq j$. The molecular ground state $|k_0^{HO}\rangle$ is non-degenerate and resembles a standing wave. The two excited states labeled by wave vector $k_{\pm 1}$ are degenerate, and correspond to an electron moving either to the left or to the right (charge current). Thus, we assign quasi-momentum $k_m = 2\pi m/3$ with $m = -1, 0, 1$ to the molecular state $\left|k_{-1}^{HO}\right\rangle$, $\left|k_0^{HO}\right\rangle$, and $\left|k_1^{HO}\right\rangle$ respectively.

With an abbreviation i denoting the molecular states $|k_i^{HO}\rangle$, Eq.(3.1) can be cast in the second quantized form

$$\hat{H}_{N_e} = \sum_{j,\sigma} \varepsilon^0_{j,\sigma} d^+_{j\sigma} d_{j\sigma} + \frac{1}{2} \sum_{\substack{ijkl \\ \sigma,\sigma'}} \langle ij|\hat{V}_c|kl\rangle d^+_{i\sigma} d^+_{j\sigma'} d_{k\sigma'} d_{l\sigma}, \tag{3.3}$$

where $d^+_{j\sigma}$ ($d_{j\sigma}$) creates (annihilates) an electron with spin σ on the molecular orbital $\left|k_j^{HO}\right\rangle$, and ε^0_j represents the corresponding single-particle energy. We remark that the electron-electron Coulomb interaction $\langle ij|\hat{V}_c|kl\rangle$ conserves the sum of quasi-momentum for molecular states, i.e. $k_i + k_j = k_k + k_l$, for a resonant triangular TQD. Thus, the total quasi-momentum is a good quantum number of the N_e-electron system.

The Hamiltonian, Eq.(3.3), commutes with total S_y operator and the three-electron subspace can be further divided into the S_y-resolved subspaces. Later, we will apply an in-plane magnetic field $\mathbf{B}$ along $\hat{y}$ direction; therefore, we choose the

spin quantization axis along $\hat{y}$. Each configuration $|p\rangle = |i_1^p\sigma_1^p, i_2^p\sigma_2^p, i_3^p\sigma_3^p\rangle$ distributes the three electrons onto a set of molecular orbitals $\{i_1^p, i_2^p, i_3^p\}$, and has a well-defined total quasi-momentum $K^p = \sum_j k_{i_j^p}$. Because of the translational symmetry associated with a fully resonant triangular triple dot, the quasi-momenta K's which lie outside the Brillouin zone $[-2\pi/3, 2\pi/3]$ are translated back by reciprocal lattice vectors $(2\pi/3)n$ with n being some integer; this implies that K^p for any configuration can only assume one of the three possible values $K_i = 2\pi i/3$, with $i = -1, 0, 1$. Grouping the three-electron configurations by their total quasi-momentum K_i, the $S_y = -1/2$ Hamiltonian matrix written in the configurations of molecular orbitals can be arranged in the block-diagonal form with three sub-matrices, each a 3 by 3 matrix corresponding to a specific value of K_i, respectively. It follows that the eigenstates of the Hamiltonian, Eq.(3.3), also have a well-defined quasi-momentum K_i and can be written as a linear combination of only configurations in the same subspace: $\left|\bar{K}_i^m\right\rangle = \sum_p A_p^{m,i} \left|K^p\right\rangle$ with m denoting the m^{th} eigenstate in the subspace of K_i and coefficient $A_p^{m,i} \neq 0$ when $K^p = K_i$. In this notation, the eigenvalue index m starts at 1 for the ground state.

Fig.[3.2] shows the three-electron energy spectrum of a TQD [27, 75]. In terms of localized HO orbitals, the six higher levels in the inset of Fig.[3.2] are composed mostly of doubly-occupied configurations, whereas the three lowest energy levels are mainly composed of singly-occupied configurations

$$\left|\bar{K}_s^1\right\rangle = \frac{1}{\sqrt{3}}(a_{1\uparrow}^+ a_{2\downarrow}^+ a_{3\downarrow}^+ |0\rangle + e^{si\frac{2\pi}{3}} a_{1\downarrow}^+ a_{2\uparrow}^+ a_{3\downarrow}^+ |0\rangle + e^{si\frac{4\pi}{3}} a_{1\downarrow}^+ a_{2\downarrow}^+ a_{3\uparrow}^+ |0\rangle), \tag{3.4}$$

where $a_{i\sigma}^+$ creates an electron with spin σ on the localized HO orbital on dot i, and $s = -1, 0, 1$. The ground state $\left|\bar{K}_0^1\right\rangle$ in the K_0 subspace has the total spin $S = 3/2$. The

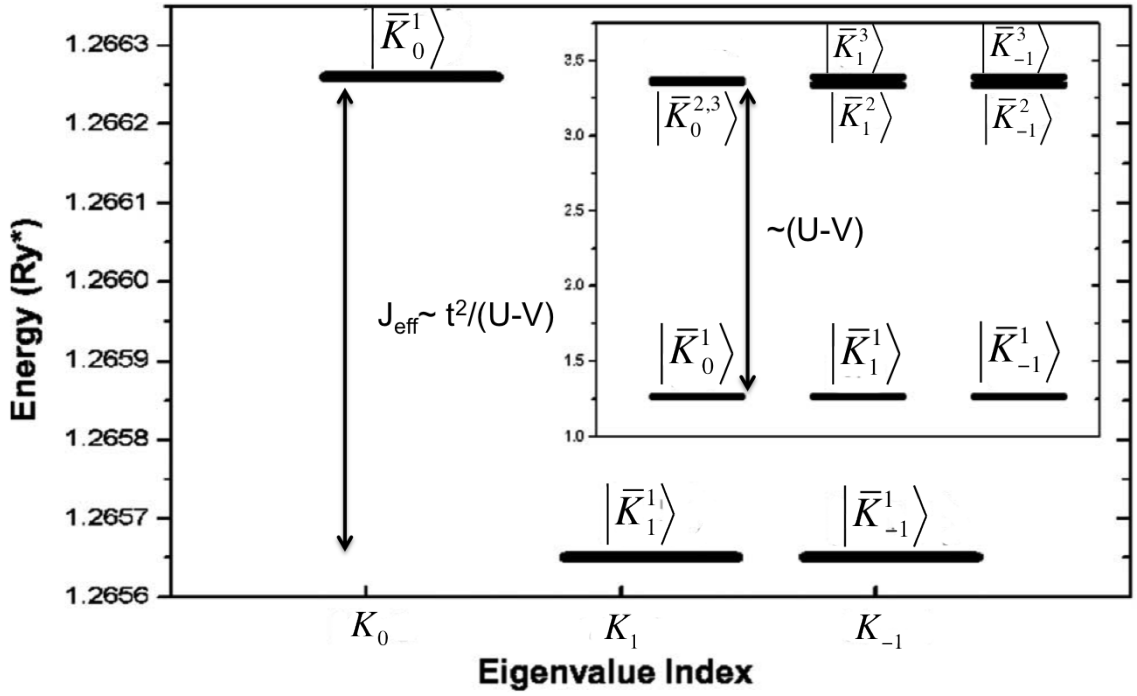

Figure 3.2: The three lowest energy levels in the $S_y = -1/2$ subspace for a TQD with one electron in each dot. These three states $|\bar{K}^1_m\rangle$ are defined in the text. The two degenerate states, $|\bar{K}^1_1\rangle$ and $|\bar{K}^1_{-1}\rangle$ form a coded qubit. Inset: energy spectrum, including singly and doubly occupied states, of three electrons in a resonant TQD. The energies are grouped by the total quasi-momentum K_i with $i = 0, 1, -1$.

ground states $|\bar{K}^1_1\rangle$ and $|\bar{K}^1_{-1}\rangle$ in the subspace K_1 and K_{-1}, respectively, constitute a well-isolated two-level system and have opposite sign for the quasi-momentum. These two coded qubit states are isolated from the spin polarized states $|\bar{K}^1_0\rangle$ with zero quasi-momentum by a gap designated as J_{eff} and isolated from the six other high-lying states by an even larger gap proportional to $U-V$, where U and V are the Coulomb repulsions between electrons on the same dot and different dots respectively.

3.2.2 Effective Models

As described in Sec.[2.1.2], results of LCHO-CI calculation can be used to derive Hubbard orbitals and parameters in the Hubbard Hamiltonian,

$$\hat{H}_{hubb} = \sum_{i=1}^{3} E_i n_{i\sigma} + \sum_{\substack{i,j=1 \\ i\neq j}}^{3} \sum_{\sigma} t_{ij} c_{i\sigma}^{\dagger} c_{j\sigma} + \frac{1}{2} \sum_{\substack{i,j=1 \\ i\neq j}}^{3} V_{ij} \rho_i \rho_j + \sum_{i=1}^{3} U_i n_{i\uparrow} n_{j\downarrow}, \tag{3.5}$$

where $c_{i\sigma}$ ($c_{i\sigma}^{\dagger}$) denotes annihilation (creation) operators for Hubbard orbitals, $n_{i\sigma} = c_{i\sigma}^{\dagger} c_{\sigma}^{\dagger}$, and $\rho_i = n_{i\uparrow} + n_{i\downarrow}$. Definitions of Hubbard parameters may be found immediately following Eq.(2.18). For a resonant TQD, all the similar parameters share just one value and we will drop the orbital indices and write, for instance, $t_{ij} = t$ and $V_{ij} = V$ etc.

Eq.(2.19) provides the necessary formula to relate the Coulomb matrix parameters U_i and V_{ij} to the microscopic details calculated in the LCHO-CI formalism. Here, we provide explicit formula for relating the single-particle parameters E_i and t_{ij} to the microscopic details,

$$\begin{aligned} E_i = {} & \langle \phi_i | \hat{H}_{sp} | \phi_i \rangle + 2\tilde{s}(\langle \phi_i | \hat{H}_{sp} | \phi_j \rangle + \langle \phi_i | \hat{H}_{sp} | \phi_k \rangle) \\ & + \tilde{s}^2(\langle \phi_j | \hat{H}_{sp} | \phi_j \rangle + \langle \phi_k | \hat{H}_{sp} | \phi_k \rangle + 2\langle \phi_j | \hat{H}_{sp} | \phi_k \rangle), \end{aligned} \tag{3.6a}$$

$$\begin{aligned} t_{ij} = {} & \langle \phi_i | \hat{H}_{sp} | \phi_j \rangle + \tilde{s}(\langle \phi_i | \hat{H}_{sp} | \phi_i \rangle + \langle \phi_j | \hat{H}_{sp} | \phi_j \rangle + \langle \phi_i | \hat{H}_{sp} | \phi_k \rangle + \langle \phi_j | \hat{H}_{sp} | \phi_k \rangle) \\ & + \tilde{s}^2(\langle \phi_k | \hat{H}_{sp} | \phi_k \rangle + \langle \phi_i | \hat{H}_{sp} | \phi_j \rangle + \langle \phi_i | \hat{H}_{sp} | \phi_k \rangle + \langle \phi_j | \hat{H}_{sp} | \phi_k \rangle), \end{aligned} \tag{3.6b}$$

where $\tilde{s} = \frac{1}{3}(\frac{1}{\sqrt{1+2s}} - \frac{1}{\sqrt{1-s}})$ is the off-diagonal matrix element for the matrix $\mathbf{S}^{-1/2}$, Eq.(2.17), and $s = \langle \phi_i | \phi_j \rangle$.

In order to analyze two coupled TQDMs, we model them with the following Hamil-

tonian,

$$\hat{H}_2 \;=\; \hat{H}^L_{hubb} + \hat{H}^R_{hubb} + + \sum_\sigma t' \left(\hat{c}^\dagger_{3\sigma} \hat{c}_{4\sigma} + \hat{c}^\dagger_{4\sigma} \hat{c}_{3\sigma} \right) + V' \hat{\rho}_3 \hat{\rho}_4, \tag{3.7}$$

where $\hat{H}^L_{hubb}$ ($\hat{H}^R_{hubb}$) represents a single TQDM Hubbard Hamiltonian, Eq.(3.5), for the left (right) TQDM. Furthermore, we index the Hubbard orbitals as shown in Fig.[3.1a] where the third and the fourth orbitals ($i = 3, 4$) belong to the two adjacent dots connecting the two TQDMs. The parameters t' and V' represent the inter-TQDM tunneling matrix element and inter-molecular Coulomb interactions. V' is scaled from V by the ratio of distance between adjacent dots in a TQDM and the inter-TQDM distance. t' is simply taken to be an adjustable variable. In our model, we consider the parameters corresponding to the regime of strong Coulomb interactions: $t' < t \ll V' < V < U$.

Next, we map the low energy spectrum of the Hubbard Hamiltonians, Eq.(3.5) and Eq.(3.7), onto the Heisenberg Hamiltonian as discussed in Sec.[2.1.3],

$$\hat{H}_J = \sum_{i<j} J_{ij} \mathbf{S}_i \cdot \mathbf{S}_j, \tag{3.8}$$

where we ignore the constant term $\frac{1}{4} n_i n_j$, appearing in Eq.(2.21), which just introduces an overall shift of energy without further implications at the half-filled regime. We remind that the coded qubit levels are defined as follows,

$$|q_\pm\rangle \;=\; \frac{1}{\sqrt{3}} \sum_{n=1}^{3} e^{\pm i 2\pi (n-1)/3} \, |n\rangle \,, \tag{3.9}$$

where $|n\rangle = S^+_n \, |{\downarrow_1}{\downarrow_2}{\downarrow_3}\rangle$. If we represent the Heisenberg Hamiltonian in the basis of $\{|q_-\rangle \,, |q_+\rangle\}$, then we get the effective Hamiltonian for the coded qubit,

$$\hat{H}_{1q} = \frac{1}{2} \left(J_{12} - \frac{1}{2} J_{13} - \frac{1}{2} J_{23} \right) \sigma_x + \frac{\sqrt{3}}{4} \left(J_{13} - J_{23} \right) \sigma_y. \tag{3.10}$$

Eq.(3.10) is a spin Hamiltonian with an effective, in-plane magnetic field given by the exchange interactions.

We compute the exchange constants J_{ij} from the Hubbard Hamiltonian (3.5) through perturbation theory in strong Coulomb interaction regime ($U-V >> t_{ij}, |E_i - E_j|$). We find

$$J_{ij} = 2|t_{ij}|^2 \left(\frac{1}{U - V + (E_i - E_j)} + \frac{1}{U - V - (E_i - E_j)} \right). \tag{3.11}$$

The exchange interaction can be controlled by either tuning the tunneling matrix element t_{ij} by, for example, additional gates controlling the height of the tunneling barrier, or by biasing the dots and changing their on-site energy $E_{i(j)}$.

3.2.3 Chiral States

In the discussion of the microscopic model, we showed that a fully resonant TQD has a doubly degenerate ground state, $\left|\bar{K}^1_1\right\rangle$ and $\left|\bar{K}^1_{-1}\right\rangle$, in the $S_y = -1/2$ subspace. These two states were shown to possess opposite sign for the quasi-momentum, $K_{\pm 1}$. Given Eq.(3.4) and Eq.(3.9), we can see that $\left|\bar{K}^1_{\pm 1}\right\rangle$ and $|q_\pm\rangle$ are just different representations of the same states in different models. The quasi-momentum in the microscopic model is translated into the chirality in the Heisenberg spin model.

We now show that the states $|q_\pm\rangle$ are indeed the eigenstates (with eigenvalues of opposite signs) of the chirality operator, $\sum_{i<j<k} \mathbf{S}_i \cdot (\mathbf{S}_j \times \mathbf{S}_k)$, which measures the degree of collinearity of the three spins. For this purpose, we simply need to act with the operator $\mathbf{S}_1 \cdot (\mathbf{S}_2 \times \mathbf{S}_3)$ on $|q_\pm\rangle$ and see if we get back the same states.

In order to prove the claim, we first expand the operator,

$$\begin{aligned}\mathbf{S}_1 \cdot (\mathbf{S}_2 \times \mathbf{S}_3) =& \frac{-i}{2} \left(S_{1z'} \left[S_2^- S_3^+ - S_2^- S_3^+ \right] + S_{2z'} \left[S_1^+ S_3^- - S_1^- S_3^+ \right] \right. \\ & \left. + S_{3z'} \left[S_1^- S_2^+ - S_1^+ S_2^- \right] \right), \end{aligned} \tag{3.12}$$

where a change of variables is made such that $(x \to y', y \to z', z \to x')$, and $S_i^{\pm} = S_{ix'} \pm S_{iy'}$. We make this transformation in order to conform to the standard notation that quantization axis is usually labelled with z. The effects of this operator acting on the three singly occupied configurations in $S_y = -1/2$ subspace are summarized below,

$$\mathbf{S}_1 \cdot (\mathbf{S}_2 \times \mathbf{S}_3) \left| \uparrow\downarrow\downarrow \right\rangle = \quad \frac{i}{2} \left[S_1^- S_2^+ S_{3z'} - S_1^- S_3^+ S_{2z'} \right] \left| \uparrow\downarrow\downarrow \right\rangle = \quad \frac{i}{4} \left[\left| \downarrow\uparrow\downarrow \right\rangle - \left| \downarrow\downarrow\uparrow \right\rangle \right], \tag{3.13a}$$

$$\mathbf{S}_1 \cdot (\mathbf{S}_2 \times \mathbf{S}_3) \left| \downarrow\uparrow\downarrow \right\rangle = \quad \frac{i}{4} \left[S_2^- S_3^+ S_{1z'} - S_1^+ S_2^- S_{3z'} \right] \left| \downarrow\uparrow\downarrow \right\rangle = \quad \frac{i}{4} \left[\left| \downarrow\downarrow\uparrow \right\rangle - \left| \uparrow\downarrow\downarrow \right\rangle \right], \tag{3.13b}$$

$$\mathbf{S}_1 \cdot (\mathbf{S}_2 \times \mathbf{S}_3) \left| \downarrow\downarrow\uparrow \right\rangle = \quad \frac{i}{4} \left[S_3^- S_1^+ S_{2z'} - S_2^+ S_3^- S_{1z'} \right] \left| \downarrow\downarrow\uparrow \right\rangle = \quad \frac{i}{4} \left[\left| \uparrow\downarrow\downarrow \right\rangle - \left| \downarrow\uparrow\downarrow \right\rangle \right], \tag{3.13c}$$

where we see that the effects of the chirality operator is to either move the minority spin (spin up) forward with positive phase, or move the minority spin backwards with negative phase.

With these results, we now evaluate

$$\begin{aligned}\mathbf{S}_1 \cdot (\mathbf{S}_2 \times \mathbf{S}_3) \left| q_{\pm} \right\rangle &= \frac{i}{4} \left[\left(e^{\pm i \frac{4\pi}{3}} - e^{\pm i \frac{2\pi}{3}} \right) \left| \uparrow\downarrow\downarrow \right\rangle + \left(1 - e^{\pm i \frac{4\pi}{3}} \right) \left| \downarrow\uparrow\downarrow \right\rangle + \left(e^{\pm i \frac{2\pi}{3}} - 1 \right) \left| \downarrow\downarrow\uparrow \right\rangle \right], \\ &= \pm \frac{1}{2} \sin\left(\frac{2\pi}{3} \right) \left[\left| \uparrow\downarrow\downarrow \right\rangle + e^{\pm i \frac{2\pi}{3}} \left| \downarrow\uparrow\downarrow \right\rangle + e^{\pm i \frac{4\pi}{3}} \left| \downarrow\downarrow\uparrow \right\rangle \right], \\ &= \pm \frac{\sqrt{3}}{4} \left| q_{\pm} \right\rangle. \end{aligned} \tag{3.14}$$

These two states, $|q_{\pm}\rangle$, can now be more intuitively described as the minority spin currents moving either to the left or to the right as in Resonant Valence Bond (RVB) plaquette [80, 81, 82, 83].

3.3 Quantum Information Processing with Coded Qubits

In this section, we describe the necessary preparations and initializations of coded qubits. Next, we discuss the generation of single and double qubit operations by pulsing the voltages on the gates. At the end, we propose to use a perpendicular field to split the two chiral states and use chirality-to-charge (analogous to spin-to-charge conversion) to perform projective measurement on the state of the coded qubit.

3.3.1 Single coded qubit: preparation and initialization

First, we remark that the chirality operator is insensitive to the overall direction of spin polarization but just measures the collinearity. Therefore, besides the two chiral states (coded qubit levels) $|q_{\pm}\rangle$ in the $S_y = -1/2$ subspace; there exist another pair of chiral states (not the intended coded qubit levels) with the same eigenvalues in the $S_y = 1/2$ subspace. This other pair of chiral states are the time-reversal counterparts of the coded qubit levels. In order to ensure that quantum information is encoded in the desired pair of chiral states, it is necessary to break the time-reversal symmetry and separate the two S_y subspaces. This can be done by applying a static uniform in-plane magnetic field $\mathbf{B}$ along $\hat{y}$ direction. Fig.[3.3a] presents a

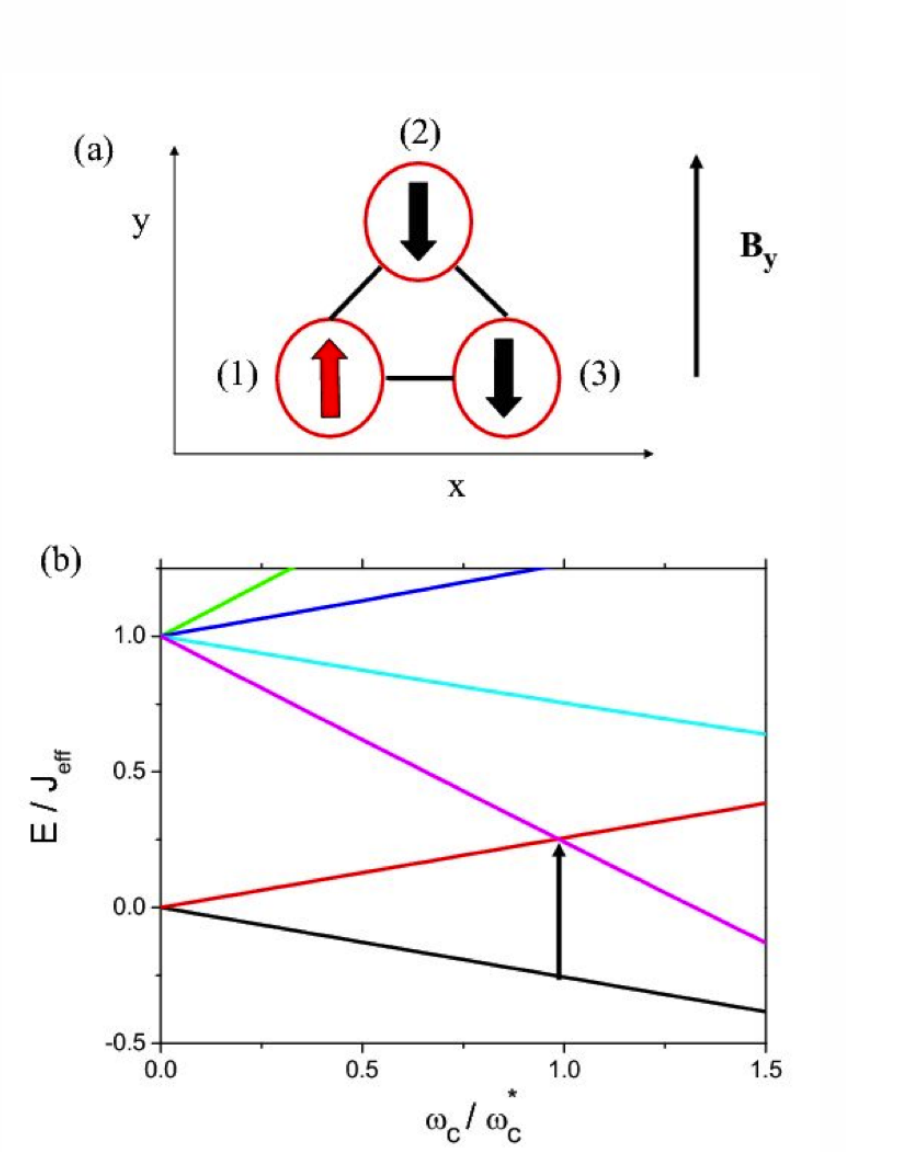

Figure 3.3: (a). A schematic of a single TQD initialized in $S_y = -1/2$ subspace under a B_y field. The B_y field breaks the discrete rotational symmetry. (b). The energy spectrum of a triangular TQD as a function of ω_c/ω_c^*, where ω_c is the cyclotron frequency used in LCHO-CI calculation. ω_c^* corresponds to a magnetic field B^* such that the gap between computational subspace (the lowest energy level in the plot) and the rest of spectrum is maximized as indicated by the black arrow.

schematics of how the applied field used in the calculation is oriented with respect to the TQD geometry. Fig.[3.3b] shows the energy spectrum (obtained from LCHO-CI calculation) as a function of the applied field. At zero field, the origin on the axis, the ground state is four-fold degenerate, with a pair of chiral states from the $S_y = 1/2$ and $S_y = -1/2$ subspace, respectively. The first excited state with $S = 3/2$ is also four-fold degenerate at zero field, and is separated from the ground state by J_{eff}. At non-zero field, the four-fold degenerate ground state is separated into two branches, each contains a pair of chiral states with the same S_y value.

The application of the in-plane field $\mathbf{B}$ also helps to suppress the spin-flipping process due to interactions with environment. The spin-flipping process will remove the coded qubit from its computational space (the $S_y = -1/2$ subspace) and allow the loss of quantum information encoded in the coded qubit. We avoid applying the magnetic field in the perpendicular direction, because it activates undesirable, higher order spin-spin interactions [84, 85], whereas the magnetic field applied in the plane only modifies the on-site energies of QDs: for a B_y field, QDs 1 and 3 energy levels are $E_{1(3)}(B) = E_{1(3)}(0) + 1/2\omega_c(R/2)^2 + g\mu B S_y$, where R is the spatial separation of QDs 1 and 3 and $\omega_c = eB_z/m_e^* c$ is the cyclotron frequency, while the QD 2 energy level only acquires the Zeeman term. Hence the magnetic field in the z direction effectively lowers the energy of the QD 2 by $\Delta E_2 = -1/2\omega_c(R/2)^2$ with respect to QDs 1 and 3.

We remark there exists an optimal value for the applied field as marked with ω_c^* in Fig.[3.3b]. The two possible computational spaces corresponding to pairs of chiral states in $S_y = \pm 1/2$ separate energetically with increasing magnetic field,

while one of the spin polarized states decreases in energy. At magnetic field B^*, such that $J_{eff} = 2g\mu B^*$, the energy gap between the computational subspace (the lowest branch) and any other levels in the spectrum is maximized and this is the working point that can maintain the longest coherence time of the coded qubit. In Fig.[3.3b], the optimal cyclotron frequency ω_c^* corresponds to $B^* = 0.69T$. However, as discussed above, the magnetic field effectively biases the QD 2. This removes the degeneracy of the two qubit levels and rotates them from their zero magnetic field states. The energy splitting of the two coded qubit levels as a function of applied magnetic field is shown in Fig.[3.4a]. The splitting is a fraction of the large energy scale J_{eff}. For the largest gap, i.e., $B = B^*$, the splitting is Δ. In order to restore the degeneracy of the two coded qubit levels, one can apply a voltage to the QD 2. In Fig.[3.4b], microscopic calculations done using LCHO-CI method show that a positive voltage bias on the QD 2 can indeed bring the TQD back on resonance in the presence of a B field. We have now established the coded qubit and the optimal working conditions.

In order to operate the coded qubit, we need to initialize it. We propose to initialize the coded qubit by turning off both interactions J_{12} and J_{13}. The only remaining interaction is between QDs 2 and 3. The ground state of a TQD, $|L_0\rangle = |\downarrow_1\rangle \otimes \left(\frac{1}{\sqrt{2}}\left(|\uparrow_2\downarrow_3\rangle - |\downarrow_2\uparrow_3\rangle\right)\right)$, becomes a product of a spin down state of an electron on the QD 1 and a singlet state of electrons across QDs 2 and 3. A singlet across QDs 2 and 3 can be generated in real time starting from two electrons in a biased QD 3, and then adiabatically transferring one electron to QD 2. Once the state $|L_0\rangle = \frac{-i}{\sqrt{2}}(e^{i2\pi/3}|q_-\rangle - e^{-i2\pi/3}|q_+\rangle)$ is generated, we may perform single qubit operations $R^{\hat{n}}(\pi/2)$ with $\hat{n} = (\sqrt{3}/2, 1/2, 0)$ to obtain chiral state $|q_-\rangle$. The single qubit

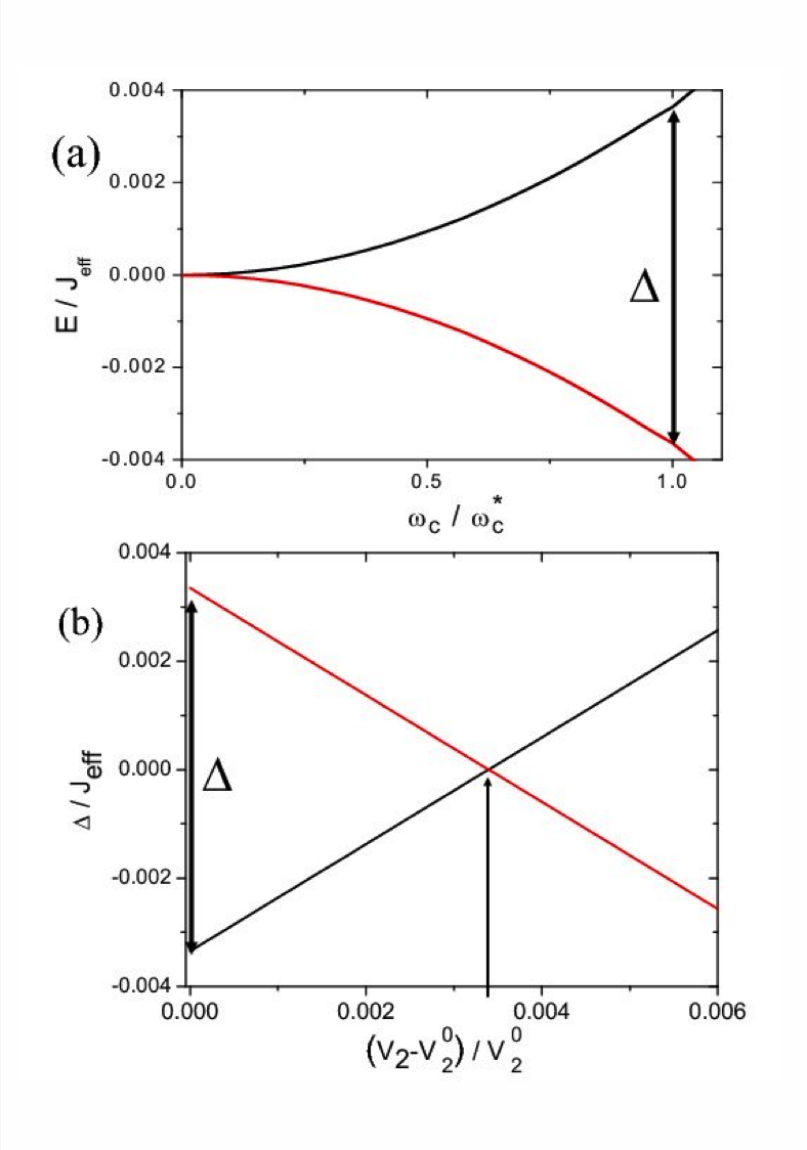

Figure 3.4: (Color online) (a). The energy spectrum of qubit levels (the zoom in of the lowest level in Fig. (2b)) as a function of ω_c/ω_c^*. The B_z field splits the doubly degenerate ground state, and Δ corresponds to the gap between the two levels at ω_c^* or equivalently at B_z^*. (b). The energy spectrum of the qubit levels under B_z^* as a function of voltage V_2 on QD2, and V_2^0 is the unbiased voltage at resonant condition when there is no external B field. The splitting of levels under B field can be restored via gate voltage tuning.

operation is explained in the following section and we define $R^{\hat{n}}(\theta) = e^{-i\frac{\theta}{2}\hat{n}\cdot\sigma}$.

3.3.2 Coherent Operations: single qubit gates

We first discuss single qubit operations. Eq.(3.10) shows that we can electrically tune an effective in-plane magnetic field to rotate the coded qubit (an effective spin-1/2 particle). If we take $J_{13} = J_{23}$, and let $2J_{12} > J_{13} + J_{23}$, then the Heisenberg Hamiltonian corresponds to a σ_x operation. If we take $J_{23} > J_{13}$ and $2J_{12} = J_{13} + J_{23}$, then the coded qubit Hamiltonian Eq.(3.10) corresponds to σ_y operation. The capability to rotate a qubit with respect to two different axes on a Bloch sphere allows us to generate arbitrary single qubit operations. In particular, a rotation of angle θ around the z axis on the Bloch sphere can be achieved by the following Euler rotations: $R^{\hat{z}}(\theta) = R^{\hat{y}}(-\pi/2)R^{\hat{x}}(\theta)R^{\hat{y}}(\pi/2)$. For typical GaAs parameters, the resonant exchange interaction is J $\approx 30\ \mu eV$, comparable with experiments. It will thus take ~ 0.1 ns to complete a 2π rotation.

In practice, the tuning of the exchange interaction is done through biasing QDs in order to modify the on-site energies. As long as the bias condition $|\Delta E| << U - V$ is satisfied, we expect the quantum state to remain in the qubit subspace during the process of tuning the exchange interactions as discussed in Ref. [63].

3.3.3 Coherent Operations: double qubit gates

We now turn to discuss two coded qubit operations using both Hubbard and Heisenberg models. Starting with the Hubbard Hamiltonian, Eq.(3.7), we derive perturbatively the Heisenberg Hamiltonian for a six-electron complex with a set of

exchange interactions given by:

$$\begin{aligned} J_{12} = J_{56} = J_a &= \frac{4t^2}{U - V}, \\ J_{13} = J_{23} = J_{45} = J_{46} = J_b &= \frac{2t^2}{(U - V + V')} + \frac{2t^2}{U - V - V'}, \\ J_{34} = J_c &= \frac{4t'^2}{U - V'}, \end{aligned} \tag{3.15}$$

where all other exchange interactions are turned off. For all the Hubbard parameters considered in this study, i.e. weak inter-TQD tunneling and strong Coulomb interaction, J_c is about two order of magnitudes smaller than J_a and J_b, mainly due to the fact that $t' < t/2$.

We treat the inter-TQD exchange interaction, scaled by J_c, perturbatively to derive an effective interaction in the coupled coded qubits subspace, $\{|q_+^L\rangle|q_+^R\rangle$, $|q_+^L\rangle|q_-^R\rangle, |q_-^L\rangle|q_+^R\rangle, |q_-^L\rangle|q_-^R\rangle\}$, where the superscript L and R stand for left and right TQD. The effective qubit-qubit Hamiltonian reads

$$\hat{H}_{2cq} = 4|\alpha'|(\hat{n} \cdot \vec{\sigma}_L)(\hat{n} \cdot \vec{\sigma}_R) + 2|\beta'|\hat{m} \cdot \vec{\sigma}_L + 2|\beta'|\hat{m} \cdot \vec{\sigma}_R, \tag{3.16}$$

where $\alpha' = e^{-i2\pi/3} J_c/9$, and $\beta' = e^{-i\pi/3}\,(-J_a/2 + J_b/2 + J_c/27)$. $\vec{\sigma}_L$ and $\vec{\sigma}_R$ are the effective Pauli matrices for the left and right coded qubit respectively. The effective magnetic field, defined by $2|\beta'|\hat{m}$, and the direction vectors, $\hat{n}$ and $\hat{m}$, presented in Eq.(3.16), are determined by the exchange interactions as follows: $\hat{n} = \left(\sqrt{|\alpha'| + Re(\alpha')}/\sqrt{2|\alpha'|},\ \sqrt{|\alpha'| - Re(\alpha')}/\sqrt{2|\alpha'|}, 0\right), \hat{m} = (Re(\beta')/|\beta'|, Im(\beta')/|\beta'|, 0)$. Thus, the effective Hamiltonian for two coded qubits is equivalent to a generalized XY Hamiltonian under a uniform in-plane magnetic field for two spins. With the current form of the double qubit Hamiltonian, it is not obvious as to what two-qubit gates can be easily generated. Such a dilemma can be avoided if one rotates the

effective double qubit Hamiltonian, Eq.(3.16), from the chirality basis to the Jacobi basis, $\left\{|L_0^L\rangle|L_0^R\rangle, |L_0^L\rangle|L_1^R\rangle, |L_1^L\rangle|L_0^R\rangle, |L_1^L\rangle|L_1^R\rangle\right\}$. The rotated Hamiltonian reads

$$\hat{H}_{2Lq} = \alpha\sigma_L^z\sigma_R^z + \beta\sigma_L^z + \beta\sigma_R^z, \tag{3.17}$$

where $\alpha = J_c/9$, and $\beta = -J_a/2 + J_b/2 + J_c/18$. The Jacobi state $|L_0\rangle$ is defined in Sec.[3.3.1] where we discuss the initialization of the coded qubit. The Jacobi state $|L_1\rangle = \sqrt{1/3}|\downarrow_1\rangle|T_{23}^0\rangle - \sqrt{2/3}|\uparrow_1\rangle|T_{23}^-\rangle$, where $|T_{23}^0\rangle = \frac{1}{\sqrt{2}}\left(c_{2\uparrow}^+c_{3\downarrow}^+ - c_{2\downarrow}^+c_{3\uparrow}^+\right)|0\rangle$ is a $S_y = 0$ triplet state of electrons on QDs 2 and 3 and $|T_{23}^-\rangle = c_{2\downarrow}^+c_{3\downarrow}^+|0\rangle$ is a $S_y = -1$ triplet state of electrons on QDs 2 and 3. Similarly, $|L_1\rangle = -1/\sqrt{2}(e^{i2\pi/3}|q_-\rangle + e^{-i2\pi/3}|q_+\rangle)$ can also be written as a linear combination of the coded qubit levels. Therefore, this rotation of basis only requires single qubit operations applied to each coded qubit independently; the two Hamiltonians, Eq.(3.16) and Eq.(3.17), are locally equivalent [86]. In this transformed representation, the effective Ising model gives a much more intuitive and well-studied dynamics in NMR literature [87]. Now, it becomes obvious that one way to proceed is to suppress the effective field β in Eq.(3.17) in order to obtain an exact Ising Hamiltonian used in NMR experiments. The J_c exchange interaction is responsible for the coupling between two TQDs, and it should ideally be kept about 2 orders of magnitude smaller than J_a and J_b in order for the perturbative analysis to provide good approximations. The value of J_a and J_b should thus be chosen very close to each other in order to bring $\beta = J_b/2 + J_c/18 - J_a/2 = 0$. In summary, each TQD involved in double-qubit operation should be kept in an almost resonant condition. The small deviation between J_a and J_b is needed to offset the weak coupling due to J_c in order to suppress the effective magnetic field β in the Ising model.

As Ising interactions can be used to generate the controlled-phase gate [88], we show how to generate double qubit operations with chirality-based coded qubits. The following is the sequence of gate operations to simulate the Ising interaction between chirality-based coded qubits

$$\begin{aligned} e^{-i\hat{H}_{2Lq}t} =& R_L^x(\pi/2)R_L^z(\pi/6)R_R^x(\pi/2)R_R^z(\pi/6)e^{-i\hat{H}_{2cq}t} \\ & R_L^z(-\pi/6)R_L^x(-\pi/2)R_R^z(-\pi/6)R_R^x(-\pi/2), \end{aligned} \tag{3.18}$$

where $R^j_{L(R)}(\theta) = e^{-i\frac{\theta}{2}\sigma^j_{L(R)}}$ represents the rotation of the left (L) or right (R) qubit on its Bloch sphere by angle θ with respect to j axis. If we set $t = \pi/\alpha$ in Eq.(3.18), where α is defined in Eq.(3.17), then the controlled-phase gate is generated as follows[87],

$$U_{cphase} = \sqrt{i}R_L^z(-\pi/2)R_R^z(-\pi/2)e^{-i\hat{H}_{2Lq}(\pi/\alpha)}. \tag{3.19}$$

Similarly, we can also generate a CNOT gate by the following elementary operations[87]

$$U_{cnot} = iR_L^z(\pi/2)R_R^z(-\pi/2)R_R^x(\pi/2)e^{-i\hat{H}_{2Lq}(\pi/\alpha)}R_R^y(\pi/2). \tag{3.20}$$

The important operation building an entanglement between the two coded qubit is $e^{-i\hat{H}_{2Lq}t}$. For both controlled-phase and CNOT gates, the time needed for the entanglement buildup is given by $\pi/\alpha \approx 1$ ps, about 2 orders of magnitude faster than typical single qubit operations.

By counting the number of operations involved in Eq.(3.18) and Eq.(3.19), it takes 4 and 12 elementary operations to generate a controlled-phase gate with coded qubit in the Jacobi and chirality basis, respectively. To generate the CNOT gate, it will take one additional step in both the Jacobi and chirality basis. At this point, we compare the double qubit operation derived in this section with the original proposal

put forth by DiVincenzo [25] et. al. In the original proposal, it takes 19 elementary steps to generate the CNOT gate, and the quantum states will evolve and escape the qubit subspace for a finite period of time during the operations. In the present proposal, it will takes 5 steps to generate the CNOT gate in the Jacobi basis, and the quantum state never escapes the qubit subspace. We compare the results in the Jacobi basis, because the qubits of a linear spin chain proposed by DiVincenzo et. al. do not have chirality. This significant reduction in the complexity of generating non-trivial double qubit operations is due to the weak coupling between the 2 TQDs in our model. In the case of the original proposal, the coupling strength between 2 coded qubits is as strong as the internal coupling strength between the spins of a coded qubit (i.e. $t' = t$); such a strong coupling imposes the view of one molecule with six constituent dots as opposed to two weakly coupled TQDs.

Fig.[3.5] shows results of exact diagonalization of the Hubbard Hamiltonian for two coupled TQDs as a function of increasing coupling t' between the two molecules. The inset shows the entire energy spectrum at $t'/t = 0.2$. The low energy spectrum consists of four levels, characterized mostly by the two lowest levels of each TQD. These 4 low-lying energy levels are well separated from the rest of the spectrum and constitute the two coupled coded qubit subspace. The low-lying spectrum contains a doubly degenerate level, which is a signature of the Ising model in an external field. The large gap that separates the two-qubit subspace from the rest of the states in the Hilbert space is due to the weak coupling between the 2 TQDs. The gap decreases as the inter-TQD coupling strength increases. The large energy gap is responsible for the suppression of quantum states escape out of the qubit subspace. In practice,

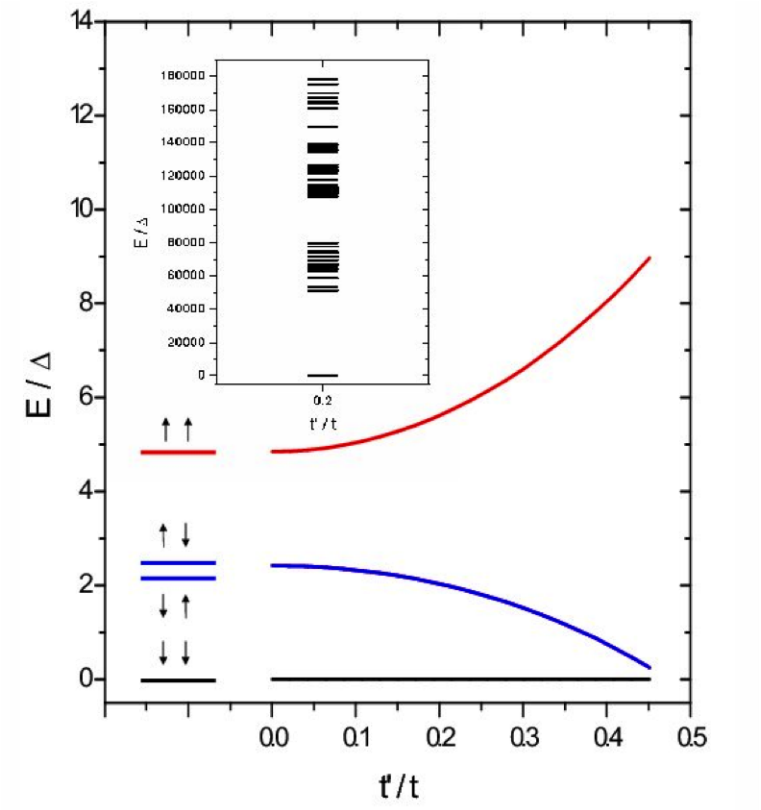

Figure 3.5: The four lowest energy levels of 2 coupled triangular TQDs as a function of inter-TQD tunneling t'. The energy spectrum resembles that of the Ising model with an external field: a doubly degenerate levels corresponding to state $|\downarrow\uparrow\rangle$ and $|\uparrow\downarrow\rangle$ and two unique levels $|\downarrow\downarrow\rangle$ and $|\uparrow\uparrow\rangle$. "$X2$" denotes a doubly degenerate level. Inset: The entire energy spectrum at $t'/t = 0.2$ calculated with LCHO-CI method.

the inter-TQD exchange interaction, J_c, should be tuned by modifying the tunneling parameter t'. Fig. (3.5) shows that the Ising energy spectrum is maintained over a wide range of values of t', and hence the Ising model Hamiltonian describes the coupling of two coded qubits very well.

3.3.4 Measurement of a single coded qubit

Next, we discuss the measurement of a coded qubit. Several proposals [83, 89, 64] have already discussed various methods of detecting chirality of a triangular (three-body) antiferromagnetic cluster.

For our specific proposal, we would like to draw analogy to the single-shot readout of an electron spin in a single QD as presented in Ref. [90]. This scheme of detecting an electron spin is based on spin-to-charge conversion. In the presence of an applied magnetic field, the Zeeman effect splits the two spin states of an electron. Furthermore, the QD potential is tuned in such a way that an electron escapes the dot if it is in the high-energy spin state or it remains in the dot if it is in the low-energy spin state. By coupling a quantum point contact (QPC) next to the dot and measuring the amount of current passing through the QPC, one may determine the number of electrons trapped in the dot. Thus, if the electron escapes the dot, we know it was in a high-energy spin state or vice versa. This simple proposal can be generalized by noticing that all we need are two levels with different energy, such as the two spin states of a single electron in a magnetic field or the two chiral states of a three-electron complex in presence of an external field.

We propose to apply an additional perpendicular field $B_\perp$ as part of the measure-

ment procedure. Under $B_\perp$, the chiral states split in exact analogy to the Zeeman splitting of a spin 1/2 as discussed briefly in the Chapter [2], and further details maybe found in Ref. [85] and [57]. With a suitable energy spacing between the two chiral states, we may tune the TQD potential in such a way that an electron may escape the system if it is in a high-energy chiral state. Thus, any fluctuation of QPC charge measurement on the TQD help to determine which chiral state the system is in.

Experimentally, we would like to refer to extensive works [91, 92, 42] performed to characterize the tunability as well as stability of TQD devices. More recently, Laird et. al. [93] also demonstrated experimentally the initialization, coherent exchange and readout of a coded qubit based on a linear half-filled TQD by adopting a specific pulsing technique [94] that was first exploited to demonstrate coherent exchange and readout in a double dot system. For Laird's experiments, the Jacobi coded qubit basis is used and the measurement of the qubit is done by measuring the total spin of the electrons in QD 2 and QD 3 for instance. As have already shown in Sec.[3.3.1] and Sec.[3.3.3], the Jacobi states, $|L_{0(1)}\rangle$ have either a singlet or a triplet state across QD 2 and QD 3.

3.4 Decoherence due to Fluctuating Charged Impurities

In this section, we discuss the effects of fluctuating charged impurities, which were observed in the experiment [95] with GaAs quantum dots. In Ref.[95], the

origin of the fluctuating charged impurity is proposed. In their model, a charged impurity appears when, in a leakage current, electrons tunnel through the Schottky barrier under the gates into the conduction band and become trapped near the active region of the device. The charged impurity disappears when the trapped electron escapes. Since the underlying physics of the trapping and release of charged impurity is complicated, we will just model the dynamics of the charged impurities according to the experimental results in Ref.[95]. In our model, the appearance and position of a charged impurity and the time interval between its successive appearances are random events generated with a uniformly distributed random generator.

The electrical noise due to the fluctuating charged impurity is believed to lead to severe decoherence to a charge qubit in a multi-dot device. Since the coded qubit levels depend on not only the spin properties of the three-electron complex but also the orbital degrees of freedom, it is a necessity to evaluate how strongly the electrical noise due to a charged impurity couples to the coded qubit and induces decoherence.

3.4.1 Triple Quantum Dot Molecule with Charged Impurity

In order to analyze the effects of a charged impurity, we return to Eq.(3.1) and add the Coulomb interaction between a charged impurity and the electrons in the TQD,

$$\hat{H}_{N_e} = \sum_i \left(-\vec{\nabla}_i^2 + V_{TQD}(\vec{r}_i) \right) + \sum_{i<j} \frac{2}{|\vec{r}_i - \vec{r}_j|} + \sum_i \frac{2}{|\vec{r}_i - \vec{R}_{imp}|}, \tag{3.21}$$

where $\vec{R}_{imp} = (R_{imp}, \theta_{imp}, Z_{imp})$ is the position of the impurity in cylindrical coordinates.

In second quantized form, where indices i, j, k, l denotes the single-particle molecular orbitals, the N_e Hamiltonian, Eq.(3.21), reads:

$$\hat{H}_{N_e} = \sum_{j\sigma} \varepsilon_j^0 d_{j\sigma}^+ d_{j\sigma} + \frac{1}{2} \sum_{\substack{ijkl \\ \sigma,\sigma'}} \langle ij|\hat{V}|kl\rangle d_{i\sigma}^+ d_{j\sigma'}^+ d_{k\sigma'} d_{l\sigma} + \sum_{\substack{ij \\ \sigma}} \langle i|\hat{V}_{imp}|j\rangle d_{i\sigma}^+ d_{j\sigma}, \tag{3.22}$$

where the last sum represents the interaction $\langle i|\hat{V}_{imp}|j\rangle$ between electron and the positively charged impurity. The effect of the charged impurity, the last term in (3.22), is to break the discrete rotational symmetry associated with the fully resonant triangular triple dot, and mix the electronic configurations belonging to different total quasi-momentum K_i.

Next, we re-derive the Hubbard model parameters E_i and t_{ij}, which incorporate the effect of the charged impurity in Eq.(3.22). The modified parameters read,

$$\begin{aligned} E_i =& E_i^0 + \langle\phi_i|\hat{V}_{imp}|\phi_i\rangle + 2\tilde{s}(\langle\phi_i|\hat{V}_{imp}|\phi_j\rangle + \langle\phi_i|\hat{V}_{imp}|\phi_k\rangle) \qquad (3.23a) \\ &+ \tilde{s}^2(\langle\phi_j|\hat{V}_{imp}|\phi_j\rangle + \langle\phi_k|\hat{V}_{imp}|\phi_k\rangle + 2\langle\phi_j|\hat{V}_{imp}|\phi_k\rangle) \\ t_{ij} =& t_{ij}^0 + \langle\phi_i|\hat{V}_{imp}|\phi_j\rangle + \tilde{s}(\langle\phi_i|\hat{V}_{imp}|\phi_i\rangle + \langle\phi_j|\hat{V}_{imp}|\phi_j\rangle + \langle\phi_i|\hat{V}_{imp}|\phi_k\rangle + \langle\phi_j|\hat{V}_{imp}|\phi_k\rangle) \\ &+ \tilde{s}^2(\langle\phi_k|\hat{V}_{imp}|\phi_k\rangle + \langle\phi_i|\hat{V}_{imp}|\phi_j\rangle + \langle\phi_i|\hat{V}_{imp}|\phi_k\rangle + \langle\phi_j|\hat{V}_{imp}|\phi_k\rangle), \qquad (3.23b) \end{aligned}$$

where $\hat{V}_{imp} = \sum_{ij,\sigma} \langle i|\hat{V}_{imp}|j\rangle d_{i\sigma}^+ d_{j\sigma}$ is the last term in Eq.(3.22). E_i^0 and t_{ij}^0 are the original Hubbard parameters derived in Eq.(3.6a) in the absence of a charged impurity. We remark that Coulomb repulsion parameters U and V are not modified in the present case.

Since the exchange interaction J_{ij} in the Heisenberg model acts as an effective magnetic field in the computational subspace of the coded qubit, the charged impurity acts as an additional magnetic field through the functional dependence of J_{ij} on the

on-site energies and the tunnel couplings. Due to fluctuations of the charged impurity, the dynamics of a coded qubit is translated into a problem of effective spin evolving in the presence of a random magnetic field.

3.4.2 Effects of Impurity on the One-Electron Energy Spectrum

We now analyze the effect of a charged impurity, the last term in Eq.(3.21), on the one-electron energy spectrum. We only consider an impurity at positions far away for the problem to be treated perturbatively. This assumption is not too restrictive as Ref.[95] suggests that the application of an overall positive voltage to the top gate, the heterostructure can significantly reduce the telegraph noise.

After some algebra, the one electron Hamiltonian, written in the basis of molecular states $\{\left|k_0^{HO}\right\rangle, |k_1^{HO}\rangle, |k_{-1}^{HO}\rangle\}$, reads

$$H_{1el} = \begin{pmatrix} \varepsilon_{k_0}^0 + C_{00}^{ov}(\bar{E}_{imp} + 2\bar{t}_{imp}) & C_{01}^{ov}(\widetilde{\delta E}_{imp} - \widetilde{\delta} t_{imp}) & C_{01}^{ov}(\widetilde{\delta E}_{imp} - \widetilde{\delta} t_{imp})^* \\ C_{01}^{ov}(\widetilde{\delta E}_{imp} - \widetilde{\delta} t_{imp})^* & \varepsilon_{k_{-1}}^0 + C_{11}^{ov}(\bar{E}_{imp} - \bar{t}_{imp}) & C_{11}^{ov}(\widetilde{\delta E}_{imp} + 2\widetilde{\delta} t_{imp}) \\ C_{01}^{ov}(\widetilde{\delta E}_{imp} - \widetilde{\delta} t_{imp}) & C_{11}^{ov}(\widetilde{\delta E}_{imp} + 2\widetilde{\delta} t_{imp})^* & \varepsilon_{k_{+1}}^0 + C_{11}^{ov}(\bar{E}_{imp} - \bar{t}_{imp}) \end{pmatrix}. \tag{3.24}$$

The terms in the diagonal, $\varepsilon_{k_n}^0, n = 0, -1, 1$, give the energy of the molecular ground state $|k_0^{HO}\rangle$ and two degenerate excited states $|k_{-1}^{HO}\rangle, |k_{+1}^{HO}\rangle$ respectively. All remaining terms correspond to impurity effects. Here $\bar{E}_{imp} = \frac{1}{3}\sum_{j=1}^{3} E_j^{imp}$ is the average shift of the energy levels due to impurity, with $E_j^{imp} = \langle\phi_j|\hat{V}_{imp}|\phi_j\rangle$. $\bar{t}_{imp} = \frac{1}{3}\sum_{i<j=1}^{3} t_{ij}^{imp}, i \neq j$ is the average shift of the tunneling matrix elements due to impurity, with $t_{ij}^{imp} = \langle\phi_i|\hat{V}_{imp}|\phi_j\rangle$. $\widetilde{\delta E}_{imp} = \frac{1}{3}\sum_{j=1}^{3} \delta E_j^{imp} e^{i\frac{2\pi}{3}(j-1)}$ is related to a shift in quantum dot

energy measured from the average shift due to impurity , $\delta E_i^{imp} = E_i^{imp} - \bar{E}_{imp}$, and $\widetilde{\delta t}_{imp} = \frac{1}{3}(\delta t_{23}^{imp} + \delta t_{13}^{imp} e^{i\frac{2\pi}{3}} + \delta t_{12}^{imp} e^{i\frac{4\pi}{3}})$ depends on the deviation of each tunneling matrix element from their average $\delta t_{ij}^{imp} = t_{ij}^{imp} - \bar{t}_{imp}, i \neq j$. Coefficients $C_{00}^{ov} = \frac{1}{(1+2s)}$, $C_{01}^{ov} = \frac{1}{\sqrt{1-s}\sqrt{1+2s}}$ and $C_{11}^{ov} = \frac{1}{(1-s)}$ with $s = \langle \phi_i | \phi_j \rangle, i \neq j$ account for the non-orthogonality of the HO basis.

Next, we analyze the effects of the charged impurity on the single-particle Hamiltonian matrix, Eq.(3.24), step by step. In Fig.[3.6], from left to right, the single-particle energy spectra are calculated with inclusion of more types of impurity-dependent terms in the matrix, Eq.(3.24). For this figure, the charged impurity is assigned the following coordinates: $R_{imp} = 3R_{TQD}$, $\theta_{imp} = \pi/3$ and $Z_{imp} = 4R_{TQD}$. We start on the left of Fig.[3.6] with the one electron spectrum in the absence of impurity. In the second column, we include the effect, $\bar{E}_{imp}$, of impurity on on-site energies for the exact diagonalization of the matrix. In the third column, we also turn on the effect, $\bar{t}_{imp}$, of impurity on inter-dot tunneling. We see that these effects of impurity are to lower the energy of all levels proportional to the average impurity shift, $\bar{E}_{imp}$, and increase the energy gap between ground and excited states by three times the average impurity induced tunneling matrix element , $3\bar{t}_{imp}$. In our numerical example this shift is small due to the small overlaps between localized orbitals ($s = 2.64 \cdot 10^{-3}$). Next we consider the coupling of states $|k_1^{HO}\rangle$ and $|k_{-1}^{HO}\rangle$ by including $\delta\tilde{E}_{imp}$ and $\tilde{\delta t}_{imp}$ within the 2 by 2 sub-matrix in the fourth column of Fig. 3.6. The energy gap is given by $\Delta\varepsilon_{GAP}^{1el} = 2|C_{11}^{ov}(\widetilde{\delta E}_{imp} + 2\widetilde{\delta t}_{imp})|$. Due to the small overlaps , i.e., $\delta t_{ij}^{imp} \approx 10^{-3}\delta E_i^{imp}$, the energy gap created by impurity can be approximated by

$$\Delta\varepsilon_{GAP}^{1el} \approx 2|\widetilde{\delta E}_{imp}| = \frac{2}{3}\sqrt{(E_1^{imp} - \frac{E_2^{imp} + E_3^{imp}}{2})^2 + \frac{3}{4}(E_2^{imp} - E_3^{imp})^2} \qquad (3.25)$$

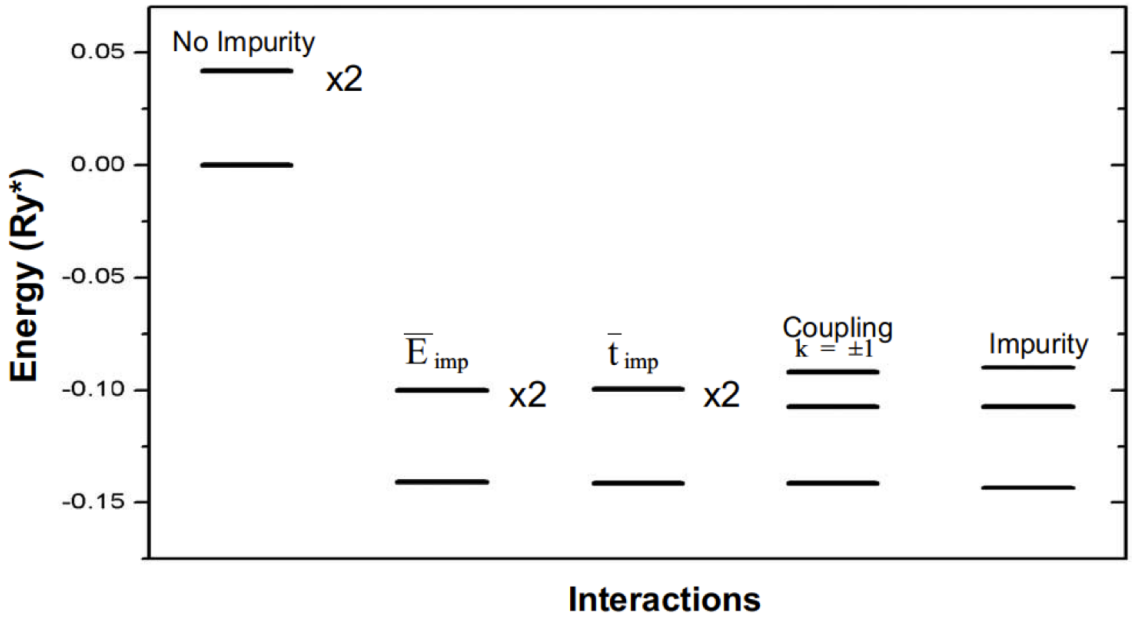

Figure 3.6: Evolution of the energy levels of one electron in a triple quantum dot in the presence of a charged impurity as function of interaction type. See text for details. The "x2" denotes a doubly degenerate level.

If we neglect the coupling of the excited states to the $|k_0^{HO}\rangle$ state which is lower in energy, we conclude that the energy gap caused by the impurity is proportional to the differences between the impurity-dependent on-site shifts $E_i^{imp} = \langle\phi_i|\frac{-2}{|\vec{r}-\vec{R}_{imp}|}|\phi_i\rangle$. Making a Taylor series expansion and keeping only the first term, we find that the energy shift due to the impurity potential of dot i is $E_i^{imp} \approx \frac{-2}{|\vec{R}_i-\vec{R}_{imp}|}$, where $\vec{R}_i$ is the position of the center of dot i. Therefore the energy gap created by the impurity is proportional to the differences between the values of the impurity potential at the center of each dot. In the last column, we simply perform exact diagonalization of Eq.(3.24), which includes all types of interactions.

Fig.[3.7] shows the single-particle spectra of the TQD as a function of impurity positions calculated by exact diagonalization of Eq.(3.21) with $N_e = 1$. The spectra

show the splitting of the doubly degenerate levels, its dependence on the distance of the impurity from the TQD, and on the position with respect to symmetry axis of the TQD. The charged impurity modifies the one electron spectra through direct Coulomb interaction, which mixes states $|k_1^{HO}\rangle$ and $|k_{-1}^{HO}\rangle$ and re-distributes charge density on the dots, as a function of charged impurity positions. Hence, results from Fig.[3.7] indicate that any quantum information processing schemes trying to utilize the electron's charge degree of freedom [23, 62] will have to consider the decoherence channel induced by the charge fluctuations.

3.4.3 Effects of an Impurity on the Coded Qubit Levels

We first diagonalize the three-electron Hamiltonian, Eq. (3.21), in the presence of impurity in the basis of $\{|\bar{K}_i^m\rangle\}$ presented in Sec.[3.2.1]. The impurity matrix elements in this basis are calculated as a linear combination of the impurity matrix elements in the basis of configurations $\{|K^p\rangle\}$:

$$\langle \bar{K}_i^m|\hat{V}_{imp}|\bar{K}_j^{m'}\rangle = \sum_p \sum_{q=1} A_p^{i,m} A_q^{j,m'} \langle K^p|\hat{V}_{imp}|K^q\rangle, \tag{3.26}$$

with

$$\langle K^p|\hat{V}_{imp}|K^q\rangle = \left(\langle 0|d_{k_{p3\uparrow}} d_{k_{p2\uparrow}} d_{k_{p1\downarrow}}\right) \left(\sum_{n=-1}^{1}\sum_{m=-1}^{1}\sum_{\sigma} \tilde{V}_{nm}^{imp} d_{k_n\sigma}^{+} d_{k_m\sigma}\right) \left(d_{k_{q1\downarrow}}^{+} d_{k_{q2\uparrow}}^{+} d_{k_{q3\uparrow}}^{+}|0\rangle\right),$$

which is zero unless configurations $|K^p\rangle$ and $|K^q\rangle$ differ at most by one of the spin-orbitals. $A_p^{i,m}$ are the coefficients of the three-electron eigenfunctions $\{|K_i^m\rangle\}$ written in terms of the configurations $\{|K^p\rangle\}$ and $\tilde{V}_{nm}^{imp} = \langle k_n|\frac{-2}{|\vec{r}-\vec{R}_{imp}|}|k_m\rangle$ are the single-particle impurity-dependent matrix elements. As shown, the impurity-induced effect on the three-electron complex is to scatter a state $\left|\bar{K}_i^m\right\rangle$ out of the K_i subspace.

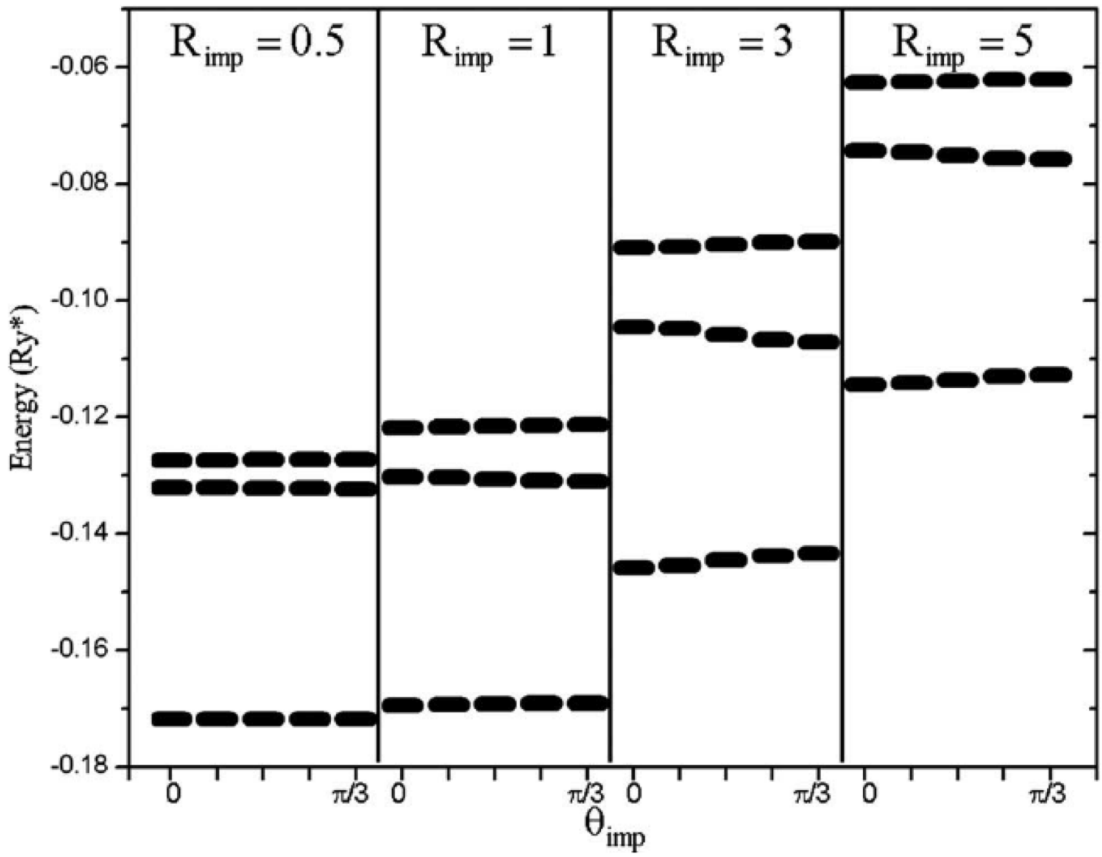

Figure 3.7: Energy spectrum of one electron in a TQD in the presence of an impurity located in the plane $Z_{imp} = 4R_{TQD}$ as a function of R_{imp} and θ_{imp}. R_{imp} is given in units of R_{TQD}. θ_{imp} is measured from the symmetry axis that goes through the center of a quantum dot. The zero energy is set to the ground state level of the resonant TQD.

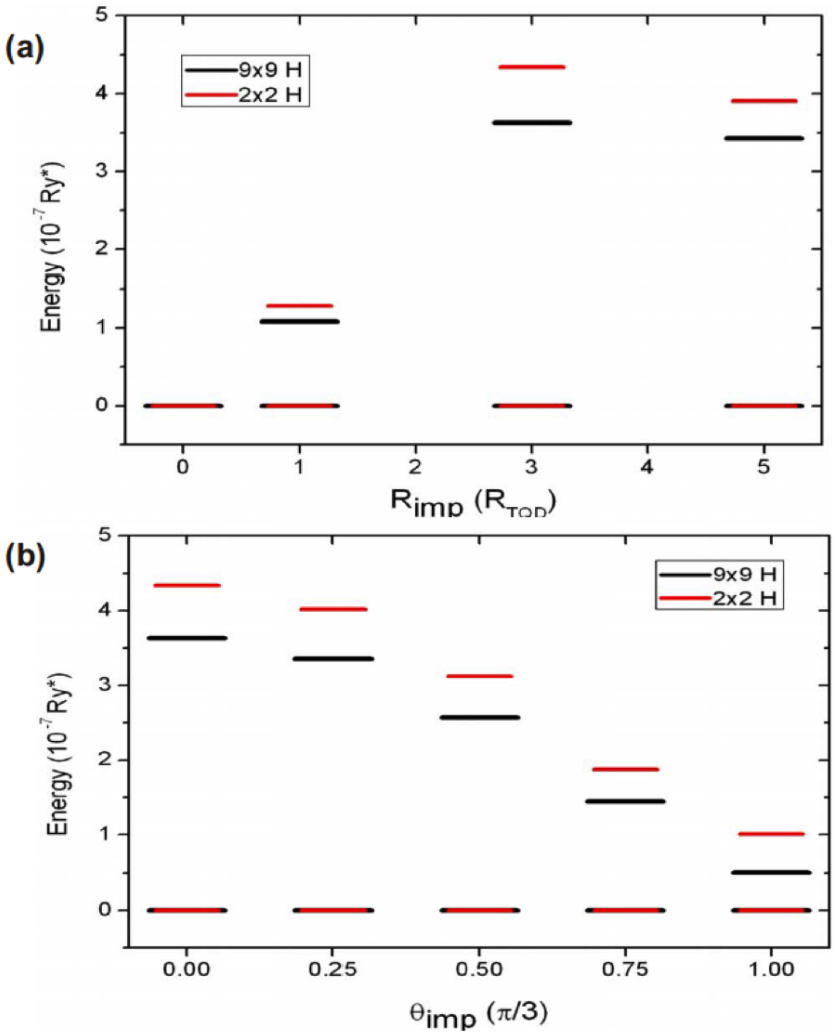

Figure 3.8: Two lowest energy levels of three electrons in a TQD in the presence of an impurity for different impurity positions in the plane $Z_{imp} = 4R_{TQD}$, with ground level normalized to zero. Top: Radius dependance for $\theta_{imp} = 0$. Bottom: Angle dependance for impurity $R_{imp} = 3R_{TQD}$.

Fig.[3.8a, b] shows the splitting of low-energy levels (black lines) of a coded qubit obtained by the diagonalization of the full Hamiltonian for various distances between the TQD and the charged impurity. We remark that the coded qubit levels are not split when the radius $R_{imp} = 0$ as shown in the left corner of Fig.[3.8a]. When $R_{imp} = 0$, the charged impurity sits on the symmetry axis of the TQD, the coded qubit is decoupled from the charged impurity. This is one unique feature of the Decoherence Free Subspace.

The full Hamiltonian containing all doubly and singly occupied configurations can be approximated by the 2 by 2 Hamiltonian in the computation subspace (two lowest states in the $S_y = -1/2$ subspace) with basis vectors $|K_1^1\rangle$ and $|K_{-1}^1\rangle$. The spectra obtained by diagonalizing this approximate 2 by 2 Hamiltonian, shown as red lines in Fig.[3.8a,b], agree well with results of the full calculations.

Let us now analyze the effects of a charged impurity on the coded qubit described by the Heisenberg model. We recall that there are three eigenstates $|q_\pm\rangle$ (the coded qubit levels) and $|q_0\rangle$ in the Heisenberg model of three localized spins. After some algebra, the Heisenberg Hamiltonian incorporating the effects of the charged impurity in the basis of $|q_s\rangle$ reads

$$H_J = \begin{bmatrix} -3/4J_{av} & 3/2\Delta^* & 0 \\ 3/2\Delta & -3/4J_{av} & 0 \\ 0 & 0 & 3/4J_{av} \end{bmatrix}, \tag{3.27}$$

where $J_{av} = \frac{J_{12}+J_{13}+J_{23}}{3}$, $\Delta = \frac{J_{23}+e^{i\frac{2\pi}{3}}J_{12}+e^{i\frac{4\pi}{3}}J_{13}}{3}$, and the exchange couplings are positive. The upper 2 by 2 sub-matrix spanned by the coded qubit levels $|q_\pm\rangle$ is decoupled from the spin-3/2 state $|q_0\rangle$.

In the Heisenberg model, the charged impurity-induced energy gap between the coded qubit levels is given by:

$$\Delta\varepsilon_{GAP}^{3el} = 3|\Delta| = \sqrt{(J_{23} - \frac{J_{12}+J_{13}}{2})^2 + \frac{3}{4}(J_{12}-J_{13})^2}. \tag{3.28}$$

We see that the energy gap in the three electron TQD created by the impurity depends on differences in J_{ij}, which depend on $(t_{ij})^2$ and ΔE_{ij} through Eq.(3.11). For a resonant TQD, we set the exchange constants $J_{ij} = J_0$ in the absence of charged impurity. In the presence of the charged impurity, neglecting the dependence of the tunneling matrix elements on the impurity potential allows us to express the gap in the coded qubit spectrum in terms of the exchange constant J_0 in the absence of impurity, and $(\Delta E_{ij}/U)^2$:

$$\Delta\varepsilon_{GAP}^{3el} = J_0\sqrt{((\Delta E_{23}/U)^2 - \frac{(\Delta E_{12}/U)^2 + (\Delta E_{13}/U)^2}{2})^2 + \frac{3}{4}((\Delta E_{12}/U)^2 - (\Delta E_{13}/U)^2)^2}. \tag{3.29}$$

We see that while the splitting of the single-particle spectrum is proportional to differences of single-particle energies ΔE_{ij}, the splitting of coded qubit levels is proportional to differences in $(\Delta E_{ij}/U)^2$. Since $\Delta E_{ij} << U$, the energy gap created by the impurity in the three electron spectrum is several orders of magnitude smaller than the gap created in the one-electron spectrum. The effect of charged impurity is to modify the spin distribution of the half-filled TQD through much weaker exchange interactions.

3.4.4 Mapping of Charge Fluctuation Induced Decoherence into Spin in a Random Magnetic Field Problem

We first derive the magnitudes and direction of the effective magnetic field directly from the microscopic model. We represent the Hamiltonian, Eq.(3.22), in the basis of eigenvectors in the absence of charged impurity. We only take the 2 by 2 sub-matrix spanned by the levels $\left|K^1_{1(-1)}\right\rangle$ and the Hamiltonian reads,

$$\hat{H}^{qubit} = \mathbf{B}^{eff}_x \sigma_x + \mathbf{B}^{eff}_y \sigma_y, \tag{3.30}$$

where the impurity-induced effective magnetic field $\vec{B}^{eff}$ does not have a z component. The in-plane components are given by $B^{eff}_x = Re\langle K^1_1|\hat{V}_{imp}|K^1_{-1}\rangle$ and $B^{eff}_y = -Im\langle K^1_1|\hat{V}_{imp}|K^1_{-1}\rangle$. The effective field flips the spin and leads to dephasing of the coded qubit. By now, we have successfully mapped the charged impurity induced decoherence problem to a problem of dephasing of a spin by a random magnetic field [96, 97, 98]. We have shown how to compute this effective field once the fluctuating impurity is identified.

We now describe the charge fluctuations in greater detail. We simulate the fluctuations of the charged impurity, and map the sequence of charged impurity appearances into a problem of spin in the presence of a random magnetic field. The fluctuation of the field is modeled in a way fitting to the experimental conditions in Ref. [95]. First, the magnetic field fluctuates in an abrupt and instantaneous fashion. Between transitions, the effective field is held constant in both direction and magnitude. The changes in both the directions and the magnitudes are assumed to have no correlations between the transitions, thus a Markovian approximation is made. Furthermore,

the time period between successive transitions is much longer than the time scale for the inherent dynamics of the coded qubit. Under these conditions, the effects of the fluctuating random magnetic field are similar to the ensemble average of different initial conditions of the random field as discussed in Ref. [99].

We now turn to estimate T_2^*, the shortest time scale for decoherence, of the coded qubit due to the fluctuating in-plane magnetic field [96, 97]. Following Ref. [95], we expect each charged impurity to last $\sim 1.0s$, with quiet interval of $0.2s$ between successive appearances, on average. These experimental findings suggest that there is a significant mismatch between charged impurity fluctuating time scale and inherent coded qubit dynamics time scale, which is characterized by $\Delta\epsilon_{GAP}^{3el}/\hbar = O(\mu s)$. Hence we only need simulate the time evolution of the coded qubit in the presence of a single charged impurity. First, we initialize a coded qubit at $t = 0$ in state $|0\rangle$. Next, we randomly select the position of the impurity, its switch-on time τ^{imp}, the moment the charged impurity is turned on with respect to $t = 0$, and the lifetime τ^{imp}. We then simulate the time evolution of the coded qubit up to a certain time t^*. This constitutes one complete numerical experiment. We repeat the same procedures N times; each time we initialize the coded qubit in exactly the same state but let it evolve in the presence of a different charged impurity. The averaged time evolution, based on these N numerical experiments, of the off-diagonal density matrix elements of the coded qubit suffers exponential decay, which is characterized by T_2^*.

Fig.[3.9a] shows the positions of N=200 randomly generated charged impurities used in this study. For each of these 200 charged impurities, we perform a LCHO-CI calculation to obtain the effective magnetic field as explained before. Fig.[3.9b] shows

the distribution of effective magnetic fields. Next, we specify the fluctuating aspects of the effective magnetic field by assigning the lifetime τ_i^{imp} and switch-on time T_i^{imp} to the $i-th$ charged impurity. The random generation of τ_i^{imp} and T_i^{imp} is done with the mean value of the uniform distributions equal to $1.0s$ and $0.2s$ as extracted from Ref. [95].

At this stage, we have completely specified the fluctuating magnetic field due to charged impurities. We next solve the Bloch equation of the coded qubit separately for each experiment,

$$\frac{d\mathbf{S}_i}{dt} = \gamma \mathbf{S}_i \times (\mathbf{B}_i^{imp}(t) + \mathbf{B}^{ext}), \tag{3.31}$$

where $S_x = \rho_{12} + \rho_{21}$, $S_y = i(\rho_{12} - \rho_{21})$, and $S_z = \rho_{22} - \rho_{11}$, ρ_{ij} are density matrix elements of the coded qubit, $\mathbf{B}_i^{imp}(t)$ is the effective magnetic field due to the $i-th$ impurity, $\mathbf{B}^{ext}$ denotes the effective external magnetic field, and γ is effective gyromagnetic ratio of the coded qubit inferred from $\gamma|\mathbf{B}_i^{imp}(t)|\hbar = \Delta\epsilon_{GAP}^{3el}$. Let us follow through the entire computational procedure for one particular impurity. In Fig.[3.9a] and Fig.[3.9b], a circle is drawn respectively around the charged impurity position no. 5 and the associated effective magnetic field derived from LCHO-CI calculation. Fig.[3.9c] shows the fluctuation of $\mathbf{B}_5^{imp}$, which is turned on at T_5^{imp} and lasts for τ_5^{imp}. Fig.[3.9d] shows the time evolution of Bloch vector component $S_x(t)$ for the coded qubit in the presence of $\mathbf{B}^{ext} + \mathbf{B}_5^{imp}$, and $\mathbf{B}^{ext} = \langle \mathbf{B}^{imp} \rangle = \sum_i \mathbf{B}_i^{imp}(t)/N$. As shown in the figure, the coded qubit always undergoes coherent time evolution even in the presence of charge fluctuations. The dephasing of Bloch vector, similar to inhomogeneous broadening effects in NMR characterized by T_2^*, only emerges from averaging the time evolutions of the coded qubit over N impurities, i.e. $< \mathbf{S}(\mathbf{t}) >=$

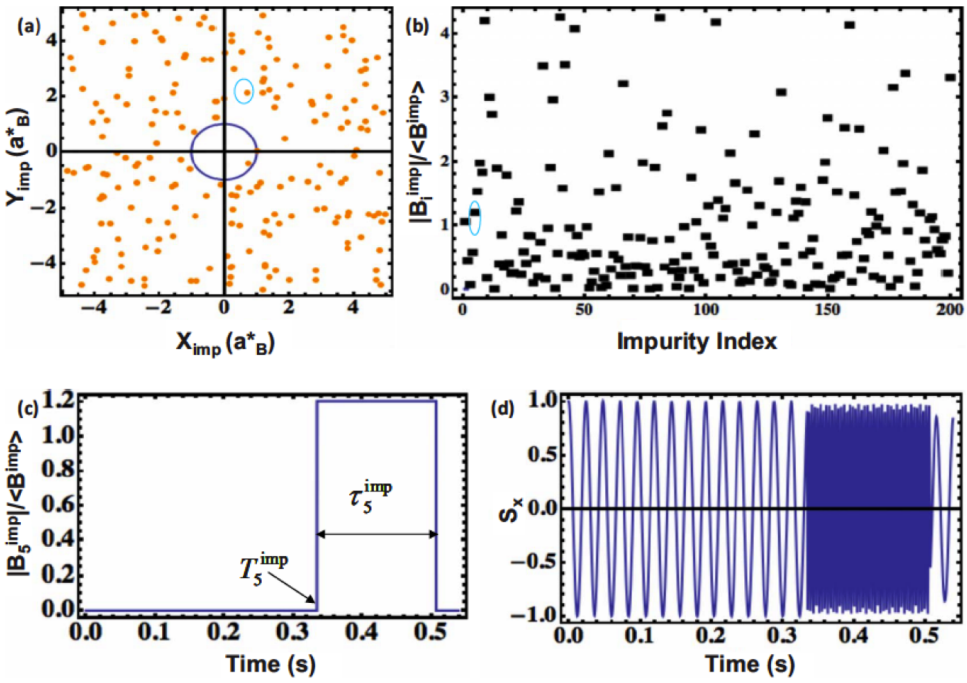

Figure 3.9: Top Left: The x and y coordinates of 200 charged impurities randomly generated in a rectangular box restricted in x, y, and z dimensions from -5 R_{TQD} to 5 R_{TQD}, from -5 R_{TQD} to 5 R_{TQD}, and from 4 R_{TQD} to 8 R_{TQD} respectively. The blue circle of radius 1 R_{TQD} around the origin outlines the size of the TQD device while the center of the TQD is located at the origin. The circled impurity is used in experiment no. 5. Top Right: The magnitudes of effective magnetic fields due to 200 charged impurities in the ensemble. The circled effective magnetic field is used in experiment no. 5. Lower Left: The fluctuation of the effective magnetic field in experiment no. 5 is specified by T_5^{imp}, the time it is switched on, and τ_5^{imp}, its lifetime. Lower Right: The simulated time evolution of Bloch vector x component, $S_x(t)$, in effective magnetic field $\mathbf{B}^{ext} + \mathbf{B}_5^{imp}$, for experiment no. 5. In this study, we set $\mathbf{B}^{ext} =< \mathbf{B}^{imp} >$.

$\sum_i \mathbf{S}_i(t)/N$ suffers exponential decay.

To estimate T_2^*, we fit $< \mathbf{S}(\mathbf{t}) >$ with the effective Bloch equation with parameter T_2^*,

$$\frac{d\mathbf{S}_{eff}}{dt} = \gamma \mathbf{S}_{eff} \times \mathbf{B}^{ext} - \frac{\mathbf{S}_{eff,\perp}}{T_2^*}, \tag{3.32}$$

where $\mathbf{S}_{eff}$ denotes the effective Bloch vector, $\mathbf{S}_{eff,\perp}$ denotes the effective Bloch vector components in perpendicular direction to the externally applied field. Fig.[3.10] shows the simulated and fitted result of $< S_x(t) >$ in the presence of external field with magnitude equal to the mean value of charged impurity induced effective magnetic field in the ensemble, $\mathbf{B}^{ext} =< \mathbf{B}^{imp} >$. The extracted result is $T_2^* = 0.2s$. This value of T_2^* is a function of $< T^{imp} >$, $< \tau^{imp} >$, and averaged distance of the charged impurity from the TQD. We find that T_2^* is dominated by $< T^{imp} >$. If impurities appear and disappear continuously and we consider an ensemble of coded qubits, each initialized in a different and static in-plane magnetic field, then T_2^* is on the order of tens of microseconds. These times are much longer than the reported dephasing times of electron spins due to nuclear spins [94]

3.4.5 Conclusion

In the first part of the chapter, we present a theory of quantum circuits based on qubits encoded in chirality of electron spin complexes in gated lateral semiconductor TQDMs with one electron spin in each dot. Using microscopic Hamiltonian in LCHO-CI formalism and exact diagonalization techniques we show there exists an optimized, in-plane B^* field that one should use to define the optimal computational space. We have shown how to perform specific single qubit operations around the x, y, and z

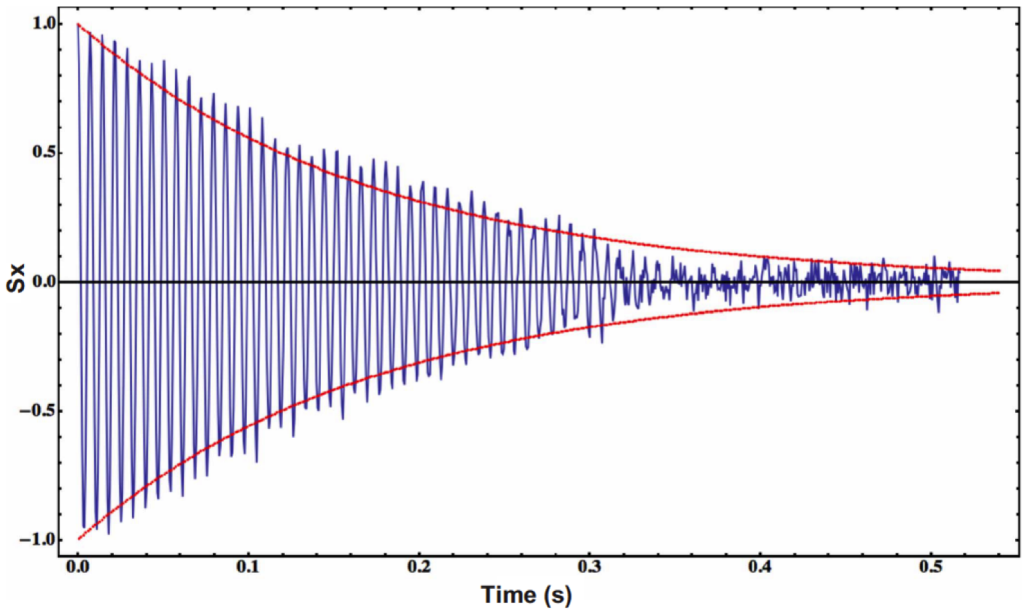

Figure 3.10: The oscillating blue curves represents the simulated time evolution of the averaged Bloch vector x component, $< S_x(t) >$. The red curve shows the envelope of the decaying oscillation for the effective Bloch vector x component, $S_{eff,x}(t)$.

axes as well as initialization and readout of coded qubits. An effective interaction for two coded qubits has been derived and nontrivial double qubit operations, CNOT and controlled phase gates, demonstrated. The understanding of the coupling between 2 coded qubits is significantly improved with the successful mapping of the microscopic Hamiltonian for 6 QDs to 2 effective spins.

In the second part, we study decoherence of a coded qubit by a fluctuating charged impurity. The electrical noise due to the fluctuating charged impurity is shown to severely affect a charged qubit in a multi-dot device. However, the effect on a coded qubit is significantly suppressed. This can be understood from the analysis of the interaction between these two different qubits with the charged impurity. In the case of charged qubit, the system-environment interaction scaled as the direct Coulomb interaction; whereas in the case of coded qubits, the system-environment interaction is

proportional to the exchange interaction within the coded qubit. From our numerical study, the coded qubit has a long coherence time and is robust against this particular channel of decoherence.

Chapter 4

Macroscopic Quantum States in a Chain of Linear TQDs

In this chapter, we show how nanostructuring of a metallic gate of a field-effect transistor (FET) converts the electron channel of a FET to an artificial Haldane chain with a gap in the energy spectrum. A specially designed gate structure creates a chain of triple quantum dot molecules. The electrons localized in the molecules realize a spin-half Heisenberg chain with spin-spin interactions alternating between ferromagnetic and anti-ferromagnetic. The quantum state of a FET is a semiconductor implementation of an integer spin-one antiferromagnetic Heisenberg chain with a unique correlated ground state and a finite energy gap, originally conjectured by Haldane.

4.1 Introduction

Haldane predicted that a spin-one antiferromagnetic Heisenberg chain has a unique ground state with a finite gap [100]. Affleck *et al.* obtained an exact analytical solution of the ground state with a finite gap in an isotropic spin-one chain with a special biquadratic interaction [101] and suggested that the ground state of the Heisenberg spin-one chain has the valence-bond-solid state character [102]. These predictions were subsequently confirmed by numerical calculations [103, 104, 105, 106] and experimental studies [107, 108, 109] in quasi-one-dimensional complex compounds. In this work, we propose a way of realizing an effective spin-one chain in a system of lateral gated quantum dots (QD) in a field effect transistor (FET) semiconductor structure. In a double quantum dot molecule, the ground state of the two-electron system is always spin singlet without an external magnetic field. Therefore, the effective spin-spin interaction between two electrons localized in respective quantum dots is always antiferromagnetic. In Chapter [2] and Ref. [110], it was shown that the spin-spin interaction can be tuned, both in magnitude and sign, by bringing another quantum dot that contains two electrons to make a triple quantum dot (TQD) molecule with 4 electrons or 2 holes. The presence of the doubly-occupied dot enables us to generate a triplet ground state due to the tunnelling between QDs. When all three dots are on resonance, a triple quantum dot system in triangular geometry with four electrons has a spin triplet ground state. As we lower the energy level of one of the dots, this dot will have two electrons and the other two dots will have single electron each. If the energy level of the doubly occupied dot is well below the energy levels of the other two dots, the system is similar to a double quantum dot with

spin singlet ground state. Therefore, there is a critical value of the bias that changes the ground state between spin singlet and spin triplet. Near the critical value, the effective interaction between the two localized electrons in the singly occupied dots can be tuned by the bias, both in magnitude and sign. When tuned to be in triplet ground state with total spin S=1, the TQD molecule can be used as a building block of a spin-one Heisenberg chain system.

4.2 Theory and methods

The architecture of the proposed linear chain of TQD molecules in a semiconductor device is shown in Fig.[4.1a]. By patterning the top metallic gate in a typical metal-oxide-semiconductor field-effect-transistor (MOSFET) device, one can create local potential minima in the two-dimensional electron gas (2DEG) and each potential minimum represents a quantum dot. Progress in the experimental technique allows precise control of the potential profile of the 2DEG and the number of electrons in each QD [40, 94, 61, 91, 42]. For individual control of each QD, many plunger gates will be needed and the gate pattern would be more complicated than shown in Fig.[4.1a]. Each TQD molecule consists of three quantum dots of which one contains two electrons and the other two dots contain single electron (see Fig.[4.1b]). The doubly occupied dots in neighbouring TQD molecules are in the opposite position to minimize the effects of the Coulomb interaction of those dots.

The physics of a quantum dot network is well described by the Hubbard model [36, 57]. For simplicity, we will assume that the on-site Coulomb repulsion U is the same for all QDs, the Coulomb interaction between two electrons in different

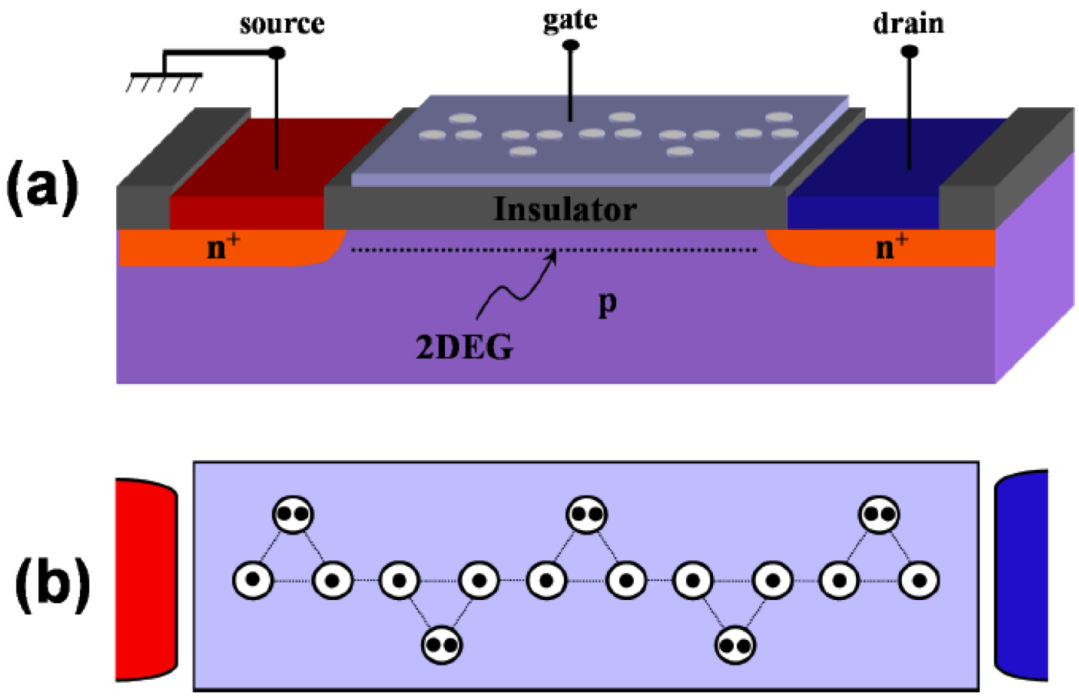

Figure 4.1: Schematic picture of the triple quantum dot chain on a semiconductor device. (a) The triple quantum dot chain is defined by a top gate, with a pattern of holes to create potential minima in the two-dimensional electron gas in the active region below. (b) For the realization of an effective spin-one chain, each dot on the linear chain contains a single electron and the other dots on the top and bottom contain two electrons.

dots in the same molecule is V, and two electrons in different molecules interact via Coulomb interaction V' only when they are in neighbouring QDs. The intra-molecular tunnelling is t, and the inter-molecular tunnelling t' is only allowed between two neighbouring dots. In an isolated TQD molecule, we can occupy one of the dots with two electrons and the other two dots with a single electron each by lowering the potential energy of the doubly occupied dot.

In the present TQD chain system, the inter-molecular Coulomb interaction V' effectively raises the energy levels of the singly occupied dots compared to the doubly occupied dots. By controlling V' the ground state of a TQD molecule can be changed from singlet to triplet. The only exceptions are two end dots which have no neighbouring molecules. Thus we assume that the energy levels of the two end dots are raised by V' by external gates. In second quantized form, the Hubbard Hamiltonian with a single level per site is given by

$$\begin{aligned} \hat{H}_{\text{Hubbard}} &= \sum_{i,\sigma} \varepsilon_i c_{i\sigma}^\dagger c_{i\sigma} + \sum_{i \neq j} \sum_{\sigma} t_{ij} c_{i\sigma}^\dagger c_{j\sigma} \\ &\quad + \sum_i U \hat{n}_{i\uparrow} \hat{n}_{i\downarrow} + \frac{1}{2} \sum_{i \neq j} V_{ij} \hat{n}_i \hat{n}_j \\ &\equiv \hat{H}_0 + \hat{H}_T + \hat{H}_U + \hat{H}_V \ , \end{aligned} \tag{4.1}$$

where i, j are indices for QD sites, $\sigma = \uparrow, \downarrow$ is the spin, $\hat{n}_{i\sigma} = c_{i\sigma}^\dagger c_{i\sigma}$ is the number of electrons with spin σ in QD i, and $\hat{n}_i = \hat{n}_{i\uparrow} + \hat{n}_{i\downarrow}$ is the total number of electrons in QD i. $t_{ij} = t$ and $V_{ij} = V$ for i and j in the same molecule and $t_{ij} = t'$ and $V_{ij} = V'$ if i and j are in different molecules but neighbouring each other. All the other V_{ij} and t_{ij} are zero. The QD energy level is $\varepsilon_i = \varepsilon_0$ for all i except for the first and last QDs where $\varepsilon_i = \varepsilon_0 + V'$. Most of the parameters are highly tunable but, in typical

devices, the strong Coulomb repulsion is much larger than tunnelling between dots. In those cases, the number of electrons in each dot is well defined and the tunnelling Hamiltonian $\hat{H}_T$ gives rise to effective interactions between well localized electrons. In following numerical examples we use $\varepsilon_0 = 0$, U=2.0, V=0.5, V'=0.2, t=-0.05 and t'=-0.02 in units of the effective Rydberg defined by $Ry = m_e^* e^4/2\epsilon^2\hbar^2$. m_e^* is the electron effective mass, e is the electron charge and ϵ is the dielectric constant. For GaAs, for example, Ry is about 6meV. These parameters are based on the first experimental realization of a lateral TQD molecule device [91] and the theoretical model for the charging diagram of the device [36]. The sign of the tunnelling elements t and t' can be determined by comparing the Hubbard model and the more microscopic linear-combination-of-harmonic-oscillator (LCHO) model [36, 57].

For a system with a charge configuration as shown in Fig.[4.2a], we can obtain an effective Hamiltonian corresponding to a Heisenberg Hamiltonian of a chain of localized electron spins (Fig.[4.2b]) by treating the tunnelling Hamiltonian $\hat{H}_T$ as a perturbation for the parameter range $|t|, |t'| \ll V, V' \ll U$ [110]. The resulting spin-half chain has alternating ferromagnetic and antiferromagnetic interactions as envisaged in the works of, e.g., Hida [111] and Hung and Gong [112]. We derive up to the third order (with respect to the tunnel couplings) in the perturbative analysis of the effective Hamiltonian, which reads

$$\hat{H}_{\text{eff}} \;=\; E_0 + J \sum_{m=1}^{N_M} \mathbf{s}_{3m-2} \cdot \mathbf{s}_{3m} + J' \sum_{m=1}^{N_M-1} \mathbf{s}_{3m} \cdot \mathbf{s}_{3m+1} \;, \tag{4.2}$$

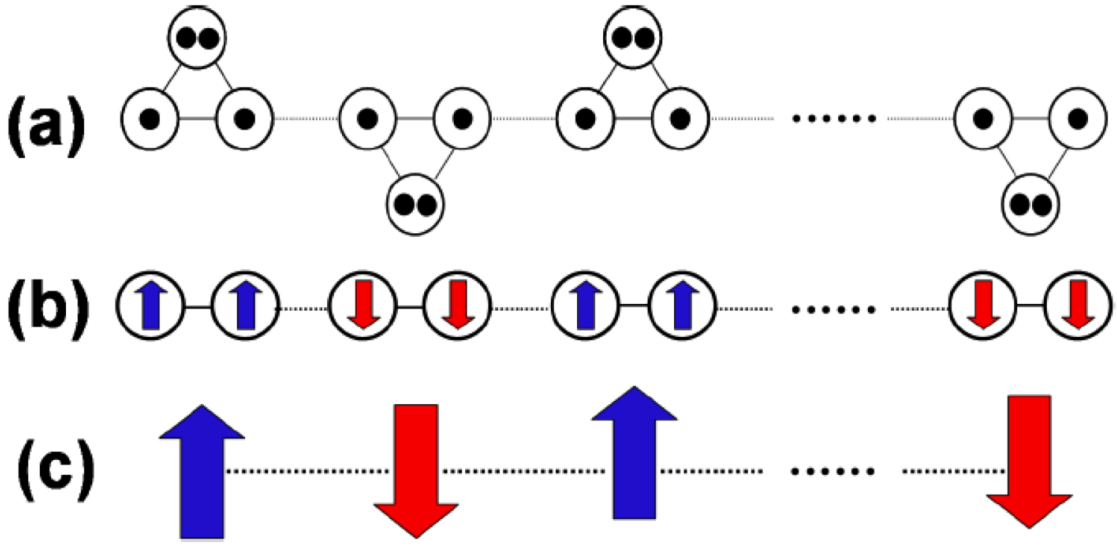

Figure 4.2: Different models for the chain of triple quantum dot molecules. (a) In Hubbard model, each dot has a single level and they are connected by the tunnelling and Coulomb interaction. (b) When the Coulomb interaction is strong and the tunnelling can be considered as a perturbation, the singly occupied dots are represented with localized spins with alternating spin-spin interaction. (c) If the intra-molecular ferromagnetic interaction J is much stronger than the inter-molecular antiferromagnetic interaction J', each molecule is in spin triplet state and the system can be considered as a spin-one antiferromagnetic Heisenberg chain.

where

$$
\begin{aligned}
E_0 &= 4N_M\varepsilon_0 + N_M U + 5N_M V + (N_M+1)\,V' \\
&- \frac{2|t|^2 N_M}{V'} - \frac{|t|^2 N_M}{U-V} - \frac{|t'|^2\,(N_M-1)}{U-V'} - \frac{|t|^3 N_M}{V'^2}\ , \qquad (4.3)\\
J &= \frac{4|t|^2}{U-V} - \frac{4|t|^3}{V'^2}\ , \qquad (4.4)\\
J' &= \frac{4|t'|^2}{U-V'}\ . \qquad (4.5)
\end{aligned}
$$

m is the index for TQD molecules and N_M is the number of TQD molecules in the chain. The intra-molecular spin-spin interaction J consists of two terms. The first term $4|t|^2/(U-V)$ is the usual antiferromagnetic (positive sign) superexchange term. The second term $-4|t|^3/V'^2$ is ferromagnetic (negative sign) term which comes from third order processes involving the doubly occupied dot. The third order process connects $(\uparrow,\downarrow)$ and $(\downarrow,\uparrow)$ configurations of the singly occupied dots. It consists of three tunneling events of which two changes the sign of the state, leaving the overall sign unchanged. Thus the third order off-diagonal terms are proportional to $t^3 = -|t|^3$. This leads to effective ferromagnetic interaction between two localized spins. This third order term is comparable to the second order superexchange term in magnitude for $V' \ll (U-V)$, and for small enough V' the overall interaction J can be either ferromagnetic or antiferromagnetic depending on the values of the parameters. Near the critical value of V' where $J = 0$, each molecule has one doubly occupied dot and two singly occupied dots, and the effective spin-spin interaction between the two localized spins changes between ferromagnetic and antiferromagnetic. The critical value of V' can be obtained by solving $J = 0$:

$$V'_c = \sqrt{|t|(U-V)}\ . \qquad (4.6)$$

We need to tune V' to be smaller than V'_c for ferromagnetic intra-molecular interaction, and larger than V'_c for antiferromagnetic interaction. On the other hand, the inter-molecular spin-spin interaction between two neighbouring electrons is always antiferromagnetic due to the superexchange. This effective spin-half chain Hamiltonian gives a clearer picture of the system and describes the low energy physics as will be shown below. Another important advantage of this effective Hamiltonian is that it reduces the dimension of the Hilbert space significantly and allows us to study much longer chains by exactly solving the associated eigenvalue problem. The solution of the full Hubbard Hamiltonian is numerically demanding for chains with more than 5 molecules since the dimension of the Hilbert space rapidly exceeds 10^6.

4.3 Results and discussion

Fig.[4.3] shows the lowest eigenvalues of the Hubbard model (green triangles) and the effective spin-half chain model (red circles) for a chain of up to 5 molecules using Jacobi-Davidson method implemented in the PRIMME library [113]. Each eigenstate is labeled by the total spin S. The values of $J = -5.83 \times 10^{-3}$ and $J' = 8.89 \times 10^{-4}$ used in Eq. (4.2) are obtained from parameters of the microscopic model using Eqs. (4.4) and (4.5). It is clear that the effective spin-half chain Hamiltonian describes the low energy levels of the Hubbard model quite well, reproducing the main features such as (i) the spin singlet ($S = 0$) ground state for an even number of molecules and spin triplet ($S = 1$) ground state for an odd number of molecules, (ii) the decrease of the gap between spin singlet and spin triplet states with the number of molecules, and (iii) appearance of the Haldane gap between the ground state and

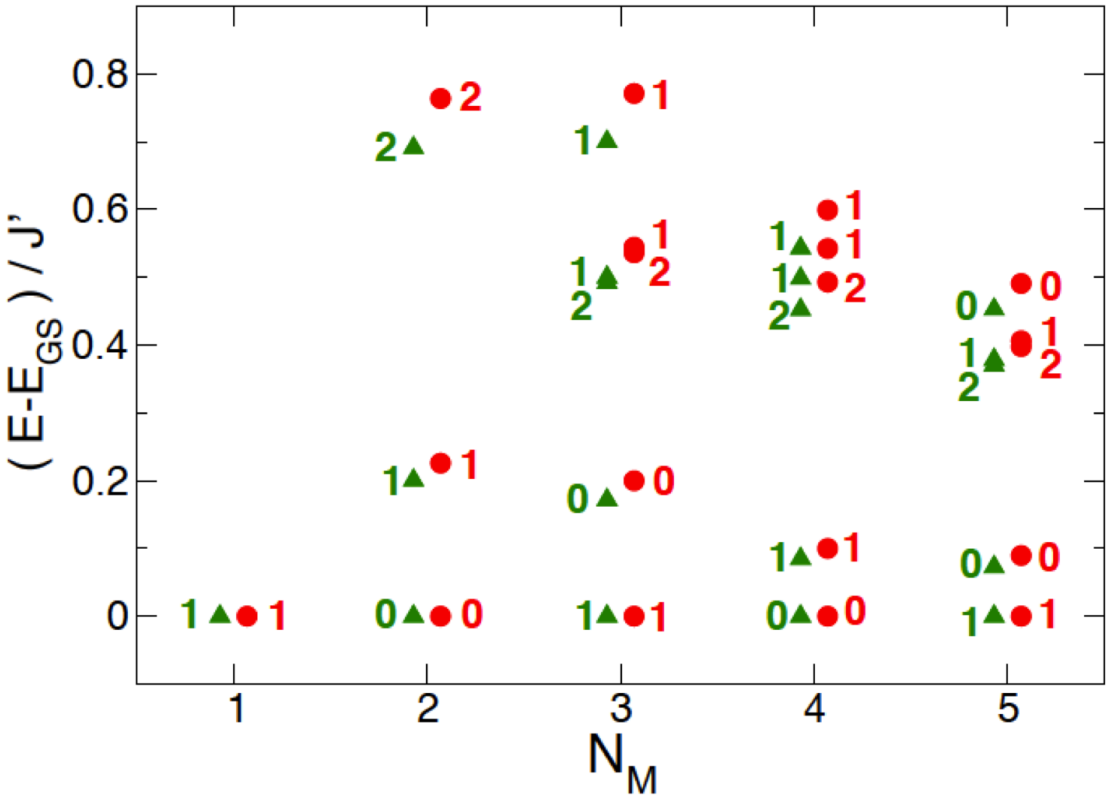

Figure 4.3: Comparison of Hubbard model and spin-half chain model. The effective Hamiltonian of spin-half chain with alternating spin-spin interaction describes the low energy states of the full Hubbard Hamiltonian very well both qualitatively and quantitatively. Green triangles are the lowest eigenstates of the Hubbard Hamiltonian and red circles are the eigenstates of the effective spin-half chain Hamiltonian. The numbers adjacent to the triangles and circles represent the total spin of each eigenstates. The result is shown for TQD chains with up to 5 molecules.

spin quintuplet ($S = 2$) excited states. In the limiting case of $J/J' \to -\infty$, *i.e.*, if the intra-molecular ferromagnetic interaction is extremely strong compared to the inter-molecular antiferromagnetic interaction, each molecule will be in a triplet state and the system will be a chain of spin-one dimers (Fig.[4.2c]). Thus the ground state will be separated from excited states by the Haldane gap as the length of the chain increases. Even for modest values of J/J', the system will have a robust ground state with a finite energy gap.

Fig.[4.4] shows the formation of Haldane gap as function of increasing number N_M of triple quantum dot molecules described by the Heisenberg Hamiltonian, Eq. (4.2). The Haldane gap for N_M up to 5 molecules is also shown in Fig.[4.3]. Note that the energies in Fig.[4.3] and Fig.[4.4] are scaled with respect to the inter-molecular antiferromagnetic interaction J' of the spin-half chain. The results for the spin $S = 1/2$ finite chain are compared with results for the spin $S = 1$ chain in Fig.[4.4]. The antiferromagnetic interaction $J_{AF}^{(1)}$ in the spin-one chain was chosen to be 1/4 of the inter-molecular antiferromagnetic interaction J' of the spin-half chain, because the interaction is only between two neighbouring spins in the spin-half chain [112]. Main panel of Fig.[4.4] shows the energy eigenvalues of $S = 2$ excited state with respect to the ground state and the inset shows the energy difference between $S = 1$ and $S = 0$ states. The triplet-singlet gap oscillates around zero since the ground state is spin singlet(triplet) for even(odd) number of molecules, and it goes to zero as the number of molecules increases. For long chains, the ground state is four-fold degenerate ($S = 0, 1$) and there is a finite gap between the ground state and the first excited state ($S = 2$). The four-fold degeneracy can be manipulated and

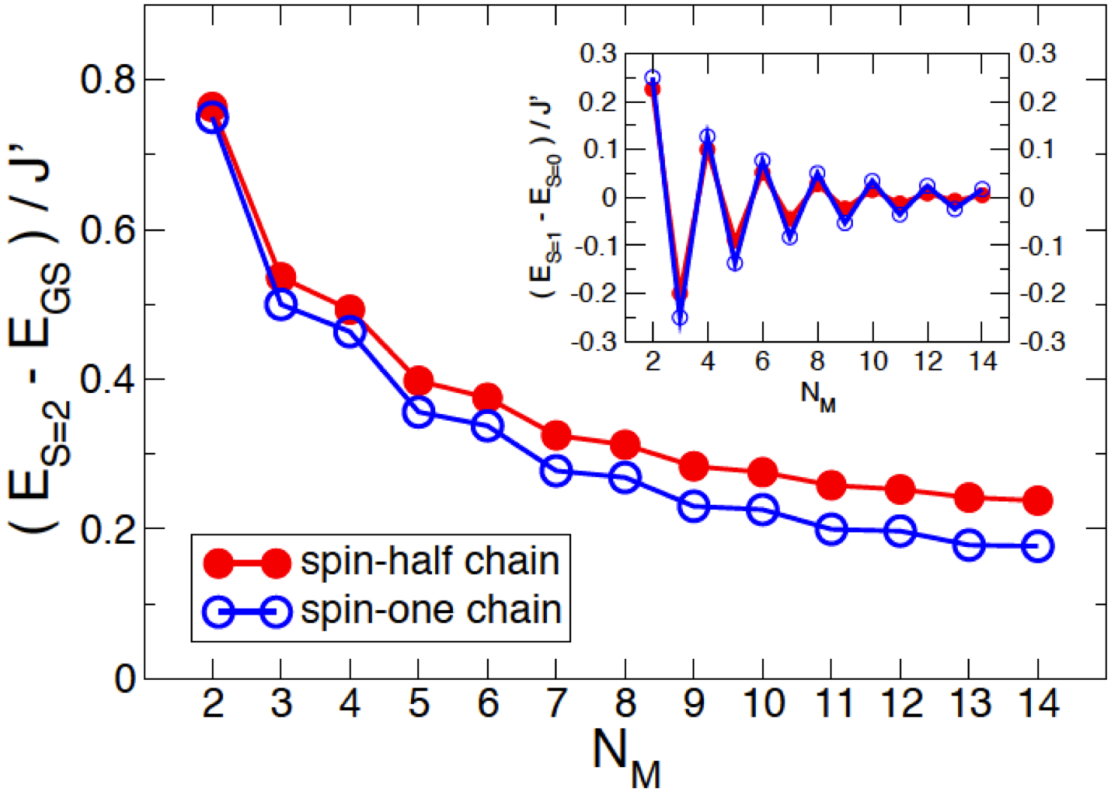

Figure 4.4: Comparison between spin-half chain and spin-one chain. The main panel shows the energy gap between spin-quintuplet(S=2) and ground state, in unit of the effective antiferromagnetic interaction J' of the spin-half chain. The energy gap reaches a finite value at infinite chain, which is the Haldane gap. Spin-half chain has a larger energy gap than the spin-one chain. The inset shows the spin-triplet (S=1) and spin-singlet (S=0) energy gap. Both spin-half alternating chain and spin-one chain show oscillating spin singlet and spin triplet ground state and the energy gap between spin singlet and triplet states decreases as the length of the chain increases and goes to zero for infinite chain.

removed by adding additional QDs with localized spin 1/2 electrons at both ends [104]. The Haldane gap is $0.41J_{AF}^{(1)}$ for an infinitely long spin-one chain [104, 105], and the energy gap of an infinite spin-half chain depends on both the ferromagnetic and antiferromagnetic interactions J and J' [111]. For $J/J' \to -\infty$, the effective antiferromagnetic interaction $J_{AF}^{(1)}$ of the spin-one chain is exactly $J'/4$. For finite J/J' the gap is larger than the Haldane gap and increases as the magnitude of J/J' decreases, reaching the maximum value at $J/J' = 0$. Around this point, the ground state is simply a chain of singlet dimers and the first excited state is a triplet [111]. With the Hubbard parameters used, we get $J/J' = -6.56$. As can be seen in Fig.[4.4], the energy gap of spin-half chain is larger than that of the spin-one chain due to the finite ferromagnetic intra-molecular interaction and it would reach a value about twice the Haldane gap of spin-one chain at infinite length [111]. Our estimate for a material such as GaAs leads to the gap of the infinite TQD chain with $J/J' = -6.56$ to be $1.07\mu eV$, which corresponds to $T = 12.4$mK. The maximum gap for $J/J' = 0$ is J' or 62mK. In addition to changing the ratio J/J', one can further increase the gap and hence strengthen the robustness of the ground state by controlling the parameters that determine $J' = 4t'^2/(U - V')$ by building quantum dot networks using self-assembled quantum dots on nanotemplates [51]. For characteristic parameters for self-assembled quantum dots U=20meV, V'=10meV, t'=10meV one can reach $J' \sim$ 40meV, exceeding room temperature at 300 K.

In real quantum dot systems disorders is always a practical concern. For the system we consider here, disorder in the parameters of the Hubbard model will effectively lead to spin chains with disordered bonding between spins. Previous work shows that

the ground state will be in random singlet phase [114] for strong disorder, but the Haldane gap phase is robust against weak disorder [115, 116].

4.4 Conclusions

In conclusion, we presented a way of realizing a macroscopic quantum state with Haldane gap in a semiconductor device. Such a robust ground state could be used as an essential part of a larger quantum circuit, extending existing semiconductor technology to quantum applications. The capability of tuning the effective spin-spin interactions can also be used to create other artificial spin systems, including ferrimagnetic ones, which are difficult to find in real materials.

Chapter 5

Herzberg Circuit and Berry's Phase in a Chirality-based Coded Qubit in a Triangular Triple Quantum Dot

In this chapter, we present a theoretical proposal for the Herzberg circuit and controlled accumulation of Berry's phase in a chirality-based coded qubit in a triangular triple quantum dot molecule with one electron spin each. The qubit is encoded in the two degenerate states of a three spin complex with total spin $S = 1/2$. Using a Hubbard and Heisenberg model the Herzberg circuit encircling the degeneracy point is realized by adiabatically tuning the successive on-site energies of quantum dots and tunnel couplings across a pair of neighbouring dots. It is explicitly shown that encircling the degeneracy point leads to the accumulation of the geometrical Berry's

phase. We show that only triangular but not linear quantum dot molecules allow for the generation of Berry's phase and we discuss a protocol to detect this geometrical phase.

5.1 Introduction

As discussed by Herzberg [117] and Berry [118], the wavefunction acquires geometric phase, Berry's phase, when it is adiabatically moved along a circuit in parameter space of the Hamiltonian, the Herzberg circuit, enclosing a degeneracy point. Since only the topology of the circuit determines whether the geometrical phase will be accumulated, the Berry's phase is insensitive to the effects of certain interactions between the system and its environment. For this reason there is interest in attempting to encode and manipulate quantum information in geometric phases, for example holonomic quantum computing [119] with generalized non-Abelian geometric phase [120].

Experimentally, Berry's phase in two level systems has already been demonstrated, including nuclear spins [121], superconducting qubit [122] and superconducting charge pump [123]. Preceding the successful experiments with superconducting circuits, theoretical studies [124, 125] investigated the relation between Berry's phase of a superconducting circuit and other measurable quantities, and even a theoretical proposal [126] for realizing geometric quantum computation with superconducting qubits was put forward.

In this chapter, we demonstrate theoretically the generation of a Herzberg circuit and Berry's phase in quantum states of a three electron complex in a triangular

triple quantum dot molecule with one electron spin each within the framework of Hubbard and Heisenberg models. The two level system, a qubit, is encoded in the two degenerate states of a three spin complex with total spin $S = 1/2$ [27, 127, 25]. An early proposal to generate a geometrical phase in degenerate one electron quantum levels of a three-atom system was discussed by Herzberg and Longuet-Higgins in Ref.[117] in 1963. A triple quantum dot (TQD) molecule studied here is related to the three-atom system. We define a two-level system [27, 127], a coded qubit, by the two lowest degenerate levels of a half-filled three electron TQD under an in-plane magnetic field. It was shown that the quantum states of coded qubit in a TQD can be manipulated by tuning the gate voltages[27, 127]. This opens the possibility described in this Chapter to engineer the Hamiltonian to undergo adiabatic and cyclic evolution along the Herzberg circuit resulting in accumulation of a Berry's phase. Recent experiments [42, 50, 93] on the linear TQD have already demonstrated the high tunability and coherently manipulation of the many-body quantum states in a TQD. Furthermore, we propose measuring the spin states of two neighbouring spins in TQDs via a spin blockade, an experimentally demonstrated technique, to extract the accumulated Berry's phase. However, we show that it is not possible to generate a Herzberg circuit for a linear triple quantum dot, only triangular triple quantum dot molecule with control over quantum dot energies and at least one tunneling amplitude is needed.

The plan of the chapter is as follows. In Sec.[5.2], we describe the system and the Hamiltonians for a linear and triangular TQD. In Sec.[5.3], we construct a Herzberg circuit generating Berry's phase in a triangular TQD. We show that it is not possible

to construct a Herzberg circuit for a linear TQD. In Sec.[5.4], a brief conclusion is given.

5.2 The model

With one electron in each dot, the extended Hubbard Hamiltonian reads,

$$\hat{H}_{hubb} = \sum_{i=1}^{3} E_i \hat{n}_{i\sigma} + \sum_{\substack{i,j=1 \\ i\neq j}}^{3} \sum_{\sigma} t_{ij}(\mathbf{B}) \hat{c}^{\dagger}_{i\sigma} \hat{c}_{j\sigma} + \frac{1}{2} \sum_{\substack{i,j=1 \\ i\neq j}}^{3} V_{ij} \hat{\rho}_i \hat{\rho}_j + \sum_{i=1}^{3} U_i \hat{n}_{i\uparrow} \hat{n}_{j\downarrow} + \sum_{\alpha} g\mu_B \mathbf{S}_{\alpha} \cdot \mathbf{B}, \tag{5.1}$$

where Hubbard parameters were defined in Sec.[2.2] and $\hat{\rho}_i = \hat{n}_{i\uparrow} + \hat{n}_{i\downarrow}$. In this study, we set $t_{ij} = t = -0.05Ry^*$, $E_i = 0$, $U_i = U = 2.0Ry^*$, and $V_{ij} = V = 0.5Ry^*$ as the initial state of the isolated triangular TQD system. $Ry^* = 5.97$ meV is the effective Rydberg in GaAs. For linear TQD case, we set $t_{13} = 0$ and $V_{13} = V/2$. We assume E_i and t_{ij} are independently tunable parameters that will be varied to generate Berry's phase.

As discussed in Chapter [2], the two arrangements of a TQD lead to two topologically different Hamiltonians. The low energy spectrum (4 spin-3/2 and 4 spin-1/2 states) of a half-filled TQD is mapped onto the Heisenberg model [84, 85, 127] with one localized spin in each dot,

$$H = \sum_{i<j} J_{ij} \mathbf{S}_i \cdot \mathbf{S}_j + \sum_{i} g\mu_B \mathbf{S}_i \cdot \mathbf{B} + \sum_{i<j<k} \chi_{ijk} \mathbf{S}_i \cdot (\mathbf{S}_j \times \mathbf{S}_k), \tag{5.2}$$

where the exchange interactions J_{ij}'s can be derived from the Hubbard model and assume the following microscopic details,

$$J_{ij} = 2|t_{ij}|^2 \left(\frac{1}{U - V + (E_i - E_j)} + \frac{1}{U - V - (E_i - E_j)} \right). \tag{5.3}$$

The coefficient χ_{ijk} for the chirality operator in Eq.(5.2) is much smaller than J_{ij} and is non-zero only for a triangular TQD in the presence of a perpendicular field.

Since the Heisenberg Hamiltonian commutes with the total S_y operator of the system, we focus on the $S_y = -1/2$ subspace. We further assume that an in-plane magnetic field B_y has been applied to separate the $S_y = -1/2$ and $S_y = 1/2$ subspaces by the Zeeman energy. In the $S_y = -1/2$ subspace, a resonant triangular TQD with all $J_{ij} = J_0$ has the following three eigenstates,

$$|q_+\rangle = \frac{1}{\sqrt{3}} \left(|\downarrow\downarrow\uparrow\rangle + \exp(i2\pi/3) \, |\downarrow\uparrow\downarrow\rangle + \exp(i4\pi/3) \, |\uparrow\downarrow\downarrow\rangle \right), \tag{5.4}$$

$$|q_-\rangle = \frac{1}{\sqrt{3}} \left(|\downarrow\downarrow\uparrow\rangle + \exp(-i2\pi/3) \, |\downarrow\uparrow\downarrow\rangle + \exp(-i4\pi/3) \, |\uparrow\downarrow\downarrow\rangle \right), \tag{5.5}$$

$$\left|S_{3/2}\right\rangle = \frac{1}{\sqrt{3}} \left(|\downarrow\downarrow\uparrow\rangle + |\downarrow\uparrow\downarrow\rangle + |\uparrow\downarrow\downarrow\rangle \right). \tag{5.6}$$

where spin configurations like this $|\downarrow\downarrow\uparrow\rangle$ labels the electron spins in quantum dots from spin up in dot 1 (rightmost) to spin down in dot 3 (leftmost). The two chiral states, $|q_+\rangle$ and $|q_-\rangle$, constitute the levels of a chirality-based coded qubit in a triangular TQD. The coherent manipulation of a coded qubit is achieved by tuning the exchange interactions J_{ij}'s. In the basis of the $\{|q_\pm\rangle\}$, the Heisenberg Hamiltonian with arbitrary J_{ij}'s reads,

$$H_{tri}^{qb} = \begin{bmatrix} 0 & \frac{1}{4}(2J_{23} - J_{13} - J_{12}) - i\frac{\sqrt{3}}{4}(J_{13} - J_{12}) \\ \frac{1}{4}(2J_{23} - J_{13} - J_{12}) + i\frac{\sqrt{3}}{4}(J_{13} - J_{12}) & 0 \end{bmatrix}. \tag{5.7}$$

This matrix shows that the chirality-based coded qubit manipulated by J_{ij}'s is equivalent to spin-1/2 particle under an effective field in the $x - y$ plane.

For the case of a linear TQD where $J_{12} = J_{23} = J_0$ and $J_{13} = 0$, the three

eigenstates of the system are

$$|L_0\rangle = \frac{1}{\sqrt{2}}\left(|\downarrow\downarrow\uparrow\rangle - |\uparrow\downarrow\downarrow\rangle\right), \tag{5.8}$$

$$|L_1\rangle = \frac{1}{\sqrt{3}}\left(|\downarrow\downarrow\uparrow\rangle - 2\,|\downarrow\uparrow\downarrow\rangle + |\uparrow\downarrow\downarrow\rangle\right), \tag{5.9}$$

$$\left|S_{3/2}\right\rangle = \frac{1}{\sqrt{3}}\left(|\downarrow\downarrow\uparrow\rangle + |\downarrow\uparrow\downarrow\rangle + |\uparrow\downarrow\downarrow\rangle\right). \tag{5.10}$$

For the linear TQD, the two states, $|L_0\rangle$ and $|L_1\rangle$ constitute the levels of a coded qubit in a linear TQD. These three states above are commonly referred to as Jacobi states. The 2 Jacobi states used for the coded qubit may be physically distinguished by the joint spin states on dot 1 and dot 3. For $|L_0\rangle$, the spins in dot 1 and dot 3 form a spin singlet; while the spins in dot 1 and dot 3 form a linear combination of spin triplets with $S_y = -1$ and $S_y = 0$ in $|L_1\rangle$. Similar to the coded qubit in triangular TQD, we present the Heisenberg Hamiltonian of a linear TQD with arbitrary J_{ij}'s in the basis of $\{\left|L_{0(1)}\right\rangle\}$,

$$H_{lin}^{qb} = \begin{bmatrix} \frac{1}{4}\left(J_{12}+J_{23}\right) & \frac{\sqrt{3}}{4}\left(J_{23}-J_{12}\right) \\ \frac{\sqrt{3}}{4}\left(J_{23}-J_{12}\right) & -\frac{1}{4}\left(J_{12}+J_{23}\right) \end{bmatrix}. \tag{5.11}$$

Different from the chirality-based coded qubit, the Jacobi states-defined coded qubit in a linear TQD is equivalent to a spin-1/2 particle under an effective field in the $x-z$ plane. Finally, we remark that this Jacobi basis of a linear TQD also diagonalize resonant triangular TQD. In a triangular TQD, the ground state is doubly degenerate, so the two Jacobi states, $|L_0\rangle$ and $|L_1\rangle$ are related to the chirality states $|q_\pm\rangle$ via simple unitary transformation.

5.3 Generation and Detection of Berry's phase

In the previous section, we presented the Hamiltonian for a coded qubit in both chirality basis (triangular TQD) and Jacobi basis (linear TQD), and compared a coded qubit to a spin-1/2 particle. The coded qubit Hamiltonian, $H(\mathbf{R}) = \mathbf{R} \cdot \mathbf{S}$, is the spin Hamiltonian in the presence of an effective field, $\mathbf{R} = (X, Y, Z)$, where the field is expressed in terms of exchange couplings J_{ij}. By adiabatically varying the direction of the magnetic field around a closed circuit that encircles the diabolical point [128, 118, 117]in the parameter space of $\mathbf{R}$, the system undergoes a cyclic evolution and accumulates Berry's phase. The diabolical point is the point at which the two-level system is degenerate in the parameter space of $\mathbf{R}$.

To generate Berry's phase, we need to vary exchange couplings to rotate the effective magnetic field $\mathbf{R}$. We note that the real and imaginary part of the off-diagonal matrix element in Eq.(5.7) can be independently set to either positive or negative value, if we assume the capability to independently control all three exchange interactions. Thus, we can engineer the effective field $\mathbf{R}$ for a chirality-based coded qubit to adiabatically traverse a closed circuit that encircles the origin in the parameter space. The next task is then to tune the exchange interactions with experimentally accessible quantities, such as E_i and t_{ij}. Since we need to independently control three exchange interactions, we need to vary at least three variables. Experimentally, it is usually more desirable to tune the on-site energies than the tunnel couplings. So the simplest attempt is to vary just the on-site energy of each dot. However, this simple attempt fails, because each exchange interaction J_{ij} depends on the on-site energies of dot i and dot j through the energy difference $\Delta E_{ij} = E_i - E_j$. We note a constraint

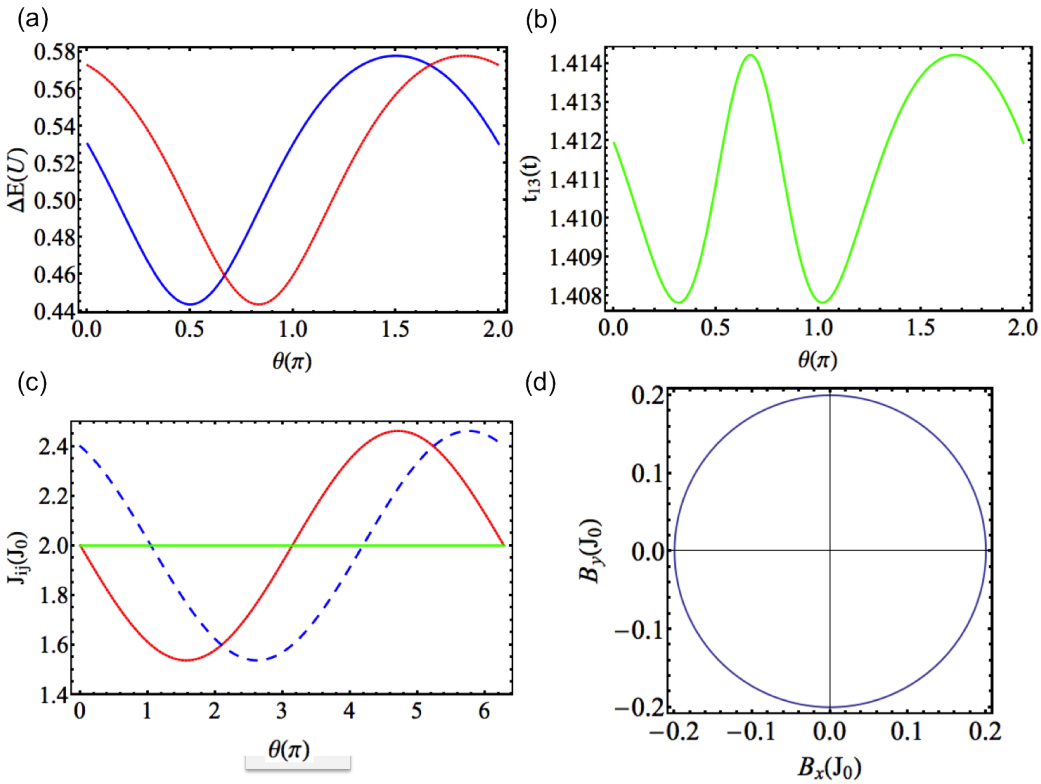

Figure 5.1: (a) Variations of ΔE_{12} (blue curve) and ΔE_{23} (red curve) over one round on the closed circuit. Note that the variations is comparable to U, the largest energy scale of the Hubbard model. (b) Variation of t_{13} over one round on the closed circuit. (c) The values of J_{ij}, computed with Eq.(5.3), over one round on the closed circuit. J_{12} is red, J_{23} is blue, and J_{13} is green. This circuit is generated under the constraint that J_{13} is held constant. (d) Parametric plot of the closed circuit itself in the parameter space $\mathbf{R}$ for the coded qubit (effective two-level system). The x and y components of the circle are related to the J_{ij} via the real and imaginary components of the off-diagonal matrix element in Eq.(5.7).

$\Delta E_{12} + \Delta E_{23} + \Delta E_{31} = 0$ exists for these three energy differences. Therefore, we have actually two degrees of freedom with the three on-site energies. We need to tune at least one tunnel coupling. For instance, the effective field can be rotated in a perfect circle with a radius J by tuning E_1, E_3, and t_{13}, while $E_2 = E$, $t_{23} = t_{12} = t$ are being held constant. Furthermore, we select values of E_1, E_3, and t_{13} at each point on the circle such that $J_{13} = \frac{4\gamma}{\sqrt{3}}J$ is obeyed at all times, and γ is some chosen constant. Given these conditions, we need to tune three parameters according to

$$E_1(\theta) = E + \sqrt{(U-V)^2 - \frac{4(U-V)|t|^2}{\frac{J}{\beta}(\gamma - \sin\theta)}}, \tag{5.12}$$

$$E_3(\theta) = E + \sqrt{(U-V)^2 - \frac{4(U-V)|t|^2}{\frac{J}{2\alpha}\cos\theta + \frac{J}{2\beta}(2\gamma - \sin\theta)}}, \tag{5.13}$$

$$t_{13}(\theta) = \sqrt{\frac{((U-V)^2 - (E_1 - E_3)^2)\gamma J}{4\beta(U-V)}}, \tag{5.14}$$

where $\alpha = 1/4$, $\beta = \sqrt{3}/4$, and θ is the accumulated angle on the closed circuit. Fig.[5.1a] and Fig.[5.1b] present the variations of the ΔE_{12}, ΔE_{23} and t_{13} as functions of θ, and Fig.[5.1c] shows the variations of J_{ij} in response to the changes in the Hubbard parameters. Fig.[5.1d] shows the Herzberg circuit with radius J in the parametric space $\mathbf{R}$ for the effective spin-1/2 model. Although the circuit presented in Fig.[5.1] indeed encloses the diabolical point in the parameter space, it is based on the Heisenberg model for an effective two-level system. The two lowest states in the $S_y = -1/2$ subspace constitute a two-level system modelled by Heisenberg Hamiltonian only when on-site Coulomb repulsion is the dominant energy scale. If we look at the scale of variations for ΔE_{13} and ΔE_{23} in Fig.[5.1], the variations are as high as 0.58 U at certain points on the circuit. Thus, the validity of the Heisenberg model becomes questionable over the course of transporting the system around the

circuit. Thus, we expect that a more realistic circuit, which minimizes the variations of ΔE_{ij} in order to ensure the validity of the Heisenberg model, would require to tune more than just three variables. For instance, Fig.[5.2a] and Fig.[5.2b] present another circuit, which vary on-site energy E_1, E_3 and all t_{ij} in order to produce identical J_{ij} as shown in Fig.[5.1c] and also the same circle in Fig.[5.1d]. By moderately varying t_{12} and t_{23}, we observe that the variations of ΔE_{ij} are significantly suppressed as shown in Fig.[5.2a]. Fig.[5.3a] and Fig.[5.3b] compare the energy gap between the lowest three levels in the Hubbard model and the Heisenberg model in the $S_y = -1/2$ subspace for the circuits presented in Fig.[5.1] and Fig.[5.2], respectively. As shown, the second circuit, which varies all three tunnel couplings provides a better agreement between the Hubbard and Heisenberg model. For many tasks, such as manipulating the quantum state of a coded qubit via dynamical phases, a fast tuning of on-site energies is preferred to the tuning of tunnel couplings. However, for the adiabatic accumulation of geometrical phases the gating operations can be done at a slower rate, with the tuning of the tunnel couplings more favourable in this case.

The accumulated Berry's phase, $\phi_{\pm}(C)$, for the coded qubit level $|q_{\pm}\rangle$, after one round along a closed circuit C (that encloses the origin) is simply $\phi_{\pm}(C) = \mp i\frac{1}{2}\Omega(C)$, where $\Omega(C)$ is the solid angle subtended by the closed circuit C with respect to the origin of the parameter space. For the chirality-based coded qubit, the effective field is restricted to lie in the $x-y$ plane as implied by Eq.(5.7). The solid angle subtended by any closed circuit in the $x-y$ plane of the parameter space is either 0 or π, and this result depends solely on whether the closed circuit encircles the origin (diabolical point) or not. Fig.[5.4] shows the numerical computation of accumulated geometrical

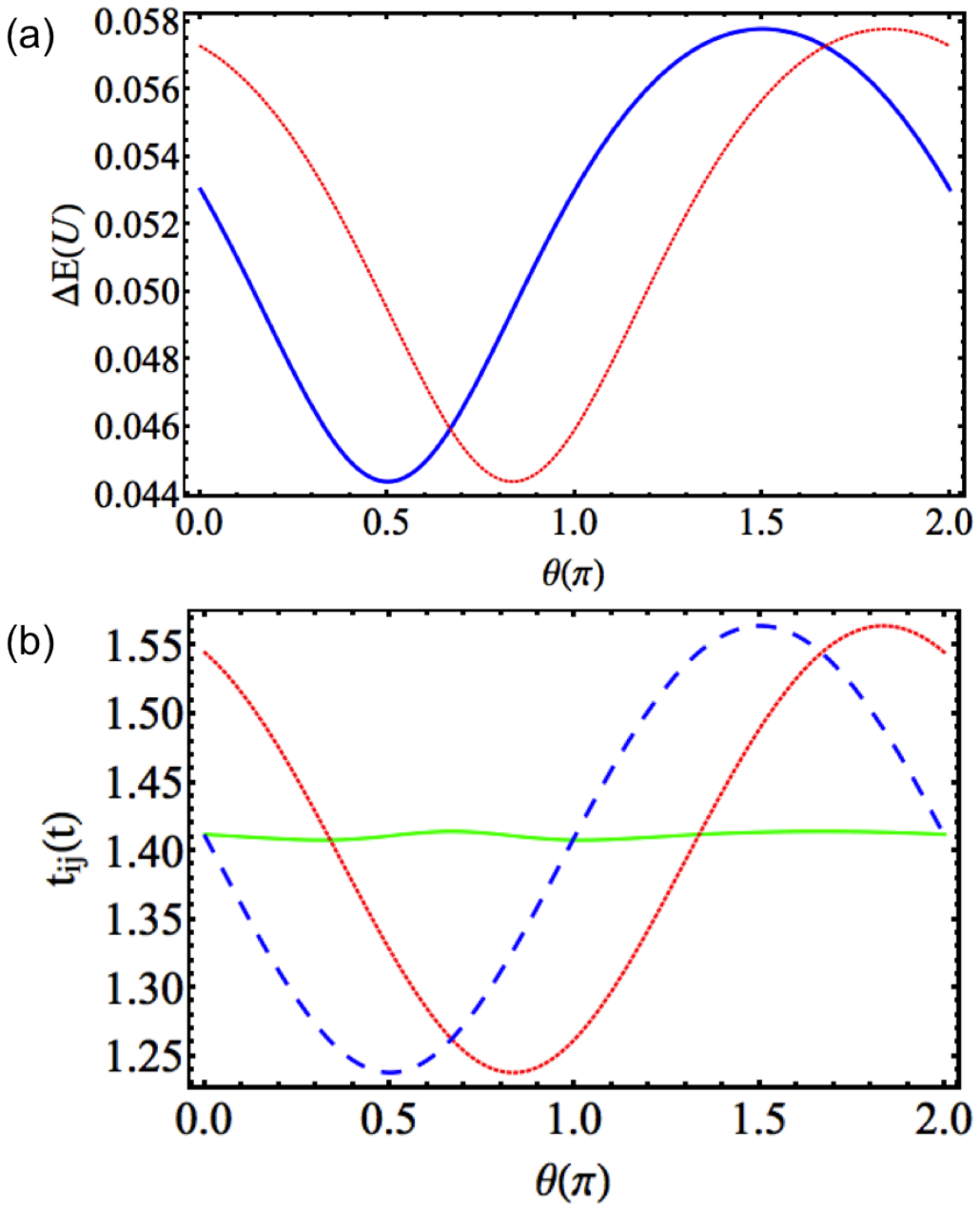

Figure 5.2: (a) Variations of ΔE_{12} (blue) and ΔE_{23} (red) over one round on the closed circuit. The variations of ΔE_{ij} are significantly suppressed when compared to Fig.[5.1a]. This is because we vary all t_{ij}. (b) Variation of t_{ij} over one round on the closed circuit. t_{12} is blue, t_{23} is red, and t_{13} is green. The values of t_{ij} are chosen specifically to reproduce the same J_{ij} in Fig.[5.1c] and reduce the variations of ΔE_i.

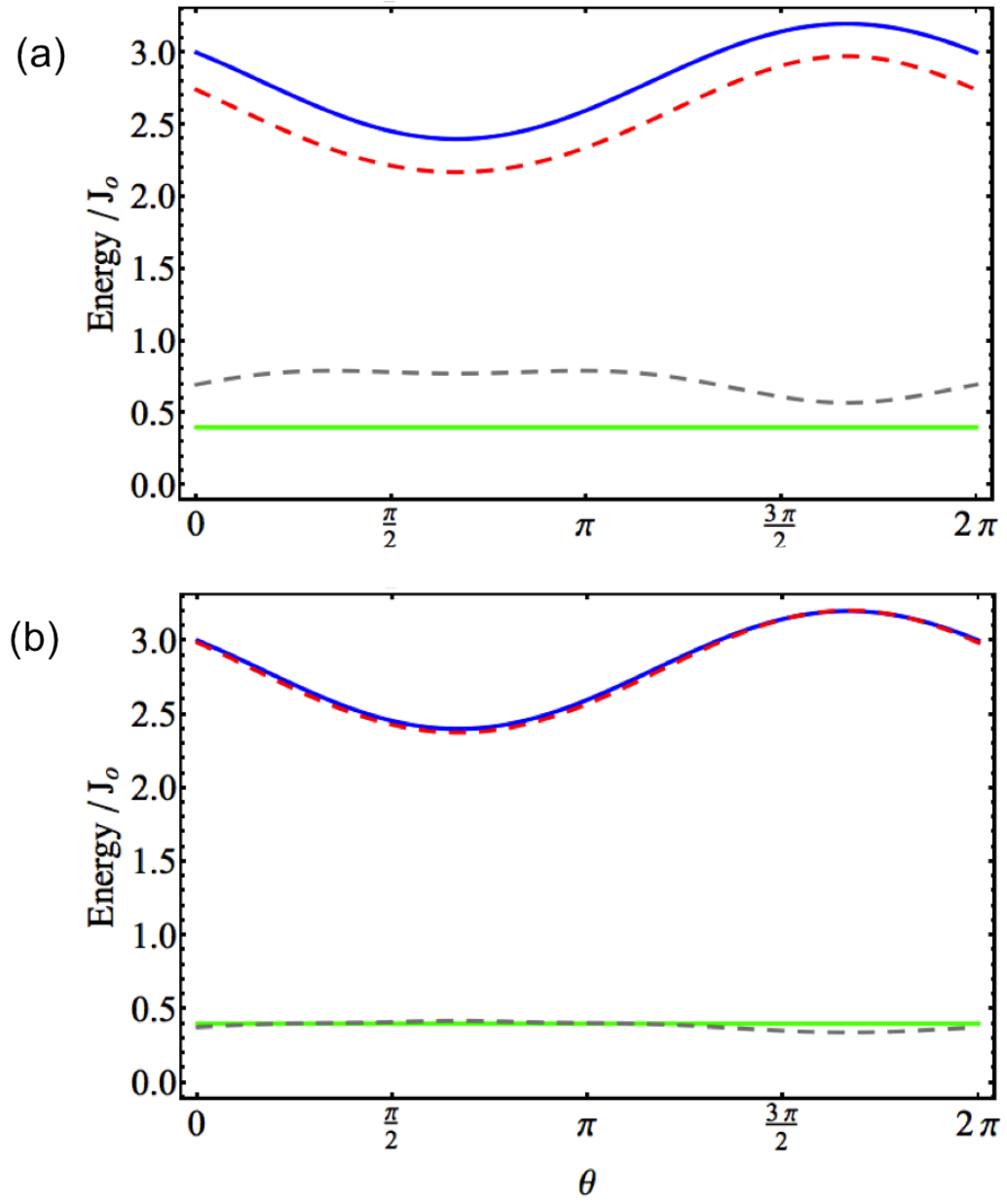

Figure 5.3: (a) The energy gap $\epsilon_2 - \epsilon_1$ (higher one in the plot) as well as $\epsilon_1 - \epsilon_0$ (lower one in the plot) in both Hubbard (dotted curve) and Heisenberg (solid curve) model for the circuit presented in Fig.[5.1]. ϵ_i is the i-th eigenenergy of the system. (b) The same energy gaps in both Hubbard (dotted) and Heisenberg (solid) model for the circuit presented in Fig.[5.2]. In both (a) and (b), the green, solid curve which represents the energy gap between the two coded qubit level is a constant over the closed circuit. This is because we transport the coded qubit on a constant energy surface as implied by the parametric plot of $\{B_x, B_y\}$ for the coded qubit (effective two-level system) in Fig.[5.1d].

phase for the coded qubit along the Herzberg circuit. After one round on the circuit, the state accumulates a phase of π in agreement with the theory. To get Fig.[5.4], we simulate the time evolution, $\psi(\theta)$, of the coded qubit by varying the on-site energies and tunnel coupling according to Eq.(5.12) - Eq.(5.14). We use the angle θ, which denotes the fraction of the Herzberg circuit, as a time variable. Next, we take the definition of geometrical phase [118],

$$\psi(\theta) = Te^{-\frac{i}{\hbar}\int d\theta' E_n(\mathbf{R}(\theta))} e^{i\gamma(\theta)} \left|n(\mathbf{R}(\theta))\right\rangle, \tag{5.15}$$

where $E_n(\mathbf{R}(\theta))$ and $|n(\mathbf{R}(\theta))\rangle$ are the n-th eigenenergy and eigenfunction for the Hamiltonian with parameter $\mathbf{R}$. We remark that $|n(\mathbf{R}(\theta))\rangle$ should be chosen to be single-valued and the phases of the eigenstates at different $\mathbf{R}$ should be continuously differentiable with respect to $\mathbf{R}$. $\gamma(\theta)$ is the accumulated Berry's phase. From Eq.(5.15), one may extract the accumulated Berry's phase in a numerical calculation.

Let us now turn to the experimental observation of Berry's phase using quantum interference. The restriction of having an effective in-plane magnetic field $\mathbf{R} = (X, Y)$ makes the experimental probing of Berry's phase difficult because we have very limited interference between components of the wavefunction. Therefore, it is essential to have a closed circuit that lies above the $x - y$ plane so the solid angle subtended by the circuit is given by $\Omega = 2\pi(1 - \cos\Theta)$, where $\cos\Theta$ is the direction cosine of the effective field along the z direction. To generate an effective field along the z direction, we need to apply a magnetic field perpendicular to the triangular TQD. The perpendicular field turns on the chiral term in Eq.(5.2). Since the chiral states are eigenstates of the chirality operator, the chirality term acts as a σ_z operation in the computational space. The coefficient, χ_{ijk}, attached to the chirality operator is

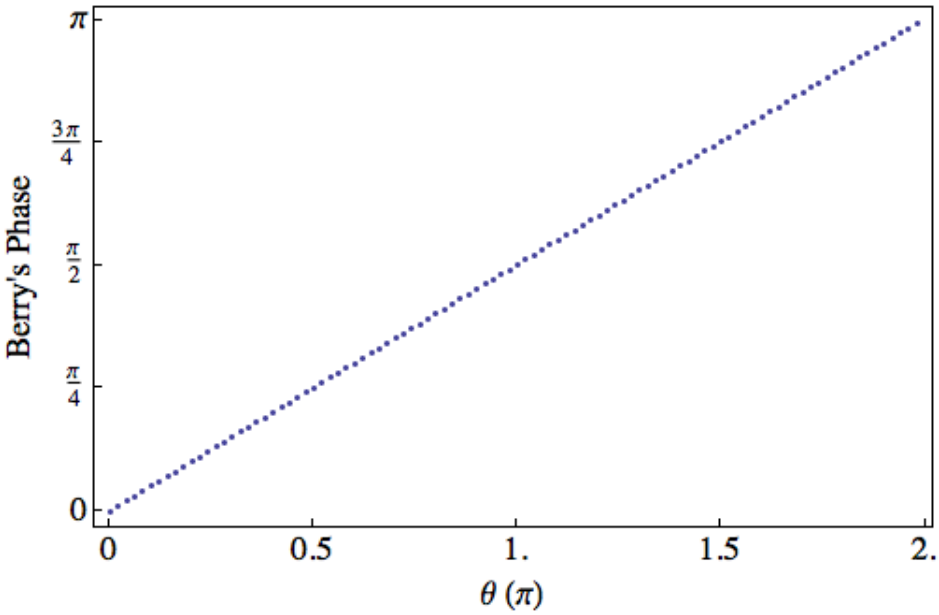

Figure 5.4: Accumulation of Berry's phase by the coded qubit level, $|q_+\rangle$. At the end of the Herzberg circuit, $\theta = 2\pi$, the accumulated phase is π, in agreement with theory.

$\approx t^3/U^2$. If we take $t = -0.05$ and $U = 2.0$, the values used to generate Fig.[5.2], then χ_{ijk} is about two to three orders of magnitude smaller than J_{ij}'s. It is important to realize that χ_{ijk}, derived from third order perturbation theory, also depends on the TQD parameters such as t_{ij}, and differences of on-site energies through terms like $\frac{1}{(U-V+\Delta E_{ij})(U-V+\Delta E_{kl})}$. Therefore, as the system is adiabatically transported on a closed circuit by varying the gate voltage, the magnitude of this effective z field will oscillate in its magnitude. Furthermore, an estimated change of the effective z field over the course of one complete circuit is two to three orders of magnitude smaller than due to the J_{ij}'s.

With all the necessary ingredients in place, we now describe a possible procedure to experimentally detect Berry's phase in a triangular TQD. First, we prepare the coded

qubit in a linear superposition of the form $\frac{1}{\sqrt{2}}|q_+\rangle + \frac{1}{\sqrt{2}}|q_-\rangle$ by having an effective field $\mathbf{R}$ along the y direction. Next, we follow Eqs.(5.12)-(5.14) to tune E_1, E_3, and t_{13} under the perpendicular magnetic field to accumulate the geometrical phase over one closed circuit lying above the $x-y$ plane. Over the course of transporting the system around the circuit, the system acquires both dynamical and geometrical phases. Therefore, we next have to perform a spin-echo [126, 122, 121] procedure to eliminate the dynamical phases. For this spin-echo procedure, we perform a NOT operation on the coded qubit to flip the two chiral states. Then we transport the system around the same circuit in the opposite direction. In this way, the dynamical phases will add destructively while the geometrical phases will add constructively. At the end of the second round along the circuit, the system now has only Berry's phase left. The final task is to perform quantum interferometry to extract Berry's phase from the system. At this stage, it is important to recall the Jacobi states, $|L_0\rangle$ and $|L_1\rangle$, which can be distinguished by the joint spin states on dot 1 and dot 3. We remark that experiments [94, 61] have already demonstrated that the joint spin states between two neighbouring dots can be measured by the spin blockade phenomenon. If the charge detection shows that we can make a transition from $(1,1,1)$ to $(2,1,0)$, then we have a $|L_0\rangle$ state in the triangular TQD. Therefore, by simply projecting the chirality-based coded qubit into the Jacobi states, the probability of detecting $|L_0\rangle$ state is given by

$$P(L_0) = \frac{3}{2}\cos 2\Omega - \frac{\sqrt{3}}{2}\sin 2\Omega. \tag{5.16}$$

As mentioned in the previous section, the two bases are related by a unitary transformation. The measurements in the Jacobi basis thus implicitly provide the needed

quantum interference to extract Berry's phase.

We now focus on the case of the coded qubit in a linear TQD. We note that the diagonal elements of the Hamiltonian, Eq.(5.11), are always a positive quantity because of the fact that $J_{ij} > 0$, a condition dictated by the microscopic details given in Eq.(5.3), in which U is the largest energy scale for strongly correlated system. This observation implies that when we map the coded qubit in a linear TQD to a spin-1/2 particle, the magnetic field is restricted to having a positive z component. Hence we conclude that it is not possible to generate Berry's phase with a coded qubit in a linear TQD.

5.4 Conclusion

In summary, we presented a theoretical proposal for the Herzberg circuit and controlled accumulation of Berry's phase in a qubit encoded in the two degenerate chirality states of a three spin complex with total spin $S = 1/2$ in a triangular triple quantum dot molecule with one electron spin each. Using a Hubbard and Heisenberg model the Herzberg circuit encircling the degeneracy point is realized by adiabatically tuning the successive on-site energies of quantum dots and tunnel couplings across pairs of neighbouring dots. It is explicitly shown that encircling the degeneracy point leads to the accumulation of the geometrical Berry's phase. We show that only the triangular but not the linear quantum dot molecule allows for the generation of Berry's phase and we discuss a protocol to detect this geometrical phase in interference experiments relying on the spin blockade spectroscopy.

Chapter 6

Sequential Tunneling and Spin Blockade in a Linear Triple Quantum Dot

In this chapter, we present a theory of electronic properties and the spin blockade phenomena in a gated linear triple quantum dot. Quadruple points where four different charge configurations are on resonance, particularly involving the (1,1,1) configuration, are considered. In the symmetric case, the central dot is biased to higher energy and a single electron tunnels through the device when the (1,1,1) configuration is resonant with the (1,0,1),(2,0,1), and (1,0,2) configurations. The electronic properties of a triple quantum dot are described by a Hubbard model containing two orbitals in the two unbiased dots and a single orbital in the biased dot. The transport through the triple quantum dot molecule involves both singly and doubly occupied configurations and necessitates the description of the (1,1,1) configuration beyond the

Heisenberg model discussed in Chapter [2]. Exact eigenstates of the triple quantum dot molecule with up to three electrons are used to compute the current assuming weak coupling to the leads and a non-equilibrium occupation of quantum molecule states obtained from the rate equation. The intra-molecular relaxation processes due to acoustic phonons and cotunneling with the leads are included, and are shown to play a crucial role in the spin blockade effect. We find a quantum interference-based spin blockade phenomenon at low source-drain bias and a distinct spin blockade due to a trap state at higher bias. We also show that, for an asymmetric quadruple point with the (0,1,1),(1,1,1,),(0,2,1), and (0,1,2) configurations on resonance, the spin blockade is analogous to the spin blockade in a double quantum dot.

6.1 Introduction

Gated quantum dots (QDs) [40, 129, 32, 61, 22, 21, 42, 93] with controlled electron numbers are a testbed for probing fundamental many-body physics as well as a promising platform for building spintronics and quantum information processing (QIP) devices [59]. Until recently, most experimental and theoretical investigations of quantum circuits based on electron spin focused on the single and double quantum dot (DQD) devices [32, 59]. Many essential tasks for operating a qubit have been demonstrated in DQDs. For instance, coherent manipulation and readout of one [61] and two [94] spin states have already been experimentally achieved using spin blockade [40, 41, 46] . In DQDs, spin blockade is used to detect spin using spin-to-charge conversion. For instance, the $(0, 2)$ charge configuration cannot be obtained from the $(1, 1)$ configuration if the electron spin in the left dot is parallel to

the electron spin in the right dot. Detected charge on the right dot depends on the relative spin orientations of the two electrons. Thus, spin blockade detects spin states (triplet or singlet) of the two electrons in transport spectroscopy or charge sensing measurement [40, 41, 46]. A physical signature of spin blockade at the triple point, $(0,1) \rightarrow (1,1) \rightarrow (0,2)$, is the current rectification under different bias directions. In positive (forward) bias direction, triplet states will not be populated, and the quantum dot molecule does not exhibit negative differential conductance. In negative (reverse) bias direction, current suppression is pronounced once the transitions to the $(1,1)$ triplet states become accessible in the transport window.

A nontrivial extension of the quantum circuit based on electron spin is the triple quantum dot (TQD) with one electron each. This can be appreciated by the comparison of the quantum optical properties of a two-level versus three-level systems. Recent charging and transport spectroscopy experiments [42, 50, 36, 130] on the TQDs have mapped out the stability diagram of the devices down to a few electrons. The electronic properties of a triple quantum dot have been investigated theoretically, including topological Hunds rules [36], spin-selective Aharonov-Bohm oscillations [39, 131], the implementation of a coded qubit [25, 27, 127], voltage-controlled spin manipulation [132, 110], entangled GHZ state generation [74, 133], non-Fermi-liquid behaviour [71, 134, 135] in a triangular TQD as well as coherent tunneling adiabatic passage (CTAP) processes for a single electron in a LTQD [55, 56]. All these theoretical predictions as well as quantum information processing in a TQD require an ability to spectroscopically detect spin by, *e.g.*, spin blockade.

In recent experiments Granger [50] *et. al.* and Laird [93] *et. al.* carried out

transport spectroscopy and charge sensing measurement on a LTQD molecule with one electron in each dots. This configuration, denoted by $(1,1,1)$, was tuned to be resonant with the two electron configuration $(1,0,1)$. It was assumed that transport proceeded through $\{(2,0,1),(1,1,1),(1,0,2)\}$ resonant configurations, which implied that the central dot was biased to higher energy. The presence of doubly occupied dots in the configurations makes the Heisenberg model of localized spin configurations inapplicable and a microscopic model is required to study the electronic and transport properties of this TQD system.

In this chapter, we extend our earlier theory of a TQD [27, 36, 75, 68] to biased linear molecule at quadruple points (QPs) and describe spin blockade as a spectroscopic tool allowing the readout of electron spin. We analyze the electronic and spin properties of a LTQD as a function of energies of each dot within a single-band or multi-band Hubbard model. The knowledge of the wave functions of a single-band Hubbard model allows for the qualitative understanding of the low-bias transport through the device, but including more than one orbital in the dot will be shown to be crucial for spin blockade. Two different QPs involving the $(1,1,1)$ configuration are considered: (a) symmetrical QP (SQP) with $(1,0,1),(2,0,1),(1,1,1),(1,0,2)$ configurations on resonance, and (b) asymmetrical QP (AQP) with $(0,1,1),(1,1,1),(0,2,1),(0,1,2)$ configurations on resonance. For SQP, the transport goes through $(1,0,1) \rightarrow (2,0,1) \rightarrow (1,1,1) \rightarrow (1,0,2)$ channels, while $(0,1,1) \rightarrow (1,1,1) \rightarrow (0,2,1) \rightarrow (0,1,2)$ is the transport channel for the AQP. Current is calculated in sequential tunneling approximation between the TQD and the leads, using rate equations [39, 136] to calculate the non-equilibrium steady state occupation of TQD states with a source-drain bias.

We use Fermi's Golden Rule to calculate the transition rates between TQD states by adding or removing an electron due to the coupling between the TQD molecule and the leads, and also the transition rate between TQD states with the same number of electrons due to the interaction with acoustic phonons [137, 138].

The plan of this chapter is as follows. In Sec.[6.2], we describe the system and the Hamiltonians. In Sec.[6.3], our approach on the transport based on the sequential tunneling between the leads and the TQD molecule and rate equations are explained in detail. The transition rates due to different mechanisms are also discussed. In Sec.[6.4.1], we present results of current calculations for the SQP, and discuss the mechanism of quantum spin blockade at low bias. In Sec.[6.4.2], we present results of transport calculations for conventional spin blockade at the SQP under high source drain bias and at the AQP, and discuss how the system at the AQP can behave qualitatively as a double dot around a similar triple point with $(0,1),(1,1),(0,2)$ configurations. A brief conclusion is given in Sec.[6.5].

6.2 Model

Fig.[6.1] presents a schematic diagram of a LTQD in contact with the two semi-infinite leads and the energy levels of the single QD orbitals. The metallic leads are modelled by one dimensional tight binding chains. Each quantum dot, defined by metallic gates on top of GaAlAs/GaAs heterojunction and represented here by a circle contains a controlled number of electrons, e.g., one electron each [$(1,1,1)$ configuration] in (a) and $(1,0,1)$ configuration in (b). Electrons can tunnel between dots 1 and 2, and between dots 2 and 3, but there is no direct tunnel coupling between

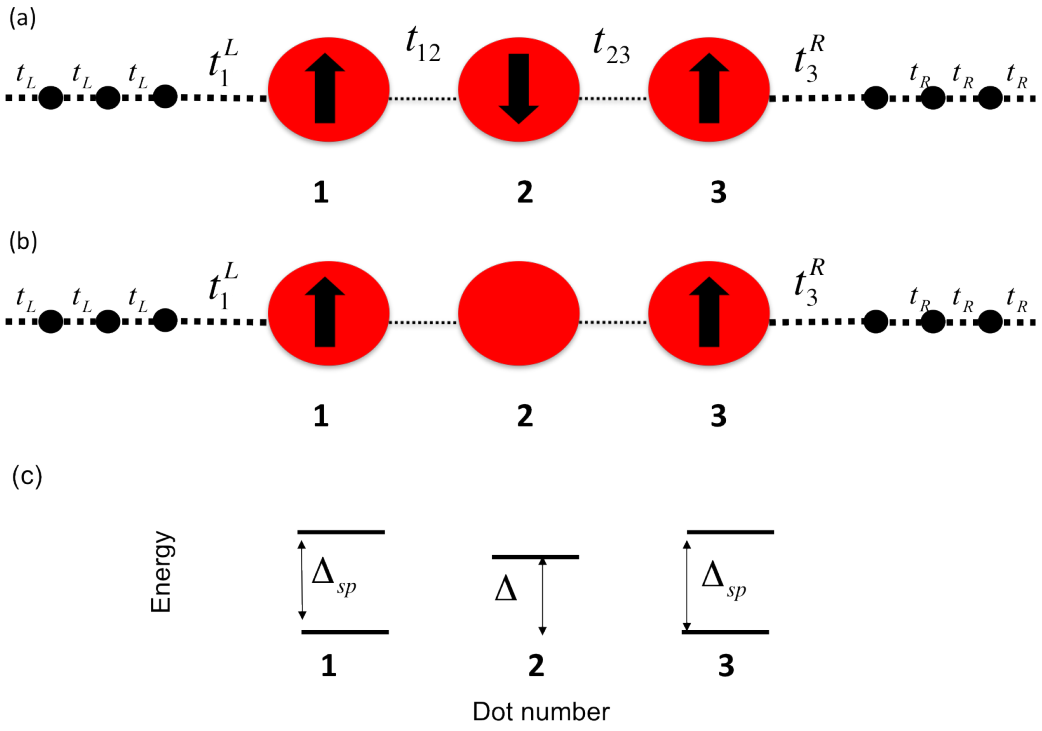

Figure 6.1: (a) Schematics of a linear TQD connected to leads. The leads are modelled with 1D tight binding chain of electrons with tunnel coupling t_1^L and t_3^R for left and right lead respectively. The system is trapped in an $(1, 1, 1)$ configuration. (b) Another schematics of a linear TQD connected to leads. The system is trapped in an $(1, 0, 1)$ configuration. (c) Schematics of single particle energy spectrum of a triple quantum dot when the central dot is biased with Δ. The gap Δ_{sp} denote the energy difference between S and P orbitals on a dot.

the two edge dots. Fig.[6.1c] shows the single particle levels of the individual dots in the LTQD without interdot tunneling. The lowest energy bars denote S orbitals (the ground orbitals) in each dot. The energy of the central dot is raised by an applied voltage Δ. This bias can be used, for example, in order to localize the two electrons in dots 1 and 3 as shown in Fig.[6.1b]. In this study, Δ, comparable to Coulomb repulsion U, is used to bring the configurations such as $(1,1,1)$ and $(1,0,2)$ on resonance as shown in Fig.[6.2]. We find it is essential to include the excited states, P orbitals, in dots 1 and 3 in order to properly account for the transport properties at the SQP. The energy separation, Δ_{sp}, between S and P orbitals may also be comparable to Δ. Thus, the electronic properties of a LTQD are described by a multi-band Hubbard model with parameters derived from a microscopic Linear Combination of Harmonic Orbitals-Configuration Interaction (LCHO-CI) approach, introduced in Sec.[2.1.1], for given voltages on the gates[75]. With $\hat{c}_{i\sigma}$ ($\hat{c}^{\dagger}_{i\sigma}$) denoting annihilation (creation) operators for an electron with spin σ on orbital i, the five-level Hubbard Hamiltonian reads:

$$\hat{H}_D = \sum_{i=1,\sigma}^{5} E_i(V_{sd})\hat{n}_{i\sigma} + \sum_{\substack{i,j=1,\sigma \\ j\neq i}}^{5} t_{ij}\hat{c}^{\dagger}_{i\sigma}\hat{c}_{j\sigma} + \sum_{i=1}^{5} U_i\hat{n}_{i\uparrow}\hat{n}_{i\downarrow} + \frac{1}{2}\sum_{i,j=1}^{5} V_{ij}\hat{\rho}_i\hat{\rho}_j, \qquad (6.1)$$

where the Hubbard parameters were defined in Sec.[2.1.2]. We assign indices $i = 1, 2, 3$ to S orbitals of dots 1, 2 and 3 respectively. The indices $i = 4, 5$ denote excited P orbitals. We will consider only single excited orbitals in both dot 1 (i=4) and dot 3 (i=5) for the TQD molecule at SQP. For the AQP case with $(0,1,1)$ base configuration, the excited orbitals are in dot 2 (i=4) and dot 3 (i=5). The excited orbital in the biased dot does not play any significant role.

The TQD device is connected to left and right lead ($r = L, R$) as shown in

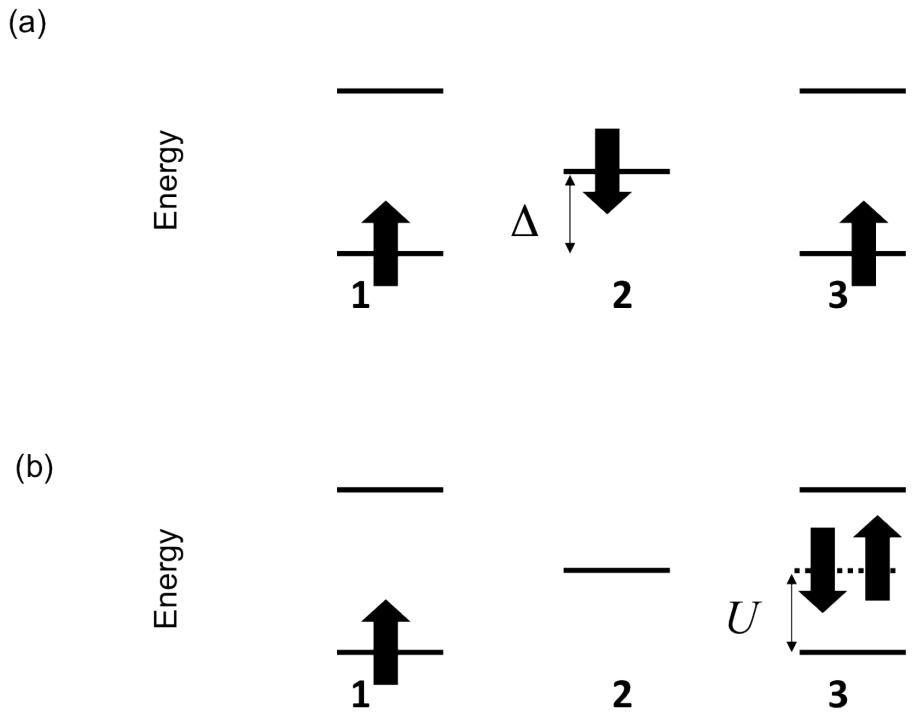

Figure 6.2: (a) One of the (1,1,1) configuration. (b) One of the (1,0,2) configuration. At SQP, the bias Δ in dot 2 should be $U + V' - 2V$ in order for the two configurations to have the same energy.

Fig.[6.1a]. Electrons in the leads fill up the noninteracting states of semi-infinite tight-binding chains with a bulk dispersion relation $\epsilon_r(k) = 2t_r \cos(ka)$ up to a Fermi level $\mu_{L(R)}$, where t_r is the tunnel coupling between the sites on lead r, a is the distance between sites of a tight-binding chain, and k denotes the wave vector of the plane wave in the chain. The interaction between the leads and the device is modelled as,

$$\hat{H}_{rD} = \sum_{i_r,\sigma} \sum_{k} \left(\tilde{t}_i^r(k) \hat{d}_{k\sigma}^\dagger \hat{c}_{i_r\sigma} + h.c. \right), \tag{6.2}$$

where $\tilde{t}_i^r(k) = t_i^r e^{i2\pi k a m_r}/\sqrt{2\pi}$ is the tunnel coupling between the mode k of the $r = L(R)$ lead and orbital i_r localized on the left dot ($r = L$) or the right dot ($r = R$) and m_r in the exponent of $\tilde{t}_i^r(k)$ is $1(-1)$ for $r = L(R)$. $\hat{d}_{k\sigma}^\dagger$ creates an electron with momentum k and spin σ in the lead r. In this study, $t_i^R = 0$ for orbitals not on the right edge dot and $t_i^L = 0$ for orbitals not on the left edge dot.

Interactions with phonons have already been shown to be important to understand the incoherent transport properties of double quantum dots at high bias in Ref.[138], for instance. We include interaction of electrons in the LTQD with bulk longitudinal acoustic (LA) phonons via deformation potential as the mechanism of phonon-induced relaxation at low temperature. The electron-phonon interacting Hamiltonian reads,

$$\hat{H}_{e-ph} = \sum_{i,j=1,\sigma}^{5} \sum_{q} M_{ij}(\mathbf{q}) \left(\hat{b}_{\mathbf{q}} + \hat{b}_{-\mathbf{q}}^\dagger \right) \hat{c}_{i\sigma}^\dagger \hat{c}_{j\sigma}, \tag{6.3}$$

where $\mathbf{q}$ is the phonon momentum, i and j are TQD orbitals, and $\hat{b}_{\mathbf{q}}(\hat{b}_{\mathbf{q}}^\dagger)$ operator annihilates (creates) a phonon with momentum $\mathbf{q}$. $M_{ij}(\mathbf{q}) = \Lambda(q) \int \psi_i(r)^* \exp(-i\mathbf{q} \cdot \mathbf{r}) \psi_j(r)$ is the electron-phonon scattering matrix element, $\psi_i(r)$ is a single particle wave function, and $\Lambda(q) = \sqrt{\frac{D^2 \hbar q}{2\rho c_s}}$ for deformation potential D, GaAs mass density

ρ, and speed of sound c_s in GaAs. The phonon scattering matrix element, $M_{ij}(\mathbf{q})$, depends on the single particle wave function $\psi_i(r)$ which is obtained from the LCHO [75] formalism.

6.3 Theory of Sequential Tunneling

Theory of sequential tunneling through a triangular triple quantum dot molecule has been described in detail in Ref. [39]. Here we extend the approach of Ref. [39] to include both electron-phonon interaction and cotunneling and apply this theory to describe current and spin blockade in a linear triple quantum dot. Following Ref. [39], current between lead r and a TQD device in the vicinity of a quadrupole point involving $N = 2$ and $N + 1 = 3$ electrons can be written as a difference between the current from the lead to the triple quantum dot and a current from the triple quantum dot back to the lead r:

$$I_{rD} = -e\sum_{i_r,\sigma}\sum_{\alpha_N,\beta_{N+1}} W_r^{seq}(\alpha_N \to \beta_{N+1})P_{\alpha_N} + e\sum_{i_r,\sigma}\sum_{\alpha_N,\beta_{N+1}} W_r^{seq}(\beta_{N+1} \to \alpha_N)P_{\beta_{N+1}}, \tag{6.4}$$

where $|\alpha_N\rangle$ is an N-electron many-body eigenstate of the isolated TQD with energy E_{α_N} and associated steady state probability P_{α_N}, which is obtained by solving the rate equation, Eq.(6.5), below. The sequential tunneling rate, $W_r^{seq}(\alpha_N \to \beta_{N+1})$, provides the rate of transition for the TQD from an N-electron α_N state to an $(N+1)$-electron state due to first order perturbation from the lead r. Details of sequential tunneling rates will be provided later.

The probabilities, P_{α_N}, are the diagonal matrix elements of the reduced density

matrix ρ. The time evolution of these diagonal matrix elements is described by the Pauli master equation,

$$\dot{P}_{\alpha_N} = \sum_{N'=2}^{3} \sum_{\beta_{N'}} P_{\beta_{N'}} W(\beta_{N'} \to \alpha_N) - P_{\alpha_N} W(\alpha_N \to \beta_{N'}), \tag{6.5}$$

where transition rates $W_{\alpha_N \to \beta_{N'}}$ are calculated using Fermi's Golden Rule. We consider sequential tunneling rate, W_r^{seq}, in first order in coupling to the lead r, intra TQD phonon-induced relaxation rate, W^{ph}, and second order cotunneling rate, W_r^{cot}. The master equation is solved to obtain steady-state solution for the probabilities, P_{α_N}, by setting the time derivative to be zero.

With the coupling to a lead r, $\sum_{k,\sigma} \hat{d}_{k\sigma} \left(\sum_i \tilde{t}_i^r(k) \hat{c}_i^\dagger \right) + h.c.$, the first order sequential tunneling rates read

$$W_r^{seq}(\alpha_N \to \beta_{N+1}) = \frac{2\pi}{\hbar} \sum_k \left| \langle \beta_{N+1} | \sum_i \tilde{t}_i^r(k) \hat{c}_{i\sigma}^\dagger | \alpha_N \rangle \right|^2 \delta\left(\omega_{\alpha\beta} - \epsilon_{rk}\right) f_r(\omega_{\alpha\beta}), \tag{6.6a}$$

$$W_r^{seq}(\beta_{N+1} \to \alpha_N) = \frac{2\pi}{\hbar} \sum_k \left| \langle \alpha_N | \sum_i \tilde{t}_i^r(k) \hat{c}_{i\sigma} | \beta_{N+1} \rangle \right|^2 \delta\left(\omega_{\alpha\beta} - \epsilon_{rk}\right) \left(1 - f_r(\omega_{\alpha\beta})\right), \tag{6.6b}$$

where $f_r(\epsilon) = 1/\left(\exp[(\epsilon - \mu_r)/k_B T] + 1\right)$ is the Fermi function of the lead r, $\omega_{\alpha\beta} = E_{\beta_{N+1}} - E_{\alpha_N}$, and ϵ_{rk} is the energy of a state associated with wave vector k of lead r. We remark that the summation over index i in the sequential tunneling rate refers to summing the tunneling contributions from the S and P orbitals in a quantum dot. By expanding the norms of the complex-valued matrix elements in above equations and introducing an integration variable ω, the sequential tunneling rates can be also

expressed as follows,

$$W_r^{seq}(\alpha_N \to \beta_{N+1}) = \frac{2\pi}{\hbar} \sum_{i,j} \int d\omega A_{ij}^{\alpha\beta}(\omega) B_{ij}^r(\omega) f_r(\omega_{\alpha\beta}), \tag{6.7a}$$

$$W_r^{seq}(\beta_{N+1} \to \alpha_N) = \frac{2\pi}{\hbar} \sum_{i,j} \int d\omega A_{ij}^{\alpha\beta}(\omega) B_{ij}^r(\omega)(1 - f_r(\omega_{\alpha\beta})), \tag{6.7b}$$

with generalized spectral functions [139] of the TQD, $A_{ij}^{\alpha\beta} = \sum_\sigma \langle \alpha_N | \hat{c}_{i\sigma} | \beta_{N+1} \rangle \langle \beta_{N+1} | \hat{c}_{j\sigma}^\dagger | \alpha_N \rangle$ $\delta(\omega - \omega_{\alpha\beta})$, and generalized spectral function of the lead r, $B_{ij}^r(\omega) = \sum_k \tilde{t}_i^r(k)(\tilde{t}_j^r(k))^* \delta(\omega - \epsilon_{rk})$. By substituting the sequential tunneling rates in Eq.(6.4) with Eq.(6.7), one can relate the current through a TQD with the spectral functions of the TQD and the leads.

We now provide relaxation rates due to electron-phonon interaction and cotunneling. For large source-drain bias voltage $|eV_{sd}| \gg |t_{ij}|$, the change in the on-site energy of dots due to the source-drain bias will take the system off the resonance, away from the QP. In this regime, the current is dominated by inelastic tunneling between orbitals of neighbouring quantum dots due to electron-phonon interaction. The phonon emission-induced relaxation rate [138] reads,

$$W^{ph}(\alpha_N \to \beta_N) = \frac{2\pi}{\hbar} \sum_{\mathbf{q}} \left| \sum_{i,j,\sigma} M_{ij}(\mathbf{q}) \langle \beta_N | \hat{c}_{i\sigma} \hat{c}_{j\sigma}^\dagger | \alpha_N \rangle \right|^2 \delta\left(E_{\alpha_N} - E_{\beta_N} - \hbar\omega_{\mathbf{q}}\right) g(\hbar\omega_{\mathbf{q}}, T), \tag{6.8}$$

where $\hbar\omega_{\mathbf{q}} = \hbar c_s |\mathbf{q}|$ is phonon energy, and $g(\hbar\omega_{\mathbf{q}})$ is the thermal occupation number for phonon mode $\mathbf{q}$ at temperature T. Spin blockade occurs when the spin-3/2 polarized states $|\alpha_3\rangle$ become trap state, with $W_r^{seq}(\alpha_3 \to \beta_2) = 0$. However, the spin blockade can be lifted if we allow cotunneling. We consider cotunneling transition rate [140, 141], which involves an exchange of electrons between a lead r and the TQD

in a spin 3/2 state,

$$W_r^{cot}(\alpha_3 \to \beta_3) = \frac{2\pi}{\hbar} \sum_{\sigma,\sigma',k,k'} f_r(\epsilon_{k'_r}^{\sigma'})(1 - f_r(\epsilon_{k_r}^{\sigma}))\delta\left(E_{\beta_3} - E_{\alpha_3} + \epsilon_{k_r}^{\sigma} - \epsilon_{k'_r}^{\sigma'}\right) \times \left| \sum_{\gamma_2,i,i'} t_i^r(k_r) t_{i'}^r(k'_{r'}) \frac{\left(C_{\alpha_3\gamma_2}^{i'_r\sigma'}\right)^* C_{\beta_3\gamma_2}^{i_r\sigma}}{E_{\alpha_3} - E_{\gamma_2} - \epsilon_{k_r}^{\sigma}} \right|^2, \quad (6.9)$$

where $C_{\alpha_3,\gamma_2}^{i\sigma} = \langle \alpha_3 | \hat{c}_{i\sigma}^\dagger | \gamma_2 \rangle$, $|\gamma_2\rangle$ is a triplet state, and $\epsilon_{k_r}^{\sigma}$ is the energy for an electron with wave vector k and spin σ of the lead r.

6.4 Transport and Spin Blockade

In this section, we compute and discuss the transport properties and spin blockade in a linear triple quantum dot at both SQP and AQP. We set on-site Coulomb repulsion between S orbitals to be $U_{11} = U_{22} = U_{33} = U = 3.0$ meV, and we use U as the unit of energy scale. For S and P orbitals in the same dot, we set $U_{14} = U_{35} = U' = 0.94U$, and $U_{44} = U_{55} = U'' = 0.96U$ for P orbitals in the same dot. We set $t_{i,j} = t = -6.0 \cdot 10^{-3}\, U$ for tunneling between S orbitals in neighbouring dots. We set $t_{ij} = t' = -6.2 \cdot 10^{-3}\, U$ for tunneling between the S and P orbitals on neighbouring dots. We set $V_{ij} = V = 0.2\, U$ between neighbouring dots and $V_{ij} = V' = 0.1\, U$ between dots 1 and 3. The energy difference between S and P energy levels, Δ_{sp}, in the same dot is taken to be 0.8 U and 0.25 U in different cases considered below.

The tunnel coupling for the tight binding chain in the leads is taken as $t_L = t_R = -2.0U$. The large tunnel coupling for the leads allows a wide energy band, which increases the number of available levels for transport. As for the dot-lead

tunnel coupling t_i^r, we set $t_1^L = -1.0 \cdot 10^{-3}U$ and $t_4^L = -1.1 \cdot 10^{-3}U$. Only the S and P orbital in dot 1 is connected to the left lead. Symmetrically, we set $t_3^R = t_1^L$, and $t_5^R = t_4^L$. The rest of the tunnel coupling parameters are zero in our model. For interaction between electrons in the TQD and bulk LA (longitudinal acoustic) phonons, we use the following GaAs parameters: $\Lambda(q) = \sqrt{D^2\hbar\omega_q/2\rho c_s^2}$, where $D = 2.9\,U$, $\rho = 5300\,kg/m^3$, $c_s = 3700m/s$ and $\omega_q = c_s q$.

We measure current in unit of $I_0 = e|t_1^L|^2/\hbar|t_L|$. We assume total potential difference eV_{sd} across the two leads and a linear decrease of this potential across the device. The chemical potentials on the two leads are given by $\mu_L = eV_{sd}/2$ and $\mu_R = -eV_{sd}/2$. The on-site energies are given by $E_{1,(4)}(V_{sd}) = E^0_{1,(4)} + eV_{sd}/6$, $E_{i_2} = E^0_{i_2}$, and $E_{3,(5)}(V_{sd}) = E^0_{3,(5)} - eV_{sd}/6$ respectively, and electron temperature in all calculations is set to $k_BT = 2.0 \cdot 10^{-3}\,U$.

In Chapter [2], we solve for the eigenstates of a central-dot biased LTQD. When Δ is large, the ground state in the triplet subspace ($S_y = 1$) can be written as

$$|T^+\rangle = \gamma\left(|T_{13}\rangle + \frac{\gamma_1}{\gamma}|T_{12}\rangle + \frac{\gamma_2}{\gamma}|T_{23}\rangle\right), \tag{6.10}$$

where $|T_{ij}\rangle = \hat{c}^\dagger_{i\uparrow}\hat{c}^\dagger_{j\uparrow}|0\rangle$. The state $|T^+\rangle$ is predominantly characterized by $|T_{13}\rangle$, and $|\gamma_1| = |\gamma_2| \ll 1$. We remark that the corresponding eigenstate in $(S = 1, S_y = 0)$ and $(S = 1, S_y = 1)$ subspaces are denoted by $|T^0\rangle$ and $|T^-\rangle$, and these states are obtained from $|T^+\rangle$ after flipping one of the spins and performing the proper anti-symmetrization of the wavefunction, and after flipping both spins, respectively. For the singlet subspace, we will simply denote the ground state as $|S\rangle$ in this chapter.

Similarly, we also borrow the notations, defined in Sec.[2.2.3], for the three-electron $S_y = 1/2$ subspace $|a\rangle = \hat{c}^\dagger_{1\uparrow}\hat{c}^\dagger_{2\uparrow}\hat{c}^\dagger_{3\downarrow}|0\rangle$, $|b\rangle = \hat{c}^\dagger_{1\uparrow}\hat{c}^\dagger_{2\downarrow}\hat{c}^\dagger_{3\uparrow}|0\rangle$, $|c\rangle = \hat{c}^\dagger_{1\downarrow}\hat{c}^\dagger_{2\uparrow}\hat{c}^\dagger_{3\uparrow}|0\rangle$, $|d\rangle =$

$\hat{c}^{\dagger}_{1\uparrow}\hat{c}^{\dagger}_{1\downarrow}\hat{c}^{\dagger}_{3\uparrow}|0\rangle$, and $|e\rangle = \hat{c}^{\dagger}_{1\uparrow}\hat{c}^{\dagger}_{3\uparrow}\hat{c}^{\dagger}_{3\downarrow}|0\rangle$. All five configurations belong to the $S_y = 1/2$ subspace. The first three have one electron per dot, $(1,1,1)$ configuration. $|d\rangle$ and $|e\rangle$ denote a $(2,0,1)$ and $(1,0,2)$ configuration, respectively. Based on these five configurations, we define the following four states: $|L_0\rangle = \frac{1}{\sqrt{2}}(|a\rangle - |c\rangle)$, $|L_1\rangle = \frac{1}{\sqrt{6}}(|a\rangle - 2|b\rangle + |c\rangle)$, $|X\rangle = \frac{1}{\sqrt{2}}(|d\rangle + |e\rangle)$, and $|Y\rangle = \frac{1}{\sqrt{2}}(|d\rangle - |e\rangle)$. As shown in Chapter [2], the three-electron Hubbard Hamiltonian when expressed in the truncated basis of these four states is reduced to two separate 2 by 2 sub-matrix, and the eigenstates read $|L_0^+\rangle = \cos(\phi)|L_0\rangle + \sin(\phi)|X\rangle$, $|L_0^-\rangle = \sin(\phi)|L_0\rangle - \cos(\phi)|X\rangle$, $|L_1^+\rangle = \cos(\theta)|L_1\rangle + \sin(\theta)|Y\rangle$, and $|L_1^-\rangle = \sin(\theta)|L_1\rangle - \cos(\theta)|Y\rangle$, where $\tan(2\phi) = t/\xi$, $\tan(2\theta) = \sqrt{3}t/\xi$, and $\xi = (\Delta + 2V' - U - V)/2$. In the subsequent discussion, these four eigenstates $\left|L^{\pm}_{0,1}\right\rangle$ and their counterparts in the $S_y = -1/2$ subspace will be used to understand the transport properties of a LTQD.

6.4.1 Quantum Interference-based Spin Blockade

We first consider transport through the SQP: $\{(1,0,1), (2,0,1), (1,1,1), (1,0,2)\}$, and we put P orbitals ($i = 4, 5$) in dot 1 and 3 respectively. We set $E_1 = E_3 = -U - V'$ and $E_2 = -2V$ in order to bring the four charge configurations into resonance. For the present case, we set a high single particle level spacing $\Delta_{SP} = 0.8U$ on the edge dots. A large energy spacing between the S and P orbitals allows one to focus on a few lowest states for transport at bias $|eV_{sd}| \ll U$. For instance, Fig.[6.3] shows the energy diagrams of the relevant 2-electron and 3-electron states near the SQP as a function of V_{sd}. The inset in Fig.[6.3] categorizes the states associated with the energies in the main figure. There are four active 2-electron states: one singlet $|S\rangle$,

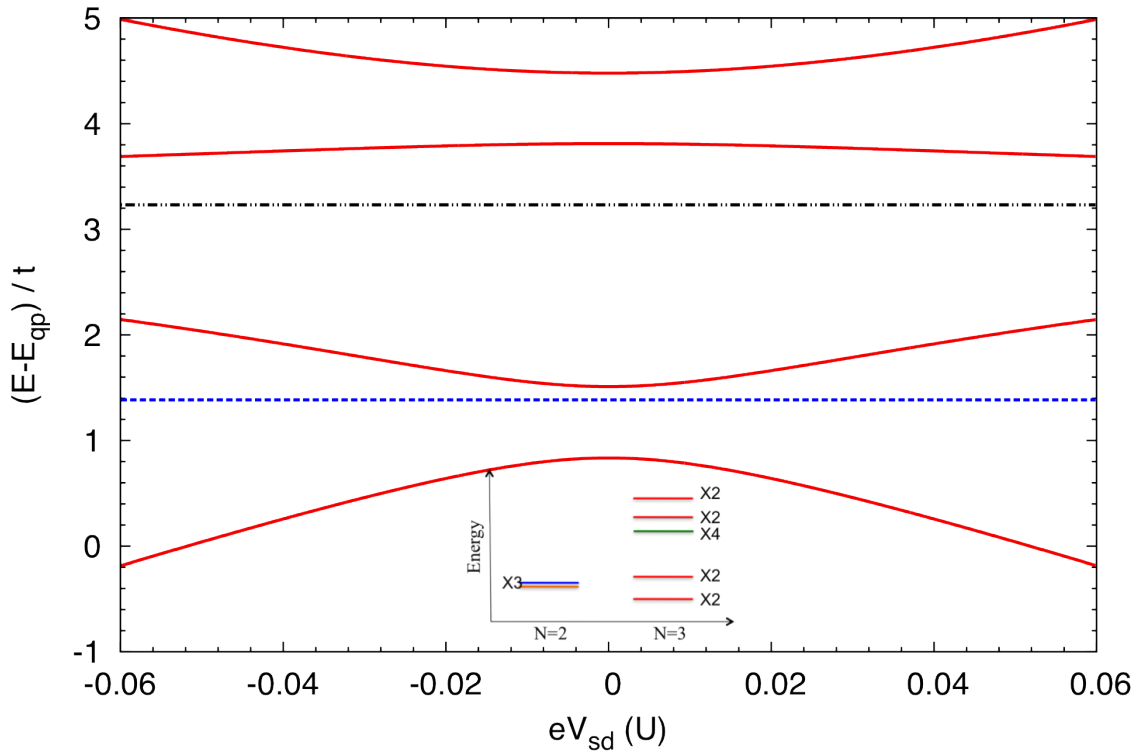

Figure 6.3: The energy spectrum of a multi-band Hubbard model as a function of source-drain bias. In the figure, the blue curve represents the four 2-electron states. They are very close in energy and looks degenerate in the energy resolution present here. The black curve is the quadruply degenerate spin-3/2 states. The red curves are each doubly degenerate spin-1/2 states. Inset: A summary of the states involved in the main figure at a particular value of V_{sd}. E_{qp} is the energy of the configuration at the quadruple point.

and triply degenerate triplet states, $|T^{\pm,0}\rangle$. For $N = 3$ subspace, there are four spin-1/2 states below the spin-3/2 states. The four spin-1/2 states are $|L_1^+\rangle$ and $|L_0^+\rangle$ and their counterpart in the $S_y = -1/2$ subspace. In the absence of magnetic field, these states remain degenerate. Next up in the three-electron subspace are the quadruply degenerate spin-3/2 states, $|S = 3/2, S_y = \pm 1/2, \pm 3/2\rangle$. The last four levels are $|L_1^-\rangle$ and $|L_0^-\rangle$ states and their counterpart in $S_y = -1/2$ subspace.

Under small V_{sd} and large Δ_{sp}, the wavefunctions remain similar to the ones obtained from single-band Hubbard Hamiltonian at zero V_{sd} in Sec.2.2. We emphasize that these three electron states are admixtures of $(2, 0, 1)$, $(1, 1, 1)$, and $(1, 0, 2)$ configurations with comparable weights except the spin-polarized states. Fig.[6.4a] presents the three-electron energy levels as a function of bias Δ on the central dot. According to our analysis in Sec.[2.2], when Δ is large, the lowest few three-electron states can be expressed as linear combinations of either $|L_1\rangle$ and $|Y\rangle$, or $|L_0\rangle$ and $|X\rangle$. Fig.[6.4b] shows the contributions of $|L_1\rangle$ and $|Y\rangle$ to the three-electron ground state. At the SQP, the three-electron ground state $|L_1^+\rangle$ is an admixture of almost 50% $|L_1\rangle$ and 50% $|Y\rangle$ as shown in Fig.[6.4b]. Based on the analysis of wavefunctions in the single-band Hubbard model, the only dark channels in the LTQD are the spin-3/2 states. As the spin-3/2 wavefunctions, $|S = 3/2, S_y = \pm 1/2, \pm 3/2\rangle$, do not overlap significantly with the two-electron triplet states, $|T^{\pm,0}\rangle$, when an electron is added or removed from the edge dots, the conventional spin blockade is not expected in this regime.

Fig.[6.5a] shows the transport response $I(V_{sd})$ of a LTQD and Fig.[6.5b] shows the steady state occupation probability of the four spin-3/2 states as functions of

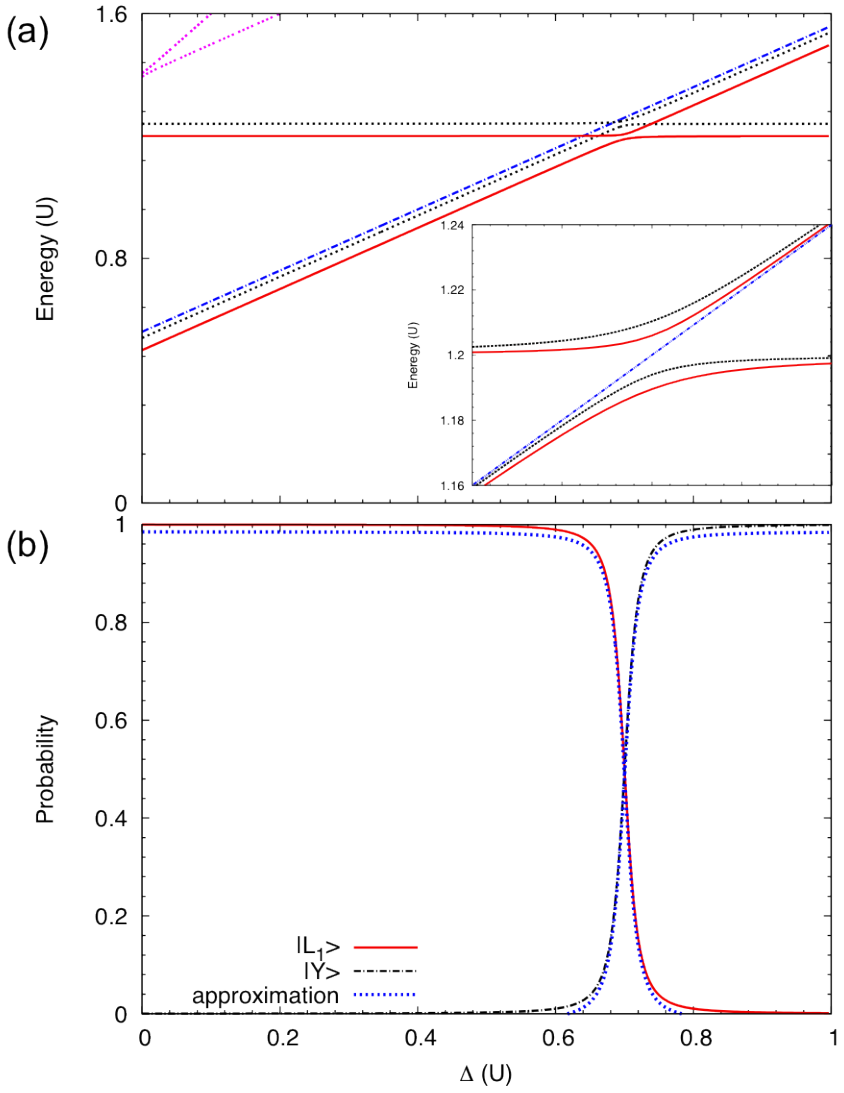

Figure 6.4: (a) The energy spectrum of a single-band Hubbard model with three electron in the $S_y = 1/2$ subspace. As Δ increases, the five levels converges towards the quadruple point (the anti-crossing point). The blue curve, spin-3/2 state, do not interact with the other states. In the main figures, the energy levels are artificially shifted by a constant values for better views. The inset shows the proper energy levels near the anti-crossing point. (b) shows the projection of the ground state onto $|L_1\rangle$ (the red curve) and $|Y\rangle$ (the black curve) obtained from numerical calculations. The blue-dashed lines provides the same information but obtained from the analytical approximation for $|L_1^+\rangle = \cos(\theta)\,|L_1\rangle + \sin(\theta)\,|Y\rangle$ discussed in the text.

V_{sd} . This was done without the cotunneling effect. The $I - V_{sd}$ curve is symmetrical with respect to the bias direction as it should be at SQP. The most prominent feature is that the vanishing of the current and therefore significant negative differential conductance associated with high occupation probability of the spin-3/2 states. As shown in Fig.[6.5a], the current is completely suppressed at a very limited bias regime, this is very different from the $I - V$ curve in the spin blockade regime in a DQD. These numerical results are obtained from a five-level Hubbard model, and the negative differential conductance is not reproduced when we use just the three-level Hubbard model for the transport calculation. This implies that this negative differential conductance is related to the existence of the high-energy P orbitals.

In order to explain this negative differential conductance, we need to study $S_y = 3/2$ subspace with all five orbitals. There are 10 possible configurations for three spin-up electrons in five orbitals. Using the Hubbard model with these five orbitals, the configuration with the lowest energy is $|\bar{a}\rangle = \hat{c}^{\dagger}_{1\uparrow}\hat{c}^{\dagger}_{2\uparrow}\hat{c}^{\dagger}_{3\uparrow}|0\rangle$, and the next two configurations are $\left|\bar{b}\right\rangle = \hat{c}^{\dagger}_{1\uparrow}\hat{c}^{\dagger}_{3\uparrow}\hat{c}^{\dagger}_{5\uparrow}|0\rangle$ and $|\bar{c}\rangle = \hat{c}^{\dagger}_{1\uparrow}\hat{c}^{\dagger}_{3\uparrow}\hat{c}^{\dagger}_{4\uparrow}|0\rangle$. Configuration $|\bar{a}\rangle$ is separated from $\left|\bar{b}\right\rangle$ and $|\bar{c}\rangle$ by an energy gap of $\sim U + \Delta_{sp} - \Delta$. The other 7 configurations are even further away in energy. The Hamiltonian of this low energy configuration subspace in the basis of $\{\left|\bar{b}\right\rangle, |\bar{a}\rangle, |\bar{c}\rangle\}$ is,

$$H_{3/2} = \begin{bmatrix} E_1 + 2E_3 + \Delta_{sp} + U' + 2V & -t' & 0 \\ -t' & E_1 + E_2 + E_3 + 2V' + V & -t' \\ 0 & -t' & 2E_1 + E_3 + \Delta_{sp} + U' + 2V \end{bmatrix}, \tag{6.11}$$

where E_1 and E_3 are almost identical when V_{sd} is small. This Hamiltonian matrix looks similar to the 2-electron triplet Hamiltonian, Eq.(2.28), presented in Sec.[2.2.2]

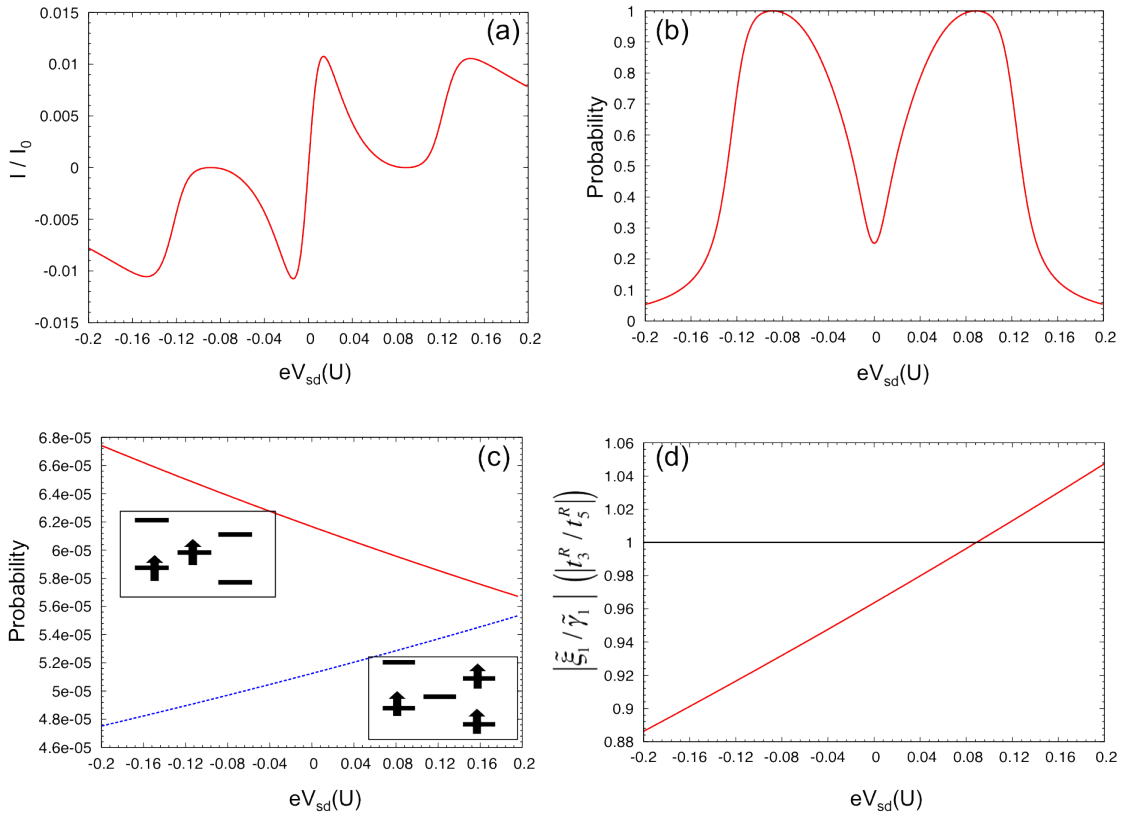

Figure 6.5: (a), the transport response $I(V_{sd})$ of a LTQD at the SQP and low source-drain bias. (b), the steady-state occupation probability of the spin-3/2 states as a function of V_{sd}. Panel (a) and (b) together indicates the spin-3/2 states are related to the bi-directional, quantum interference-based dark channel in a LTQD. (c), projection of the triplet state $|T^+\rangle$ onto the configuration $\hat{c}^\dagger_{1\uparrow}\hat{c}^\dagger_{2\uparrow}|0\rangle$, and the projection of the spin-3/2 state $|3/2\rangle$ onto the configuration $\hat{c}^\dagger_{1\uparrow}\hat{c}^\dagger_{3\uparrow}\hat{c}^\dagger_{5\uparrow}|0\rangle$. (d), Ratio of matrix elements $|\frac{\eta_1}{\gamma_1}|$ (see text for the definition) in the unit of the ratio $|\frac{t_3^R}{t_5^R}|$. Dark channel is formed when the red curve (the computed ratio) intercepts $y = 1$ line in the figure. Panel (c) and (d) are presented to illustrate the formation of the dark channel in the positive bias direction. For analyzing the dark channel in the negative bias direction, another two states, $\hat{c}^\dagger_{2\uparrow}\hat{c}^\dagger_{3\uparrow}|0\rangle$ and $\hat{c}^\dagger_{1\uparrow}\hat{c}^\dagger_{3\uparrow}\hat{c}^\dagger_{4\uparrow}|0\rangle$ should be picked for similar analysis.

with one exception: the tunneling matrix elements acquires a negative phase for the three electron system. This negative phase is simply due to the anticommutation relation between fermionic operators. Exact diagonalization of the above Hamiltonian gives a ground state,

$$|3/2\rangle = \eta\left(|\bar{a}\rangle + \frac{\eta_1}{\eta}\left|\bar{b}\right\rangle + \frac{\eta_2}{\eta}|\bar{c}\rangle\right), \tag{6.12}$$

where coefficients $\eta_{1(2)}$ are of the same order of magnitude as the coefficients $\gamma_{1(2)}$ for $|T^+\rangle$ in Eq.(6.10). This can be understood by analyzing the Hamiltonians. The energy difference between the configuration $|T_{12}\rangle$ and $|T_{13}\rangle$ is given by $|\Delta + V' - V|$. The energy difference between the configurations $\left|\bar{b}\right\rangle$ and $|\bar{a}\rangle$ is given by $|\Delta - \Delta_{sp} - U' - V + 2V'|$. Considering the fact that Δ and Δ_{sp} are both on the order of U, the two energy gaps are actually comparable. In general, hybridization of configurations $|i\rangle$ and $|j\rangle$ in a wavefunction can be estimated by the ratio $\frac{\langle i|H|j\rangle}{E_i - E_j}$. In our case, the S-P tunnel coupling t' is also on the same order of magnitude as the S-S tunnel coupling t. This explain why $\eta_{1(2)}$ are comparable to $\gamma_{1(2)}$ in magnitude. Furthermore, $\eta_{1(2)}$ have opposite signs with respect to $\gamma_{1(2)}$ because the off-diagonal matrix elements in Eq.(6.11) and Eq.(2.31) have opposite signs. Fig.[6.5c] presents the norm of γ_1 and η_1 from the exact diagonalization of the five-level Hubbard model as a function of V_{sd}.

Next, we look at the rate equation for the state $|3/2\rangle$ when the system is subject to a positive source-drain bias, i.e. charging electron from left dot but removing electron from right:

$$\frac{dP_{3/2}}{dt} = -W_R^{seq}(3/2 \to T^+)P_{3/2} + W_L^{seq}(T^+ \to 3/2)P_{T^+}\ . \tag{6.13}$$

Note that the only allowed 2-electron state is T^+ because the total spin cannot change by more than 1/2 by adding an electron. The phonon relaxation does not play a role

here because $|3/2\rangle$ and $|T^+\rangle$ are the lowest energy states in their own spin-resolved subspaces, respectively. For simplicity, we have ignored the cotunneling contribution in this analysis, but numerical results in Fig.[6.5] are also obtained without the cotunneling terms. In order for $|3/2\rangle$ to be a trap state, the outgoing part of the rate equation should be almost equal to zero. The outgoing sequential rate is, approximately,

$$\begin{aligned} W_R^{seq}(3/2 \to T^+) &= \frac{2\pi}{\hbar} \sum_k \left| \langle T^+|\tilde{t}_3^R(k)\hat{c}_{3\uparrow}|3/2\rangle + \langle T^+|\tilde{t}_5^R(k)\hat{c}_{5\uparrow}|3/2\rangle \right|^2 \\ &\quad \times \delta(E_{3/2} - E_{T^+} - \epsilon_{kR})(1 - f_R), \\ &= \frac{2\pi}{\hbar} \sum_k \left| \left(|\gamma_1|t_3^R - |\eta_1|t_5^R\right) \frac{e^{-ika}}{\sqrt{2\pi}} \right|^2 \delta(E_{3/2} - E_{T^+} - \epsilon_{kR})(1 - f_R), \end{aligned} \tag{6.14}$$

where $\tilde{t}_i^R(k) = t_i^R e^{-ika}/\sqrt{2\pi}$ and f_R is the fermi function for the right lead. The coefficients γ_1 and η_1 are defined in Eq.(6.10) and Eq.(6.12), respectively. The expression $\left(|\gamma_1|t_3^R - |\eta_1|t_5^R\right)$ gives the interference between the two possible paths of removing an electron (via the S and P orbital) from the right dot. The minus sign in the expression stem from the fact that η_1 and γ_1 have opposite signs, and the origin of this sign difference was already explained immediately following the Eq.(6.11). We see that the condition for the quenching of the sequential tunneling rate is $|\gamma_1/\eta_1| = |t_5^R/t_3^R|$. Fig.[6.5d] presents the ratio $|\gamma_1/\eta_1|$ as a function of V_{sd}. At points of strongest current suppression, we observe that the ratio indeed matches the ratio of $|t_5^R/t_3^R|$. In short, the negative differential conductance sets in whenever the two possible paths of electronic transport become comparable in amplitude and interferes destructively. This destructive interference is possible only for the transport channels through spin-3/2

states. In terms of spin configurations, the transport channel $|3/2\rangle \rightarrow |T^+\rangle$ involves the two paths $(\uparrow_1, \uparrow_2, \uparrow_3) \rightarrow (\uparrow_1, \uparrow_2)$ and $(\uparrow_1, \uparrow_3, \uparrow_5) \rightarrow (\uparrow_1, \uparrow_3)$, which can destructively interfere. For all other transport channels, electronic transport occurs with much higher probability amplitude via the S orbital in the edge dots at low source-drain bias. The existence of the dark channel through $|3/2\rangle$ makes the TQD molecule trapped in $|3/2\rangle$ state.

Fig.[6.6a, b] show the current through the LTQD and the steady state probability distribution for the spin-3/2 states in the parameter space of $(E_1 = E_3, E_2)$ at a small bias, $eV_{sd} = 0.01\ U$, respectively . In this calculation, the cotunneling effect is included. Although the quantum interference-based spin blockade is formed under a very specific condition, Fig.[6.6b] shows that the interference-based spin blockade can still be observed in the parameter space of on-site energies. The cotunneling effects can be analyzed when we add terms $\sum_{r=L,R}\sum_{\beta_3} W_r^{cot}(\beta_3 \rightarrow 3/2)P^{\beta_3} - \sum_{r=L,R}\sum_{\beta_3} W_r^{cot}(3/2 \rightarrow \beta_3)P^{3/2}$, where $|\beta_3\rangle$ is a three-electron state with $S = 1/2$, to Eq.(6.13). In Eq.(6.14), we analyze the condition for the transition rate from $|3/2\rangle$ to $|T^+\rangle$ to vanish. With cotunneling included in the model, we should analyze the condition for the transition rate from $|3/2\rangle$ to each $|\beta_3\rangle$ state to vanish. In principle, each transport channel has its unique condition for the quenching, and the interference-based quantum spin blockade will be lifted if not all channels are quenched. However, the additional rates due to cotunneling are much smaller in amplitude as they scale with $|t_1^L|^4$ for the second order processes. The system still gets blockaded in the spin-3/2 state when the sequential tunneling driven transition $(W_R^{seq}(3/2 \rightarrow T^+))$ vanishes, because the incoming rate $W_L^{seq}(T^+ \rightarrow 3/2)$, a first order

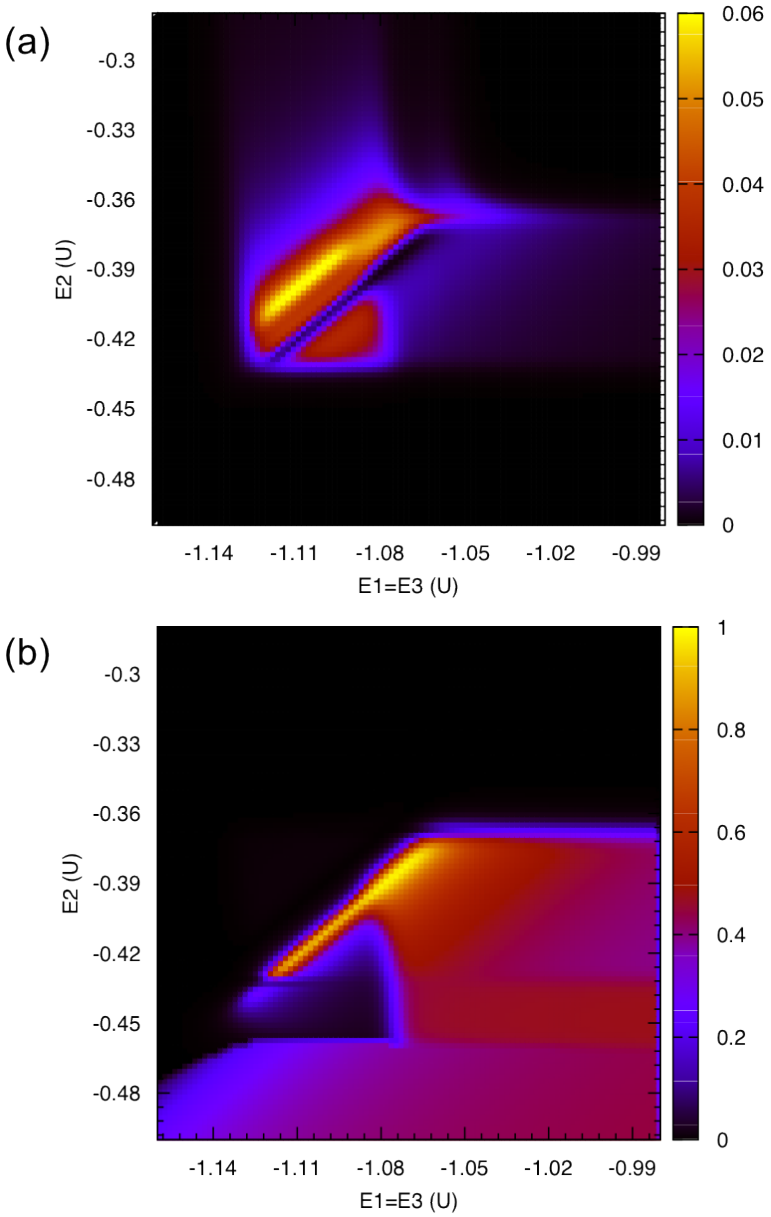

Figure 6.6: (a), the transport response of the LTQD in the parameter space of ($E_1 = E_3, E_2$). The transport region manifests a rounded boundary, which indicate the states involves in the electronic transport are highly hybridized states. The transport region is separated into two parts by a thin line of strong current suppression. This is the region of dark channels. (b), the steady-state occupation probability for spin-3/2 states. High amount of spin-3/2 states are found exactly where the currents vanishes in Panel (a).

process, scales with $|t_1^L|^2$ and is around 5 orders of magnitude larger than by the rates driven by cotunneling processes.

6.4.2 Symmetrical and Asymmetrical Spin Blockade

Next, we look at the SQP again with a different single-particle level spacing, $\Delta_{sp} = 0.25$ U. In this case, we will consider a wider range of source-drain bias with $eV_{sd} > U$. Fig.[6.7a] shows the transport response, $I(V_{sd})$, of the TQD near the SQP. We again have a symmetric $I(V_{sd})$ relation with respect to the bias directions and, therefore, the observed negative differential conductance is also bi-directional. We will focus on the positive bias direction for the following discussion. We note that there are 2 regions where the current is strongly suppressed in the positive bias direction in Fig.[6.7a]. One point is at the low bias regime, $eV_{sd} \ll U$, and the other point is at the high bias regime such that on-site triplet occupation is allowed in the transport window. From Fig.[6.7b], we see that the system is trapped in $(1, 1, 1)$ spin 3/2 states whenever the current is significantly suppressed in Fig.[6.7a]. The strong current suppression at the low bias is due to the quantum interference-based spin blockade we described in the previous section. As source-drain bias is further increased, the wavefunction inside the LTQD also change. Gradually one path of electronic transport become preferred and the likelihood of quantum interference vanishes. At the high bias, the second current suppression is identified to be the more familiar spin blockade phenomenon in the double quantum dot, and it is characterized by an extended region of current suppression over a wider range of source-drain bias in Fig.[6.7b]. At high bias, hybridization of levels become insignificant, and it is instructive to look at

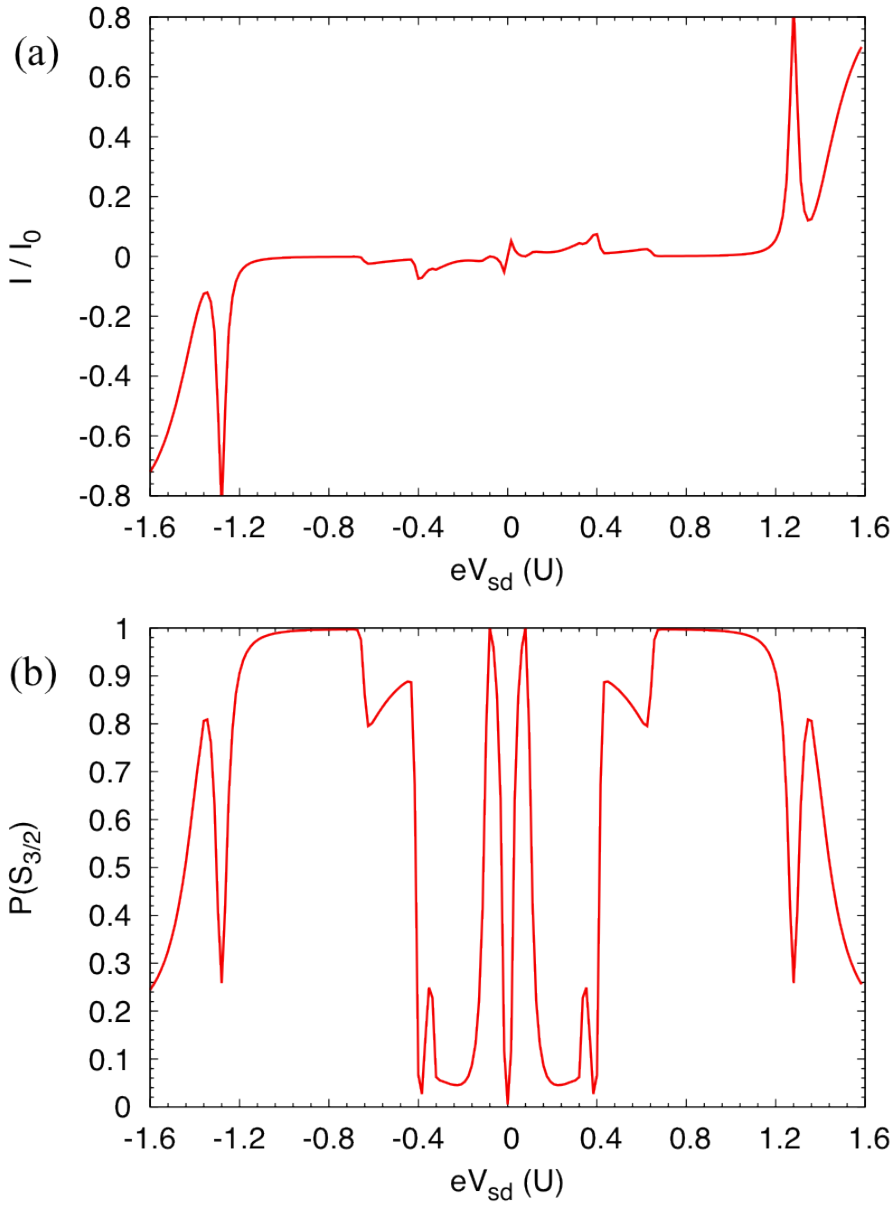

Figure 6.7: (a), the transport response of the LTQD at SQP as a function of V_{sd}. At high bias (in both bias direction), we observe a robust negative differential conductance. (b), the steady-state occupation probability for spin-3/2 states. The peaks near the low- the figure Indeed, the current suppression is associated with the spin-3/2 states. The much more extended current suppression is due to the spin blockade phenomenon.

each eigenstate as a particular localized configuration. Fig.[6.8] presents a detailed schematics of how this high bias spin blockade is formed and lifted in the linear TQD at high bias. The spin blockade is formed when the on-site triplet becomes accessible in the left dot but not in the right dot in the transport window when a positive bias is applied. Due to the phonon-induced relaxation, the on-site triplet in the left dot will relax by allowing electron-phonon scattering to re-distribute the electron from the P orbital on the edge dot onto the S orbital in the central dot. When the on-site triplet state in the right dot is still too high in energy for occupation, the system gets stuck in this $(1,1,1)$ spin-3/2 configuration. This spin blockade is lifted when the bias is further increased so the on-site triplet become accessible in the right dot too. Then the phonon-induced relaxation will again help transfer the electron from the central dot onto the right dot. We remark that the spin blockade does not happen in this model if the phonon-induced relaxation mechanism is removed. From this picture, we can derive the spin blockade regime from the parameters we used. The energies of the relevant configurations are

$$\begin{aligned}
E(\uparrow_1\uparrow_3) &= E_1 + E_3 + V' = -2.1U \ , \\
E(\uparrow_1\uparrow_3\uparrow_4) &= 2E_1 + \Delta_{sp} + E_3 + U' + 2V' + \frac{eV_{sd}}{6} = -1.91U + \frac{eV_{sd}}{6} \ , \\
E(\uparrow_1\uparrow_2\uparrow_3) &= E_1 + E_2 + E_3 + 2V = -2.1U \ , \\
E(\uparrow_1\uparrow_3\uparrow_5) &= E_1 + 2E_3 + \Delta_{sp} + U' + 2V' - \frac{eV_{sd}}{6} = -1.91U - \frac{eV_{sd}}{6} \ .
\end{aligned}$$

For an electron to move from the left lead to the TQD, $E(\uparrow_1\uparrow_3)+\epsilon_e$=$E(\uparrow_1\uparrow_3\uparrow_4)$ for an electron energy $\varepsilon_e \leq \mu_L = eV_{sd}/2$. Thus, we get $eV_{sd} \geq 0.57U$. $E(\uparrow_1\uparrow_2\uparrow_3)$ is always lower than $E(\uparrow_1\uparrow_3\uparrow_4)$ for forward bias, so the relaxation from $|\uparrow_1\uparrow_3\uparrow_4\rangle$ to $|\uparrow_1\uparrow_2\uparrow_3\rangle$ is allowed. For the spin blockade to occur, the transition from $|\uparrow_1\uparrow_2\uparrow_3\rangle$ to $|\uparrow_1\uparrow_3\uparrow_4\rangle$

should not be possible by phonon emission. So, $E(\uparrow_1\uparrow_2\uparrow_3) < E(\uparrow_1\uparrow_3\uparrow_5)$, which leads to $eV_{sd} < 1.14U$. Therefore, the spin blockade regime is $0.57U \leq eV_{sd} < 1.14U$, which agrees very well with the numerical result in Fig.[6.7a].

Next we consider the transport response of the linear TQD at the AQP: (011), (012), (021), and (111). We again use a five-level Hubbard Hamiltonian for transport calculation. We put a S orbital in the left dot, and a S and P orbitals in the central dot and the right dot. In weak tunnel coupling limit, the 4 charge configurations should be on resonance, and we set $E_1 = -V - V'$ and $E_2 = E_3 = -U - V$. Fig.[6.9a] show the $I(V_{sd})$ of the TQD near the AQP. As expected, the transport response of the TQD near the AQP is very different under the two bias directions. Fig.[6.9b] confirms the spin blockade where the current is severely suppressed in the positive bias direction in Fig.[6.9a]. This phenomenon is in close analogy with the case of a DQD, and can be easily explained. In the positive bias, electron is injected from the left dot. The transition from $(0,1,1)$ triplet to a $(1,1,1)$ spin 3/2 state does not require the formation of on-site triplet. In the negative bias direction, electron is injected from the right and transition from $(0,1,1)$ triplet state to a spin 3/2 state require the formation of an on-site triplet in the right dot. Therefore, before the bias threshold $\mu_R^* = E(0,1,2^*) - E(0,1,1)$, no spin blockade is expected to be formed. $(0,1,2^*)$ represent a charge configuration in which one of the electrons occupies the P orbital in dot 3. When the applied bias exceeds the threshold, the condition $E(0,1,2^*) \geq E(0,2^*,1) \geq E(1,1,1)$ is also satisfied. Thus, either due to resonant tunneling or inelastic process, this additional electron can always be removed from the right lead. Therefore, there is no spin blockade in the negative bias direction. We

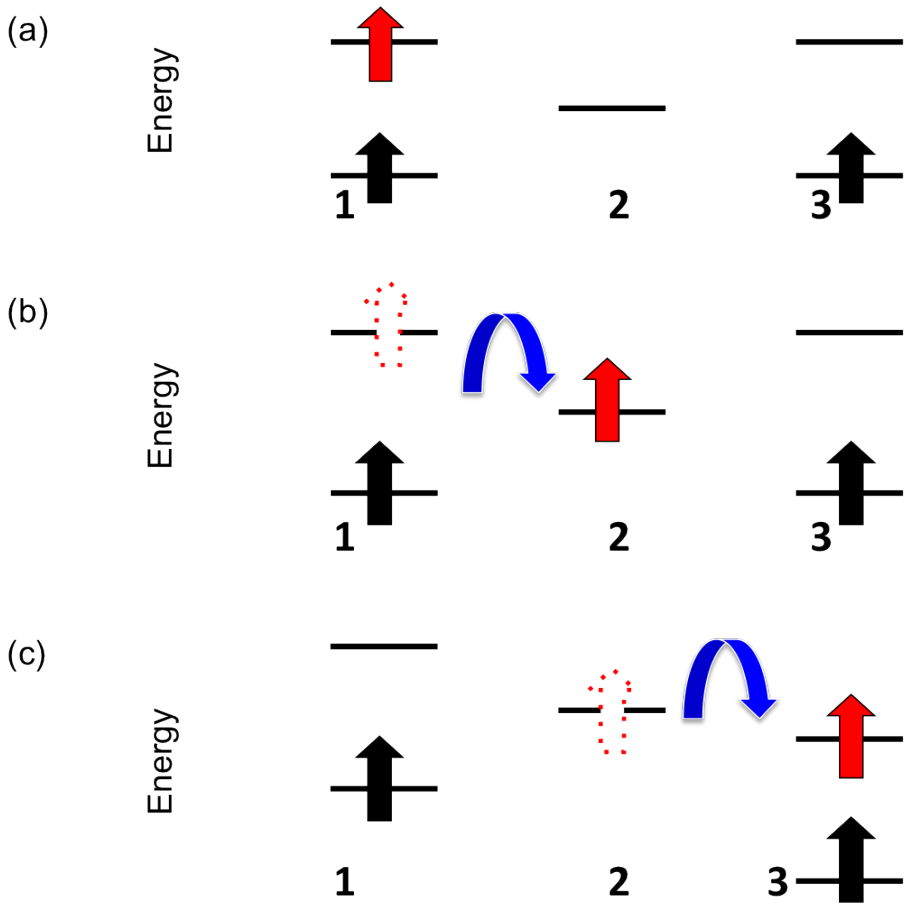

Figure 6.8: (a), an (1,0,2) configuration obtained from the (1,0,1) configuration when an additional electron is charged onto the P orbital of dot 1. Due to phonon-induced relaxation in the model, the added spins moves from P orbitals in dot 1 to the S orbital in dot 2. However, it does not proceed further to the dot 3 because this will cost energy. (c) At larger source-drain bias in the positive direction, the energy levels in dot 3 is lowered with respect to that of dot 2. Thus, phonon-induced relaxation assist the electron to move onto dot 2.

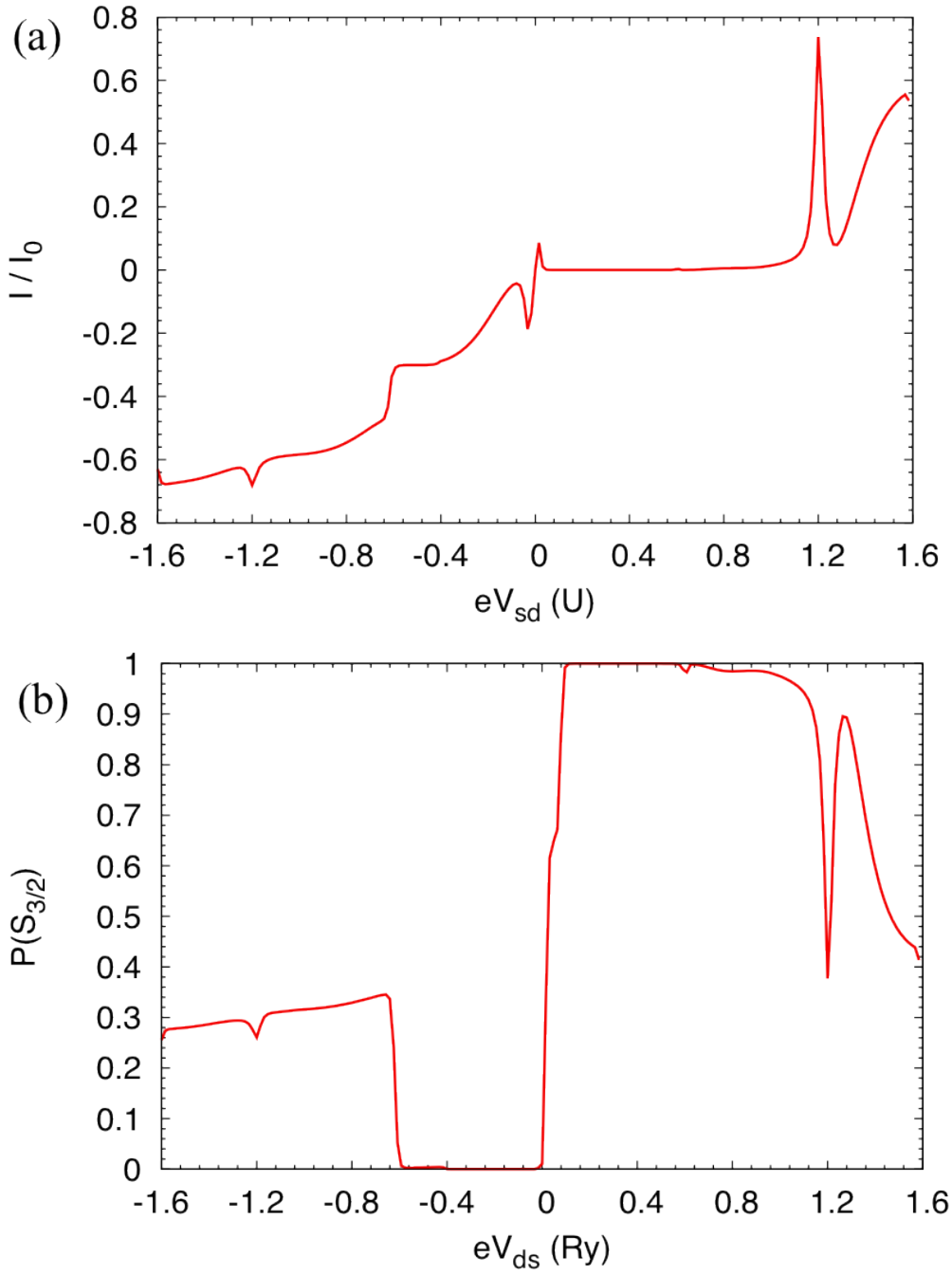

Figure 6.9: (a), the transport response of the LTQD at AQP as a function of V_{sd}. The electronic transport manifest asymmetrical response with respect to the bias direction. Similar to a DQD, current suppression is only observed in one direction of the bias. (b), the steady-state occupation probability for spin-3/2 states. The current suppression is associated with the spin-3/2 states.

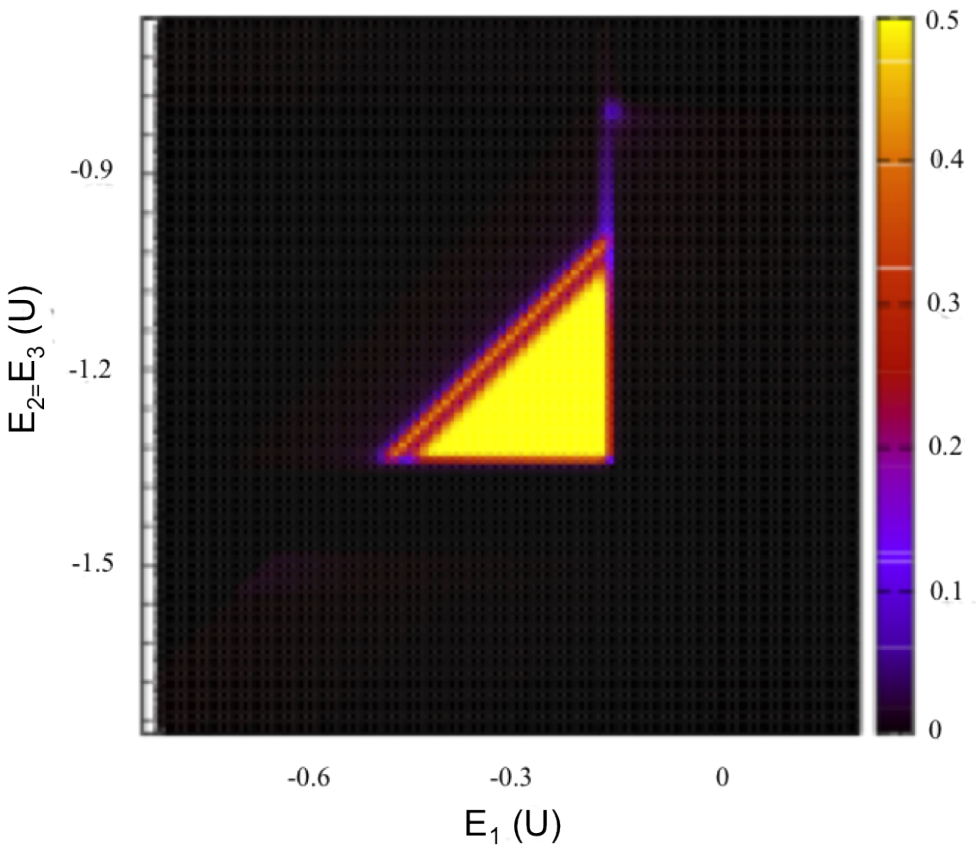

Figure 6.10: The transport response of the LTQD at AQP in the parameter space $(E_1, E_2 = E_3)$.

remark that the spin blockade at AQP can be formed without the assistance of any relaxation mechanism. So the spin blockade of a TQD at AQP is almost identical to the spin blockade in a DQD. Fig.[6.10] presents the transport triangle in the parameter space $(E_1, E_2 = E_3)$ at a positive bias. In this figure, the light trail at the tip of the triangle is proportional to the on-site singlet-triplet gap on the central dot. This transport triangle, although generated under the specific condition $E_2 = E_3$, provides similar information that one can extract from the transport triangle for the DQD.

6.5 Conclusion

We presented a theory of electronic properties and transport through a linear triple quantum dot with one electron spin each. We show that the spin blockade can serve as a spectroscopic tool for the detection of different spin states. Two different QPs containing the $(1,1,1)$ configuration were discussed. A multi-band Hubbard model with five levels was used to describe the electronic properties and investigate the spin blockade phenomenon in a LTQD. For both QPs, strong current suppression and negative differential conductance was predicted. At the SQP, suppression in conductance was obtained under two different source-drain bias regimes. When the bias is small, the electronic transport involving spin-3/2 states takes place either via the S or P orbitals in the edge dot with comparable amplitude and results in a destructive interference. In high bias regime where electron tunnels onto the P orbital in the edge dot, spin blockade is facilitated by spin-conserving relaxation mechanisms, such as interaction with acoustical phonons studied here, and formation of the trap state. At the SQP, the spin blockade phenomenon is bi-directional, in contrast with the spin blockade in a DQD. We also discussed spin blockade at the AQP. The spin blockade formation and lifting in this case is in close analogy to the DQD case. The formation of the spin blockade does not involve any on-site triplets, only the lifting of the spin blockade requires the access to the on-site triplet states in the transport window. Similar to the DQD, the spin blockade phenomenon at AQP occurs only in one of the bias directions.

Chapter 7

Valence Hole Qubit in Self-Assembled Quantum Dots

In this chapter, we present a theory of valence holes based qubits in p-doped self-assembled quantum dots within the 4-band $k \cdot p$ formalism. The two qubit levels are identified with the two chiralities of the doubly degenerate ground state. We show that single qubit operations can be implemented with static magnetic field applied along the z axis (growth direction) for $\hat{\sigma}_z$ operation and with magnetic field in the quantum dot plane, x direction, for $\hat{\sigma}_x$ operation. The coupling of two dots and hence the double qubit operations are shown to be sensitive to the orientation of the two quantum dots. For vertical qubit arrays, there exists an optimal qubit separation suitable for the voltage control of qubit-qubit interactions.

7.1 Motivation

There is currently interest in using single electron spins in quantum dots (QDs) for quantum information processing (QIP) applications [17, 18, 142, 32, 58, 59]. In $III-V$ semiconductor quantum dots, such as $GaAs$, spins of conduction band electrons couple to nuclear spins of the host material and suffer decoherence due to hyperfine interactions. However, valence hole states are built from atomic p-type orbitals, which are expected to minimize the hyperfine interaction between the hole and surrounding nuclear spins [143]. The spin of a valence hole as a qubit is expected to have longer coherence time. A theory of heavy holes as qubits has been developed in the single band approximation [143, 144, 145]. The justification for the use of the heavy hole single band approximation is that strain and QD confinement suppress the coupling between heavy hole (HH) and light hole (LH) bands. Under such an assumption, the qubit levels are defined by the $J_z = +3/2$ and $J_z = -3/2$ HH states.

In such a model, the exchange coupling J needed to generate entanglement between spins of two holes is proportional to t^2/U, where t is the tunneling strength of the hole and U is the on-site Coulomb energy. However, recent theoretical [146] and experimental [147] work show that in two vertically coupled disk-like QDs the spin orbit (SO) coupling between HH and LH bands changes the sign of the effective tunneling matrix element t as a function of inter-dot distance. If the inter-dot distance is smaller than a critical value, the hole state is mainly symmetric. However, if the inter-dot distance passes the critical value, the hole state is mainly antisymmetric. These results suggest that a description of an array of hole-based qubits requires taking into account the hole tunneling between dots with SO coupling between HH

and LH bands. The theory of valence holes in quantum dots with strong SO coupling has been developed already [148, 149, 150, 151, 152, 153]. In this theory hole spin is strongly coupled to orbital motion and valence hole states are treated as Luttinger spinors. The two HH ground states are replaced by two Luttinger spinors [152] with different chiralities.

In this chapter, we develop a theory of qubits based on the chirality of the valence hole-based Luttinger spinors. We are particularly interested in square-like self-assembled quantum dots grown on nanotemplates [51] , which due to scalable architecture may lead to quantum information processing devices. We start with a single hole confined in an isolated QD. We explicitly define the qubit as two chirality states of Luttinger spinor and show how to perform single qubit operations. Our theory reproduces results obtained earlier by Kyrychenko and Kossut [153]. Next, we investigate the tunneling of a valence hole in two orientations of two coupled square QDs as illustrated in Fig.[7.1]. The tunneling barriers for vertically coupled quantum dots (VCQDs) and laterally coupled quantum dots (LCQDs) are modelled as finite potential wells, as shown in Fig.[7.1]. The tunnel barrier strength is characterized by the band-offset between the dot and the barrier material. For VCQDs, we verify the results [147] obtained for disk quantum dots showing the reversal of ground state character from symmetric to antisymmetric as a function of inter-dot distance. Close to the reversal, the vanishing of tunneling of a Luttinger spinor hole in VCQDs allows the benefit of strong confinement defined by growth with the possibility to control tunneling and hence double qubit operations using additional metallic gates.

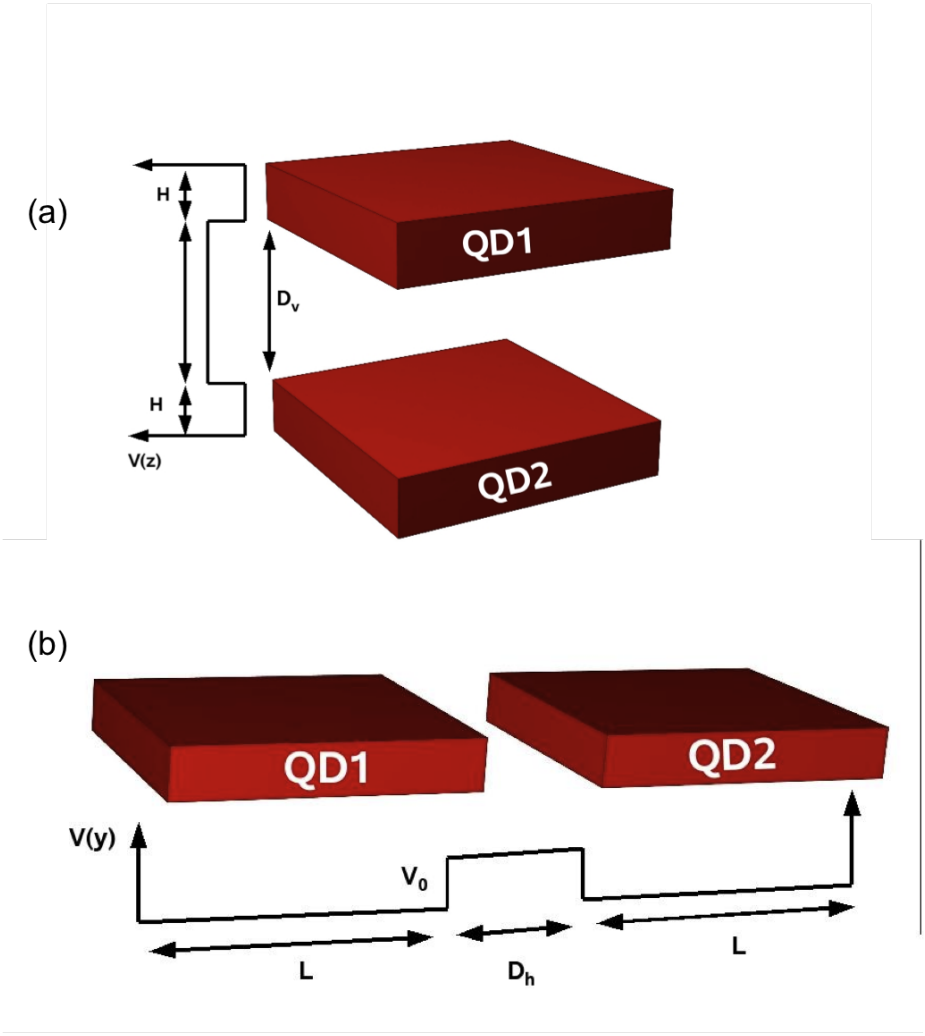

Figure 7.1: Schematics of (a) square vertically coupled quantum dots (VCQDs) of side lengths L=20nm and height H=2nm separated by a potential barrier V_0 of width D_v along the vertical direction. (b) Square laterally coupled quantum dots (LCQDs) of same side lengths L, height H separated by a potential barrier V_0 of width D_h along the horizontal direction.

7.2 Model

Following Ref. [152] , we expand the wavefunction of a valence hole confined to a nanostructure defined by confining potential $V(\mathbf{r})$ in terms of $J_z = 3/2, -1/2, 1/2, -3/2$ Bloch basis functions. The 4-band Luttinger Kohn (LK) Hamiltonian [154] reads,

$$\hat{H}_{LK} = \begin{pmatrix} \hat{P}^+ & \hat{R} & -\hat{S} & 0 \\ \hat{R}^* & \hat{P}^- & 0 & \hat{S} \\ -\hat{S}^* & 0 & \hat{P}^- & \hat{R} \\ 0 & \hat{S}^* & \hat{R}^* & \hat{P}^+ \end{pmatrix} + V(\mathbf{r})\mathbf{I} + \kappa\Omega\mathbf{J}\cdot\hat{\mathbf{B}}, \tag{7.1}$$

where $\mathbf{I}$ is the identity matrix, $\hbar$ is Planck's constant, $\Omega = \hbar eB/m_0c$ is the cyclotron energy, and κ is a material parameter. $V(\mathbf{r})$ represents a 3D infinite potential well in case of a single QD in this study. The operator $\mathbf{J}$ is the angular momentum operator for spin 3/2 particle defined in Ref. [154]. The operators in Eq.(7.1) are defined as follows

$$\begin{aligned} \hat{P}^+ &= \frac{\hbar^2}{2m_0}[(\gamma_1+\gamma_2)({\Pi_x}^2+{\Pi_y}^2)+(\gamma_1-2\gamma_2){\Pi_z}^2], \\ \hat{P}^- &= \frac{\hbar^2}{2m_0}[(\gamma_1-\gamma_2)({\Pi_x}^2+{\Pi_y}^2)+(\gamma_1+2\gamma_2){\Pi_z}^2], \\ \hat{R} &= \frac{\hbar^2}{2m_0}(-\sqrt{3})\gamma_{23}{\Pi_-}^2, \\ \hat{S} &= \frac{\hbar^2}{2m_0}(2\sqrt{3})\gamma_3\Pi_-\Pi_z, \end{aligned} \tag{7.2}$$

where $\gamma_{1,2,3}$ represent the Luttinger material parameters, $\gamma_{23} = (\gamma_2+\gamma_3)/2$, $\Pi_a = k_a - (e/c\hbar)\,(\mathbf{A})_a$, $k_a = -i\frac{\partial}{\partial a}$, $a = x, y, z$, and $k_- = k_x - ik_y$. For this study, we choose InGaAs/GaAs QDs. The InGaAs Luttinger material parameters are $\gamma_1 = 11.01$, $\gamma_2 = 4.18$, and $\gamma_3 = 4.84$. The subscript 0 means no external field in this study.

The LK Hamiltonian in Eq.(7.1) exhibits several symmetries that we use to characterize the Luttinger spinors (the eigenstates of the LK Hamiltonian). The confining potential along the z direction is symmetric with respect to the origin defined in the middle of the structure; yet, due to spin-orbit coupling between different bands, our system does not have definite parity symmetry along the z direction but the time reversal symmetry of the system demands the two HH bands have opposite parity. The same also holds for LH bands. This allows us to define the chirality operator [152, 146] which reads,

$$\hat{\chi}_z = \begin{pmatrix} \hat{i}_z & 0 & 0 & 0 \\ 0 & \hat{i}_z & 0 & 0 \\ 0 & 0 & -\hat{i}_z & 0 \\ 0 & 0 & 0 & -\hat{i}_z \end{pmatrix}, \tag{7.3}$$

where $\hat{i}_z$ is the inversion operator with respect to the z variable. The $\hat{\chi}_z$ operator has 2 eigenvalues, which we denote by $\uparrow$, and $\downarrow$. In the case of $\chi_z = \uparrow$, the Luttinger spinors have even parity with respect to z for the first two components of the spinor and odd parity with respect to z for the last two components of the spinor. In the case of $\chi_z = \downarrow$, the parity pattern is reversed between the first two and last two components of the spinor. Furthermore, square QDs also have parity symmetry in the $x-y$ plane, and we may define another parity operator $\hat{\chi}_{xy}$ analogous to the $\hat{\chi}_z$ by replacing $\hat{i}_z$ with $\hat{i}_x\hat{i}_y$ on the diagonal terms in Eq.(7.3), where $\hat{i}_x$ and $\hat{i}_y$ are inversion operators along the x and the y direction respectively. Arguments for the $\hat{\chi}_z$ operator also apply to the $\hat{\chi}_{xy}$ operator. The only difference is that the $\hat{R}$ operator in Eq.(7.2) involves $(k_-)^2$ term which prevents further separation of x and y variables. Again, $\hat{\chi}_{xy}$ has 2 eigenvalues denoted by $\chi_{xy} = +1$ and $\chi_{xy} = -1$. For $\chi_{xy} = +1$, the first

two components of the spinor must have the same parity with respect to x and y, and the last two components of the spinor must have opposite parity with respect to x and y. For $\chi_{xy} = -1$, the Luttinger spinors again have the parity pattern switched between the first two and last two components.

The 4-band valence hole spinors in a square QD have well defined structures. The Bloch function part of the Luttinger spinors is determined by the lattice symmetries; while the envelope function part of Luttinger spinors is obtained from Eq.(7.1). In our analysis, we expand the envelope function of the Luttinger spinors in eigenstates of the 3D infinite potential well of the size of our computational box. As mentioned, the chirality and the $x-y$ parity symmetries allow us to label Luttinger spinors by χ_z, χ_{xy}, and N, which index the N^{th} eigenstate of subspace χ_z and χ_{xy}. For instance, the N^{th} state of the subspace $\chi_z =\uparrow$ and $\chi_{xy} = +1$ reads

$$|\uparrow, +1, N\rangle = \sum_{\substack{n+m=2p-1 \\ n'+m'=2p}} \begin{pmatrix} C_{nm1}^{\uparrow,+1,N,3/2}\xi_n(x)\xi_m(y)\cos\left(\frac{\pi z}{W_z}\right)|\frac{3}{2}\rangle \\ C_{nm1}^{\uparrow,+1,N,-1/2}\xi_n(x)\xi_m(y)\cos\left(\frac{\pi z}{W_z}\right)|-\frac{1}{2}\rangle \\ C_{n'm'2}^{\uparrow,+1,N,1/2}\xi_{n'}(x)\xi_{m'}(y)\sin\left(\frac{2\pi z}{W_z}\right)|\frac{1}{2}\rangle \\ C_{n'm'2}^{\uparrow,+1,N,-3/2}\xi_{n'}(x)\xi_{m'}(y)\sin\left(\frac{2\pi z}{W_z}\right)|-\frac{3}{2}\rangle \end{pmatrix}, \tag{7.4}$$

where $p = 1, 2, 3, ...$ are positive integers. $C_{nml}^{\chi_z,\chi_{xy},N,J_z}$ represents the coefficient for the envelope function of a specific component $|J_z\rangle$ of Luttinger spinors. In our study, we assume that the confinement along the z direction is strong, so we only need to consider the first 2 eigenfunctions of the 1D infinite potential well in this direction. $\xi_{s_r}(r) = \sqrt{\frac{2}{W_r}}\cos\left(\frac{s_r\pi r}{W_r}\right)$ if s_r is odd and $\sqrt{\frac{2}{W_r}}\sin\left(\frac{s_r\pi r}{W_r}\right)$ if s_r is even. W_r is the computation box length along the r direction. $|J_z = \pm\frac{3}{2}, \pm\frac{1}{2}\rangle$ represents the Bloch functions [154] of zincblende structure with the total angular momentum projection

J_z. The other Luttinger spinors have distinguishable parity patterns derived from Eq.(7.4) by switching either the parity pattern with respect to the $x-y$ variable or the z variable between first two and last two components of the spinor.

From here onwards, the Luttinger spinor is written with the components corresponding to the Bloch functions in the order $J_z = 3/2, -1/2, +1/2, -3/2$ as done in Eq.(7.4), and we will no longer explicitly write out the Bloch functions $|J_z\rangle$.

7.3 Hole states in single quantum dot

In this analysis, we take the entire Luttinger spinor as a representation of valence hole state confined in the quantum dots as opposed to adopting the HH single band approximation [143, 144]. Due to the time reversal symmetry, we have a doubly degenerate ground state with distinct chirality at zero field. We encode the qubit with the chirality, χ_z, of the ground state Luttinger spinors. We show that static magnetic fields applied along the z and the x direction indeed act as $\hat{\sigma}_x$ and $\hat{\sigma}_z$ operators respectively in the qubit subspace. This result assures all the basic ingredients needed to perform arbitrary single qubit rotations.

7.3.1 Hole under B_z field

By diagonalizing the LK Hamiltonian for a square QD, we find that the 2 ground states are characterized by quantum numbers $(\chi_z = \uparrow, \chi_{xy} = -1)$ and $(\chi_z = \downarrow, \chi_{xy} = +1)$ respectively. Let us denote the state with $|\chi_z = \uparrow\rangle$ by $|1\rangle$, and the other state

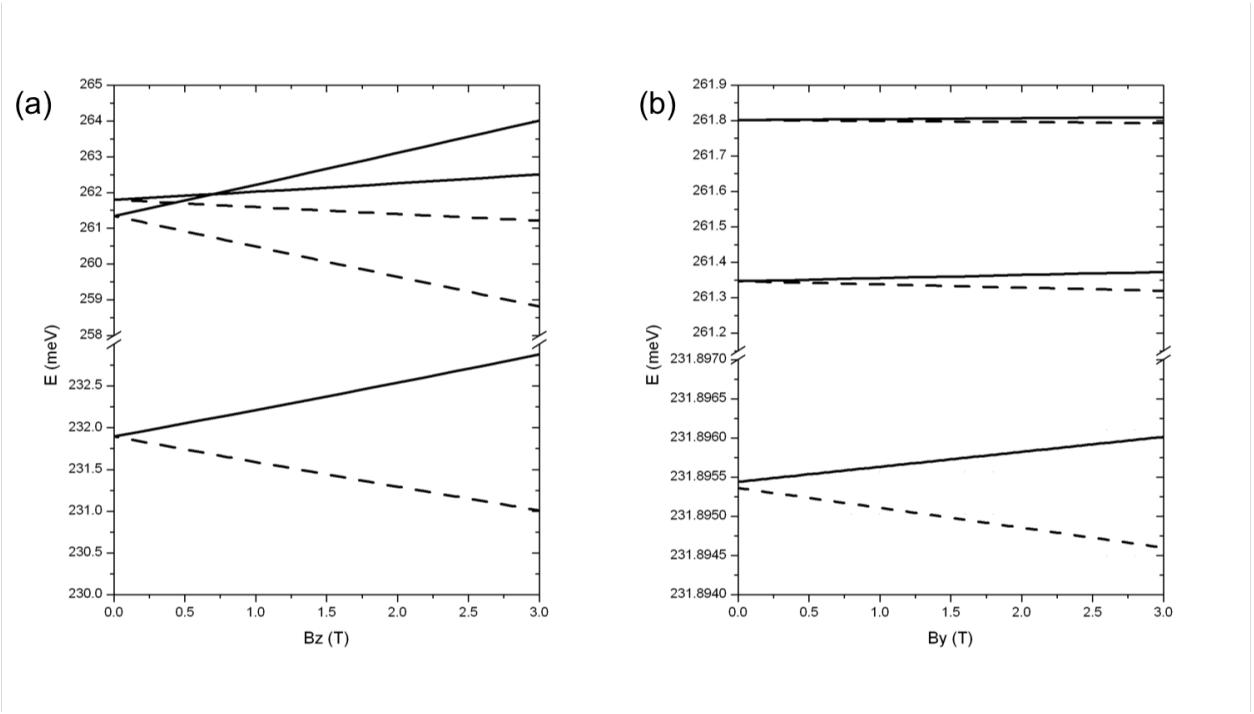

Figure 7.2: Energy levels of the 6 lowest lying hole states as a function of (a) magnetic field B_z (applied in the z direction) and (b) magnetic field B_x (applied in the x direction).

with $|\chi_z = \downarrow\rangle$ by $|0\rangle$. We give an approximate form of the envelope wave functions

$$|1\rangle = \begin{pmatrix} a\xi_1(x)\xi_1(y)\xi_1(z) \\ b\xi_2(x)\xi_2(y)\xi_1(z) \\ \left[c_1\xi_1(x)\xi_2(y) + c_2\xi_2(x)\xi_1(y)\right]\xi_2(z) \\ \left[d_1\xi_1(x)\xi_2(y) + d_2\xi_2(x)\xi_1(y)\right]\xi_2(z) \end{pmatrix}, \tag{7.5}$$

where $\xi_1(r) = \sqrt{\frac{2}{W_r}}\cos\left(\frac{\pi r}{W_r}\right)$ and $\xi_2(r) = \sqrt{\frac{2}{W_r}}\sin\left(\frac{2\pi r}{W_r}\right)$. $|0\rangle$ is obtained by applying the time reversal operator to $|1\rangle$. According to Kramer's degeneracy theorem, $|0\rangle$ will have the same set of envelope functions in Eq.(7.5) but complex conjugated and in a reversed order in the spinor. Due to the strong confinement along the z direction, the ground states of the system will contain a dominant contribution from the HH states. Therefore, the states $|0\rangle$ and $|1\rangle$ correspond to either a $+3/2$ HH or $-3/2$ HH occupying the $(1,1,1)$ orbital of a 3D infinite potential box.

To analyze the system in the presence of external field $\mathbf{B}$ in arbitrary direction, we use the gauge $\mathbf{A} = (-B_z y/2, B_z x/2, B_x y - B_y x)$. First, we consider the system under an external field B_z. Fig.[7.2a] shows the energy spectrum of a single square dot charged with one valence hole as a function of B_z. We see that the qubit subspace, the 2 lowest energy levels, are well isolated from the rest of the energy spectrum across a wide range of applied field. Due to the weak coupling between the qubit subspace and other excited states, we may treat the effects of B_z fields by the first order Löwdin perturbation theory [155], which is simply a projection of the full LK Hamiltonian into the qubit subspace. The entire LK Hamiltonian is decomposed into 2 parts: unperturbed Hamiltonian at the zero field and additional perturbing Hamiltonian due to the field. The additional Hamiltonian with external field B_z leads to $\hat{P}_1^{+(-)}$

operators of the form

$$\begin{aligned}\hat{P}_1^{+} &= \frac{\hbar^2}{2m_0}(\gamma_1+\gamma_2)\left[(\omega_z)^2(x^2+y^2)+\omega_z(xk_y-yk_x)\right],\\ \hat{P}_1^{-} &= \frac{\hbar^2}{2m_0}(\gamma_1-\gamma_2)\left[(\omega_z)^2(x^2+y^2)+\omega_z(xk_y-yk_x)\right],\end{aligned} \tag{7.6}$$

where $\omega_z = \frac{eB_z}{c\hbar}$. Whether the applied field can break the chirality symmetry $\hat{\chi}_z$ and the x-y parity symmetry $\hat{\chi}_{xy}$ depends on the commutation relations between $\hat{P}_1^{+(-)}$ operators and inversion operators $\hat{i}_z$ and $\hat{i}_x\hat{i}_y$. Since $\hat{P}_1^{+(-)}$ commute with $\hat{i}_z$, the Hamiltonian can not mix the 2 spinors of different chiralities. Indeed, when we project the Hamiltonian we find the off-diagonal matrix elements $\langle 1|\hat{H}_{LK}|0\rangle = 0$, and the diagonal matrix elements $\langle 1|\hat{H}_{LK}|1\rangle$ and $\langle 0|\hat{H}_{LK}|0\rangle$ differ only by the Zeeman energy. The diagonal matrix elements read,

$$\begin{aligned}\langle 1|\hat{H}_{LK}|1\rangle &= \kappa\Omega(|a|^2-|d_1|^2-|d_2|^2)(3/2)+\\ &\quad \kappa\Omega(-|b|^2+|c_1|^2+|c_2|^2)(1/2),\\ \langle 0|\hat{H}_{LK}|0\rangle &= -\langle 1|\hat{H}_{LK}|1\rangle,\end{aligned} \tag{7.7}$$

where the coefficients a, b, c, d are defined in Eq.(7.5). As the ground state of flat QDs has dominant contributions from HH components, typically $|a|^2 \approx 0.9$ is much greater than the magnitude of other coefficients. In HH single band approximation, one simply sets $|a| = 1$ and other coefficients to be 0.

7.3.2 Hole under B_x field

Next, we consider the system subject to a constant B_x field. Fig.[7.2b] shows the energy spectrum of a single square QD charged with one valence hole as a function of

B_x. The two qubit states are again well isolated from the rest of the energy spectrum across a wide range of B_x. Hence, we repeat the same procedure to derive an effective Hamiltonian for the qubit. The vector potential is $\mathbf{A} = (0, 0, B_x y)$ and the $\hat{P}_1^{+(-)}$ operators for the additional LK Hamiltonian with B_x field read

$$\begin{aligned} \hat{P}_1^+ &= \frac{\hbar^2}{2m_0}(\gamma_1 - 2\gamma_2)\left[(\omega_x)^2 y^2 - 2\omega_x y k_z\right], \\ \hat{P}_1^- &= \frac{\hbar^2}{2m_0}(\gamma_1 + 2\gamma_2)\left[(\omega_x)^2 y^2 - 2\omega_x y k_z\right], \end{aligned} \tag{7.8}$$

where $\omega_x = \frac{eB_x}{c\hbar}$. We find that the diagonal matrix elements $\langle 1|\hat{H}_{LK}|1\rangle = \langle 0|\hat{H}_{LK}|0\rangle$, and the off-diagonal matrix elements are given by

$$\begin{aligned} \langle 1|\hat{H}_{LK}|0\rangle &= \langle g^{-3/2}|\hat{P}_1^+|g^{3/2}\rangle + \langle g^{3/2}|\hat{P}_1^+|g^{-3/2}\rangle + \\ &\quad \langle g^{-1/2}|\hat{P}_1^-|g^{1/2}\rangle + \langle g^{1/2}|\hat{P}_1^-|g^{-1/2}\rangle - \\ &\quad \langle g^{-1/2}|\hat{S}^*|g^{3/2}\rangle + \langle g^{3/2}|\hat{S}^*|g^{-1/2}\rangle - \\ &\quad \langle g^{-3/2}|\hat{S}|g^{1/2}\rangle + \langle g^{1/2}|\hat{S}|g^{-3/2}\rangle, \\ &\approx \Omega_x(\gamma_1 - 2\gamma_2)\frac{W_y}{W_z} Im(d_1^* a). \end{aligned} \tag{7.9}$$

where $\Omega_x = \hbar e B_x/mc$. $|g^i\rangle$ stands for the envelope function of the i hole states in Eq.(7.5), for instance, $\langle \mathbf{r}|g^{3/2}\rangle = a\xi_1(x)\xi_1(y)\xi_1(z)$. The matrix elements $\langle g^{-3/2}|\hat{P}_1^+|g^{3/2}\rangle$ do not suggest coupling of +3/2 HH and -3/2 HH. Rather, it actually represents the coupling of a chirality up ($\chi_z = \uparrow$) +3/2 HH with a chirality down ($\chi_z = \downarrow$) +3/2 HH. Due to time reversal symmetry, the chirality down +3/2 HH must have the same envelope function as the chirality up -3/2 HH. Similar argument applies to all other matrix elements in Eq.(7.9). We further remark that the off-diagonal matrix element contains pairs of complex conjugates; thus, the matrix element is real-valued.

The mixing of the qubit states is due to the simultaneous breaking of the parity symmetry in the $x-y$ plane and the inversion symmetry along the z direction; for instance, we refer to the term yk_z in both $\hat{P}_1^+$ and $\hat{P}_1^-$ operators in Eq.(7.8) as responsible for the breaking of symmetries. The fact that we may couple the qubit states by static fields is in contradiction to analysis done in the HH single band approximation [144]. In HH single band approximation, the single qubit operation cannot be done by electron spin resonance (ESR) techniques because the magnetic field cannot couple two HH states (in the leading dipole approximation). More sophisticated techniques such as electric dipole spin resonance (EDSR) are needed. However, in our proposal, we define qubit states with the entire Luttinger spinor, which is an admixture of all HHs and LHs, and the mixing of the two qubit states is due to the coupling between the two Luttinger spinors as manifested in Eq.(7.9).

The $\hat{\sigma}_z$ operator for our proposed Luttinger spinor based qubit is essentially driven by the Zeeman energy; whereas the $\hat{\sigma}_x$ operator is based on the mixing of valence hole components by vector potential $\mathbf{A}$ and SO coupling. Due to the different mechanisms of how the 2 qubit states are operated on by B_z and B_x field, the effective g factor (for a simple spin in an external field) seems to have much stronger transverse component [156], $g_\perp >> g_{//}$. Hence it takes more time to perform a spin flip process with the Luttinger spinor based qubit. We will characterize the single qubit operating time with the $\hbar/\Delta E_{gap}$, where ΔE_{gap} is the energy difference between ground and first excited state under B_x field. From Fig.[7.2b], we see the characteristic time is around 1.5 ns when $B_x = 1T$. However, modulating the strain of the host material can relax the QD confinement along the z direction, induce a stronger planar component of the

g factors and improve the single qubit operating time.

Finally, we remark that the Luttinger spinor based qubits are susceptible to the same channels of decoherence that are already discussed for valence hole confined in QDs in Refs. [145, 157, 158, 159]. However, electric field fluctuation in the background of the host material will not affect the Luttinger spinor based qubits. As the electric field induced dipole transitions, $\langle\psi_j|e\mathbf{E}(t)\cdot\mathbf{r}|\psi_i\rangle$, conserve the time reversal symmetry, the two qubit states, which are Kramers doublets, will not be mixed.

7.4 Hole states in coupled quantum dots

We now turn to the analysis of double qubit operations with the Luttinger spinors based qubits. Our proposal for double qubit operations with the valence holes-based qubits relies on the following assumptions. First, we consider 2 valence holes localized in two different QDs in the weak tunneling limit and only the on-site Coulomb interaction is taken into account. Second, we consider that each QD only contains the two relevant qubit states. Under these assumptions, the hole-hole interacting Hamiltonian in second quantization reads [152]

$$\begin{aligned} H_{2h} &= \sum_{j,p} \epsilon_{jp} c^{\dagger}_{jp} c_{jp} + \sum_{j} t \left(c^{\dagger}_{jp'} c_{jp} + c^{\dagger}_{jp} c_{jp'} \right) \\ &+ \frac{1}{2} \sum_{\substack{j_{1p}, j_{2p} \\ j_{3p}, j_{4p} \\ p}} U_{j_{1p} j_{2p} j_{3p} j_{4p}} c^{\dagger}_{j_{1p}} c^{\dagger}_{j_{2p}} c_{j_{3p}} c_{j_{4p}}, \end{aligned} \tag{7.10}$$

where p are indices for QD number 1 and 2, $p \neq p'$, ϵ_{jp} is the energy of valence hole state $|j\rangle$ on the $p-th$ dot, t is the tunneling parameter between QDs, and $U_{j_1 j_2 j_3 j_4}$ is the on-site Coulomb interaction, with the matrix elements given in the appendix.

This Hamiltonian can be greatly simplified because the Coulomb interaction conserves the chirality of 2 holes in the following manner: (a) if $\chi_{z_1} = \chi_{z_2}$ and $\chi_{z_3} = \chi_{z_4}$, $U_{j_1 j_2 j_3 j_4} = U_c$, (b) if $\chi_{z_1} \neq \chi_{z_2}$ and $\chi_{z_3} \neq \chi_{z_4}$, $U_{j_1 j_2 j_3 j_4} = U_x$, (c) if just one of the valence holes switches chirality, U = 0. Taking also into account that we only consider 2 states of distinct chirality on each QD, the on-site Coulomb interactions term in Eq.(7.10) reduces to [152]

$$U = \frac{1}{2}\left(U_c + U_x\right)\hat{n}_j \hat{n}_{j'}, \tag{7.11}$$

where $\hat{n}_{j(j')}$ is the number operator, and j, j' represents the 2 chirality states on a QD. Different from electron spins, the on-site Coulomb interaction between valence holes is composed of a direct Coulomb term U_c and an exchange term U_x which enhances the overall interaction. However, apart from this difference, once we have parameterized the tunneling parameter t and U, we have the Hubbard Hamiltonian. In the strong Coulomb regime, the interaction between 2 localized particles in the Hubbard model can be reduced to two spins with the Heisenberg exchange constants J proportional to t^2/U.

An interesting phenomenon [147] associated with valence holes is the possibility of engineering t to be either positive, zero or negative in a stack of vertically coupled cylindrical QDs by simply tuning the inter-dot distance. As the exchange coupling between 2 qubits is directly proportional to t^2, this implies qubit-qubit interactions can be turned on and off as needed. We would like to investigate whether the similar phenomenon will happen with square QDs stacked either in a vertical or lateral structure.

To estimate the magnitude of t, we rely on a tight-binding picture in which a

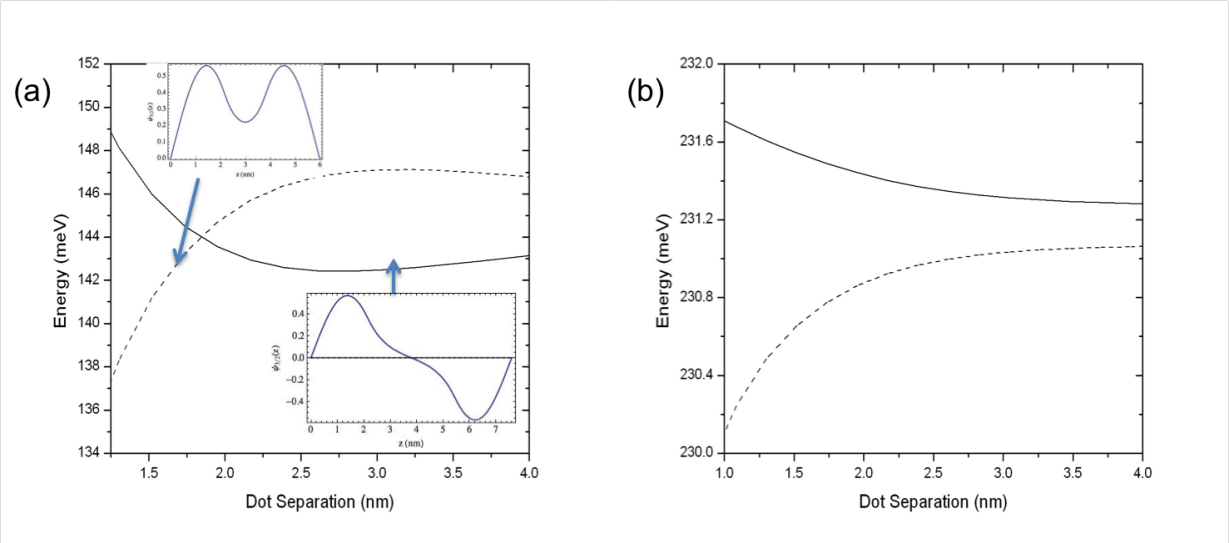

Figure 7.3: Energy levels of the two lowest hole states as a function of the inter-dot distance in: (a) VCQDs (vertically coupled quantum dots) and (b) LCQDs (laterally coupled quantum dots). The critical distance at which the tunneling element is zero occurs around 1.8 nm in (a). The solid curve represents $\chi_z = \uparrow$ state and the dashed curve represents the $\chi_z = \downarrow$ state. Inset: The dominant heavy hole component of the ground state before and after the crossing.

valence hole tunnels between the two dots and the hybridization of local orbitals gives a symmetric state, $1/\sqrt{2}(|1\rangle + |2\rangle)$ with energy $E_0 - t$ and an antisymmetric state, $1/\sqrt{2}(|1\rangle - |2\rangle)$ with energy $E_0 + t$. Thus, the energy gap between first excited state and ground state is $2t$. We compute the energy spectrum of a single valence hole in a double QD by exact diagonalizing Eq.(7.1), then extract the value of t from the calculated energy gap.

7.4.1 Hole states in vertically coupled quantum dots

The potential $V(\mathbf{r})$ of VCQDs is modeled with an infinite potential well along the x and the y direction and double well potential profile along the z direction. In the barrier region between the dots, we set a constant finite potential of 320 meV

corresponding to the band offset between InGaAs and GaAs, same as reported in Ref. [146], so we may draw a comparison between square-like and disk-like dots.

As shown in Fig.[7.3a], the lowest energy levels of different chirality subspaces cross at a certain inter-dot distance. The insets of Fig.[7.3a] present the most dominant HH wavefunction profile along the z direction of the ground state before and after the crossing point. The wavefunction plots show the reversal of symmetry for the ground state of the system. Similar phenomenon occurs in both square and disk dots. These results confirm that the effects of HH and LH mixing is insensitive to the confining potential in the $x - y$ plane. These results also imply that we can shut down any undesirable hole - hole interaction between holes localized in different dots if the inter-dot distance is chosen at the point where the crossing occurs in Fig.[7.3a].

7.4.2 Hole states in laterally coupled quantum dots

The potential of LCQDs is modeled similar to that of VCQDs except that the double well potential profile lies along the y direction. Our result, Fig.[7.3b], shows no crossing of lowest energy states from distinct chirality subspaces. We understand that the confinement strength along the z direction plays a crucial role in determining how much HH and LH bands mix, because QDs are quasi-two dimensional devices with a much smaller dimension along the z direction. In the case of VCQDs, the coupled dots relax significantly the confinement strength of the hole states along the z direction and bring the LH and HH energies closer. However, a LCQDs structure relaxes confinement strength in the $x - y$ plane which does not facilitate the mixing of HH and LH states. Hence no reversal of the ground state as a function of the

distance is observed.

7.5 Conclusion

In summary, we consider the Luttinger spinor description of confined valence hole states in QDs. We identify the two qubit levels with two chiralities of the lowest energy Kramers doublet and suggest that B_z and B_x fields act analogously to the $\hat{\sigma}_z$ and $\hat{\sigma}_x$ operators. For arrays of hole qubits, we study tunneling of holes in vertical and lateral architecture as the mechanism facilitating the qubit-qubit interaction. We show that tunneling can be arrested for vertical pairs of quantum dots but not for lateral architecture. The capability to switch the sign of the effective tunneling t in VCQDs is demonstrated. This suggests the possibility of turning off the exchange interaction. With such exchange interaction being very small one can envisage tuning this interaction with additional metallic gates.

Chapter 8

Conclusion

In this thesis, we have presented studies of electronic and spin properties of quantum dots. The detailed knowledge of how these properties depend on external fields and gates help us to manipulate these nanostructures for potential quantum information storage and processing. Furthermore, we derive low energy effective Hamiltonians for quantum dots because quantum information processing involves only a few states in the device. Effective Hamiltonians provide the benefits of a simpler view of the physical system, and makes the connection between model of quantum circuit and the physical system more transparent. The rest of this chapter presents a summary of the key points in each of the previous chapters.

In Chapter [2], we presented a detailed analysis of the electronic and spin properties of triple quantum dot as a function of number of electrons, bias on the central dot, topology, and magnetic field. A 4-electron triangular triple quantum dot undergoes triplet-singlet transitions under biasing of the central dot. This unique feature leads to the proposal of an artificial spin-1 chain discussed in Ref. [132] and Chapter [4].

A triangular TQD undergoes Aharonov-Bohm oscillations in the presence of a magnetic flux. With $N_e = 2$ / 4, the system undergoes periodic singlet-triplet transition (triplet-singlet transition) until the Zeeman energy takes over and prefers a polarized ground state. At half-filled, the chiral states also undergoes oscillations but with a much smaller amplitude.

In Chapter [3], we showed that a half-filled triple quantum dot can indeed be used as a coded qubit, originally proposed by DiVincenzo et. al. [25]. We laid out all the necessary ingredients for a chirality-based coded qubit by providing the details of preparations, initializations, and coherent operations of coded qubits in triple quantum dot molecules. We derived an effective qubit-qubit interaction assuming the form of Ising interaction. We also studied the robustness of the coded qubit against fluctuating charged impurity induced decoherence, and found the coded qubit has a long coherence time in the presence of electrostatic noise.

In Chapter [4], we showed the emergence of macroscopic quantum states in a chain of triple quantum dot molecules, each is charged with four electrons (or two holes). The electrons localized in the molecules realize a spin-half Heisenberg chain with spin-spin interactions alternating between ferromagnetic and anti-ferromagnetic. When ferromagnetic interaction is much stronger than the anti-ferromagnetic interaction, the system can be viewed as an artificial spin-1 chain studied by Haldane. As the size of the chain increases, the system develops a large energy gap, also known as Haldane gap, which isolates a few states from the rest of the spectrum. These few isolated states are very robust and may be used for quantum information processing.

In Chapter [5], we showed how to generate and measure Berry's phase with a

generalized Herzberg's circuit in a triangular triple quantum dot.

In Chapter [6], we presented a theory of sequential tunneling and spin blockade in a linear triple quantum dot at 2 different quadruple points: symmetric quadruple point and asymmetric quadruple point. At the symmetric quadruple point, the system is trapped in a quantum interference-based spin blockade. At the high bias, we find that the spin blockade is symmetric with respect to bias direction, and the spin blockade is facilitated by some spin-conserving relaxation mechanism such as interaction with phonons. At asymmetric quadruple point, the spin blockade phenomenon in a triple quantum dot is similar to the spin blockade phenomenon in a double quantum dot.

In Chapter [7], we presented a theory of valence hole-based qubit within the 4-band $k{\cdot}p$ formalism. The qubit was represented with Luttinger Kohn spinor containing both heavy hole and light hole components. We showed that single qubit operations can be implemented with static magnetic field applied along the z axis (growth direction) for $\hat{\sigma}_z$ operation and with magnetic field in the quantum dot plane, x direction, for $\hat{\sigma}_x$ operation. The tunneling of the valence hole qubit is sensitive to the orientation of how two quantum dots are coupled. When two quantum dots are coupled in the vertical direction (also growth direction), there exists an optimal qubit separation suitable for the voltage control of qubit-qubit interactions.

Bibliography

[1] R. P. Feynman, International Journal of Theoretical Physics **21**, 467 (1982).

[2] S. Wiesner, Sigact News **15**, 78 (1983).

[3] C. H. Bennett, F. Bessette, B. G., S. L., and S. J., **5**, 3 (1992).

[4] C. H. Bennett, G. Brassard, C. Crépeau, and M.-H. Skubiszewska, in *Proceedings of the 11th Annual International Cryptology Conference on Advances in Cryptology* (Springer-Verlag, London, UK, 1992), CRYPTO '91, pp. 351–366, ISBN 3-540-55188-3.

[5] G. Brassard, C. Crepeau, R. Jozsa, and D. Langlois, in *Proceedings of 34th Annual Symposium on Foundations of Computer Science* (IEEE Computer Society, 1993), pp. 362–371.

[6] D. Deutsch, Proc. R. Soc. London Ser. A **400**, 97 (1985).

[7] D. P. DiVincenzo, Science **270**, 255 (1995).

[8] P. W. Shor, SIAM Review **41**, 303 (1999).

[9] L. K. Grover, in *Proceedings of the twenty-eighth annual ACM symposium on Theory of computing* (ACM, New York, NY, USA, 1996), STOC '96, pp. 212–219.

[10] D. P. DiVincenzo, Fortschr. Phys. **48**, 771 (2000).

[11] A. M. Steane, Phys. Rev. Lett. **77**, 793 (1995).

[12] A. M. Steane, Proc. Roy. Soc. Lond. A **452**, 2551 (1996).

[13] P. Shor, in *Proceedings of the Symposium on the Foundations of Computer Science* (IEEE, Press, Los Alamitos, CA, 1996).

[14] P. Shor, Phys. Rev. A **52**, 2493 (1995).

[15] A. Panos and A. W. Cross, Phys. Rev. Lett. **98**, 220502 (2007).

[16] L. I. Chuang, L. M. K. Vandersypen, X. Zhou, L. D. W., and S. Lloyd, Nature **393**, 143 (1998).

[17] J. A. Brum and P. Hawrylak, Superlattices Microstruct. **22**, 431 (1997).

[18] D. Loss and D. P. DiVincenzo, Phys. Rev. A **57**, 120 (1998).

[19] M. Bayer, P. Hawrylak, K. Hinzer, S. Fafard, M. Korkusinski, Z. R. Wasilewski, O. Stern, and A. Forchel, Science **291**, 451 (2001).

[20] G. Burkard, D. Loss, and D. P. DiVincenzo, Nature **393**, 133 (1998).

[21] M. Pioro-Ladrière, T. Obata, Y. Tokura, Y. S. Shin, T. Kubo, K. Yoshida, T. Taniyama, and S. Tarucha, Nat Phys **4**, 776 (2008).

[22] K. C. Nowack, F. H. L. Koppens, Y. V. Nazarov, and L. M. K. Vandersypen, Science **318**, 1430 (2007).

[23] E. Laird, C.Barthel, E.I.Rashba, C.M.Marcus, M.P.Hanson, and A.C.Gossard, Phys. Rev. Lett. **99** (2007).

[24] J. Levy, Phys. Rev. Lett. **89**, 147902 (2002).

[25] D. DiVincenzo, D. Bacon, J. Kempe, and G. Burkard, Nature **408**, 339 (2000).

[26] D. Bacon, J. Kempe, D. A. Lidar, and K. B. Whaley, Phys. Rev. Lett. **85**, 1758 (2000).

[27] P. Hawrylak and M. Korkusinski, Solid State Commun. **136**, 508 (2005).

[28] D. Bimberg, M. Grundmann, and N. N. Ledentsov, *"Quantum Dot Heterostructures"* (Wiley, New York, 1999).

[29] T. Chakraborty, Comments Condes. Matter Phys. **16**, 35 (1992).

[30] M. A. Kastner, Phys. Today **46**, 23 (1993).

[31] L. Jacak, P. Hawrylak, and A. Wojs, *Quantum Dots* (Springer-Verlag, Berlin, 1998).

[32] R. Hanson, L. P. Kouwenhoven, J. R. Petta, S. Tarucha, and L. Vandersypen, Rev. Mod. Phys. **79**, 1217 (2007).

[33] W. G. van der Wiel, S. De Franceschi, J. M. Elzerman, T. Fujisawa, S. Tarucha, and L. P. Kouwenhoven, Rev. Mod. Phys. **75**, 1 (2002).

[34] L. P. Kouwenhoven, D. G. Austing, and S. Tarucha, Rep. Prog. Phys. **64**, 701 (2001).

[35] L. P. Kouwenhoven, T. H. Oosterkamp, M. W. S. Danoesastro, M. Eto, D. G. Austing, T. Honda, and S. Tarucha, Science **278**, 1788 (1997).

[36] M. Korkusinski, I. P. Gimenez, P. Hawrylak, L. Gaudreau, S. Studenikin, and A. Sachrajda, Phys. Rev. B **75** (2007).

[37] M. Korkusinski, *"Correlations in semiconductor quantum dots"* (Ph.D. Dissertation, University of Ottawa, 2004).

[38] R. Hanson, *"Electron spins in semiconductor quantum dots"* (Ph.D. Dissertation, Delft, 2005).

[39] Y. P. Shim, F. Delgado, and P. Hawrylak, Phys. Rev. B **80**, 115305 (2009).

[40] M. Ciorga, A. S. Sachrajda, P. Hawrylak, C. Gould, P. Zawadzki, S. Jullian, Y. Feng, and Z. Wasilewski, Phys. Rev. B **61**, R16315 (2000).

[41] A. C. Johnson, J. R. Petta, C. M. Marcus, M. P. Hanson, and A. C. Gossard, Phys. Rev. B **72**, 165308 (2005).

[42] L. Gaudreau, A. Kam, G. Granger, S. A. Studenikin, P. Zawadzki, and A. S. Sachrajda, Appl. Phys. Lett. **95**, 193101 (2009).

[43] M. Field, C. G. Smith, M. Pepper, D. A. Ritchie, and J. E. F. Frost, Phys. Rev. Lett. **70**, 1311 (1993).

[44] D. Sprinzak, Y. Ji, M. Heiblum, D. Mahalu, and H. Shtrikman, Phys. Rev. Lett. **88**, 176805 (2002).

[45] J. M. Elzerman, R. Hanson, J. S. Greidanus, L. H. Willems van Beveren, S. De Franceschi, L. M. K. Vandersypen, S. Tarucha, and L. P. Kouwenhoven, Phys. Rev. B **67**, 161308 (2003).

[46] K. Ono, D. G. Austing, Y. Tokura, and S. Tarucha, Science **297**, 1313 (2002).

[47] C. López-Monís, J. Iñarrea, and G. Platero, New J. Phys. **13**, 053010 (2011).

[48] G. M., J. J. Krich, J. M. Taylor, H. Bluhm, B. I. Halperin, C. M. Marcus, M. Stopa, A. Yacoby, and M. D. Lukin, Phys. Rev. Lett. **104**, 226807 (2010).

[49] J. Baugh, Y. Kitamura, K. Ono, and T. S., Phys. Rev. Lett. **99**, 096804 (2007).

[50] G. Granger, L. Gaudreau, A. Kam, and M. Pioro-Ladrière, Phys. Rev. B **82**, 075304 (2010).

[51] M. Reimer, W. McKinnon, J. Lapointe, D. Dalacu, P. J. Poole, G. C. Aers, D. Kim, M. Korkusinski, P. Hawrylak, and R. L. Williams, Physica E **40**, 1790 (2007).

[52] R. L. William, G. C. Aers, P. J. Poole, J. Lefebvre, and D. Chithranti, Physica E **13**, 1200 (2002).

[53] C. H. Bennett, G. Brassard, C. Crepeau, R. Jozsa, A. Peres, and W. Wootters, Phys. Rev. Lett. **70**, 1895 (1993).

[54] M. Reimann, Stephanie and M. Manninen, Rev. Mod. Phys. **74**, 1283 (2002).

[55] A. Greentree, J. Cole, A. Hamilton, and L. Hollenberg, Phys. Rev. B **70**, 235317 (2004).

[56] C. Emary, Phys. Rev. B **76**, 245319 (2007).

[57] F. Delgado, Y. P. Shim, M. Korkusinski, and P. Hawrylak, Phys. Rev. B **76** (2007).

[58] A. Sachrajda, P. Hawrylak, and M. Ciorga, *Nano-spintronics with lateral quantum dots* ("Electronic Transport in Quantum Dots", ed. by J. P. Bird, Kluwer Academic Publishers, Boston, 2003).

[59] M. Korkusinski and P. Hawrylak, *Coded qubits based on electron spins* (in book "Semiconductor quantum bits", ed. by O. Benson and F. Henneberger, World Scientific, 2008).

[60] R. Hanson, B. Witkamp, L. Vandersypen, and L. K. L.H. Willems van Beveren, J.M. Elzerman, Phys. Rev. Lett **91**, 196802 (2003).

[61] F. Koppens, C. Buizert, K. Tielrooij, and I. Vink, Nature **442**, 766 (2006).

[62] M. Ladrière, Y. Tokura, T. Obata, T. Kubo, and S. Tarucha, Appl. Phys. Lett. **90** (2007).

[63] Y. S. Weinstein and C. S. Hellberg, Phys. Rev. A **72**, 022319 (2005).

[64] B. Georgeot and F. Mila, arXiv:0902.4652v1.

[65] M. Trif, F. Troiani, D. Stepanenko, and D. Loss, Phys. Rev. Lett. **101**, 217201 (2008).

[66] L. Viola, E. M. Fortunato, M. A. Pravia, E. Knill, R. Laflamme, and D. G. Cory, Science **293**, 2059 (2001).

[67] D. A. Lidar and K. B. Whaley, *Decoherence-Free Subspaces and Subsystems* (in book "Irreversible Quantum Dynamics", ed. by F. Benatti and R. Floreanini, Springer, 2003).

[68] I. P. Gimenez, C. Y. Hsieh, M. Korkusinski, and P. Hawrylak, Phys. Rev. B **79**, 205311 (2009).

[69] A. M. Lobos and A. A. Aligia, Phys. Rev. B **74**, 165417 (2006).

[70] Y. Avishai, T. Kuzmenko, and K. Kikoin, Physica E **29**, 334 (2005).

[71] K. Ingersent, A. Ludwig, and I. Affleck, Phys. Rev. Lett. **95**, 257204 (2005).

[72] M. Eibl, N. Kiesel, M. Bourennane, C. Kurtsiefer, and H. Weinfurter, Phys. Rev. Lett. **92**, 077901 (2004).

[73] S. Ghosh, G. Kar, A. Roy, D. Sarkar, and U. Sen, New Journal of Physics **4**, 48 (2002), URL `http://stacks.iop.org/1367-2630/4/48`.

[74] B. Röthlisberger, J. Lehmann, D. Saraga, P. Traber, and D. Loss, Phys. Rev. Lett. **100**, 100502 (2008).

[75] I. P. Gimenez, M. Korkusinski, and P. Hawrylak, Phys. Rev. B **76**, 075336 (2007).

[76] V. Dobrovitski, A. Feiguin, D. Awschalom, and R. Hanson, Phys. Rev. B **77**, 245212 (2008).

[77] W. Witzel and S. Das Sarma, Phys. Rev. B **74**, 35322 (2006).

[78] W. Coish and D. Loss, Phys. Rev. B **70**, 195340 (2004).

[79] W. Yao, R.-B. Liu, and L. Sham, Phys. Rev. B **74**, 195301 (2006).

[80] X. G. Wen, F. Wilczek, and A. Zee, Phys. Rev. B **39**, 11413 (1989).

[81] E. Fradkin, *Field Theories of Condensed Matter Systems* (Addison-Wesley, 1991).

[82] G. Tatara and N. Garcia, Phys. Rev. Lett. **91**, 076806 (2003).

[83] L. N. Bulaevskii, C. D. Batista, M. V. Mostovoy, and D. I. Khomskii, Phys. Rev. B. **78**, 024402 (2008).

[84] V. Scarola, K. Park, and S. Sarma, Phys. Rev. Lett. **93**, 120503 (2004).

[85] V. Scarola and S. Das Sarma, Phys. Rev. A **71**, 032340 (2005).

[86] Y. Makhlin, Quantum Information Processing **1**, 243 (2002).

[87] L. M. K. Vandersypen and I. L. Chuang, Rev. Mod. Phys. **76**, 1037 (2005).

[88] M. A. Nielsen and I. L. Chuang, *Quantum Computation and Quantum Information* (Cambridge University Press, 2000).

[89] H.-J. Cao and L. Hu, Phys. Lett. A **72**, 2971 (2008).

[90] J. Elzerman, R. Hanson, L. Willems van Beveren, B. Witkamp, L. Vandersypen, and L. Kouwenhoven, Nature **430**, 431 (2004).

[91] L. Gaudreau, S. Studenikin, A. Sachrajda, P. Zawadzki, A. Kam, J. Lapointe, M. Korkusinski, and P. Hawrylak, Phys. Rev. Lett. **97**, 036807 (2006).

[92] D. Schröer, A. Greentree, L. Gaudreau, K. Eberl, L. Hollenberg, J. Kotthaus, and S. Ludwig, Phys. Rev. B **76**, 075306 (2007).

[93] E. Laird, J. Taylor, D. DiVincenzo, C. Marcus, M. Hanson, and A. Gossard, Phys. Rev. B **82** (2010).

[94] J. Petta, A. Johnson, J. Taylor, E. Laird, A. Yacoby, M. D. Lukin, C. M. Marcus, and M. P. Hanson, Science **309**, 2180 (2005).

[95] M. Pioro-Ladriere, J. H. Davies, A. R. Long, A. S. Sachrajda, L. Gaudreau, P. Zawadzki, and J. Lapointe, Phys. Rev. B **72**, 115331 (2005).

[96] V. Pokrovsky and N. Sinitsyn, Phys. Rev. B **69**, 10414 (2004).

[97] I. A. Merkulov, A. L. Efros, and M. Rosen, Phys. Rev. B **65**, 205309 (2002).

[98] J. M. Taylor, J. R. Petta, A. C. Johnson, A. Yacoby, C. M. Marcus, and M. D. Lukin, Phys. Rev. B **76**, 035315 (2007).

[99] W. Zhang, N. Konstantinidis, K. A. Al-Hassanieh, and V. V. Dobrovitski, J. Phys.: Condens. Matter **19**, 083202 (2007).

[100] F. D. Haldane, Phys. Lett. **93A**, 464 (1983).

[101] I. Afflect, T. Kennedy, E. H. Lieb, and H. Tasaki, Phys. Rev. Lett. **59**, 799 (1987).

[102] I. Affleck, T. Kennedy, E. H. Lieb, and H. Tasaki, Commun. Math. Phys. **115**, 477 (1988).

[103] M. P. Nightingale and H. W. J. Blöte, Phys. Rev. B **33**, 659 (1986).

[104] S. R. White, Phys. Rev. Lett. **69**, 2863 (1992).

[105] S. R. White and D. A. Huse, Phys. Rev. B **48**, 3844 (1993).

[106] S. R. White and I. Afflect, Phys. Rev. B **77**, 134437 (2008).

[107] W. J. L. Buyers, R. M. Morra, R. L. Armstrong, M. J. Hogan, P. Gerlach, and K. Hirakawa, Phys. Rev. Lett. **56**, 371 (1986).

[108] R. M. Morra, W. J. L. Buyers, R. L. Armstrong, and K. Hirakawa, Phys. Rev. B **38**, 543 (1988).

[109] E. Čižmár, M. Ozerov, O. Ignatchik, T. P. Papageorgiou, J. Wosnitza, S. A. Zvyagin, J. Krzystek, Z. Zhou, C. Landee, B. R. Landry, et al., New Journal of Physics **10**, 33008 (2008).

[110] Y.-P. Shim and P. Hawrylak, Phys. Rev. B **78**, 165317 (2008).

[111] K. Hida, Phys. Rev. B **45**, 2207 (1992).

[112] H. H. Hung and D. C. Gong, Phys. Rev. B **71**, 54413 (2005).

[113] A. Stathopouos and J. R. McCombs, SIAM J. Sci. Comput. **29**, 2162 (2007).

[114] D. S. Fisher, Phys. Rev. B **50**, 3799 (1994).

[115] R. A. Hyman and Y. K., Phys. Rev. Lett. **78**, 1783 (1997).

[116] A. Saguia and B. Boechat, Phys. Rev. Lett. **89**, 117202 (2002).

[117] G. Herzberg and H. Longuet-Higgins, Discuss. Faraday Soc. **35**, 77 (1963).

[118] M. Berry and F. R. S, Proc. R. Soc. Lond. A **392**, 45 (1984).

[119] A. C. Carollo and V. Vedral, *Holonomic Quantum Computation* (Wiley-VCH Verlag GmbH, 2008), pp. 381–387.

[120] P. Jiannis, Z. Paolo, and R. Mario, Phys. Rev. A **61**, 010305 (2000).

[121] J. A. Jones, V. Vedral, A. Ekert, and G. Castagnoli, Nature **403**, 1 (2000).

[122] P. J. Leek, J. M. Fink, A. Blais, R. Bianchetti, M. Göppl, J. M. Gambetta, D. I. Schuster, L. Frunzio, R. J. Schoelkopf, and A. Wallraff, Science **318**, 1889 (2007).

[123] M. Möttönen, J. Vartiainen, and J. Pekola, Phys. Rev. Lett. **100**, 177201 (2008).

[124] M. Aunola and J. Toppari, Phys. Rev. B **68**, 020502(R) (2003).

[125] J. P. Pekola, J. J. Toppari, M. Aunola, M. T. Savolainen, and D. V. Averin, Phys. Rev. B **60**, R9931 (1999).

[126] G. Falci, R. Fazio, G. M. Palma, J. Siewert, and V. Vedral, Nature **407**, 355 (2000).

[127] C.-Y. Hsieh and P. Hawrylak, Phys. Rev. B **82**, 205311 (2010).

[128] M. Berry and M. Wilkinson, Proc. R. Soc. Lond. A **392**, 16 (1984).

[129] P. Hawrylak, Phys. Rev. B **60**, 5597 (1999).

[130] K. Grove-Rasmussen, H. I. Jørgensen, T. Hayashi, P. E. Lindelof, and T. Fujisawa, Nano Lett. **8**, 1055 (2008).

[131] F. Delgado, Y. Shim, M. Korkusinski, and L. Gaudreau, Phys. Rev. Lett. **101**, 226810 (2008).

[132] Y.-P. Shim, A. Sharma, C.-Y. Hsieh, and P. Hawrylak, Solid State Communications **150**, 2065 (2010).

[133] A. Sharma and P. Hawrylak, Phys. Rev. B **83**, 125311 (2011).

[134] R. Žitko and J. Bonča, Phys. Rev. Lett. **98**, 047203 (2007).

[135] A. Lobos and A. Aligia, Phys. Rev. B **74**, 165417 (2006).

[136] B. Muralidharan and S. Datta, Phys. Rev. B **76**, 035432 (2007).

[137] M. Florescu and P. Hawrylak, Phys. Rev. B **73**, 045304 (2006).

[138] J. Iñarrea, G. Platero, and A. H. MacDonald, Phys. Rev. B **76**, 085329 (2008).

[139] E. Vaz and J. Kyriakidis, J. Chem. Phys. **129**, 24703 (2008).

[140] T. Hansen, V. Mujica, and M. A. Ratner, Nano Lett. **8**, 3525 (2008).

[141] F. Qassemi, W. Coish, and F. Wilhelm, Phys. Rev. Lett. **102**, 176806 (2009).

[142] G. Burkard, D. Loss, D. P. DiVincenzo, and J. A. Smolin, Phys. Rev. B **16**, 11404 (1999).

[143] B. D. Gerardot, D. Brunner, P. A. Dalgarno, P. Öhberg, M. K. S. Seidi, K. Karrai, N. G. Stoltz, P. M. Petroff, and R. J. Warburton, Nature **451**, 441 (2007).

[144] D. V. Bulaev and D. Loss, Phys. Rev. Lett. **98**, 097202 (2007).

[145] D. V. Bulaev and D. Loss, Phys. Rev. Lett **95**, 076805 (2005).

[146] J. I. Climente, M. Korkusinski, G. Goldoni, and P. Hawrylak, Phys. Rev. B **78**, 115323 (2008).

[147] M. Doty, J. Climente, M. Korkusinski, M. Scheibner, A. Bracker, P. Hawrylak, and D. Gammon, Phys. Rev. Lett. **102**, 47401 (2009).

[148] F. B. Pedersen and Y.-C. Chang, Phys. Rev. B **53**, 1507 (1996).

[149] T. Darnhofer, U. R$\acute{}$orssler, and D. A. Broido, Phys. Rev. B **52**, 14376 (1995).

[150] D. A. Broido, A. Cros, and U. R$\acute{}$orssler, Phys. Rev. B **45**, 11395 (1992).

[151] P. C. Sercel and K. J. Vahala, Phys. Rev. B **42**, 3690 (1990).

[152] L. G. C. Rego, P. Hawrylak, and J. A. Brum, Phys. Rev. B **55**, 15694 (1997).

[153] F. V. Kyrychenko and J. Kossut, Phys. Rev. B **70**, 205317 (2004).

[154] J. M. Luttinger and W. Kohn, Phys. Rev. **97**, 869 (1955).

[155] P.-O. Löwdin, J. Chem. Phys. **19**, 1396 (1951).

[156] H. W. van Kesteren, E. C. Cosman, W. van der Poel, and C. Foxon, Phys. Rev. B **41**, 5283 (1990).

[157] L. M. Woods, T. L. Reinecke, and R. Kotlyar, Phys. Rev. B. **69**, 125330 (2004).

[158] S. Laurent, B. Eble, O. Krebs, A. Lemaitre, B. Urbaszek, X. Marie, T. Amand, and P. Voisin, Phys. Rev. Lett. **94**, 076805 (2005).

[159] Y. A. Serebrennikov, Phys. Lett. A **372**, 3307 (2008).

Appendix A

Linear Combination of Harmonic Oscillator - Configuration Interaction

In this appendix, we fill in the details of the LCHO-CI calculation. In Sec.[2.1.1], the LCHO-CI formalism is introduced to study electronic system confined in a nanostructure. However, technical details such as the derivation of Fock-Darwin states (the basis of the single particle orbitals), and the evaluation of Hamiltonian matrix elements including the Coulomb scattering matrix elements are omitted in the main text. These details are provided here.

A.1 Single Particle in a Parabolic Dot with Magnetic Field

Consider an electron is confined in a 2D parabolic potential and in the presence of an external field, directed perpendicular to the 2D parabolic potential. The single-particle Hamiltonian reads,

$$\hat{H}_{FD} = \frac{1}{2m^*}\left(\mathbf{P} + \frac{e}{c}\mathbf{A}(\mathbf{r})\right)^2 + \frac{1}{2}m^*\omega_0^2\left(x^2+y^2\right), \tag{A.1}$$

where c is speed of light, $-e$ is electron charge, m^* is the effective mass, ω_0 is the confining frequency of the parabolic potential, and the vector potential $\mathbf{A}(\mathbf{r}) = \frac{1}{2}\mathbf{B}\times\mathbf{r} = \frac{B}{2}\left(-y\hat{x}+x\hat{y}\right)$ and $\mathbf{B} = B\hat{z}$. Substituting the explicit functional form of $\mathbf{A}$ into Eq.(A.1) and expanding the canonical momentum operators, Eq.(A.1) can be written as

$$\begin{aligned}\hat{H}_{FD} &= \frac{1}{2m^*}\left(\left(p_x - \frac{eB}{2c}y\right)^2 + \left(p_y + \frac{eB}{2c}x\right)^2\right) + \frac{m^*\omega_0^2}{2}(x^2+y^2) \\ &= \frac{1}{2m^*}(p_x^2+p_y^2) + \frac{\omega_c}{2}\hat{L}_z + \frac{m^*\omega_h^2}{2}(x^2+y^2),\end{aligned} \tag{A.2}$$

where $\hat{L}_z = -yp_x + xp_y$ is the z component of the angular momentum operator, and $\omega_h = \sqrt{\omega_o^2 + \omega_c^2/4}$ is the confining frequency with cyclotron frequency $\omega_c = eB/m^*c$. We ignore the spin degree of freedom since the quantization axis of the spins is parallel to the applied field, and there is no spin mixing term in the Hamiltonian.

Before we solve the Hamiltonian, we first transform it into an dimensionless form. We introduce effective Bohr radius, a_0, and effective Rydberg, R_y, for the unit of

distance and energy, respectively,

$$a_0 = \frac{\epsilon\hbar^2}{m^*e^2}, \tag{A.3}$$

$$R_y = \frac{\hbar^2}{2m^*a_0^2} = \frac{m^*e^4}{2\epsilon^2\hbar^2}, \tag{A.4}$$

where ϵ is the dielectric constant.

The dimensionless Hamiltonian reads,

$$\hat{H}_{FD} = -\nabla_{\tilde{x}}^2 - \nabla_{\tilde{y}}^2 + \frac{1}{2}\Omega_c L_{\tilde{z}} + \frac{1}{4}\Omega_h^2(\tilde{x}^2 + \tilde{y}^2), \tag{A.5}$$

where the tilda $\tilde{}$ is used to represent dimensionless quantity, such as $\tilde{x} = x/a_0$, $\Omega_{c(h)} = \hbar\omega_{c(h)}/R_y$. For simplicity, we drop the tilda with the understanding that all variables are now dimensionless in the rest of this appendix.

A.1.1 Fock-Darwin Orbitals

We introduce a pair of complex variables,

$$z = x + iy, \tag{A.6a}$$

$$\bar{z} = x - iy, \tag{A.6b}$$

and corresponding differential operators,

$$\partial_z = \frac{1}{2}(\partial_x - i\partial_y), \tag{A.7}$$

$$\partial_{\bar{z}} = \frac{1}{2}(\partial_x + i\partial_y). \tag{A.8}$$

The newly defined variables satisfy the commutation relation $[z, \partial_z] = [\bar{z}, \partial_{\bar{z}}] = -1$, and commutators of all other combinations of z, $\bar{z}$, ∂_z, and $\partial_{\bar{z}}$ are zero. Furthermore,

z and $\bar{z}$ form a Hermitian conjugate pair, and ∂_z and -$\partial_{\bar{z}}$ form another Hermitian conjugate pair.

Substituting the complex-valued variables into the Hamiltonian, Eq.(A.2), gives

$$\begin{aligned}
\hat{H}_{FD} &= -4\partial_z\partial_{\bar{z}} + \frac{1}{2}\left(z\partial_z - \bar{z}\partial_{\bar{z}}\right) + \frac{1}{4}\Omega_h^2 z\bar{z} \\
&= \frac{1}{4}\Omega_h^2\left(z\bar{z} - \frac{16}{\Omega_h^2}\partial_z\partial_{\bar{z}}\right) + \frac{\Omega_c}{2}\left(z\partial_z - \bar{z}\partial_{\bar{z}}\right) \\
&= \frac{1}{8}\Omega_h^2\left(\left[z - \frac{4}{\Omega_h}\partial_{\bar{z}}\right]\left[\bar{z} + \frac{4}{\Omega_h}\partial_z\right] + \left[\bar{z} - \frac{4}{\Omega_h}\partial_z\right]\left[z + \frac{4}{\Omega_h}\partial_{\bar{z}}\right]\right) \\
&= -\frac{\Omega_h}{2}\left([z,\partial_z] + [\bar{z},\partial_{\bar{z}}]\right) + \frac{\Omega_c}{2}\left(z\partial_z - \bar{z}\partial_{\bar{z}}\right), \\
&= \Omega_h\left(a^\dagger a + b^\dagger b\right) + \Omega_h + \frac{\Omega_c}{2}\left(a^\dagger a - b^\dagger b\right) \\
&= \Omega_+\left(a^\dagger a + \frac{1}{2}\right) + \Omega_-\left(b^\dagger b + \frac{1}{2}\right), \qquad \text{(A.9)}
\end{aligned}$$

where $\Omega_\pm = \Omega_h \pm \frac{\Omega_c}{2}$. In the last two lines of Eq.(A.9), we introduce the creation and annihilation operators,

$$a^\dagger = \frac{1}{\sqrt{2}}\left(\frac{\sqrt{\Omega_h}}{2}z - \frac{2}{\sqrt{\Omega_h}}\partial_{\bar{z}}\right), \qquad \text{(A.10a)}$$

$$a = \frac{1}{\sqrt{2}}\left(\frac{\sqrt{\Omega_h}}{2}\bar{z} + \frac{2}{\sqrt{\Omega_h}}\partial_z\right), \qquad \text{(A.10b)}$$

$$b^\dagger = \frac{1}{\sqrt{2}}\left(\frac{\sqrt{\Omega_h}}{2}\bar{z} - \frac{2}{\sqrt{\Omega_h}}\partial_z\right), \qquad \text{(A.10c)}$$

$$b = \frac{1}{\sqrt{2}}\left(\frac{\sqrt{\Omega_h}}{2}z + \frac{2}{\sqrt{\Omega_h}}\partial_{\bar{z}}\right). \qquad \text{(A.10d)}$$

These operators also satisfy the following commutation relations, $\left[a, a^\dagger\right] = \left[b, b^\dagger\right] = 1$ and $[a,b] = \left[a, b^\dagger\right] = \left[a^\dagger, b\right] = \left[a^\dagger, b^\dagger\right] = 0$.

The transformed Hamiltonian, Eq.(A.9), represents a 2D anisotropic harmonic oscillator with different hybrid magnetic frequencies. The eigenenergies of the system read

$$\epsilon_{nm} = \hbar\omega_+\left(n + \frac{1}{2}\right) + \hbar\omega_-\left(m + \frac{1}{2}\right), \qquad \text{(A.11)}$$

and the eigenstates (also known as Fock-Darwin (FD) states) are given by

$$|nm\rangle = \frac{(a^\dagger)^n (b^\dagger)^m}{\sqrt{n!m!}} |00\rangle \,. \tag{A.12}$$

A.1.2 Fock-Darwin Orbitals in terms of Harmonic Oscillator Orbitals

In order to evaluate Hamiltonian matrix elements, it is important to know the spatial representation of the FD orbital, $\langle r| nm\rangle$, which can be obtained in several different ways. Here, we will express the FD orbitals as a linear combination of harmonic orbitals (HO), solutions of the quantum harmonic oscillator problem. We now study an auxiliary problem, a 2D quantum harmonic oscillator with confining frequency ω_h,

$$\begin{aligned}
\hat{H}_{HO} &= -\nabla_x^2 - \nabla_y^2 + \frac{1}{4}\Omega_h^2 \left(x^2 + y^2\right), \\
&= \Omega_h \left[\left(\tfrac{\Omega_h}{4} x^2 - \tfrac{1}{\Omega_h} \nabla_x^2 \right) + \left(\tfrac{\Omega_h}{4} x^2 - \tfrac{1}{\Omega_h} \nabla_x^2 \right) \right], \\
&= \Omega_h \left[\left(\tfrac{\sqrt{\Omega}}{2} x - \tfrac{1}{\sqrt{\Omega}} \nabla_x \right) \left(\tfrac{\sqrt{\Omega}}{2} x + \tfrac{1}{\sqrt{\Omega}} \nabla_x \right) \right. \\
&\quad \left. + \left(\tfrac{\sqrt{\Omega_h}}{2} y - \tfrac{1}{\sqrt{\Omega}} \nabla_y \right) \left(\tfrac{\sqrt{\Omega}}{2} x + \tfrac{1}{\sqrt{\Omega}} \nabla_y \right) \right] + \Omega_h, \\
&= \Omega_h \left(a_x^\dagger a_x + a_y^\dagger a_y + 1 \right),
\end{aligned} \tag{A.13}$$

where the creation/annihilation operators are defined as follows

$$a_x^\dagger = \frac{1}{\sqrt{2}}\left(\sqrt{\frac{\Omega_h}{2}}x - \sqrt{\frac{2}{\Omega_h}}\nabla_x\right), \tag{A.14a}$$

$$a_x = \frac{1}{\sqrt{2}}\left(\sqrt{\frac{\Omega_h}{2}}x + \sqrt{\frac{2}{\omega_h}}\nabla_x\right), \tag{A.14b}$$

$$a_y^\dagger = \frac{1}{\sqrt{2}}\left(\sqrt{\frac{\Omega_h}{2}}y - \sqrt{\frac{2}{\Omega_h}}\nabla_y\right), \tag{A.14c}$$

$$a_y = \frac{1}{\sqrt{2}}\left(\sqrt{\frac{\Omega_h}{2}}x + \sqrt{\frac{2}{\Omega_h}}\nabla_y\right), \tag{A.14d}$$

and they obey the commutation relations $\left[a_x, a_x^\dagger\right] = \left[a_y, a_y^\dagger\right] = 1$ and $[a_x, a_y] = \left[a_x^\dagger, a_y^\dagger\right] = 0$.

Based on Eq.(A.6), Eq.(A.10) and Eq.(A.14), we can relate the FD orbital-based creation/annihilation operators to the auxiliary HO orbital-based creation/annihilation operators,

$$a^\dagger = \frac{1}{\sqrt{2}}\left(a_x^\dagger + ia_y^\dagger\right), \tag{A.15a}$$

$$a = \frac{1}{\sqrt{2}}\left(a_x - ia_y\right), \tag{A.15b}$$

$$b^\dagger = \frac{1}{\sqrt{2}}\left(a_x^\dagger - ia_y^\dagger\right), \tag{A.15c}$$

$$b = \frac{1}{\sqrt{2}}\left(a_x - ia_y\right). \tag{A.15d}$$

With these relations, we find

$$
\begin{aligned}
|nm\rangle &= \frac{(a^\dagger)^n (b^\dagger)^m}{\sqrt{n!m!}} |00\rangle \\
&= \frac{1}{\sqrt{n!m!2^{n+m}}} \left(a_x^\dagger + i a_y^\dagger\right)^n \left(a_x^\dagger - i a_y^\dagger\right)^m |00\rangle \\
&= \frac{1}{\sqrt{n!m!2^{n+m}}} \sum_{k=0}^{n} \sum_{l=0}^{m} \left({}_nC_k\right) \left({}_mC_l\right) (-i)^l \left(a_x^\dagger\right)^{n+m-k-l} \left(a_y^\dagger\right)^{k+l} |00\rangle \\
&= \sum_{s=0}^{n+m} \left\{ \frac{1}{\sqrt{n!m!2^{n+m}}} \sum_{k=max(0,s-m)}^{min(s,n)} \left({}_nC_k\right) \left({}_mC_{s-k}\right) i^k (-i)^{s-k} \right\} \left(a_x^\dagger\right)^{n+m-s} \left(a_y^\dagger\right)^s |00\rangle \\
&= \sum_{s=0}^{n+m} A_s^{nm} \, |n+m-s, s\rangle_{HO} \, ,
\end{aligned}
\tag{A.16}
$$

where $|nm\rangle_{HO} = \frac{(a_x^\dagger)^n (a_y^\dagger)^m}{\sqrt{n!m!}} |00\rangle_{HO}$, and $|00\rangle = |00\rangle_{HO}$. We remark that the auxiliary quantum harmonic oscillator is specifically chosen such that the FD state $|00\rangle$ is also the ground state of the auxiliary quantum harmonic oscillator. The coefficient A_s^{nm} is defined within the bracket in the fourth line of Eq.(A.16). The combination notation denotes

$${}_mC_k = \begin{pmatrix} m \\ k \end{pmatrix} = \frac{m!}{k!(m-k)!} \tag{A.17}$$

In the spatial representation, we denote

$$
\begin{aligned}
\langle \mathbf{r} | nm \rangle_{HO} &= \phi_{nm}^{HO}(\mathbf{r}), \\
&= \sqrt{\frac{1}{2\pi l_h^2}} \sqrt{\frac{1}{n!m!2^{n+m}}} H_n\left(\frac{x}{\sqrt{2} l_h}\right) H_m\left(\frac{y}{\sqrt{2} l_h}\right) \exp\left(-\frac{x^2+y^2}{4 l_h^2}\right),
\end{aligned}
\tag{A.18}
$$

where the hybrid magnetic length is given by $l_h = \sqrt{\frac{1}{\Omega_h}}$. The spatial representation

of FD orbitals are then given by

$$\begin{aligned}\langle \mathbf{r}|nm\rangle &= \phi_{nm}(\mathbf{r}), \\ &= \sum_{s=0}^{n+m} A_s^{nm}\phi^{HO}_{(n+m-s)s}(\mathbf{r}).\end{aligned} \tag{A.19}$$

A.2 Single Particle in a Multi-Dot Device

Next, we consider a system of N_{QD} tunnel-coupled quantum dots with N_{PL} plunger gates. The single particle Hamiltonian reads,

$$\hat{H}_{sp} = \left(-i\nabla + \frac{\Omega_c}{2}\mathbf{A}(\mathbf{r})\right)^2 - \sum_{i=1}^{N_{QD}} V_i(\mathbf{r}) + \sum_{j=1}^{N_{PL}} \mathbf{V}_{B,j}(\mathbf{r}), \tag{A.20}$$

where the confining potential $V_i(\mathbf{r})$ is given in Eq.(2.2) and plunger gate potential $V_{B,j}(\mathbf{r})$ is given in Eq.(2.3). We define the dimensionless gauge $\tilde{\mathbf{A}} = \frac{1}{2}\hat{B}\times\mathbf{r}$ with unit direction vector $\hat{B}$. Not explicitly shown in Eq.(A.20), however, it is useful to also define $\Omega_{0j} = \sqrt{4\tilde{V}_j^0/\tilde{d}_j^2} = \hbar\omega_0/R_y$, which is the dimensionless confining frequency of a harmonic oscillator localized on dot j.

As discussed in Sec.[2.1.1], Eq.(A.20) is represented as a Hamiltonian matrix in the basis of FD orbitals localized on quantum dots. The Schrödinger equation becomes a generalized eigenvalue problem, $\mathbf{H}_{sp}\mathbf{a} = \epsilon\mathbf{S}\mathbf{a}$. Now, we show how to evaluate matrix elements of overlapping matrix $\mathbf{S}$ and single-particle Hamiltonian $\mathbf{H}_{sp}$.

In previous section, we derived FD orbitals, $\langle \mathbf{r}|nm\rangle = \phi_{nm}(\mathbf{r})$, which are solutions to Eq.(A.5). In the current section, we have FD orbitals localized on different orbitals, so we introduce an additional index i such that $\langle \mathbf{r}|inm\rangle = \phi_{inm}(\mathbf{r})$ denotes the (n,m) FD orbital in the i-th dot. In the absence of any external magnetic field, one finds $\phi_{inm}(\mathbf{r}) = \phi_{nm}(\mathbf{r}-\mathbf{r}_i)$ with $\mathbf{r}_i$ is the position coordinate for the $i-$th dot. However,

in the presence of a magnetic field, $\phi_{nm}(\mathbf{r}-\mathbf{r}_i)$ and $\phi_{nm}(\mathbf{r}-\mathbf{r}_i)$ are related by the gauge transformation

$$\phi_{inm}(\mathbf{r}) = \exp\left(-i\frac{\Omega_c}{4}\left(-y_i x + x_i y\right)\right)\phi_{nm}(\mathbf{r}-\mathbf{r}_i), \tag{A.21}$$

where the factor $\exp\left(-i\frac{\Omega_c}{4}\left(-y_i x + x_i y\right)\right)$ corresponds to the standard gauge transformation to get vector potential centered at the global origin, $\mathbf{A} = \frac{1}{2}(-y\hat{i} + x\hat{y})$, from the vector potential centered at the local origin, $\mathbf{A}_i = \frac{1}{2}\left(-(y-y_i)\hat{x} + (x-x_i)\hat{y}\right)$. Now, we have an explicit definition of the single particle basis $\{\phi_{inm}(\mathbf{r})\}$.

Next, we consider

$$\begin{aligned}
\mathbf{S}_{\alpha,\alpha'} &= \langle inm|i'n'm'\rangle \\
&= \int d\mathbf{r}\phi^*_{inm}(\mathbf{r})\phi_{i'n'm'}(\mathbf{r}) \\
&= \int d\mathbf{r}e^{i\frac{\Omega_c}{4}(-(y_i-y_{i'})x+(x_i-x_{i'})y)}\phi^*_{nm}(\mathbf{r}-\mathbf{r}_i)\phi_{n'm'}(\mathbf{r}-\mathbf{r}_{i'}) \\
&= \sum_{l=0}^{n+m}\sum_{l=0}^{n'+m'}\left(A_l^{nm}\right)^*)\, A_{l'}^{n'm'}\int d\mathbf{r} \\
&\quad e^{i\frac{\Omega_c}{4}(-(y_i-y_{i'})x+(x_i-x_{i'})y)}\left(\phi^{HO}_{n_x,n_y}(\mathbf{r}-\mathbf{r}_i)\right)^*\phi^{HO}_{n'_x,n'_y}(\mathbf{r}-\mathbf{r}_{i'}),
\end{aligned} \tag{A.22}$$

where α and α' are composite index for (i,n,m) and (i',n',m') of FD orbitals, respectively. In the last line of Eq.(A.22), we introduce $(n_x,n_y) = (n+m-l,l)$ and $\left(n'_x,n'_y\right) = (n'+m'-l',l')$. The product of localized harmonic oscillator functions $\phi^{HO}_{n_x n_y}(\mathbf{r}-\mathbf{r}_i)\phi^{HO}_{n'_x n'_y}(\mathbf{r}-\mathbf{r}_{i'})$ can be expanded explicitly with Eq.(A.18). Thus the last

line of Eq.(A.22) can be written as

$$\begin{aligned}
\mathbf{S}_{\alpha,\alpha'} &= \sum_{l=0}^{n+m}\sum_{l=0}^{n'+m'} \left(A_l^{nm}\right)^*) A_{l'}^{n'm'} \frac{1}{2\pi l_{hi} l_{hi'}} \frac{1}{n_x! n_y! n'_x! n'_y! 2^{n_x+n_y+n'_x+n'_y}} \\
&\times \int dx H_{n_x}\left(\frac{x-x_i}{\sqrt{2}l_{hi}}\right) H_{n'_x}\left(\frac{x-x_{i'}}{\sqrt{2}l_{hi'}}\right) e^{i\frac{\Omega_c}{4}(-(y_i-y_{i'})x) - \frac{(x-x_i)^2}{4l_{hi}^2} - \frac{(x-x_{i'})^2}{4l_{hi'}^2}} \\
&\times \int dy H_{n_y}\left(\frac{y-y_i}{\sqrt{2}l_{hi}}\right) H_{n'_y}\left(\frac{y-y_{i'}}{\sqrt{2}l_{hi'}}\right) e^{i\frac{\Omega_c}{4}(x_i-x_{i'})y) - \frac{(y-y_i)^2}{4l_{hi}^2} - \frac{(y-y_{i'})^2}{4l_{hi'}^2}}, \quad \text{(A.23)}
\end{aligned}$$

where the last two lines indicates that the integral is a series of integrations of product of Gaussian functions and Hermite polynomials. In general, analytical formula exist for this kind of generalized Gaussian integrals. We now show how to derive them.

First, we explicit expand the Hermite polynomials in the definition of the HO orbitals, Eq.(A.18). For instance, we consider

$$\begin{aligned}
H_{n_x}\left(\frac{x-x_i}{\sqrt{2}l_{hi}}\right) &= \sum_{i=0}^{n_x} h_{n_x,i}\left(\frac{x-x_i}{\sqrt{2}l_{hi}}\right)^i \\
&= \sum_{i=0}^{n_x} h_{n_x,i} \sum_{k=0}^{i} {}_iC_k x^k (-x_i)^{i-k} \\
&= \sum_{k=0}^{n_x} \left\{ \sum_{i=k}^{n_x} \left(\frac{1}{\sqrt{2}l_{hi}}\right)_i^i C_k (-x_i)^{i-k} \right\} x^k \\
&= \sum_{k=0}^{n_x} B_{n_x,k}(x_i) x^k, \quad \text{(A.24)}
\end{aligned}$$

where $h_{n_x,i}$ is the coefficient associated with x^i term of the Hermite polynomial $H_{n_x}(x)$, and the coefficient$B_{n_x,k}(x_i)$ is defined in the bracket in the third line in Eq.(A.24).

Similarly,

$$H_{n'_x}\left(\frac{x-x_{i'}}{\sqrt{2}l_{hi'}}\right) = \sum_{k'=0}^{n'_x} B_{n'_x,k'}(x_{i'}) x^{k'}. \quad \text{(A.25)}$$

Thus the product of the two is

$$\begin{aligned} H_{n_x}\left(\frac{x-x_i}{\sqrt{2}l_{hi}}\right)H_{n'_x}\left(\frac{x-x_{i'}}{\sqrt{2}l_{hi'}}\right) &= \sum_{k=0}^{n_x}\sum_{k'=0}^{n'_x} B_{n_x,k}(x_i)B_{n'_x,k'}(x_{i'})x^{k+k'}, \\ &= \sum_{s=0}^{n_x+n'_x}\left\{\sum_{k=max(0,s-n'_x)}^{min(s,n_x)} B_{n_x,k}(x_i)B_{n'_x,s-k}(x_{i'})\right\}x^s, \\ &= \sum_{s=0}^{n_x+n'_x} C_s(n_x,n'_x;x_i,x_{i'})x^s, \end{aligned} \tag{A.26}$$

where the coefficient $C_s(n_x,n'_x;x_i,x_{i'})$ is defined in the bracket in the second line.

Finally, we define a generalized Gaussian integral formula

$$\begin{aligned} I(n;a,b,c) &= \int_{-\infty}^{\infty} dx x^n e^{-(ax^2+bx+c)}, \\ &= e^{\frac{b^2-4ac}{4a}}\sum_{k'=0}^{[n/2]} {}_nC_{2k'}\left(-\frac{b}{2a}\right)^{n-2k'}\frac{(2k'+1)!!}{2^{k'}(2k'+1)}\sqrt{\pi}a^{-\frac{2k'+1}{2}} \end{aligned} \tag{A.27}$$

Using Eq.(A.26) and Eq.(A.27), Eq.(A.23) can now be written as

$$\begin{aligned} \mathbf{S}_{\alpha,\alpha'} &= \sum_{l=0}^{n+m}\sum_{l=0}^{n'+m'}\frac{(A_l^{nm})^* A_{l'}^{n'm'}}{2\pi l_{hi}l_{hi'}}\frac{C_s(n_x,n'_x;x_i,x_{i'})C_{s'}(n_y,n'-y;y_i,y_{i'})}{n_x!n_y!n'_x!n'_y!2^{n_x+n_y+n'_x+n'_y}}, \\ &\quad \times I(s;a_x,b_x,c_x)I(s';a_y,b_y,c_y), \end{aligned} \tag{A.28}$$

where the new variables appearing in the last line are defined as

$$a_x = \frac{1}{4}\left(\frac{1}{l_{hi}^2}+\frac{1}{l_{hi'}^2}\right) \tag{A.29a}$$

$$b_x = -\frac{1}{2}\left(\frac{x_i}{l_{hi}^2}+\frac{x_{i'}}{l_{hi'}^2}\right)+i\frac{\Omega_c}{4}(y_i-y_{i'}) \tag{A.29b}$$

$$c_x = \frac{1}{4}\left(\frac{x_i^2}{l_{hi}^2}+\frac{x_{i'}^2}{l_{hi'}^2}\right) \tag{A.29c}$$

$$a_y = \frac{1}{4}\left(\frac{1}{l_{hi}^2}+\frac{1}{l_{hi'}^2}\right) \tag{A.29d}$$

$$b_y = -\frac{1}{2}\left(\frac{y_i}{l_{hi}^2}+\frac{y_{i'}}{l_{hi'}^2}\right)+i\frac{\Omega_c}{4}(x_i-x_{i'}) \tag{A.29e}$$

$$c_y = \frac{1}{4}\left(\frac{y_i^2}{l_{hi}^2}+\frac{y_{i]}^2}{l_{hi'}^2}\right) \tag{A.29f}$$

Eq.(A.28) gives a general expression for the calculation of the overlap matrix elements between any two FD states in full analytical form.

Next, we turn to the discussion of the single-particle Hamiltonian matrix elements, $\langle\alpha'|\hat{H}_{sp}|\alpha\rangle$. For each state $|\alpha\rangle$, we decompose the single-particle Hamiltonian as follows,

$$\hat{H}_{sp} = \left(-i\tilde{\nabla} + \frac{\Omega_c}{2}\tilde{\mathbf{A}}(\tilde{\mathbf{r}})\right)^2 + V_i^{HO} + \delta V_i + \sum_{j\neq i}^{N_{QD}} \tilde{V}_j(\tilde{\mathbf{r}}) + \sum_{j=1}^{N_{PL}} \tilde{\mathbf{V}}_{B,j}(\tilde{\mathbf{r}}), \tag{A.30}$$

where $V_i^{HO} = -V_i^0 + \frac{\Omega_0}{4}((x-x_i)^2 + (y-y_i)^2)$. This decomposition is desirable because the state $|\alpha\rangle$ is the eigenstate of the Hamiltonian: $\left(-i\tilde{\nabla} + \frac{\Omega_c}{2}\tilde{\mathbf{A}}(\tilde{\mathbf{r}})\right)^2 + V_i^{HO}$ with eigenenergy ϵ_{inm}.

With Eq.(A.30), the matrix element read

$$\begin{aligned}\langle\alpha'|\hat{H}|\alpha\rangle &= \epsilon_{inm}\mathbf{S}_{\alpha',\alpha} + \langle\alpha'|\delta V_{i'}|\alpha\rangle \\ &\quad + \sum_{j\neq i}^{N_{QD}}\langle\alpha'|V_j|\alpha\rangle + \sum_{j}^{N_{PL}}\langle\alpha'|V_{B,j}|\alpha\rangle.\end{aligned} \tag{A.31}$$

We now procced to deriving analytical expressions for the last three matrix elements in Eq.(A.31).

First, we consider

$$\begin{aligned}\langle\alpha'|\delta V_i|\alpha\rangle &= \langle\alpha'| - V_i^0 \exp\left(\tfrac{(x-x_i)^2+(y-y_i)^2}{d_i^2}\right) - (-V_i^0 + \tfrac{\Omega_0}{4}((x-x_i)^2 + (y-y_i)^2))|\alpha\rangle \\ &= -V_i^0\langle\alpha'|\exp\left(\tfrac{-((x-x_i)^2+(y-y_i)^2)}{d_i^2}\right)|\alpha\rangle + V_i^0\mathbf{S}_{\alpha',\alpha} \\ &\quad -\tfrac{\Omega_0}{4}\left(\langle\alpha'|(x-x_i)^2|\alpha\rangle + \langle\alpha'|(y-y_i)^2|\alpha\rangle\right),\end{aligned} \tag{A.32}$$

where

$$\begin{aligned}\langle\alpha|(x-x_i)^2|\alpha'\rangle &= \sum_{l=0}^{n+m}\sum_{l'=0}^{n'+m'}\sum_{s=0}^{n_x+n'_x}\sum_{s'=0}^{n_y+n'_y}\frac{\left(A_l^{nm}\right)^* A_{l'}^{n'm'}}{2\pi l_{hi}l_{hi'}}\frac{C_s(n_x,n'_x;x_i,x_{i'})C_{s'}(n_y,n'_y;y_i,y_{i'})}{\sqrt{n_x!n'_x!n_y!n'_y!2^{n_x+n_y+n'_x+n'_y}}}\\ &\times\left(I(s+2;a_x,b_x,c_x)-2x_iI(s+1;a_x,b_x,c_x)+x_i^2I(s;a_x,b_x,c_x)\right)\\ &\times I(s';a_y,b_y,c_y), \qquad (A.33)\\ \langle\alpha|(y-y_i)^2|\alpha'\rangle &= \sum_{l=0}^{n+m}\sum_{l'=0}^{n'+m'}\sum_{s=0}^{n_x+n'_x}\sum_{s'=0}^{n_y+n'_y}\frac{\left(A_l^{nm}\right)^* A_{l'}^{n'm'}}{2\pi l_{hi}l_{hi'}}\frac{C_s(n_x,n'_x;x_i,x_{i'})C_{s'}(n_y,n'_y;y_i,y_{i'})}{\sqrt{n_x!n'_x!n_y!n'_y!2^{n_x+n_y+n'_x+n'_y}}}\\ &\times\left(I(s+2;a_y,b_y,c_y)-2y_iI(s+1;a_y,b_y,c_y)+y_i^2I(s;a_y,b_y,c_y)\right)\\ &\times I(s';a_x,b_x,c_x), \qquad (A.34)\end{aligned}$$

and

$$\begin{aligned}\langle\alpha'|\exp\left(\tfrac{-((x-x_i)^2+(y-y_i)^2)}{d_i^2}\right)|\alpha\rangle &= \sum_{l=0}^{n+m}\sum_{l'=0}^{n'+m'}\sum_{s=0}^{n_x+n'_x}\sum_{s'=0}^{n_y+n'_y}\\ &\frac{\left(A_l^{nm}\right)^* A_{l'}^{n'm'}}{2\pi l_{hi}l_{hi'}}\frac{C_s(n_x,n'_x;x_i,x_{i'})C_{s'}(n_y,n'_y;y_i,y_{i'})}{\sqrt{n_x!n'_x!n_y!n'_y!2^{n_x+n_y+n'_x+n'_y}}}\\ &\times I(s;a_x+\frac{1}{d_i^2},b_x-2\frac{x_i}{d_i^2},c_x+\frac{x_i^2}{d_i^2})\\ &\times I(s';a_y+\frac{1}{d_i^2},b_y-2\frac{y_i}{d_i^2},c_y+\frac{y_i^2}{d_i^2}). \qquad (A.35)\end{aligned}$$

Next, we consider matrix elements for $\langle\alpha'|V_j(\mathbf{r})|\alpha\rangle$, where $V_j(\mathbf{r})$ is a Gaussian

potential, and the matrix element is actually similar to Eq.(A.35). It reads

$$\begin{aligned}
\langle\alpha'|V_j(\mathbf{r})|\alpha\rangle &= -V_j^0\langle\alpha'|\exp\left(-\frac{(x-x_j)^2+(y-y_j)^2}{d_j^2}\right)|\alpha\rangle \\
&= -V_j^0\sum_{l=0}^{n+m}\sum_{l'=0}^{n'+m'}\sum_{s=0}^{n_x+n'_x}\sum_{s'=0}^{n_y+n'_y} \\
&\quad \frac{(A_l^{nm})^*\,A_{l'}^{n'm'}}{2\pi l_{hi}l_{hi'}}\frac{C_s(n_x,n'_x;x_i,x_{i'})C_{s'}(n_y,n'_y;y_i,y_{i'})}{\sqrt{n_x!n'_x!n_y!n'_y!2^{n_x+n_y+n'_x+n'_y}}} \\
&\quad \times I(s;a_x+\frac{1}{d_j^2},b_x-2\frac{x_j}{d_j^2},c_x+\frac{x_j^2}{d_j^2}) \\
&\quad \times I(s';a_y+\frac{1}{d_j^2},b_y-2\frac{y_j}{d_j^2},c_y+\frac{y_j^2}{d_j^2}).
\end{aligned} \tag{A.36}$$

Finally, we consider the last type of matrix elements,

$$\begin{aligned}
\langle\alpha'|V_{B,j}(\mathbf{r})|\alpha\rangle &= V_{B,j}^0\langle\alpha'|\exp\left(-\frac{\tilde{x}_j^2}{D_{xj}^2}-\frac{\tilde{y}_j^2}{D_{yj}^2}\right)|\alpha\rangle \\
&= V_{B,j}^0\sum_{l=0}^{n+m}\sum_{l'=0}^{n'+m'}\sum_{s=0}^{n_x+n'_x}\sum_{s'=0}^{n_y+n'_y} \\
&\quad \frac{(A_l^{nm})^*\,A_{l'}^{n'm'}}{2\pi l_{hi}l_{hi'}}\frac{C_s(n_x,n'_x;x_i,x_{i'})C_{s'}(n_y,n'_y;y_i,y_{i'})}{\sqrt{n_x!n'_x!n_y!n'_y!2^{n_x+n_y+n'_x+n'_y}}} \\
&\quad \times\int\int dxdy\,x^s y^{s'}\exp\left(-(Ax^2+By^2+Cxy+Dx+Ey+F_x+F_y)\right)
\end{aligned} \tag{A.37}$$

where the parameter in the last line are defined as follows

$$
\begin{aligned}
A &= \frac{1}{4l_{hi}^2}+\frac{1}{4l_{hi'}^2}+\frac{cos^2\eta_j}{D_{xj}^2}+\frac{sin^2\eta_j}{D_{yj}^2}, && \text{(A.38a)}\\
B &= \frac{1}{4l_{hi}^2}+\frac{1}{4l_{hi'}^2}+\frac{sin^2\eta_j}{D_{xj}^2}+\frac{cos^2\eta_j}{D_{yj}^2}, && \text{(A.38b)}\\
C &= 2\cos\eta_j\sin\eta_j\left(\frac{1}{D_{xj}^2}-\frac{1}{D_{yj}^2}\right), && \text{(A.38c)}\\
D &= -\frac{1}{2}\left(\frac{x_i}{l_{hi}^2}+\frac{x_{i'}}{l_{hi'}^2}\right)-i\frac{\Omega_c}{4}\left(y_i-y_{i'}\right)\\
&\quad -2x_{Bj}\left(\frac{\cos^2\eta_j}{D_{xj}^2}+\frac{\sin^2\eta_j}{D_{yj}^2}\right)-2y_{Bj}\cos\eta_j\sin\eta_j\left(\frac{1}{D_{xj}^2}-\frac{1}{D_{yj}^2}\right) && \text{(A.38d)}\\
E &= -\frac{1}{2}\left(\frac{y_i}{l_{hi}^2}+\frac{y_{i'}}{l_{hi'}^2}\right)+i\frac{\Omega_c}{4}\left(x_i-x_{i'}\right)\\
&\quad -2y_{Bj}\left(\frac{\sin^2\eta_j}{D_{xj}^2}+\frac{\cos^2\eta_j}{D_{yj}^2}\right)-2x_{Bj}\cos\eta_j\sin\eta_j\left(\frac{1}{D_{yj}^2}-\frac{1}{D_{xj}^2}\right) && \text{(A.38e)}\\
F_x &= \frac{x_i^2}{4l_{hi}^2}+\frac{x_{i'}^2}{4l_{hi'}^2}+x_{Bj}^2\left(\frac{\cos^2\eta_j}{D_{xj}^2}+\frac{\sin^2\eta_j}{D_{yj}^2}\right)\\
&\quad +x_{Bj}y_{Bj}\cos\eta_j\sin\eta_j\left(\frac{1}{D_{xj}^2}-\frac{1}{D_{yj}^2}\right) && \text{(A.38f)}\\
F_y &= \frac{y_i^2}{4l_{hi}^2}+\frac{y_{i'}^2}{4l_{hi'}^2}+y_{Bj}^2\left(\frac{\cos^2\eta_j}{D_{xj}^2}+\frac{\sin^2\eta_j}{D_{yj}^2}\right)\\
&\quad +x_{Bj}y_{Bj}\cos\eta_j\sin\eta_j\left(\frac{1}{D_{yj}^2}-\frac{1}{D_{xj}^2}\right), && \text{(A.38g)}
\end{aligned}
$$

where we replace x_{Bj} and y_{Bj} with their definition, Eq.(2.4), when we derive these parameters.

Due to the cross term Cxy in the last line of Eq.(A.37), we can not directly separate x and y to get two independent Gaussian integrals as we have done for all the other expressions. A change of variable is desired to obtain two decoupled variables.

More explicitly, we define $y' = y + (C/2B)x$. We can decouple the two variables

as follows,

$$\begin{aligned} & Ax^2 + By^2 + Cxy + Dx + Ey + F_x + F_y \\ = \; & Ax^2 + B\left(y^2 + \frac{Cx}{B} + \left(\frac{Cx}{2B}\right)^2\right) - \frac{C^2}{4B}x^2 + Dx + Ey + F_x + F_y \\ = \; & \left(A - \frac{C^2}{4B}\right)x^2 + \left(D - \frac{CE}{2B}\right)x + F_x + B(y')^2 + Ey' + F_y \\ = \; & \tilde{a}_x x^2 + \tilde{b}_x x + \tilde{c}_x + \tilde{a}_y (y')^2 + \tilde{b}_y y' + \tilde{c}_y, \end{aligned} \tag{A.39}$$

where the new expression in the last line has the two variables, x and y', decoupled. The definitions of $\tilde{a}_{x(y)}$, $\tilde{b}_{x(y)}$, and $\tilde{c}_{x(y)}$ are given above.

Thus, the double integral in the last line of Eq.(A.37) can now be written as

$$\begin{aligned} & \int\int dx dy' x^s \left(y' - \frac{C}{2B}x\right)^{s'} \exp\left(-(\tilde{a}_x x^2 + \tilde{b}_x x + \tilde{c}_x + \tilde{a}_y (y')^2 + \tilde{b}_y y' + \tilde{c}_y\right) \\ = \; & \sum_{k=0}^{s'} {}_{s'}C_k \left(-\frac{C}{2B}\right)^k I(s+k; \tilde{a}_x, \tilde{b}_x, \tilde{c}_x) I(s'-k; \tilde{a}_y, \tilde{b}_y, \tilde{c}_y). \end{aligned} \tag{A.40}$$

Substituting Eq.(A.40) in place of the last double integral in eq.(A.37), and the matrix elements now read

$$\begin{aligned} \langle \alpha' | V_j(\mathbf{r}) | \alpha \rangle \; = \; & \sum_{l=0}^{n+m} \sum_{l'=0}^{n'+m'} \sum_{s=0}^{n_x+n'_x} \sum_{s'=0}^{n_y+n'_y} -V_j^0 \frac{\left(A_l^{nm}\right)^* A_{l'}^{n'm'}}{2\pi l_{hi} l_{hi'}} \frac{C_s(n_x, n'_x; x_i, x_{i'}) C_{s'}(n_y, n'_y; y_i, y_{i'})}{\sqrt{n_x! n'_x! n_y! n'_y! 2^{n_x+n_y+n'_x+n'_y}}} \\ & \times \sum_{k=0}^{s'} {}_{s'}C_k \left(-\tfrac{C}{2B}\right)^k I(s+k; \tilde{a}_x, \tilde{b}_x, \tilde{c}_x) I(s'-k; \tilde{a}_y, \tilde{b}_y, \tilde{c}_y). \end{aligned} \tag{A.41}$$

Now we know how to compute the single-particle Hamiltonian matrix elements and the overlapping matrix elements with analytical formula. We can diagonalize the Hamiltonian as described in Sec.[2.1.1] to obtain the single-particle molecular orbitals and associated energies.

A.3 Many Electrons in a Multi-Dot Device

With respect to the basis of single-particle molecular states, we can write down the many-body Hamiltonian in the second quantized form,

$$\begin{aligned} \hat{H}_{N_e} &= \sum_{i,\sigma} \epsilon_{\gamma_i} d^{\dagger}_{\gamma_i\sigma} d_{\gamma_i,\sigma} + \frac{1}{2} \sum_{i,j,k,l,\sigma,\sigma'} \langle \gamma_i \gamma_j | V_c | \gamma_k \gamma_l \rangle d^{\dagger}_{\gamma_i,\sigma} d^{\dagger}_{\gamma_j,\sigma'} d_{\gamma_l,\sigma'} d_{\gamma_k,\sigma}, \\ &= \hat{H}_{sp} + \hat{H}_{ee}, \end{aligned} \tag{A.42}$$

where $\gamma' s$ are the single particle molecular states with eigenvalues $\epsilon_{\gamma' s}$. The Coulomb matrix elements are defined as follows

$$\langle \gamma_i \gamma_j | V_c | \gamma_k \gamma_l \rangle = \int d\mathbf{r} \int d\mathbf{r}' \psi^*_{\gamma_i}(\mathbf{r}) \psi^*_{\gamma_j}(\mathbf{r}') \frac{2}{|\mathbf{r} - \mathbf{r}'|} \psi_{\gamma_k}(\mathbf{r}) \psi_{\gamma_l}(\mathbf{r}'). \tag{A.43}$$

We solve Eq.(A.42) by the configuration interaction (CI) approach with N_e electrons. The first task is to build all possible configurations of electrons occupying the spin-orbitals (γ_i, σ) obtained by the LCHO method. In order to properly construct the configurations, we first set the order of the spin-orbitals as follows

$$(\gamma_i, \sigma) > (\gamma_j, \sigma') \text{ if } \begin{cases} \sigma = \uparrow \quad \text{and} \quad \sigma' = \downarrow \\ \quad \text{or} \\ \sigma = \sigma' \quad \text{and} \quad i > j \end{cases} \tag{A.44}$$

and the creation operators of smaller spin-orbitals are placed further away from the vacum state when we explicitly write out a configuration in the second quantized

form. Thus a configuration $|q_{N_e}\rangle$ with N_e electron read

$$\begin{aligned} |q_{N_e}\rangle &= \left|n^q_{1\uparrow}, n^q_{2\uparrow}, \ldots; n^q_{1\uparrow}, n^q_{2\uparrow}, \ldots\right\rangle_{N_e} \\ &= \prod_{i=1}^{N_{orb}} \left(d^\dagger_{\gamma_i,\downarrow}\right)^{n^q_{i,\downarrow}} \prod_{j=1}^{N_{orb}} \left(d^\dagger_{\gamma_j,\uparrow}\right)^{n^q_{j,\uparrow}} |0\rangle \\ &= \prod_{j=1}^{N_e} d^\dagger_{\gamma^q_j \sigma^q_j} |0\rangle \end{aligned} \tag{A.45}$$

where $n^q_{i\sigma}$ is the number of electron in the spin-orbital (γ_i, σ_i) for the configuration $|q_{N_e}\rangle$, and (γ^q_j, σ^q_j) is the $j-th$ spin-orbital for configuration $|q\rangle$. N_{orb} is the size of the single-particle basis, and also the number of single-particle molecular orbitals. The electron number operators $n^q_{i\sigma}$ satisfy the constraints $\sum_{i=1}^{N_{orb}} n^q_{i\sigma} = N_e$. For the rest of the discussion, we will drop the subscript N_e on configuration $|q_{N_e}\rangle$ with the understanding that all configurations mentioned belongs to the N_e subspace.

The matrix element of the first part, $\hat{H}_{sp}$, of Eq.(A.42) is simply given by

$$\langle q|\hat{H}_{sp}|q'\rangle = \delta_{qq'} \sum_{i=1,\sigma}^{N_{orb}} n^q_{i,\sigma} \epsilon_{\gamma_i,\sigma}, \tag{A.46}$$

where $\delta_{qq'}$ is the Kronecker delta.

Next we look at the matrix elements of the electron-electron Coulomb interaction term, $\hat{H}_{ee}$. We first need to evaluate the matrix elements in Eq.(A.44). To remove the singularity in the integral, we apply the inverse Fourier transform,

$$\frac{2}{|\mathbf{r}-\mathbf{r}'|} = \frac{1}{\pi} \int d\mathbf{q} \frac{e^{i\mathbf{q}\cdot(\mathbf{r}-\mathbf{r}')}}{q} = \frac{1}{\pi} \int_0^\infty dq \int_0^{2\pi} d\theta_q e^{i\mathbf{q}\cdot(\mathbf{r}-\mathbf{r}')}, \tag{A.47}$$

and substitute Eq.(A.47) into Eq.(A.44) to get

$$\langle \gamma_i\gamma_j|V_c|\gamma_k\gamma_l\rangle = \tfrac{1}{\pi} \textstyle\int_0^\infty dq \int_0^{2\pi} d\theta_q \int d\mathbf{r} \psi^*_{\gamma_i}(\mathbf{r}) e^{i\mathbf{q}\cdot\mathbf{r}} \psi^*_{\gamma_k}(\mathbf{r}) \int d\mathbf{r}' \psi^*_{\gamma_j}(\mathbf{r}') e^{i\mathbf{q}\cdot\mathbf{r}'} \psi^*_{\gamma_l}(\mathbf{r}'). \tag{A.48}$$

The matrix element of the plane wave can be calculated as follows

$$\begin{aligned}\langle\gamma_i|e^{i\mathbf{q}\cdot\mathbf{r}}|\gamma_k\rangle &= \sum_{\alpha,\alpha'}\left(a^i_\alpha\right)^* a^k_{\alpha'}\langle\alpha|e^{i\mathbf{q}\cdot\mathbf{r}}|\alpha'\rangle \\ &= \sum_{\alpha,\alpha'}\left(a^i_\alpha\right)^* a^k_{\alpha'}\int d\mathbf{r}\phi^*_{inm}(\mathbf{r})e^{i\mathbf{q}\cdot\mathbf{r}}\phi_{i'n'm'}(\mathbf{r}) \\ &= \sum_{\alpha,\alpha'}\left(a^i_\alpha\right)^* a^k_{\alpha'} I_{PW}(\alpha,\alpha';q\cos\theta,q\sin\theta), \end{aligned} \tag{A.49}$$

where α/α' represents composite index for $(i,n,m)/(i'n'm')$, and the plane wave integral $I_{PW}(\alpha,\alpha';q_x,q_y)$ is defined as follows

$$\begin{aligned} I_{PW}(\alpha,\alpha';q_x,q_y) &= \sum_{l=0}^{n+m}\sum_{l'=0}^{n'+m'}\sum_{s=0}^{n_x+n'_x}\sum_{s'=0}^{n_y+n'_y}\frac{\left(A^{nm}_l\right)^* A^{n'm'}_{l'}}{2\pi l_h^2}\frac{C_s(n_x,n'_x;x_i,x_{i'})C_{s'}(n_y,n'_y;y_i,y_{i'})}{\sqrt{n_x!n_y!n'_x!n'_y!2^{n_x+n_y+n'_x+n'_y}}} \\ &\quad\times I(s;a_x,b_x+iq_x,c_x)I(s';a_y,b_y+iq_y,c_y). \end{aligned} \tag{A.50}$$

Thus, from Eq.(A.49), we get

$$\begin{aligned}\langle\gamma_i\gamma_j|V_c|\gamma_k\gamma_l\rangle &= \tfrac{1}{\pi}\textstyle\sum_{\alpha,\beta,\alpha'\beta'}\left(a^i_\alpha\right)^*\left(a^j_\beta\right)^* a^k_{\alpha'}a^l_{\beta'} \\ &\quad\times\textstyle\int_0^\infty dq\int_0^{2\pi}d\theta_q I_{PW}(\alpha,\alpha';q_x,q_y)I_{PW}(\beta,\beta';-q_x,-q_y).\end{aligned} \tag{A.51}$$

Now, the Coulomb interaction matrix elements read

$$\begin{aligned}\langle q|\hat{H}_{ee}|q'\rangle &= \frac{1}{2}\sum_{i,j,k,l,\sigma,\sigma'}\langle\gamma_i\gamma_j|V_c|\gamma_k\gamma_l\rangle\langle q|d^\dagger_{\gamma_i,\sigma}d^\dagger_{\gamma_j,\sigma'}d_{\gamma,l\sigma'}d_{\gamma_k,\sigma}|q'\rangle \\ &= \frac{1}{2}\sum_{i,j,k,l}\langle\gamma_i\gamma_j|V_c|\gamma_k\gamma_l\rangle G(q,q';i,j,k,l),\end{aligned} \tag{A.52}$$

where

$$G(q,q';i,j,k,l) = \sum_{\sigma,\sigma'}\langle q|d^\dagger_{\gamma_i,\sigma}d^\dagger_{\gamma_j,\sigma'}d_{\gamma,l\sigma'}d_{\gamma_k,\sigma}|q'\rangle. \tag{A.53}$$

Putting Eq.(A.46) and Eq.(A.52) together, we have the matrix elements,

$$\langle q|\hat{H}_{N_e}|q'\rangle = \delta_{qq'}\sum_{i=1,\sigma}^{N_{orb}} n^q_{i,\sigma}\epsilon_{\gamma_i,\sigma} + \frac{1}{2}\sum_{i,j,k,l}\langle\gamma_i\gamma_j|V_c|\gamma_k\gamma_l\rangle G(q,q';i,j,k,l), \tag{A.54}$$

Appendix B

Löwdin Perturbation Theory

In this appendix, we discuss details of Löwdin perturbation theory, which has been applied to derive effective Hamiltonians, such as $t-J$ model and Heisenberg model of a triple quantum dot.

B.1 Division of Hamiltonian and Hilbert Space

Consider a general Hamiltonian of the following form,

$$\hat{H} = \hat{H}_0 + \hat{H}_1, \tag{B.1}$$

where $\hat{H}_0$ is assumed to be a Hamiltonian that we can solve exactly, and $\hat{H}_1$ is assumed to be a perturbation. In this formalism, we adopt the eigenstates of $\hat{H}_0$ to be the basis for matrix representation. Furthermore, we assume there exist gap in the energy spectrum of $\hat{H}_0$ such that the low energy states are grouped under a subspace $\mathcal{D}_A$, and the high energy state are grouped in the subspace $\mathcal{D}_B$. The Schrödinger equation

in the matrix form reads,

$$\begin{pmatrix} \mathbf{H}_{AA} & \mathbf{H}_{AB} \\ \mathbf{H}_{BA} & \mathbf{H}_{BB} \end{pmatrix} \begin{pmatrix} \mathbf{a}_A \\ \mathbf{a}_B \end{pmatrix} = \epsilon \begin{pmatrix} a_A \\ a_B \end{pmatrix} \tag{B.2}$$

The goal is to perform transformation to uncouple the two sub-matrices $\mathbf{H}_{AA}$ and $\mathbf{H}_{BB}$, so we can just focus on the sub-matrix $\mathbf{H}_{AA}$ with a restricted set of states.

B.2 Analytical Transformations

Consider a unitary operator,

$$\hat{U} = e^{i\hat{S}} = I + i\hat{S} - \frac{1}{2}\hat{S}^2 - \frac{i}{6}\hat{S}^3 + \dots \tag{B.3}$$

where $\hat{S}$ is a Hermitian operator. We perform the unitary transformation,

$$\begin{aligned} \hat{H}_f &= \hat{U}^\dagger \hat{H} \hat{U} = \left(I - i\hat{S} - \frac{1}{2}\hat{S}^2 + \frac{i}{6}\hat{S}^3 + \dots \right) \hat{H} \left(I + i\hat{S} - \frac{1}{2}\hat{S}^2 - \frac{i}{6}\hat{S}^3 + \dots \right) \\ &= \hat{H} + i\left[\hat{H}, \hat{S}\right] - \frac{1}{2}\left[\left[\hat{H}, \hat{S}\right], \hat{S}\right] - \frac{i}{6}\left[\left[\left[\hat{H}, \hat{S}\right], \hat{S}\right], \hat{S}\right] + \dots \end{aligned} \tag{B.4}$$

In this appendix, we consider all operators are represented as matrices with respect to the eigenbasis of the unperturbed Hamiltonian, $\mathbf{H}_0$.

We make an order by order expansion of operators $\mathbf{S}$ and $\mathbf{U}$,

$$\mathbf{S} = \mathbf{S}^{(1)} + \mathbf{S}^{(2)} + \mathbf{S}^{(3)} + \dots, \tag{B.5a}$$

$$\mathbf{U} = \mathbf{U}^{(0)} + \mathbf{U}^{(1)} + \mathbf{U}^{(2)} + \mathbf{U}^{(3)} + \dots, \tag{B.5b}$$

where the order is defined with respect to $\mathbf{H}_1$. Up to the third order, the two set of

matrices are related by

$$\begin{aligned}
\mathbf{U}^{(0)} &= I, \\
\mathbf{U}^{(1)} &= i\mathbf{S}^{(1)}, \\
\mathbf{U}^{(2)} &= i\mathbf{S}^{(2)} - \frac{1}{2}\left(\mathbf{S}^{(1)}\right)^2, \\
\mathbf{U}^{(3)} &= i\mathbf{S}^{(3)} - \frac{1}{2}\left(\mathbf{S}^{(1)}\mathbf{S}^{(2)} + \mathbf{S}^{(2)}\mathbf{S}^{(1)}\right) - \frac{i}{6}\left(\mathbf{S}^{(1)}\right)^3.
\end{aligned} \tag{B.6}$$

Higher order relations can be derived from Eq.((B.3) and Eq.(B.5). Similarly, we decompose the newly transformed Hamiltonian as follows,

$$\mathbf{H}_f = \mathbf{H}^{(0)} + \mathbf{H}^{(1)} + \mathbf{H}^{(2)} + \mathbf{H}^{(3)} + \ldots \tag{B.7}$$

where

$$\mathbf{H}^{(0)} = \mathbf{H}_0, \tag{B.8a}$$

$$\mathbf{H}^{(1)} = \mathbf{H}_1 + i\left[\mathbf{H}_0, \mathbf{S}^{(1)}\right], \tag{B.8b}$$

$$\mathbf{H}^{(2)} = i\left[\mathbf{H}_0, \mathbf{S}^{(2)}\right] + i\left[\mathbf{H}_1, \mathbf{S}^{(1)}\right] - \frac{1}{2}\left[\left[\mathbf{H}_0, \mathbf{S}^{(1)}\right], \mathbf{S}^{(1)}\right], \tag{B.8c}$$

$$\begin{aligned}
\mathbf{H}^{(3)} &= i\left[\mathbf{H}_0, \mathbf{S}^{(3)}\right] + i\left[\mathbf{H}_1, \mathbf{S}^{(2)}\right] - \frac{1}{2}\left[\left[\mathbf{H}_0, \mathbf{S}^{(1)}\right], \mathbf{S}^{(2)}\right] \\
&\quad -\frac{1}{2}\left[\left[\mathbf{H}_0, \mathbf{S}^{(2)}\right], \mathbf{S}^{(1)}\right] - \frac{1}{2}\left[\left[\mathbf{H}_1, \mathbf{S}^{(1)}\right], \mathbf{S}^{(1)}\right] \\
&\quad -\frac{i}{6}\left[\left[\left[\mathbf{H}_0, \mathbf{S}^{(1)}\right], \mathbf{S}^{(1)}\right], \mathbf{S}^{(1)}\right],
\end{aligned} \tag{B.8d}$$

Again, high order of $\mathbf{H}^{(n)}$ can be derived in the similar fashion.

When the unitary operator $\hat{U}$ is expanded and kept up to order n for the transformation described in Eq.(B.4), we denote the n-th cut-off transformation as $\mathbf{U}_f^{(n)} = \sum_{i=1}^{n} \mathbf{U}^{(i)}$, and the approximate Hamiltonian $\mathbf{H}_f^{(n)} = \sum_{i=0}^{n} \mathbf{H}^{(i)}$. We make several remarks at this point. First of all, $\mathbf{U}_f^{(n)}$ is not a unitary matrix because the matrix product $\left(\mathbf{U}^{(n)}\right)^\dagger \mathbf{U}^{(n)}$ contains off-diagonal matrix elements proportional of the

$(n+1)$-th order. In other words, $\mathbf{U}_f^{(n)}$ looks unitary up to the $n-$th order. Secondly, $\mathbf{H}_f^{(n)}$ is not identical to the transformed Hamiltonian, $\left(\mathbf{U}_f^{(n)}\right)^\dagger \mathbf{H}\mathbf{U}_f^{(n)}$, which contains perturbative order up to $2n$. Rather, $\mathbf{H}_f^{(n)}$ is the sum of the transformations up to the n-th order and discards the rest.

The strategy of the perturbative expansion is to find a sequence of matrices, $\mathbf{S}^{(1)}, \mathbf{S}^{(2)}, \ldots, \mathbf{S}^{(n)}$ such that the approximate Hamiltonian, $\mathbf{H}_f^{(n)}$ is exactly block-diagonal up to $n+1$-th order with two sub-matrices corresponding to the $\mathcal{D}_A$ and $\mathcal{D}_B$ subspaces respectively.

We now present the analytical derivation of $\mathbf{S}^{(n)}$ for $n = 1$, and 2. In this thesis, many effective models, such as t-J model and Heisenberg model, are derived with perturbative expansion up to second order.

B.2.1 First Order

The first order of the approximate Hamiltonian, $\mathbf{H}^{(1)}$ is given in Eq.(B.8b). Let us denote upper and lower off-diagonal blocks as $\mathbf{H}_{AB}^{(1)}$ and $\mathbf{H}_{BA}^{(1)}$ respectively. The matrix elements of the two off-diagonal matrices are related by $\left(\mathbf{H}_{AB}^{(1)}\right)_{ij} = \left(\mathbf{H}_{AB}^{(1)}\right)_{ji}^*$. Thus we only need to find $\mathbf{S}^{(1)}$ to fulfill the condition

$$\mathbf{H}_{AB}^{(1)} = \left(\mathbf{H}_1\right)_{AB} + i\left[\mathbf{H}_0, \mathbf{S}^{(1)}\right]_{AB} = 0, \tag{B.9}$$

and the other off-diagonal block, BA, will automatically be satisfied.

Let us study Eq.(B.9) in some details. The commutation between the two matri-

ces, $\left[\mathbf{H}_0, \mathbf{S}^{(1)}\right]$, can be written as

$$\begin{aligned}
\left[\mathbf{H}_0, \mathbf{S}^{(1)}\right] &= \begin{pmatrix} (\mathbf{H}_0)_{AA} & 0 \\ 0 & (\mathbf{H}_0)_{BB} \end{pmatrix} \begin{pmatrix} \mathbf{S}^{(1)}_{AA} & \mathbf{S}^{(1)}_{AB} \\ \mathbf{S}^{(1)}_{BA} & \mathbf{S}^{(1)}_{BB} \end{pmatrix} \\
&- \begin{pmatrix} \mathbf{S}^{(1)}_{AA} & \mathbf{S}^{(1)}_{AB} \\ \mathbf{S}^{(1)}_{BA} & \mathbf{S}^{(1)}_{BB} \end{pmatrix} \begin{pmatrix} (\mathbf{H}_0)_{AA} & 0 \\ 0 & (\mathbf{H}_0)_{BB} \end{pmatrix} \\
&= \begin{pmatrix} (\mathbf{H}_0)_{AA}\mathbf{S}^{(1)}_{AA} - \mathbf{S}^{(1)}_{AA}(\mathbf{H}_0)_{AA} & (\mathbf{H}_0)_{AA}\mathbf{S}^{(1)}_{AB} - \mathbf{S}^{(1)}_{AB}(\mathbf{H}_0)_{BB} \\ (\mathbf{H}_0)_{BB}\mathbf{S}^{(1)}_{BA} - \mathbf{S}^{(1)}_{BA}(\mathbf{H}_0)_{AA} & (\mathbf{H}_0)_{BB}\mathbf{S}^{(1)}_{BB} - \mathbf{S}^{(1)}_{BB}(\mathbf{H}_0)_{BB} \end{pmatrix}
\end{aligned} \tag{B.10}$$

Eq.(B.9) requires,

$$\left[\mathbf{H}_0, \mathbf{S}^{(1)}\right]_{AB} = i\,(\mathbf{H}_1)_{AB} \tag{B.11a}$$

$$\rightarrow \quad (\mathbf{H}_0)_{AA}\mathbf{S}^{(1)}_{AB} - \mathbf{S}^{(1)}_{AB}(\mathbf{H}_0)_{BB} = i\,(\mathbf{H}_1)_{AB}\,. \tag{B.11b}$$

In terms of matrix elements,

$$(\mathbf{H}_0)_{kk}\mathbf{S}^{(1)}_{kl} - \mathbf{S}^{(1)}_{kl}(\mathbf{H}_0)_{ll} = i\,(\mathbf{H}_1)_{kl}\,, \tag{B.12a}$$

$$\rightarrow \quad \left(\epsilon^0_k - \epsilon^0_l\right) S^{(1)}_{kl} = i\,(\mathbf{H}_1)_{kl}\,, \tag{B.12b}$$

$$\rightarrow \quad \mathbf{S}^{(1)}_{kl} = \frac{i\,(\mathbf{H}_1)_{kl}}{\epsilon^0_k - \epsilon^0_l}, \tag{B.12c}$$

for all states k in $\mathcal{D}_A$ and states l in $\mathcal{D}_B$.

By Hermitian property of $\mathbf{S}$,

$$\mathbf{S}^{(1)}_{lk} = (\mathbf{S}_{kl})^* = \frac{i\mathbf{H}'_{lk}}{\epsilon^0_l - \epsilon^0_k}, \tag{B.13}$$

for all states k in $\mathcal{D}_A$ and states l in $\mathcal{D}_B$.

Since Eq.(B.9) does not involve $\mathbf{S}^{(1)}_{AA}$ and $\mathbf{S}^{(1)}_{BB}$, we are free to set them to zero matrix.

With the defined $\mathbf{S}^{(1)}$, the first order transformed Hamiltonian reads,

$$\mathbf{H}^{(1)} = \begin{pmatrix} (\mathbf{H}_0)_{AA} + (\mathbf{H}_1)_{AA} & 0 \\ 0 & (\mathbf{H}_0)_{BB} + (\mathbf{H}_1)_{BB} \end{pmatrix} \tag{B.14}$$

B.2.2 Second Order

Following the same line of logic, we would like to find $\mathbf{S}^{(2)}$, which satisfy the following condition,

$$\mathbf{H}^{(2)}_{AB} = i\left[\mathbf{H}_0, \mathbf{S}^{(2)}\right]_{AB} + i\left[\mathbf{H}_1, \mathbf{S}^{(1)}\right]_{AB} - \frac{1}{2}\left[\left[\mathbf{H}_0, \mathbf{S}^{(1)}\right], \mathbf{S}^{(1)}\right]_{AB} = 0, \tag{B.15}$$

where $\mathbf{S}^{(1)}$ is given in the first order derivation.

We again expand the commutators of matrices and get

$$\begin{aligned}
\left[\mathbf{H}_0, \mathbf{S}^{(2)}\right] &= \begin{pmatrix} (\mathbf{H}_0)_{AA}\mathbf{S}^{(2)}_{AA} - \mathbf{S}^{(2)}_{AA}(\mathbf{H}_0)_{AA} & (\mathbf{H}_0)_{AA}\mathbf{S}^{(2)}_{AB} - \mathbf{S}^{(2)}_{AB}(\mathbf{H}_0)_{BB} \\ (\mathbf{H}_0)_{BB}\mathbf{S}^{(2)}_{BA} - \mathbf{S}^{(2)}_{BA}(\mathbf{H}_0)_{AA} & (\mathbf{H}_0)_{BB}\mathbf{S}^{(2)}_{BB} - \mathbf{S}^{(2)}_{BB}(\mathbf{H}_0)_{BB} \end{pmatrix}, \\
\left[\mathbf{H}_1, \mathbf{S}^{(1)}\right] &= \begin{pmatrix} (\mathbf{H}_1)_{AA}\mathbf{S}^{(1)}_{AA} - \mathbf{S}^{(1)}_{AA}(\mathbf{H}_1)_{AA} & (\mathbf{H}_1)_{AA}\mathbf{S}^{(1)}_{AB} - \mathbf{S}^{(1)}_{AB}(\mathbf{H}_1)_{BB} \\ (\mathbf{H}_1)_{BB}\mathbf{S}^{(1)}_{BA} - \mathbf{S}^{(1)}_{BA}(\mathbf{H}_1)_{AA} & (\mathbf{H}_1)_{BB}\mathbf{S}^{(1)}_{BB} - \mathbf{S}^{(1)}_{BB}(\mathbf{H}_1)_{BB} \end{pmatrix}, \\
\left[\mathbf{H}_0, \mathbf{S}^{(1)}\right] &= \begin{pmatrix} 0 & i(\mathbf{H}_1)_{AB} \\ i(\mathbf{H}_1)_{BA} & 0 \end{pmatrix}, \\
\left[\left[\mathbf{H}_0, \mathbf{S}^{(1)}\right], \mathbf{S}^{(1)}\right] &= \begin{pmatrix} i\left((\mathbf{H}_1)_{AB}\mathbf{S}^{(1)}_{BA} - \mathbf{S}^{(1)}_{AB}(\mathbf{H}_1)_{BA}\right) & 0 \\ 0 & i\left((\mathbf{H}_1)_{BA}\mathbf{S}^{(1)}_{AB} - \mathbf{S}^{(1)}_{BA}(\mathbf{H}_1)_{AB}\right) \end{pmatrix},
\end{aligned} \tag{B.16}$$

Given Eq.(B.15) and the explicit matrix forms of the commutators, one can derive specific conditions for the matrix elements for off-diagonal matrix $\mathbf{S}^{(2)}_{AB}$,

$$\begin{aligned}
\mathbf{S}^{(2)}_{kl} &= -\frac{\sum_{k'\in\mathcal{D}_A}(\mathbf{H}_1)_{kk'}\mathbf{S}^{(1)}_{k'l} - \sum_{l'\in\mathcal{D}_B}\mathbf{S}^{(1)}_{kl'}(\mathbf{H}_1)_{l'l}}{\epsilon^0_k - \epsilon^0_l}, \\
&= -i\sum_{k'\in\mathcal{D}_A}\frac{(\mathbf{H}_1)_{kk'}(\mathbf{H}_1)_{k'l}}{(\epsilon^0_k - \epsilon^0_l)(\epsilon^0_{k'} - \epsilon^0_l)} + i\sum_{l'\in\mathcal{D}_B}\frac{(\mathbf{H}_1)_{kl'}(\mathbf{H}_1)_{l'l}}{(\epsilon^0_k - \epsilon^0_l)(\epsilon^0_k - \epsilon^0_{l'})},
\end{aligned} \tag{B.17}$$

where $k, k' \in \mathcal{D}_A$ and $l, l' \in \mathcal{D}_B$. As for the BA block, we get $\mathbf{S}^{(2)}_{lk} = \left(\mathbf{S}^{(2)}_{kl}\right)^*$ by Hermitian property of $\mathbf{S}$. Again, Eq.(B.15) does not involve the diagonal-block matrices, $\mathbf{S}^{(2)}_{AA}$ and $\mathbf{S}^{(2)}_{BB}$, we can simply set them to zero.

The second order term, $\mathbf{H}^{(2)}$, of the approximate Hamiltonian now reads

$$\mathbf{H}^{(2)} = \begin{pmatrix} \frac{i}{2}\left((\mathbf{H}_1)_{AB}\,\mathbf{S}^{(1)}_{BA} - \mathbf{S}^{(1)}_{AB}\,(\mathbf{H}_1)_{BA}\right) & 0 \\ 0 & \frac{i}{2}\left((\mathbf{H}_1)_{BA}\,\mathbf{S}^{(1)}_{AB} - \mathbf{S}^{(1)}_{BA}\,(\mathbf{H}_1)_{AB}\right) \end{pmatrix} \quad \text{(B.18)}$$

If we only would like to keep the approximate Hamiltonian up to the second order, then it would read

$$\left(\mathbf{H}^{(2)}_f\right)_{AA} = (\mathbf{H}_0)_{AA} + (\mathbf{H}_1)_{AA} + \frac{i}{2}\left((\mathbf{H}_1)_{AB}\,\mathbf{S}^{(1)}_{BA} - \mathbf{S}^{(1)}_{AB}\,(\mathbf{H}_1)_{BA}\right), \quad \text{(B.19a)}$$

$$\left(\mathbf{H}^{(2)}_f\right)_{BB} = (\mathbf{H}_0)_{AA} + (\mathbf{H}_1)_{AA} + \frac{i}{2}\left((\mathbf{H}_1)_{AB}\,\mathbf{S}^{(1)}_{BA} - \mathbf{S}^{(1)}_{AB}\,(\mathbf{H}_1)_{BA}\right), \quad \text{(B.19b)}$$

$$\left(\mathbf{H}^{(2)}_f\right)_{AB} = 0, \quad \text{(B.19c)}$$

$$\left(\mathbf{H}^{(2)}_f\right)_{BA} = 0. \quad \text{(B.19d)}$$

If we need to carry out the third-order transformation, then we simply need to identify a Hermitian matrix, $\mathbf{S}^{(3)}$, which can make the off-diagonal block of Eq.(B.8d) to be strictly zero. For even higher order, the general idea still holds.

B.3 Iterative Approach to Numerical Transformation

As seen in the previous section, the expression of proper Hermitian matrix, $\mathbf{S}^{(n)}$, needed for the analytical transformation rapidly increases in complexity as n increases. This motivates a need to perform these perturbative calculations iteratively with a

computer program. In each iteration, two operations are done. The first task is to apply a first order transformation (discussed in Sec.[B.2.1]) to decouple the two subspaces $\mathcal{D}_A$ and $\mathcal{D}_B$. The second task is to orthogonalize the transformed basis. The iteration will repeat these two tasks until the matrix elements in the off-diagonal block $\left(\mathbf{H}_{MO}^{(n)}\right)_{AB}$ are bounded by some pre-defined threshold value.

Given the Hamiltonian $\mathbf{H} = \mathbf{H}_0 + \mathbf{H}_1$, we apply the first order transformation to get

$$\begin{aligned}
\mathbf{H}_M^{(1)} &= \left(\mathbf{U}^{(1)}\right)^\dagger \mathbf{H}\mathbf{U}^{(1)} \\
&= \left(\mathbf{I} - i\mathbf{S}^{(1)}\right)\left(\mathbf{H}_0 + \mathbf{H}_1\right)\left(\mathbf{I} + i\mathbf{S}^{(1)}\right) \\
&= \mathbf{H}_0 + \mathbf{H}_1 + i\left[\mathbf{H}_0, \mathbf{S}^{(1)}\right] + i\left[\mathbf{H}_1, \mathbf{S}^{(1)}\right] + \mathbf{S}^{(1)}\left(\mathbf{H}_0 + \mathbf{H}_1\right)\mathbf{S}^{(1)} \\
&= \mathbf{H}_f^{(1)} + i\left[\mathbf{H}_1, \mathbf{S}^{(1)}\right] + \mathbf{S}^{(1)}\left(\mathbf{H}_0 + \mathbf{H}_1\right)\mathbf{S}^{(1)}, \qquad \text{(B.20)}
\end{aligned}$$

where $\mathbf{S}^{(1)}$ is derived in Sec.[B.2.1].

The Schrödinger equation for the transformed Hamiltonian $\mathbf{H}_M^{(1)}$ is a generalized eigenvalue problem. This is true because the transformation $\mathbf{U}^{(1)}$ is not a unitary matrix and can be verified by $\mathbf{U}^{(1)}\left(\mathbf{U}^{(1)}\right)^\dagger = \mathbf{I} + \mathbf{S}^2$. Thus, the generalized eigenvalue problem reads,

$$\begin{aligned}
\left(\mathbf{U}^{(1)}\right)^\dagger \mathbf{H}\mathbf{a} &= \epsilon\left(\mathbf{U}^{(1)}\right)^\dagger \mathbf{a} \\
\left(\mathbf{U}^{(1)}\right)^\dagger \mathbf{H}\mathbf{U}^{(1)}\left(\mathbf{U}^{(1)}\right)^{-1}\mathbf{a} &= \epsilon\left(\mathbf{U}_f^{(1)}\right)^\dagger \mathbf{U}^{(1)}\left(\mathbf{U}^{(1)}\right)^{-1}\mathbf{a} \\
\mathbf{H}_M^{(1)}\mathbf{b}^{(1)} &= \epsilon\mathbf{M}_1\mathbf{b}^{(1)}, \qquad \text{(B.21)}
\end{aligned}$$

where $\mathbf{a}$ and ϵ are, respectively, one of the eigenvector and corresponding eigenenergies of $\mathbf{H}$, $\mathbf{b}^{(1)} = \left(\mathbf{U}^{(1)}\right)^{-1}\mathbf{a}$ and $\mathbf{M}_1 = \left(\mathbf{U}^{(1)}\right)^\dagger \mathbf{U}^{(1)}$ is the overlapping matrix for the

rotated basis. The Hamiltonian $\mathbf{H}_M^{(1)}$ can be orthogonalized by using the $\left(\sqrt{\mathbf{M}_1}\right)^{-1}$ trick discussed in Sec.[2.1.1]. The new Hamiltonian is given by

$$\begin{aligned}
\mathbf{H}_{MO}^{(1)} &= \left(\sqrt{\mathbf{M}}\right)^{-1} \mathbf{H}_M^{(1)} \left(\sqrt{\mathbf{M}}\right)^{-1}, \\
&= \left(\sqrt{\mathbf{M}}\right)^{-1} \left(\mathbf{U}^{(1)}\right)^{\dagger} \mathbf{H}\mathbf{U}^{(1)} \left(\sqrt{\mathbf{M}}\right)^{-1}, \\
&= \mathbf{Z}^{\dagger}\mathbf{H}\mathbf{Z}, \qquad \text{(B.22)}
\end{aligned}$$

where $\mathbf{Z} = \mathbf{U}^{(1)} \left(\sqrt{\mathbf{M}}\right)^{-1}$. In summary, each iteration involves two tasks: 1) applying first order transformation and 2) solving the generalized eigenvalue problem.

So far, we have shown how the matrix elements changes when we apply the transformation $\mathbf{Z}^{\dagger}\mathbf{H}\mathbf{Z}$ to the Hamiltonian matrix. The next task is to determine how the new (after transformation) and old (before transformation) basis are related.

Consider the old basis are labelled by regular alphabet, $\{|j\rangle\}$ and the new basis are labelled by Greek letters, $\{|\beta\rangle\}$. The Hamiltonian matrix elements are given by

$$\begin{aligned}
\left(\mathbf{H}_{MO}^{(1)}\right)_{\alpha,\beta} &= \sum_{ij} \left(\mathbf{Z}^{\dagger}\right)_{\alpha,i} \mathbf{H}_{i,j} \mathbf{Z}_{j,\beta}, \\
&= \sum_{i,j} \langle\alpha|\, i\rangle H_{i,j} \langle j\,|\beta\rangle\,. \qquad \text{(B.23)}
\end{aligned}$$

The two ways of relating Hamiltonian matrix elements in different basis gives $\langle j|\,\beta\rangle = \mathbf{Z}_{j,\beta}$.

If the desired threshold is not achieved, we substitute $\mathbf{H}$ with the new Hamiltonian $\mathbf{H}_{MO}^{(1)} = diag(\mathbf{H}_{MO}^{(1)}) + offdiag(\mathbf{H}_{MO}^{(1)})$ derived in the present iteration. $\mathbf{H}_{MO}^{(1)}$ is manually separated into the diagonal matrix (used in place of $\mathbf{H}_0$) and off-diagonal matrix (treated as perturbation in place of $\mathbf{H}_1$). Now we repeat the iteration. The end result of the second iteration is Hamiltonian matrix $\mathbf{H}_{MO}^{(2)}$ with a corresponding

transformation matrix $\mathbf{Z_2}$ which relates the basis before and after the rotation performed during this iteration. In general, at the end of the $n-$th iteration, we obtain $\mathbf{H}_{MO}^{(n)}$ and the final basis is related to the original basis, which is the set of eigenstates of $\mathbf{H}_0$, by the transformation matrix $\mathbf{W}_n = \mathbf{Z}_1 \ldots \mathbf{Z}_n$.

Thus at the end of the $n-$th iteration, we obtain

$$\begin{aligned} \mathbf{H}_{MO}^{(n)} &= \mathbf{W}_n^{\dagger} \mathbf{H} \mathbf{W}_n, \\ &= \mathbf{Z}_n^{\dagger} \ldots \mathbf{Z}_1^{\dagger} \mathbf{H} \mathbf{Z}_1 \ldots \mathbf{Z}_n, \end{aligned} \tag{B.24}$$

The new basis at the n-th iteration is given by $\{\left|\beta^{(n)}\right\rangle\}$, which are related to the original basis $\{|i\rangle\}$ by $|\beta\rangle^{(n)} = \sum_j (\mathbf{W}_n)_{j,\beta} |j\rangle$.

Appendix C

Cotunneling Through a Triple Quantum Dot

In this appendix, we provide a brief derivation of cotunneling rate, Eq.(6.9), presented in Chapter [6]. In particular, we consider the dominant kind of cotunneling process that involves exchanging a pair of electrons between one lead and the triple quantum dot in the spin blockade regime. This cotunneling process does not directly transport an electron through the device; rather, the system gets out of the spin-3/2 state when an exchange of electrons takes place.

First, we remind the model of the present problem. For our present purpose, we can consider the TQD is coupled to one of the leads, for instance, the left lead. The Hamiltonian for the triple quantum dot (TQD) and the left lead reads,

$$\begin{aligned} \hat{H} &= \hat{H}_0 + \hat{H}_1, \\ &= \hat{H}_{TQD} + \hat{H}_L + \hat{H}_{LD}, \end{aligned} \tag{C.1}$$

where, $\hat{H}_{TQD}$ is the five-level Hubbard model considered in Chapter [6]. $\hat{H}_L$ is the 1D tight-binding chain of free electrons located at the left lead, respectively. $\hat{H}_{LD}$ represents the interaction between the TQD and the left lead, respectively. The interacting Hamiltonian is given by

$$\hat{H}_{LD} = \sum_{i,k} \tilde{t}_i^L(k) \left(d_{k\sigma}^\dagger c_{i\sigma} + h.c. \right), \tag{C.2}$$

In this case, we take $\hat{H}_0 = \hat{H}_{TQD} + \hat{H}_L$ and $\hat{H}_1 = \hat{H}_{LD}$.

We next introduce the basis used for constructing the matrix elements for Fermi Golden Rule calculations. The eigenstates of $\hat{H}_0$ are represented as $|\Psi\rangle = |\alpha_{Ne}\rangle \otimes |L\rangle$, where $|\alpha_{Ne}\rangle$ is an Ne-electron eigenstate of $\hat{H}_{TQD}$ and $|L\rangle$ is an eigenstate of $\hat{H}_L$.

The generalized, second order Fermi Golden's rule reads,

$$W_{fi}^{(2)} = \frac{2\pi}{\hbar} \left| \sum_\mu \frac{\mathbf{H}_{f\mu}\mathbf{H}_{\mu i}}{E_\mu^0 - E_i^0} \right|^2 \delta(E_f^0 - E_i^0), \tag{C.3}$$

where $|i\rangle$, $|f\rangle$, and $|\mu\rangle$ are the eigenstates of $\hat{H}_0$ with eigenenergies E_f^0, E_i^0, and E_μ^0 respectively.

For the present problem of spin blockade in a triple quantum dot, we denote $|i\rangle = |\alpha_3\rangle |L\rangle$ as an initial eigenstate of $\hat{H}_0$ with triple quantum dot trapped in one of the four possible spin-3/2 states, i.e. $|\alpha_3\rangle \in \{|S = 3/2, S_z = \pm 1/2, \pm 3/2\rangle\}$. We then specify a final state $|f_{kk'}^{\sigma\sigma'}\rangle$ with respect to the given initial state $|i\rangle$ as

$$|f_{kk'}^{\sigma\sigma'}\rangle = |\beta_3\rangle \otimes \left(\hat{c}_{k'\sigma'} \hat{c}_{k\sigma}^\dagger \right) |L\rangle, \tag{C.4}$$

For our problem, the final state above is obtained from the initial state by exchanging a pair of electrons between the TQD and the lead. As a result of this exchange, the TQD state is scattered from $|\alpha_3\rangle$ to $|\beta_3\rangle$, which is one of the three-electron eigenstates,

while the left lead first gains an electron in state $|k_\sigma\rangle$ then loses another electron in the state $|k'_{\sigma'}\rangle$. The intermediate states, denoted by $|\mu\rangle = |\alpha_2\rangle \left(c^\dagger_{k\sigma}|L\rangle\right)$, involves only states from the 2-electron subspace because we consider the TQD is tuned to conduct current between 2-electron and 3-electron regime.

Substituting all the relevant details into Eq.(C.3), we obtain

$$\begin{aligned} W^{(2)}_{i\to f^{\sigma\sigma'}_{k_r k'_r}} &= \frac{2\pi}{\hbar}\left|\sum_{i_o,i'_o,\alpha_2} \tilde{t}^L_{i_o}(k)\left(\tilde{t}^L_{i'_o}(k')\right)^* \langle L|\hat{d}_{k\sigma}\hat{d}^\dagger_{k\sigma}|L\rangle\langle L|\hat{d}^\dagger_{k'\sigma'}\hat{d}_{k'\sigma'}|L\rangle \right. \\ &\quad \left.\times\frac{\left(A^{i'_o\sigma'}_{\alpha_3\alpha_2}\right)^* A^{i_o\sigma}_{\beta_3\alpha_2}}{E^0_{\alpha_2}-E^0_{\alpha_3}+\epsilon_{k\sigma}}\right|^2 \delta\left(E_{\beta_3}-E_{\alpha_3}+\epsilon(k)-\epsilon(k')\right), \\ &= \frac{2\pi}{\hbar}\left|\sum_{i_o,i'_o,\alpha_2} \tilde{t}^L_{i_o}(k)\left(\tilde{t}^L_{i'_o}(k')\right)^* \times \frac{\left(C^{i'_o\sigma'}_{\alpha_3\alpha_2}\right)^* C^{i_o\sigma}_{\beta_3\alpha_2}}{E^0_{\alpha_2}-E^0_{\alpha_3}+\epsilon_{k\sigma}}\right|^2 \\ &\quad \times(1-\hat{n}_{k,\sigma})\hat{n}_{k',\sigma'}\delta\left(E_{\beta_3}-E_{\alpha_3}+\epsilon(k)-\epsilon(k')\right), \end{aligned} \tag{C.5}$$

where $C^{i\sigma}_{\alpha_3\alpha_2} = \langle\alpha_3|d^\dagger_{i\sigma}|\alpha_2\rangle$, and $\hat{n}_{k\sigma} = \hat{d}^\dagger_{k\sigma}\hat{d}_{k\sigma}$.

Since we are only interested in the TQD states, we have to average the rate in Eq.(C.5) over all possible lead states $|L\rangle$ with thermal equilibrium weight. So we may write a 2nd order transition rate involving only the TQD states,

$$\begin{aligned} W^2_{\alpha_3\to\beta_3} &= \sum_{k,k'\sigma,\sigma'} F(\epsilon_{k'})(1-F(\epsilon_k)) \\ &\quad \times\frac{2\pi}{\hbar}\left|\sum_{\alpha_2,i_o,i'_o} \tilde{t}^L_{i_o}(k)\left(\tilde{t}^L_{i'_o}(k')\right)^* \frac{\left(C^{1\sigma'}_{\alpha_3\alpha_2}\right)^* C^{1\sigma}_{\beta_3\alpha_2}}{E_{\alpha_3}-E_{\gamma_2}-\epsilon(k)}\right|^2 \\ &\quad \times\delta\left(E_{\beta_3}-E_{\alpha_3}+\epsilon(k)-\epsilon(k')\right), \end{aligned} \tag{C.6}$$

where averages of $\hat{n}_{k\sigma}$ is replaced by the Fermi function $F(\epsilon) = 1/(1+\exp(\epsilon-\mu))$ with the chemical potential of lead μ.